# First-principles based treatment of charged species equilibria at electrochemical interfaces: model system of zirconium oxide and titanium oxide

by

Jing Yang

B.S., Physics, Peking University, China

Submitted to the Department of Materials Science and Engineering in partial fulfillment of the requirements for the degree of

Doctor of Philosophy

at the

MASSACHUSETTS INSTITUTE OF TECHONOLOGY

February 2020



Signature of Author: _____

Jing Yang

Department of Materials Science and Engineering

January 10th, 2020

Certified by: _____

Bilge Yildiz

Professor of Materials Science and Engineering

And Professor of Nuclear Science and Engineering

Thesis Supervisor

Accepted by: _____

Donald R. Sadoway

John F. Elliott Professor of Materials Chemistry

Chair, Department Committee on Graduate Studies

# First-principles based treatment of charged species equilibria at electrochemical interfaces: model system of zirconium oxide and titanium oxide

by

Jing Yang

Submitted to the Department of Materials Science and Engineering on Jan. 10th, 2020 in partial fulfillment of the requirements for the degree of Doctor of Philosophy

## Abstract

Ionic defects are known to influence the magnetic, electronic and transport properties of oxide materials. Understanding defect chemistry provides guidelines for defect engineering in various applications including energy storage and conversion, corrosion, and neuromorphic computing devices. While DFT calculations have been proven as a powerful tool for modeling point defects in bulk oxide materials, challenges remain for linking atomistic results with experimentally-measurable materials properties, where impurities and complicated microstructures exist and the materials deviate from ideal bulk behavior. This thesis aims to bridge this gap on two aspects. First, we study the coupled electro-chemo-mechanical effects of ionic impurities in bulk oxide materials. Second, we develop a modeling framework for describing point defect redistribution at extended defects, including grain boundaries, oxide/oxide interfaces, and oxide/water interfaces.

The first part of this thesis deals with zirconium oxide in the context of corrosion of zirconium alloys used as nuclear cladding materials in light water reactors. We provide physically-deduced diffusion coefficients for higher-level modeling as well as better mechanistic understanding of zirconium alloy corrosion by studying defect equilibria in $ZrO_2$ passive films. A first-principles based model for predicting charged species redistribution profiles at electrochemical interfaces is established and applied to $ZrO_2/Cr_2O_3$ and $ZrO_2$/water interfaces, and $ZrO_2$ grain boundaries. Defect redistribution at these extended defects can lead to significant changes in transport properties of oxides.

The second part applies similar methodology to $TiO_2$ as a model system for studying field-assisted sintering (FAST). FAST has been demonstrated for multiple ceramic materials as a promising sintering technique for shortening consolidation times and lowering sintering temperatures. By studying the defect chemistry of acceptor- and donor-$TiO_2$ and designing experiments accordingly, we show that while Joule heating is the dominant effect of the applied electric field, the shrinkage rate also correlates strongly with titanium diffusivity. Through donor doping, which increases the concentrations of fast-diffusing titanium interstitials, a higher shrinkage rate is achievable.

These results prove that first-principles base calculations are capable of predicting the defect chemistry of oxide materials that quantitatively agree with measured values. Such understanding of defect chemistry gives insights into practical defect engineering strategies that are broadly applicable to electrochemical applications.

Thesis Supervisor: Bilge Yildiz

Professor of Materials Science and Engineering and Nuclear Science and Engineering

**Acknowledgement**

I would like to express my sincere gratitude to Dr. Mostafa Youssef and my thesis advisor, Prof. Bilge Yildiz for their guidance and assistance throughout my thesis project. I would like to thank Dr. Clement Nicollet and Prof. Harry L. Tuller for collaboration on titanium oxide-related research. I am also grateful to Prof. Harry L. Tuller and Prof. Jeffrey Grossman for serving on my thesis committee and for providing constructive feedback throughout my thesis research.

During my years in the Yildiz group, I have had the pleasure to interact with many diligent and supportive colleagues and I have learned a lot from them. They are: Dr. Mostafa Youssef, Dr. Dario Marrocchelli, Dr. Yan Chen, Dr. Kiran Adepalli, Dr. Aravind Krishnamoorthy, Dr. Jonathan M. Polfus, Dr. Kiran Adepalli, Dr. Gulin Vardar, Dr. Qiyang Lu, Dr. Lixin Sun, Dr. Roland Bliem, Dr. William Bowman, Dr. Franziska Hess, Dr. Cigdem Toparli, Dr. Konstantin Klyukin, Dr. Pjotrs Zguns, Minh A. Dinh, Jiayue Wang, Dongha Kim, Yen-ting Chi, Vrindaa Somjit, William Zhou, Younggyu Kim, Sara Sand, Hantao Zhang, Seungchan Ryu, and Huijun Chen.

I would like to thank my friends, Yixiang Liu and Jinghui Miao, who kept me company.

I deeply thank my parents, Chunxiao Wu and Zhongming Yang, who supported me with love and trust.

This work is supported by the Consortium for Advanced Simulation of Light Water Reactors (CASL), an Energy Innovation Hub for Modeling and Simulation of Nuclear Reactors under U.S. Department of Energy Contract No. DE-AC05-00OR22725. Computational resources are provided by the Extreme Science and Engineering Discovery Environment (XSEDE) program for calculations performed under allocation No. TG-DMR120025 and National Energy Research Scientific Computing Center (NERSC) under allocation m2403.

# Contents

# 1 Introduction

Point defects and their redistribution controls many properties of electrical and electrochemical systems and have been of great interest for both fundamental studies [1] and device applications [2]. Ionic defects are known to influence the magnetic, electronic and transport properties of metal oxides [3-5]. Understanding the equilibrium distribution of defects serves as the foundation for studying reaction and diffusion processes in related systems. However, addressing the electronic and ionic structures of point defects, especially their redistribution at extended defects (interfaces, surfaces, grain boundaries, and dislocations), is not a trivial task. The nature of bonds between ions could be significantly altered near interfaces due to varying chemical composition, stress field and crystal structure.

Density functional theory (DFT) calculations have proven successful in predicting bulk defect equilibria at various thermodynamic conditions for oxide materials [6, 7]. Modeling ionic defect redistribution at interfaces, however, is beyond the spatial extent that DFT can currently reach by itself, and is a topic in progress. Only limited work on metal/oxide interfaces [8], gas/oxide interfaces [9], grain boundaries [10-12] and oxide PN homojunction [13] can be found in the literature. In this work, we aim to develop a comprehensive framework which starts with ab initio prediction of defect equilibria in bulk oxides, and predicts their redistribution at electrochemical interfaces. We identify the important factors that come into play in defect redistribution at electrochemical interfaces, and provide a generally-applicable tool for modeling electrochemical devices. We demonstrate that these predictions can be validated against experimentally-measured values and provide atomistic insights into transport processes in bulk oxides and their interfaces.

This introductory chapter consists of four sections. In Section 1.1, we provide a methodological background of *ab initio* study of defective oxides related to this work and the problems solved in this thesis. In Section 1.2 and Section 1.3, we introduce the technological motivations of the two model systems we selected: $ZrO_2$ and $TiO_2$. Section 1.2 introduces the corrosion of zirconium alloy used as cladding of nuclear fuels in light water reactors. Section 1.3 introduces developing field-assisted sintering (FAST) techniques for oxide materials and efforts in understanding the process mechanistically.

Last, Section 1.4 provides an outline of the rest of this thesis with brief introductions of the topics dealt in each chapter.

## 1.1 Context: exploit the predictive power of first-principles calculation for designing functional oxides

In this section, we give a background of state-of-art first-principles based modeling techniques and a brief introduction of the methods that we developed in this work.

A. Studying bulk defects from first-principle calculations

Conventional studies of defect chemistry are usually related to defect reactions and their associated mass action equilibrium constants, which are convenient for experimental interpretation. However, it's difficult to model defect reactions and obtain reaction energies from *ab initio* calculations. Instead, a grand canonical approach is developed and applied for computational studies [14], where the formation energy of individual point defect $D^q$ is calculated by:

$$E_{D^q}^{f,bulk} = E_{defected}^{DFT} - E_{perfect}^{DFT} - \sum_i \Delta N_i \mu_i + q(\mathrm{E}_{VBM} + \mu_e) + E_{MP}\,. \qquad (1.1)$$

Here $E_{defected}^{DFT}$ is the DFT-calculated energy of the defective cell, $E_{perfect}^{DFT}$ is the DFT-calculated energy of the perfect cell. $\mu_i$ denotes the chemical potential of each element involved in the cell, and $\Delta N_i$ the relative number of each type of atoms with respect to the perfect cell (e.g. $\Delta N_O = -1$ for oxygen vacancies). $E_{VBM}$ is the valence band maximum from the perfect cell. $\mu_e$ is the Fermi level of electrons relative to the valence band maximum. $E_{MP}$ is the first-order Makov-Payne correction for the finite-size supercell errors in charged defect calculations [15]. The concentration of each defect species $[\mathrm{D}^q]$ can subsequently be expressed by the Boltzmann distribution:

$$[\mathrm{D}^q] = n_D \exp(\frac{E_{D^q}^{f,bulk}}{kT}). \qquad (1.2)$$

Here $n_D$ is the number of possible sites for the defect D per unit formula, $k$ the Boltzmann constant and $T$ temperature. This formulation is only valid for the dilute limit $E_{D^q}^f \ll kT$, and for defects in solids where the entropic contribution is negligible.

The concentrations for free electrons and holes are:

$$n_c = \int_{E_{CBM}}^{\infty} g_c(E) \frac{dE}{1+\exp(\frac{E-\mu_e}{k_B T})} \tag{1.3}$$

$$p_v = \int_{-\infty}^{E_{VBM}} g_v(E) \frac{dE}{1+\exp(\frac{\mu_e - E}{k_B T})} \tag{1.4}$$

Notice that the formation energy for all charged defects, and thus their concentrations, are functions of Fermi level $\mu_e$ . $\mu_e$ is calculated by solving for the charge neutrality condition:

$$\sum_{D,q} q[D^q] + p_v - n_c = 0 \tag{1.5}$$

This scheme has been applied to tetragonal[7] and monoclinic zirconium oxide with success, reproducing experimentally-observed oxygen partial pressure dependence of electric conductivity. Furthermore, migration barriers can be calculated using the climbing image nudged elastic band method [16] and produce self-diffusivities for defect $D^q$, as shown in Figure 1-1[17].

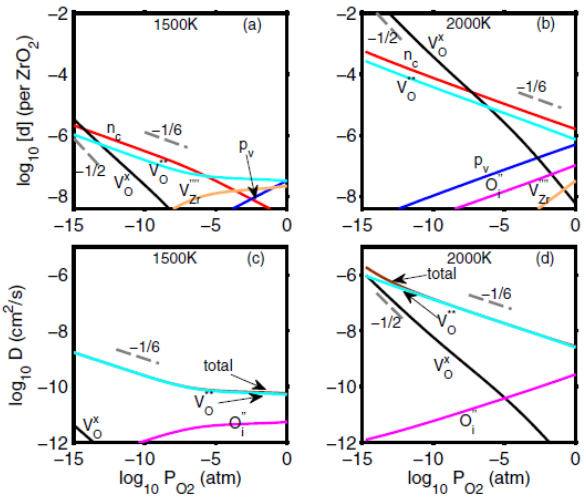


Figure 1-1. Predicted equilibrium defect concentrations for tetragonal $ZrO_2$ at (a) 1500K and (b) 2000K. Self-diffusivities for oxygen defects and total oxygen self-diffusivity at (c) 1500K and (d) 2000K. Figure adopted from Ref. [17].

B. Defect chemistry at interfaces of mixed ionic-electronic conductors

Extending the grand canonical approach for bulk materials to interfacial systems is not straightforward. It appears that the following three aspects need to be addressed comprehensively, and at the same level of theory, in order to build a self-consistent model for interfaces.

First, before considering any electronic or ionic defects, the discontinuities of valence band $\Delta E_v$ and conduction band $\Delta E_c$ immediately at the interface need to be calculated. Theoretically, this band discontinuity corresponds to the large electrostatic potential gradient at ideally abrupt point-defect-free interfaces. This discontinuity is localized in the few atomic layers in the immediate vicinity of the interface and is independent of external perturbations such as dilute doping and applied bias.

Second, charged species have different electrochemical potentials in equilibrated bulk materials. When two materials are put into contact, electronic and ionic defects start to diffuse, driven by this chemical potential difference. This leads to build-up of local electric field and in turn drives drift flux in the opposite direction. When the system equilibrates, drift and diffusion fluxes cancel out and a space-charge layer (SCL) forms, which corresponds to a flat electrochemical potential

$$\tilde{\mu}_{D^q} = \mu^0_{D^q} + kT\ln[\mathrm{D}^q] + q\phi\,, \tag{1.6}$$

where $\phi$ is the electrostatic potential in the space-charge region. In bulk material, $\mu^0_D$ equals $E^{f,bulk}_{D^q}$.

Third, atoms near the interface are in a distinct bonding environment compared to atoms in the bulk. The defect formation energy will change due to interfacial lattice relaxation and chemical composition variation. This adds the segregation energy, $\Delta E^f_{D^q}$, to the defect formation energy of ions in the vicinity of the interface. This region where the segregation energy is non-negligible is termed the core zone.

These three factors have all been recognized and evaluated in the literature, but are usually treated separately with different modeling methods. Predicting band offsets from DFT calculations has been of interest since decades ago and a number of theories have been developed [18]. One commonly accepted scheme was first proposed by Van de Walle and Martin [19] and applied in a number of studies [20, 21], which aligns the band positions to the electrostatic potential across the heterojunction. These studies consider defect-free interfaces and only evaluate the band off-sets. The space-charge potential, $\phi$, built by the drift-diffusion mechanism extends in space for several hundreds to thousands of nanometers, and is usually studied with finite-element methods in the context of semiconductor engineering. The drift-diffusion model is well-developed for

semiconductor heterojunctions [22-24], where only electrons and holes are considered as the mobile species. In that case, there is no need to consider segregation energies since free holes and electrons are assumed to be unaffected by the changes in the bonding at the interface. Only the space-charge potential causes changes in holes and electrons at the interface.

When it comes to ionic or mixed electronic-ionic conductors that are used in electrochemical devices, the ionic defect contribution cannot no longer be neglected. Ionic and electronic drift-diffusion models have been built for mixed electronic-ionic p-n homojunctions made up of p-type and n-type doped $SrTiO_3$ [13]. For such a homojunction this treatment is enough, but for a metal/oxide interfaces [8] or gas/oxide interfaces [9] which have been recently analyzed, the segregation energy is still missing. The defect segregation energy $\Delta E_{D^q}^f$, which has discrete values in each atomic layer close to the interface, can be evaluated using atomic simulation methods [25, 26] and are explicitly accounted for in this work. In fact, these segregation energies are responsible for the formation of the core zone at the interface which exhibits very different defect concentrations in comparison with the extended space charge zone.

These studies, though valuable in qualitatively understanding defect redistribution at interfaces, fail to provide a self-consistent picture taking into account simultaneously localized changes in the chemical bonding at the interface (responsible for core zone formation) and long-range Coulomb interactions in the extended space-charge zone. This will require a combination of atomistic simulation and continuum level modeling which we plan to address in this work.

Attempts have been made to establish interfacial defect chemistry theoretically [27-29]. These theories consider equilibrated defect reactions at the interface as boundary conditions. Counting defect reactions corresponds to a canonical formalism in which particles (defects) are tracked. Such a canonical formalism, while tractable if one knows a priori the important defect reactions, is not in the spirit of the predictive power of first-principle modeling [14]. So far, first-principle based models that are closest to our goal are the model for core and space-charge regions formed at grain boundaries developed in recent years [10-12], in which the segregation energy is included self-consistently in the drift-diffusion model. For such grain boundaries there are no band offsets since both sides

of the band belong to the same material. In other words, band offset is not needed in this case. Below we elaborate more on these grain boundaries models.

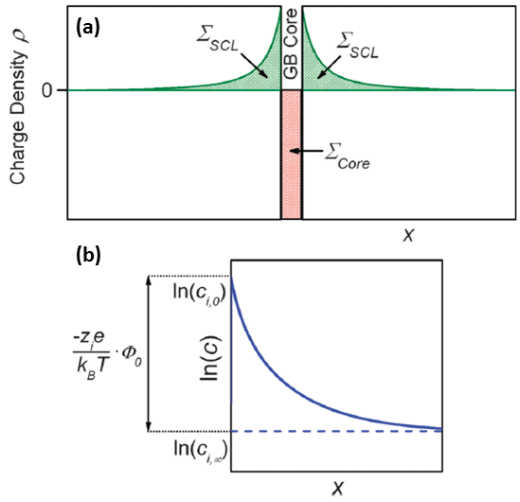


Figure 1-2. Schematic plot of (a) charge density and (b) defect concentration across a grain boundary. Taking advantage of the symmetry of grain boundary, this model only solves one side of the system. Figure taken from Ref. [12].

Figure 1-2 shows schematically the features of a space-charge zone and core zone at a grain boundary. The region close to the boundary, which is defined as the grain boundary core, has a non-zero segregation energy, $\Delta E_{D^q}^f$. This term leads to defect segregation or depletion in the core zone, and charge $\Sigma_{\text{Core}}$. According to the equilibrium condition, $\Sigma_{\text{Core}}$ needs to be compensated by charges outside the core $\Sigma_{\text{SCL}}$. Since the grain boundary is symmetric, we can solve for only one side of the system with $\Sigma_{\text{SCL}} = -\frac{1}{2}\Sigma_{\text{Core}}$ as the global neutrality condition.

The electrostatic potential follows Poisson's equation

$$\frac{d^2\phi}{dx^2} = -\frac{\rho(x)}{\varepsilon_0 \varepsilon_r}. \tag{1.7}$$

$\varepsilon_0$ and $\varepsilon_r$ are the permittivity of vacuum and relative permittivity of the host material, respectively. $\rho(x)$ is the total charge density and evaluated by summing over all electronic and ionic defects. The total potential drop in the space-charge region $\phi_0$, serves

as the boundary condition for solving Poisson's equation. By iterating over $\phi_0$ to achieve global charge neutrality, defect concentrations and $\phi(x)$ are self-consistently solved.

Several issues need to be addressed carefully when extending the current model established for grain boundaries to heterointerfaces. The difficulties come from the asymmetry of hetero-interfaces. First, there is no abrupt change in the band structure at the grain boundary. The band off-sets need to be addressed explicitly for the hetero-interface model. Second, since the electrostatic profiles are all symmetric and $\Sigma_{\text{Core}}$ is always compensated by $\Sigma_{\text{Core}}$, $\phi_0$ is the only iteration variable for the grain boundary model. On the other hand, for the hetero-interface, the potential drops on the two sides are different, adding additional complexity to the numerical model. Third, for the oxide/oxide hetero-interface, cation intermixing should be accounted for. In this thesis, we will address these issues, while extending the models to hetero-interfaces, and ultimately providing a generalized model of interfaces that can in principle be applied to any type of heterointerface including water/oxide interfaces, as we explain below.

C. Connecting defect chemistry with liquid electrochemistry

One interface of interest to this thesis is the oxide-water interface. Significant resemblance exists between ions in a liquid solution and charged defects in a solid. The idea of treating liquid water as large-gap amorphous semiconductor dates back to the 1970s and is widely acknowledged [30]. Numerous attempts, both experimental and computational, have been made to measure the absolute energy positions for liquid water [31-33]. One commonly accepted value is from Coe [34] with electron affinity of -0.12 eV and band gap of 7.0 eV. With this description, ions in liquid water could be treated in similar ways as charged point defects in solids, which serves as a bridge between electrochemistry and semiconductor physics [35]. For example, the Gibbs free energy of formation for $H^+$ ion can be expressed as:

$$\Delta G_f(\mathrm{H}^+) = \Delta \mathrm{G}_f^{\circ}(\mathrm{H}^+) - \mu_H + \mu_e \ , \tag{1.8}$$

where $\Delta G_f^{\circ}(\mathrm{H}^+)$ is the standard Gibbs free energy of formation ($T^{\circ} = 298.15\mathrm{K}$, $P^{\circ} = 1\mathrm{bar}$).

With this formulation, the grand canonical approach described previously could also account for equilibrium ion concentration in water solution. Furthermore, by making the analogy between ions in water solution and defects in solid, we unify the concepts of the electrical double layer and the space-charge zone. Immediately, previously defined $\Delta E_{D^q}^f$

in the vicinity of the interface is equivalent to the adsorption energy of ions attached to a solid surface. The core zone at a solid-solid interface corresponds to the compact layer (or Stern layer) in electrical double layer. The advantage of this generalization is that the previously established modeling scheme for solid-solid interface can now be easily applied to solid-water interfaces, and serves as the basis of our universal treatment framework.

The advantage of this fully grand-canonical approach is that it could potentially include the interplay between defects on the solid side and ions on the water side. In most existing studies on electrical double layers, only ion redistribution in the liquid electrolyte is considered. The electrode (solid) is either simplified to a single boundary value [36-39], or considered with only surface morphology change due to ion adsorption [40-42]. These studies ignore the redistribution of ionic defects in the extended space-charge region of the electrode material, which are known to impact surface catalytic properties[43]. With the unified formulation described above, this thesis will quantitatively assess the influence of water solution chemistry on the defect chemistry of the electrode material (and vice versa).

## 1.2 Corrosion of zirconium alloy as nuclear cladding material

The model systems that we choose to study are zirconium oxide and titanium oxide. $ZrO_2$ has found broad applications as a solid electrolyte in energy systems [44], as thermal barrier coating [45], in biomedical applications [46], and in resistive switching devices [47]. Our focus will be on zirconium oxide passive film in corrosive environments. Zircaloys, which form an important member of the zirconium alloys family, are widely used as nuclear cladding material in light water nuclear reactors, which serves as the first protection layer of the fuel rod.[48] Under the aggressive conditions inside a nuclear reactor, the degradation of Zircaloys increases safety risk and limits the lifetime of the fuel rods. Understanding and predicting the corrosion behaviors of Zircaloy is an important issue in the nuclear industry, which could guide the operation of nuclear reactors and help carry forward a better alloy design.

In the corrosion process, a zirconium oxide layer forms on zirconium metal. Experimental studies have shown that the corrosion rate of Zircaloy has a significant dependence on the secondary-phase particles (SPP) [49] and coolant water chemistry[50]. This work aims to utilize a bottoms-up method to study the impact of zirconium oxide

interfacing with secondary-phase particles, and with water. The goal is to quantitatively decode how defects redistribute across such interfaces, generate spatially resolved defect concentration profiles, deduce physically based diffusion coefficients and surface reaction rates for higher-level modeling.

Zirconium alloy is exposed to high-temperature coolant water (about 500~700 K) in a pressurized water reactor (PWR) [51, 52]. As the corrosion process proceeds, a $ZrO_2$ layer grows on the alloy and protects it from the corrosive environment. The cathodic reaction is the reduction of water to atomic hydrogen:

$$H_2O + 2e^- \rightarrow O^{2-} + 2H$$

Oxygen diffuses through the oxide layer through a vacancy migration mechanism and then the anodic reaction is the oxidation of zirconium metal at oxide/metal interface:

$$Zr + 2O^{2-} \rightarrow ZrO_2 + 4e^-$$

The hydrogen atoms generated in the reduction reaction could either recombine and form hydrogen gas, or diffuse through the oxide layer into zirconium metal. The latter is a detrimental process called hydrogen pickup. When hydrogen reaches its solubility limit in the metal, zirconium hydrides start to precipitate, potentially leading to embrittlement [53].

It has been observed that the alloying of Fe and Cr with Zircaloys significantly enhances their corrosion resistance [54]. Zircaloy-4, for example, contains 0.05-0.15% Cr and 0.12-0.18% Fe. These alloying elements have very low solubility in zirconium metal and precipitate as intermetallic secondary phase particles (SPPs) $Zr(Cr,Fe)_2$. These intermetallic precipitates are incorporated in the oxide layer as it starts to grow, and later, get oxidized [55]. The structure of the oxidized secondary phase particle is illustrated in Figure 1-3 (a). It has been found that corrosion rates depend on the average diameter of secondary phase particles, as shown in Figure 1-3 (b).

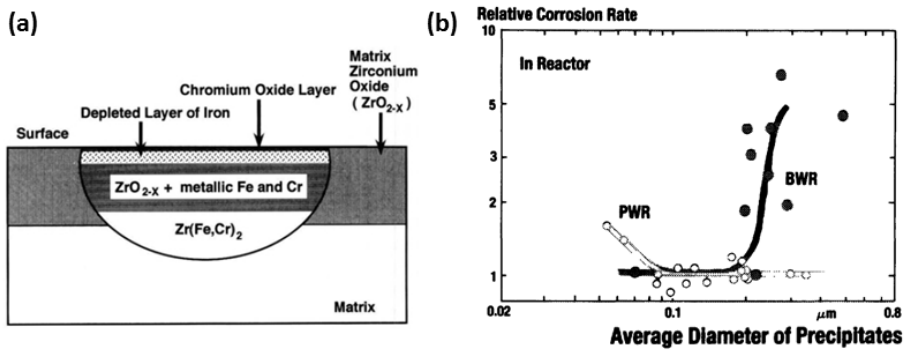


Figure 1-3. (a) schematic plot of an oxidized $Zr(Fe,Cr)_2$ secondary particle in zirconium passive film, adapted from ref. 54. (b) Dependence of corrosion rate on the average diameter of precipitates in pressurized water reactor (PWR) and boiling water reactor (BWR). Figure adapted from ref. 52.

Ion species in the water environment are also important factors for determining corrosion rate. The chemical additives of water coolants are precisely controlled to tailor the water chemistry for each type of nuclear reactor. In PWR type, boric acid is added in the coolant purposefully to absorb neutron and thus maintain reactivity control, accompanied by the introduction of lithium hydroxide, which keeps coolant water in the recommended alkaline pH range (~7.2). A tradeoff exists in the addition of LiOH. On one hand, pH-reduced environment will adversely affect the integrity of the metal alloy, so LiOH is needed for balancing with boric acid. On the other hand, it has been found that $Li^+$ could accelerate the degradation process of the zirconium oxide passive film on Zircaloys. Experimental test on Zircaloy corrosion in LiOH solution is shown in Figure 1-4.

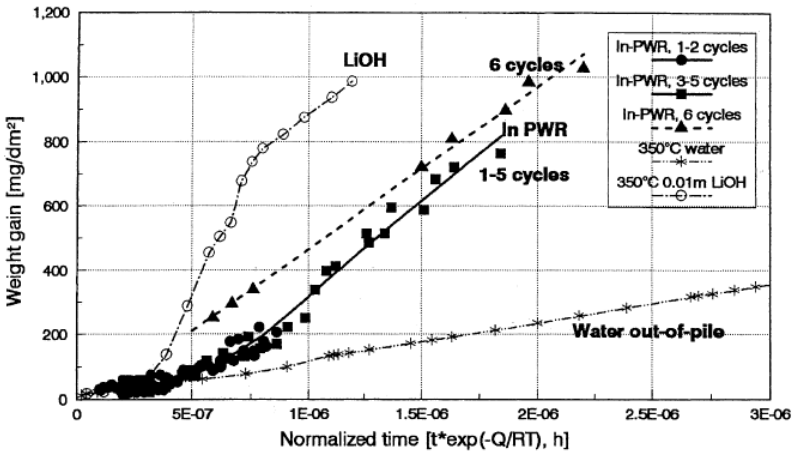


Figure 1-4. Experimental results of the film weight gain in PWR, 350°C water and 350°C 0.01m LiOH solution. Figure adapted from ref. 51.

Macro-scale models with empirical parameters for zirconium alloy corrosion have long existed [56, 57]. Successful as these models have been, they have two intrinsic shortcomings. First, they do not provide insights into the unit reactions that happen in the corrosion process. Second, empirical parameters are only valid under the experimented conditions, so the models cannot predict the performance in wider operation regimes. Recent advancements in atomistic modeling allow for developing mechanistic models. By breaking down the corrosion processes into different unit reaction steps and calculating related parameters from the *ab initio* method, we aim to gain a better understanding of the underlying mechanisms and make predictions in a wide range of thermodynamic conditions. For contributing to this higher scale corrosion kinetic modeling based on physically described unit processes, this thesis will implement the modeling framework discussed above to predict the defect distribution, transport and reaction kinetics at the zirconium oxide – SPP oxide interfaces and at the zirconium oxide-water interface.

## 1.3 Flash sintering of oxide materials

Field assisted sintering (FAST) has demonstrated great potential in reducing temperature constraints imposed on ceramic materials during sintering. By using a two-electrode configuration, and applying a DC field across yttria stabilized zirconia (YSZ) during sintering, Raj and co-workers first reported two regimes for field-assisted sintering (Figure 1-5): (1) at weak electric field, the sintering rate is enhanced without changing the character of the conventional sintering curve; (2) above a threshold electric field, an

abrupt densification occurs in mere seconds (i.e. flash Sintering) at temperatures well below normal sintering temperatures. Similar effects have also been observed for a series of other polycrystalline ceramic materials including $Al_2O_3$ [58], $SnO_2$ [59], ZnO [60] and $TiO_2$ [61].

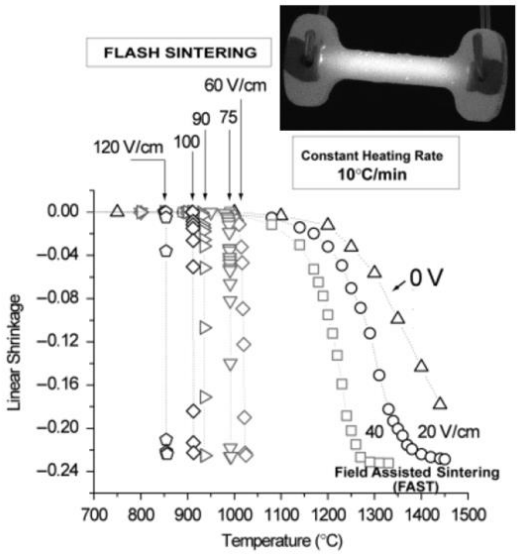


Figure 1-5. Observation of flash sintering of yttria-stabilized zirconia (3YSZ). A two-electrode dog bone-shaped specimen is used to ensure uniform field and current through the gauge section (20 mm). At weak field, the sintering rate increases slightly with increasing electric field. Above a threshold field strength (40 V/cm), the sintering process is complete in just seconds, well below normal sintering temperatures. Figures adapted from [62, 63].

Despite the phenomenological success, mechanism governing field assisted sintering is still under debate. The flash behavior is mainly attributed to a thermal runaway process [64]. This theoretical model considers two contributions to the change in sample temperature – Joule heating, which has exponential dependence due to change in conductivity in the sample, and radiative heat loss, which scales with $T^4$. At relatively low furnace temperature, $\Delta T$, the difference between sample temperature and furnace temperature, is limited. However, at critical furnace temperature, Joule heating exceeds radiative cooling over all $\Delta T$ range and the sample is continuously heated. Thermal runaway models have been successfully used to predict flash onset temperatures for different ceramic materials.

However, a field effect has also been observed in experiments where Joule heating does not exist. In situ STEM measurement during sintering revealed that instant densification occurs when a sample is put in non-contact electric fields [65]. In another case, different microstructures of the sample after sintering are observed going from anode to cathode [66]. The grain size of the sample close to the anode is smaller compared to that close to the cathode. These examples have clearly shown that electric field effect exists even if there is minimal Joule heating.

In this study, we aim to identify the separate effects of Joule heating and electric field in flash sintering. This mechanistic understanding requires knowledge of sample defect chemistry. In particular, we need to quantify sample conductivity, which governs Joule heating of the sample, as well as ionic diffusivity, which governs mass transport during sintering. We consider three possible mechanisms in which the electric field could change the sample defect chemistry. First, by applying a DC field, an effective oxygen partial pressure gradient is created across the sample. The sample close to the anode is in an oxidizing condition and close to cathode, in a reducing condition. This leads to changes in the local defect chemistry of the sample. Second, the electric field can polarize charged defects and change their formation energies and migration barriers. Third, the electric field will impact the space charge layer at grain boundaries, change the local defect distribution and thus the grain boundary diffusion. We examine Joule heating as well as the three effects of the electric field separately from the perspective of controlling the defect chemistry. We selected $TiO_2$ as the model system. We aim to study the electronic conductivity and ion diffusivity and examine the effects of doping and oxygen partial pressure on the defect chemistry.

## 1.4 Thesis outline

This remainder of this thesis is organized as follows: Chapter 2 - 8 focus on the modeling of $ZrO_2$. Chapter 2 - 4 are on the modeling of bulk defective $ZrO_2$ and Chapter 5 - 8 are on modeling extended defects in $ZrO_2$.

In Chapter 2, we predict oxygen self-diffusivities in undoped monoclinic $ZrO_2$ by combining DFT-obtained migration barriers and kinetic Monte Carlo simulation. The results show that first-principles defect calculations are capable of predicting oxygen self-diffusivities that are in quantitative agreement with experimentally-measured values.

Building on the results of Chapter 2, Chapter 3 and 4 look at the effects of dopants in bulk $ZrO_2$. Chapter 3 discusses the change in ionic and electronic conductivities and phase stability when alloying elements (Cr, Fe, Sn, and Nb) enter the oxide. Chapter 4 discusses the effects of lithium incorporation from coolant water and provide mechanistic insights into lithium-accelerated degradation of zirconium alloys.

With a comprehensive understanding of the bulk defect chemistry of $ZrO_2$, in Chapter 5, we build the framework of modeling defect redistribution across a hetero-interface from first-principles calculations. We apply this framework to the $ZrO_2/Cr_2O_3$ interface in the context of secondary phase particle formation in $ZrO_2$ passive film.

In Chapter 6 and 7, we extend the framework established in Chapter 5 to the $ZrO_2$/water interface. Chapter 6 focuses on *ab initio* molecular dynamics modeling of the $ZrO_2$/water interface and reveals the structure, kinetics, and thermodynamics of water near a $ZrO_2$ surface. Chapter 7 takes the adsorption free energies of $H^+$ and $OH^-$ ions obtained in Chapter 6 and predicts the electric double layer structure at $ZrO_2$/water interface on the continuum level.

Chapter 8 applies the interface-modeling framework to grain boundaries in $ZrO_2$. We studied Σ3 (100) twin boundary, Σ5 (210) [001] grain boundary, and Σ5 (310) [001] grain boundary of monoclinic $ZrO_2$ and predict the change in ionic and electronic conductivities with varying grain type, grain size, and thermodynamic conditions.

Chapter 9 applies similar approaches to $TiO_2$ in the context of FAST. First, we look at the bulk defect chemistry of undoped, donor-doped, and acceptor-doped $TiO_2$ and discuss how the bulk electronic conductivity and cation diffusivity affect the sintering process. Second, we model the space charge layer profiles across $TiO_2$ grain boundaries and discuss the local effect of external bias at grain boundaries.

Finally, Chapter 10 reviews the contributions of this thesis and discuss perspectives on future directions for first-principles based modeling for defective oxides.

# 2 Oxygen self-diffusion mechanisms in monoclinic $ZrO_2$ revealed and quantified by density functional theory, random walk and kinetic Monte Carlo calculations

In this chapter, we quantify oxygen self-diffusion in monoclinic-phase zirconium oxide as a function of temperature and oxygen partial pressure. Migration barriers of each type of oxygen defect were obtained by first-principles calculations. Random-walk theory was used to quantify the diffusivities of oxygen interstitials by using the calculated migration barriers. Kinetic Monte Carlo simulations were used to calculate diffusivities of oxygen vacancies by distinguishing the three-fold and four-fold coordinated lattice oxygen. By combining the equilibrium defect concentrations obtained in our previous work, together with the herein calculated diffusivity of each defect species, we present the resulting oxygen self-diffusion coefficients, and the corresponding atomistically resolved transport mechanisms. The predicted effective migration barriers and diffusion pre-factors are in reasonable agreement with experimentally reported values. This work provides insights into oxygen diffusion engineering in $ZrO_2$ related devices and parameterization for continuum transport modeling.

## 2.1 Introduction

Oxygen self-diffusion in zirconium oxide has long been a topic of interest for studying the oxidation kinetics of zirconium alloys used as cladding of nuclear fuels in light water cooled nuclear reactors.[48] Zirconium oxide is also widely used in heterogeneous catalysis [67, 68] , and more recently examined for high-*k* dielectrics in metal-oxide-semiconductor field-effect transistor (MOSFET) devices [69, 70] as well as resistive switching devices [71, 72]. In all of these technologically important applications, understanding the defect chemistry and transport properties is key to better material design, device engineering and performance modeling. In particular, such knowledge could guide design by aliovalent doping and controlling operating environmental conditions. Experimental [73-75] and computational [76-81] studies have been carried out to atomistically resolve the structure, valence states and defect chemistry in $ZrO_2$. The zirconium-oxygen system phase stability has been examined by first-principles

studies, and a range of sub-oxide structures with oxygen dissolved into the metal phase have been identified [81]. To date, many aspects of $ZrO_2$ remain unexamined atomistically in the multi-dimensional space of temperature, oxygen partial pressure, extrinsic doping, strain and microstructure. In our previous work, we predicted oxygen self-diffusion kinetics in tetragonal-$ZrO_2$ (t-$ZrO_2$) by combining first-principle calculations with random-walk theory[17], resulting in good agreement with experimental measurements. Monoclinic-$ZrO_2$ (m-$ZrO_2$) is the stable phase below 1440 K [82] and is also relevant in the applications mentioned above. In m-$ZrO_2$, the oxygen sub-lattice is distorted compared to the tetragonal phase, leading to two inequivalent sites for oxygen in the unit cell: one bonds with four zirconium atoms (O4) and one bonds with three zirconium atoms (O3). This inequivalence of oxygen sites makes a random-walk model inapplicable. There exists first-principle studies of oxygen defect migration barriers in $HfO_2$, which bears the same structure as m-$ZrO_2$ [83]. However, no comprehensive work predicting overall oxygen diffusion coefficients has been performed for oxides of this structure.

In this study, we present a systematic examination of oxygen transport properties in bulk, near-stoichiometric monoclinic-$ZrO_2$ under different thermodynamic conditions. In previous work, by combining first-principles based point defect calculations with statistical thermodynamics, we were able to predict equilibrium defect concentrations at various temperatures and oxygen partial pressures both in tetragonal[84] and monoclinic $ZrO_2$[77]. Here we calculated the migration barriers of different oxygen defect types and migration paths by first principles calculations. The results show that migration barriers corresponding to different oxygen vacancy migration paths categorized by O4 and O3 sites could differ by more than 1 eV. In order to distinguish this inequivalence of lattice oxygen sites, we quantified the oxygen vacancy diffusivity with kinetic Monte-Carlo (kMC) simulations. On the other hand, random walk theory was sufficient to obtain oxygen interstitial diffusivities. We arrive at the total oxygen self-diffusion coefficients by combining the defect equilibria and diffusivity for each of these oxygen defects over a wide range of temperature and oxygen partial pressure.

The predicted diffusion coefficient profiles show a valley shape as a function of oxygen pressure at different temperatures. Oxygen interstitials dominate in the high oxygen partial pressure regime and oxygen vacancies in the low oxygen partial pressure regime, leading to a diffusion minimum at intermediate oxygen partial pressures. Our predicted

values are in good agreement with experimentally measured diffusion coefficients under relevant thermodynamic conditions. Finally, we discuss the implications of this study on engineering oxygen transport in zirconium oxide.

## 2.2 Methods

The climbing image nudged elastic band (CI-NEB) method[16] was used to calculate migration barriers using three to five intermediate images as implemented in Transition State Tools (VTST)[16]. Energies of each image were calculated by density functional theory (DFT) with Vienna Ab initio Simulation Package (VASP)[85-88] with 2×2×2 supercell and 2×2×2 *k*-point gird. The generalized gradient approximation (GGA) with Perdew-Burke-Ernzerhof (PBE) functional[89, 90] is used. $4s^2 4p^6 4d^2 5s^2$ electrons for zirconium and $2s^2 2p^4$ for oxygen are treated as valence electrons. The plane-wave cutoff energy was set to 450 eV. Details of calculating the defect formation energies and equilibrium defect concentrations can be found in Ref. [84] , [77] and [91].

For oxygen interstitials, DFT calculations were performed with different initial guesses for the interstitial sites. Oxygen vacancies can take either O4 or O3 sites. On the other hand, the interstitial oxygen always occupies the same type of site in the relaxed, low-energy configurations. This finding validates the applicability of the random-walk theory for oxygen interstitials, as we reported earlier for oxygen diffusion in t-$ZrO_2$[17]. In principle, random-walk theory produces the same outcome as kinetic Monte Carlo simulations for oxygen interstitials, given that there are no inequivalent sites for them in m-$ZrO_2$. Therefore, the diffusivity for each oxygen interstitial species was calculated by the random-walk model[92] with

$$D_{O_i}^{q} = \sum_{k} \nu d_k^2 \exp(-\frac{E_k}{k_B T}) \ , \qquad (2.1)$$

where attempt frequency $\nu$ is taken as 5 THz. $q$ represents the different charged states of oxygen interstitials (0, -1 and -2). $E_k$ and $d_k$ are the migration barrier and hopping distance for the corresponding migration path. $k_B$ is the Boltzmann constant and $T$ is temperature. Kröger-Vink notation for defects is used throughout this paper.

The calculated migration barriers for oxygen vacancies were fed into an on-lattice kinetic Monte Carlo model [93] to account for the three-fold and four-fold coordinated oxygen site network. Simulations were performed at each temperature for $10^6$ kMC steps. The

simulation cell has one defect in the $ZrO_2$ lattice with periodic boundary condition, starting from a random initial configuration. The diffusivity is calculated from the mean square displacement with Einstein's theory of Brownian motion [94],

$$\left\langle \mathbf{r}(t)^2 \right\rangle = 6D_{V_O}^q t \,. \tag{2.2}$$

Here $\mathbf{r}(t)$ is the position of the defect referenced to the initial site at time *t*, and $D_{V_O}^q$ is the calculated diffusivity for the specific defect species $V_O^q$ at that temperature. The calculation of $D_{V_O}^q$ from the kMC trajectory involves the following. For each defect species, one trajectory of N steps is obtained from kMC run. This single trajectory is broken into N/n trajectories with n steps. For each n-step trajectory, an associated diffusivity $D_n$ is calculated by $D_n = \Delta r_n^2 / 6t_n$, where $\Delta r_n^2$ represents the total mean squared displacement of this trajectory and $t_n$ represents the total time. Due to the nature of kMC, $t_n$ is different for each n-step trajectory. The final diffusivity is calculated by averaging $D_n$ from the (N/n) trajectories. In this work, N = $10^6$ and n = $5 \times 10^3$ was used. Convergence of the simulations with these parameters are shown in the supplemental material [95]. Defect-defect interactions are ignored in all calculations under the assumption of dilute limit which is reasonable for undoped monoclinic $ZrO_2$ which does not exhibit significant deviation from stoichiometry [77, 96].

By combining the contribution to diffusion by oxygen vacancies from kMC calculations and by oxygen interstitials from random-walk theory, we obtain the total oxygen self-diffusion coefficient at different partial pressures and temperatures

$$D_{tot} = \sum_q [\mathrm{V}_O^q] D_{\mathrm{V_O}}^q + \sum_q [\mathrm{O}_i^q] D_{\mathrm{O_i}}^q \,. \tag{2.3}$$

Here [d] is the concentration of respective defect. $D_{tot}$ defined here is the isotropic diffusion coefficient of oxygen averaged over all crystallographic directions. This value is then compared with experimental values in the results section.

## 2.3 Results and discussion

The considered pathways of oxygen vacancy migration are shown schematically in Figure 2-1. Two types of oxygen sites exist in monoclinic $ZrO_2$, one type bonded with four zirconium ions (O4) and the other with three (O3). The migration paths are further

categorized by the number of zirconium ions that simultaneously share bonds with the two oxygen sites between which the migration takes place. Details of each migration path and the corresponding migration barriers are summarized in Table 2-1 and the energy profiles in Figure 2-2. For each migration path, the barrier for oxygen vacancies with 0, +1 and +2 charges are calculated.

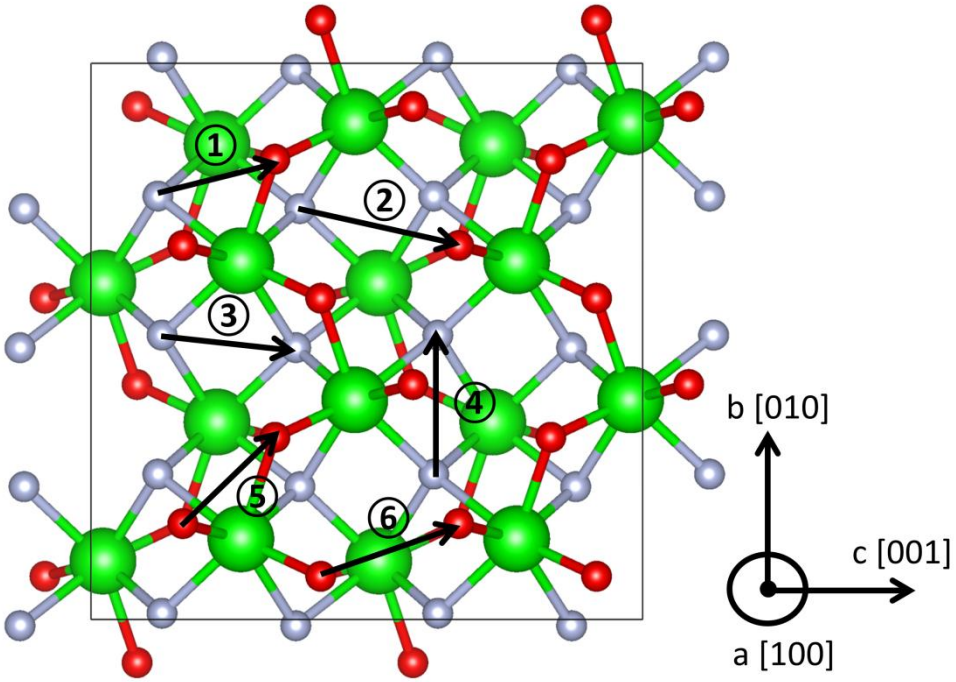


Figure 2-1. Migration paths for oxygen vacancies in m-$ZrO_2$. Large, green spheres represent Zr ions. Small red and grey spheres represent three-fold-coordinated and four-fold-coordinated oxygen ions, respectively. This figure is generated with visualization software VESTA.[97]

Table 2-1. The calculated migration paths and migration barriers (in units of eV) of oxygen vacancies in m-$ZrO_2$. The indices of each migration path are labeled in Figure 2-1. The paths are categorized by O4 and O3 oxygen sites, and how many Zr ions the two O sites share bond with. For paths between O4 and O3 sites, forward and backward barriers are different due to asymmetry of the initial and final configuration. For O4-O4 and O3-O3 paths, forward and backward barriers are equal. For O4-O4 paths, migration on ab plane and c direction are further distinguished.

| Path | From-To | Shared Zr ion | | $V_O^{\times}$ | $V_O^{\bullet}$ | $V_O^{\bullet\bullet}$ |
|---|---|---|---|---|---|---|
| 1 | O4 - O3 | 2 | forward | 1.94 | 0.91 | 0.06 |
| | | | backward | 1.84 | 1.28 | 0.78 |
| 2 | O4 - O3 | 1 | forward | 2.23 | 1.64 | 1.01 |
| | | | backward | 2.12 | 2.00 | 1.80 |
| 3 | O4 - O4, c | 2 | | 2.48 | 1.54 | 0.86 |
| 4 | O4 - O4, ab | 2 | | 2.03 | 1.20 | 0.33 |
| 5 | O3 - O3 | 2 | | 2.20 | 1.58 | 0.77 |
| 6 | O3 - O3 | 1 | | 1.32 | 1.11 | 0.73 |

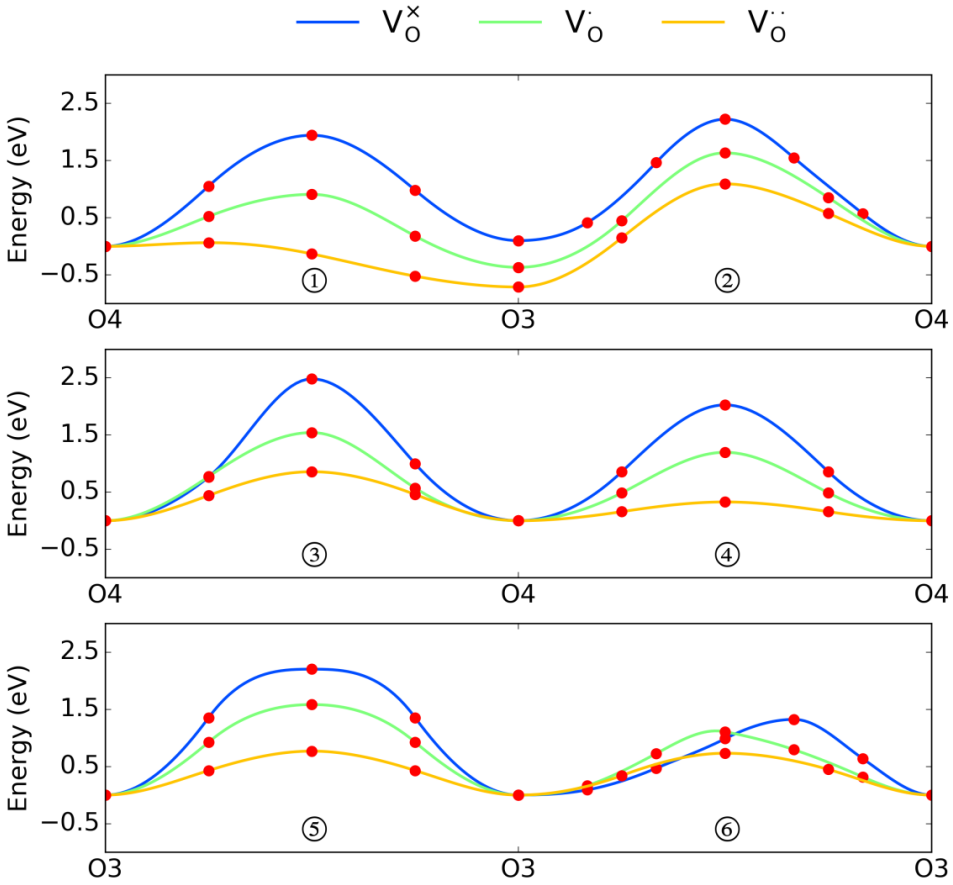


Figure 2-2. Energy profiles for oxygen migration paths labeled in Figure 2-1. Red dots are images calculated by the CI-NEB method. Fitted spline curves are produced with the VTST tools.[16]

Based on the calculated migration barrier, it is clear that for each migration path, the higher-charge-state oxygen vacancies have lower migration barriers. This can be rationalized by the fact that the diffusive jump of $V_O^{\times}$ involves the transport of the two electrons associated with the vacant site in a direction opposing the jump of the oxide ion. This opposition is accompanied with Coulombic repulsion and elevation of the activation barrier. In the case of $V_O^{\bullet}$, there is only one electron opposing the migrating oxide ion and finally in $V_O^{\bullet\bullet}$ there are no electrons to oppose the oxide ion. Similar trend has also been observed in tetragonal $ZrO_2$[17] and other oxides[98]. It is also notable that the forward migration barrier for O4-O3 sharing bonds with Zr ions is as low as 0.06 eV, which seemingly indicates very fast oxygen diffusion. However, it is shown from kMC simulations that, although oxygen hopping between these two types of sites is frequent, oxygen atoms need to go through other high-barrier migration paths in order to complete long-range diffusion.

For oxygen interstitials, octahedral interstitial sites were found to be the low-energy sites.[77] DFT calculations show that all octahedral oxygen interstitials are energetically equivalent in the $ZrO_2$ unit cell. Migration barriers for direct exchange mechanism were found to be too high (> 5 eV) and therefore only interstitialcy migration hops were considered.[99] The calculated migration barriers are 0.672 eV, 0.365 eV, and 0.530 eV respectively for $O_i^{\times}$, $O_i^{\prime}$, and $O_i^{\prime\prime}$. These results indicate oxygen interstitials have higher mobility compared to oxygen vacancies, consistent with previous experimental observation [100].

Equilibrium defect concentrations as a function of $P_{O_2}$ at 600 K and 1200 K are reproduced in Figure 2-3 (a)(b). Details of how these profiles are constructed can be found in Ref. [77]. At 600 K, the dominant oxygen-related defect is the oxygen interstitial over the entire $P_{O_2}$ range, with the dominant charge state changing from -2 to 0 at 1 atm. At 1200 K, the dominant oxygen defect transitions from oxygen vacancy with different charge states for $P_{O_2} < 10^{-12}$ atm to doubly-charged oxygen interstitial $O_i^{\prime\prime}$ at higher, more oxidizing $P_{O_2}$.

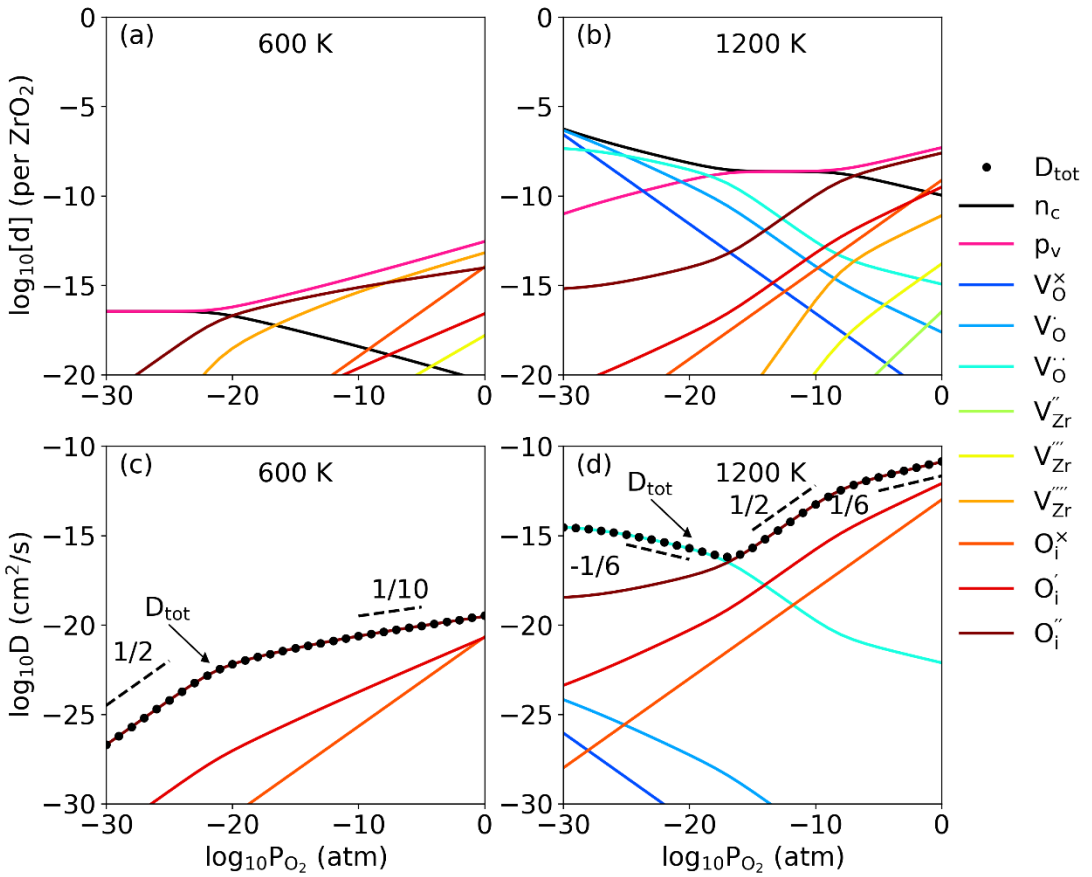


Figure 2-3. Equilibrium concentrations of electronic and ionic defects, [d] at (a) 600 K and (b) 1200 K, as a function of oxygen partial pressure. Oxygen self-diffusivity, D, calculated for each oxygen defect species and total diffusion coefficient, $D_{tot}$, with varying oxygen partial pressure at (c) 600 K and (d) 1200 K.

The total oxygen self-diffusivity profiles as well as contributions of individual oxygen defect species at the two temperatures display different features (Figure 2-3 (c) and (d)), following the defect transitions noted above. In the low-temperature case, $P_{O_2}$ dependence can be categorized into two regimes. In the low $P_{O_2}$ regime (< $10^{-20}$ atm), the dominant charged defects are holes compensated by electrons. This results in a 1/2 slope of for the concentration of the dominant oxygen defect $O_i''$, and consequently the same slope for the $\log_{10}D_{tot}$ profile. In the high $P_{O_2}$ regime (>$10^{-10}$ atm), holes are charge-balanced by

zirconium vacancies $V_{Zr}^{''''}$. Here the defect reaction is $\frac{1}{2}O_2(g) \rightarrow O_O^{\times} + \frac{1}{2}V_{Zr}^{''''} + 2h^{\bullet}$, leading to $[h^{\bullet}] = \frac{1}{4}[V_{Zr}^{''''}] \propto P_{O_2}^{1/5}$. The concentration of $O_i''$ is related to $[h^{\bullet}]$ via defect reaction $\frac{1}{2}O_2(g) \rightarrow O_i'' + 2h^{\bullet}$ and thus exhibits the 1/10 slope as shown in the $\log_{10}D_{tot}$ curve.

At high-temperature, the intermediate $P_{O_2}$ regime ($10^{-15}$ – $10^{-10}$ atm) has the same electron-hole compensation mechanism and the same dominant oxygen defect $O_i''$ as discussed above, and thus, $\log_{10}D_{tot}$ exhibits 1/2 slope. However, in the low $P_{O_2}$ regime, the two dominating types of charged defect are electrons and positively-charged oxygen vacancies. A -1/6 $\log_{10}D_{tot}$ slope is predicted by the law of mass action under the approximate charge neutrality $n_c \approx 2[V_O^{\bullet\bullet}]$, but a small discrepancy from this prediction was present in the calculated curve. This is because of the fact that $V_O^{\bullet}$ also contributes non-negligibly to the charge neutrality condition. At very low $P_{O_2}$, $V_O^{\bullet}$ and $V_O^{\times}$ predominate over $V_O^{\bullet\bullet}$ in concentration, but the diffusivity is still contributed mainly by $V_O^{\bullet\bullet}$ due to its lower migration barrier. In the high $P_{O_2}$ regime, $p_v \approx 2[O_i'']$. $\frac{1}{2}O_2(g) \rightarrow O_i'' + 2h^{\bullet}$ is the dominant defect reaction and a 1/6 slope is shown as predicted by the law of mass action.

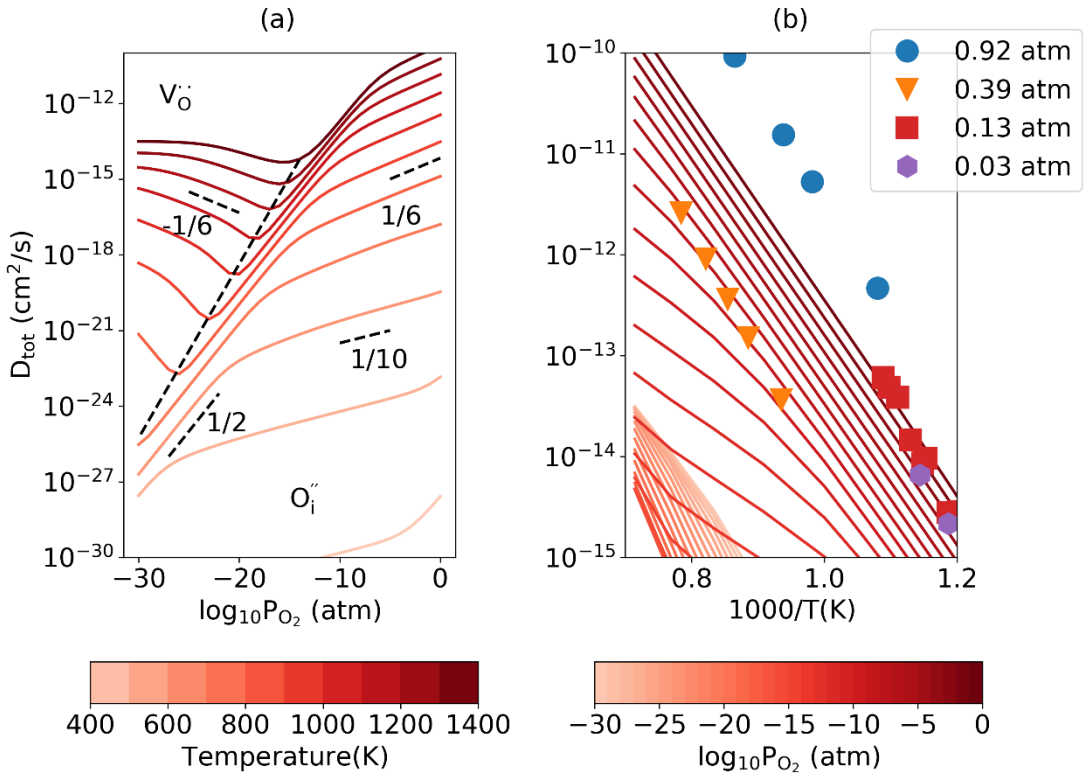


Figure 2-4. Calculated total oxygen self-diffusion coefficient plotted as a function of oxygen partial pressure and temperature. Solid symbols in (b) show experimentally measured values from references [100] (0.92 atm), [101] (0.39 atm), and [102] (0.13 and 0.03 atm).

To examine the gradual transition from the low-temperature to the high-temperature behavior, we plot the $P_{O_2}$ dependence of the total self-diffusion coefficient at different temperatures in Figure 2-4(a). There is clear appearance of a diffusion coefficient minima, or valley, as marked by the dashed line. This marks the transition between the $V_O^{\bullet\bullet}$-dominated regime to the $O_i''$-dominated regime. At low temperatures (<700 K), the entire $P_{O_2}$ range is dominated by oxygen interstitials. At higher temperatures, there is a transition between $V_O^{\bullet\bullet}$-dominated regime at low $P_{O_2}$ and $O_i''$-dominated regime at high $P_{O_2}$. The oxygen partial pressure at which this transition happens, increases with increasing temperature.

To compare with experiments, the high temperature data are replotted in Figure 2-4(b) as isobaric diffusion coefficient curves as a function of 1/*T*. At high $P_{O_2}$ (>$10^{-5}$ atm), the isobaric curves are perfectly Arrhenius. This is because the entire profile is sampled in regimes where oxygen interstitials are compensated by holes. At intermediate $P_{O_2}$ ($10^{-10}$ - $10^{-5}$ atm), non-Arrhenius behavior starts to appear, where the compensation mechanism transitions to electrons compensated by holes. At even lower $P_{O_2}$, the Arrhenius behavior is restored again because now the entire region is within the vacancy-dominated regime.

Symbols in Figure 2-4(b) represent experimentally measured values at different oxygen partial pressures as noted in the legend. [100-102] It is clear from Figure 2-4(b) that experimental measurements have considerable disagreement between each other. In particular, the trend of $D_{tot}$ varying with oxygen partial pressure is not consistent when comparing values from different studies. Here we discuss a few factors that possibly lead to this discrepancy. First, all experimental studies listed here were not conducted on single-crystal $ZrO_2$. Ref. [100] and [101] measured conductivity by $^{18}O$ diffusion experiment on $ZrO_2$ spheres, and Ref. [102] by measuring the oxidation rate of non-stoichiometric $ZrO_2$ powder to stoichiometric $ZrO_2$. It is hard to eliminate the contribution of voids, grain boundaries or other types of extended defects. Second, all diffusion models used to fit experimental profiles and obtain $D_{tot}$ assume that the rate-limiting step in the oxygen exchange/oxidation process is oxygen diffusion. This simplified assumption may lead to errors in the fitted result. This point is partially verified by Ref. [100], where the authors found that diffusivities obtained at equivalent oxygen partial pressure by $CO/CO_2$ mixture and $O_2$ gas are not consistent, indicating that surface exchange kinetics also influence the result. Third, none of these studies considers the contribution to oxygen diffusion under electric field in intrinsically formed space charge layer at oxide surface. Our study shows that the major contribution to diffusion coefficient comes from charged defects and the space charge effect should be taken into consideration [91].

Last, it is worth mentioning that experimental specimens must contain aliovalent cation impurities. For example, $Al^{3+}$ and $Nb^{5+}$ are two common impurity species, one is an acceptor and the other is a donor. These aliovalent cations could compensate each other

and make the oxide behave closer to intrinsic. However, even a small amount of n-type or p-type doping could change the dependence of defect chemistry on oxygen partial pressure. In particular, the compensating mechanism transition pressure could change due to the impurity dopants. In other words, the same defect chemistry could be achieved at different $P_{O_2}$ with different impurity contents. This could in part explain the inconsistency of $P_{O_2}$ dependence between prior experimental studies. The trend in diffusivity change from 0.03 to 0.13 atm in Ref. [102] is more reliable considering the measurements were performed on samples with the same impurity level. In Ref. [102] we see that $D_{tot}$ increases with oxygen partial pressure, which hints to an oxygen interstitial dominated mechanism and is in agreement with our prediction.

To quantitatively compare with experimentally measured values, we calculate the effective activation energies $Q$ and effective pre-factors $D^*$ by fitting the total self-diffusivity $D_{tot}$ to $D_{tot} = D^* \exp(-Q / k_B T)$. The outcome values are plotted in *Figure 2-5* and summarized in *Table 2-2*. It is not a coincidence that both the activation energy and the diffusion pre-factor curves display a valley at intermediate oxygen partial pressure. This valley again corresponds to the same transition from $V_O^{\bullet\bullet}$-dominated regime at low $P_{O_2}$ to $O_i''$-dominated regime at high $P_{O_2}$. The effective activation barrier predicted at $P_{O_2}$ = 1 atm is 2.04 eV. This is in reasonable agreement with experimentally measured values (1.96 eV[100], 2.43 eV[101] and 2.46 eV[102] respectively). This consistency indicates that all the values we are comparing with from experiments should be in the same $O_i''$-dominated regime as we predicted. This is because the formation energy of $V_O^{\bullet\bullet}$ alone exceeds 3.5 eV in this $P_{O_2}$ range and even higher activation barrier should be expected if $V_O^{\bullet\bullet}$ were the dominant species. When it comes to diffusion pre-factors, the difference between this work and experimental values, and the difference among the reported experimental values, is more pronounced. $D^*$ predicted in this study is $6.50\times10^{-3}$ cm$^2$/s at $P_{O_2}$ = 1 atm and $4.76\times10^{-3}$ cm$^2$/s at $P_{O_2}$ = 0.1 atm. The calculated value in Ref [100], [101] and [102] are $2.34\times10^{-2}$ cm$^2$/s at 0.92 atm, $9.73\times10^{-3}$ cm$^2$/s at 0.39 atm, 1.82 cm$^2$/s at 0.13 atm and $9.00\times10^{-2}$ cm$^2$/s at 0.03 atm. However, we can also see from *Figure 2-5*(b) that $D^*$ changes over orders of magnitude with varying oxygen partial pressures.

This observation is consistent with the different impurity argument we discussed above. Donor-type impurities could increase the concentration of $O_i''$ and hence create the discrepancies among $D^*$.

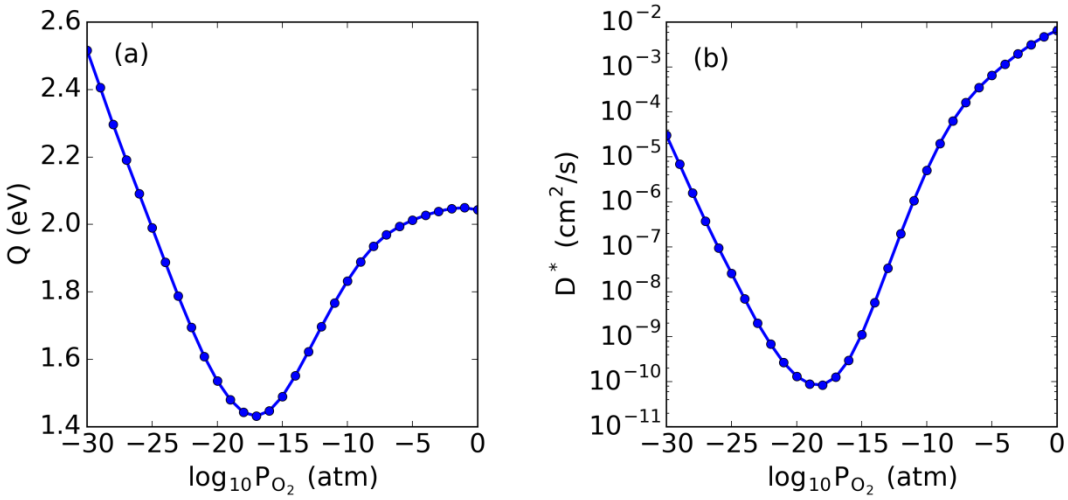


Figure 2-5. (a) Activation energies and (b) diffusion pre-factors at different oxygen partial pressures fitted to $D_{tot} = D^* \exp(-Q/k_B T)$ by using the simulated data in the high temperature regimes in Figure 2-4(b).

Table 2-2. Activation energies and diffusion pre-factors comparison between this work and experimental measurements.

| | This work | This work | This work | Ref. 1 | Ref. 2 | Ref. 3 | Ref. 3 |
|---|---|---|---|---|---|---|---|
| $P_{O_2}$ (atm) | 1 | 0.1 | 0.01 | 0.92 | 0.39 | 0.13 | 0.03 |
| Q (eV) | 2.04 | 2.05 | 2.05 | 1.96 | 2.43 | 2.46 | 2.46 |
| D* ($cm^2/s$) | 6.50 $\times 10^{-3}$ | 4.76 $\times 10^{-3}$ | 3.16 $\times 10^{-3}$ | 2.34 $\times 10^{-2}$ | 9.73 $\times 10^{-3}$ | 1.82 | 9.00 $\times 10^{-2}$ |

Lastly, we comment on the implication of these findings on the oxidation rate of the zirconium metal. Oxygen diffusion through the oxide passive film is known as one of the rate limiting steps in the oxidation process [51]. To design corrosion-resistant zirconium alloys, lower oxygen diffusivity is desirable. Looking at the isothermal curves in Figure 2-4(a), the lowest oxygen diffusion coefficient is always achieved in the intermediate pressure range where the dominating species are electrons and holes. Going to the high/low end of oxygen partial pressure, oxygen interstitial/oxygen vacancy becomes the dominant defect species that compensate with holes/electrons, and thus increases the total oxygen conductivity. This leads to the conclusion that, to engineer oxygen transport through the oxide film, it is desirable to suppress the dominant oxygen defect. Doping is one of the possible means to achieve this goal. In the high $P_{O_2}$ region, a +3 dopant could compensate with holes, reducing oxygen interstitial concentration and thus suppressing oxygen transport. A +5 dopant has similar effect in the low $P_{O_2}$ region in compensating with electrons and reducing the oxygen vacancy concentration. This finding provides guiding rules for different alloying elements that can dissolve into the growing oxide and change the oxygen defect equilibria in the relevant temperature and oxygen partial pressure space.

In light of our findings, we offer a few possible improvements on the modeling method used in this work. First, we ignored defect-defect interactions throughout this study. If we look at Figure 2-3(b), the calculated defect concentrations are generally below 10 ppm, which shows that this approximation is reasonable within the thermodynamic regime considered here. However, for high extrinsic doping concentrations, or higher temperature and lower oxygen pressure regime is of interest, it will be important to include defect-defect interactions. Second, extended defects in the oxide structure can significantly change its transport properties, for example, as we have demonstrated recently for secondary phase particles embedded in $ZrO_2$ matrix.[91] The effects of surface, grain boundaries and interfaces on oxygen diffusion are also worth exploring, and this is necessary for constructing accurate higher-level transport models as well as informing microstructure engineering for oxide materials.

## 2.4 Conclusion

In this study, we modeled oxygen self-diffusion in monoclinic-$ZrO_2$ by combining density functional theory calculations, random walk theory, and kinetic Monte Carlo simulations. The oxygen diffusion coefficient shows a clear transition between an oxygen vacancy dominated transport regime at low oxygen partial pressure to an oxygen interstitial dominated regime at high oxygen partial pressures. The results demonstrate a diffusivity minima, i.e., a valley at the transition point. The effective migration barriers and diffusion pre-factors are in reasonable agreement with those found from experimental studies. This study provides an atomistic understanding of the oxygen diffusion mechanism in monoclinic $ZrO_2$, and the findings can guide the design of zirconium oxide for different applications where oxygen transport properties at different functional conditions are of interest.

# 3 First-principles prediction of hydrogen pickup and oxidation kinetics of zirconium alloy: dopant effects from the chemo-mechanical perspective

The effect of alloying elements on zirconium alloy degradation properties has been widely studied because of its application in nuclear water reactors. It is observed in experiments that alloying elements in zirconium alloys could significantly change the oxide film growth kinetics as well as the morphology of the passive film. The goal of this work is to provide insights on the effect of alloying elements in $ZrO_2$ passive films based on first-principles calculations. To that end, we study the chemo-mechanical effect of Fe, Cr, Sn and Nb dopants in $ZrO_2$ that exist in the oxide matrix as point defects. We show that the change in defect chemistry imposed by doping is strongly correlated with the valence states of the dopants. Sn stays in the 4+ state and exists in $ZrO_2$ as neutral defect, therefore has negligible effect on the defect chemistry of $ZrO_2$. Fe and Cr, which are dominantly in +3 valence states, tend to decrease the concentration of oxygen interstitials and increase the concentration of hydrogen interstitials in $ZrO_2$, thus suppressing oxide growth while increasing hydrogen pickup. Nb, on the other hand, is predominantly +5 and has the opposite effect. Changes in defect chemistry are accompanied by change in phase stability. We have discovered that Fe and Cr can strongly stabilize tetragonal-phase $ZrO_2$ while Nb has a strong destabilizing effect. These results provide a mechanistic interpretation of experimental corrosion tests on different types of zirconium alloys as well as quantification of transport properties of the doped oxide film.

## 3.1 Introduction

Zirconium alloys are widely used as fuel cladding in water-cooled nuclear reactors [48]. During reactor operation, the zirconium alloy cladding layer is exposed to harsh corrosive environments with high temperature water, high pressure, and high irradiation [51]. Zirconium alloy corrosion places limits on its service time and fuel burnup [103]. Since the first employment of unalloyed zirconium as nuclear cladding more than fifty years ago, extensive efforts have been put into engineering zirconium alloy compositions. Typical commercially-used zirconium alloys include Zircaloy-2 (Zr–1.5% Sn, 0.14% Fe,

0.10% Cr, 0.06% Ni), Zircaloy-4 (Zr–1.5% Sn, 0.22% Fe, 0.10% Cr) [104], Zr-2.5Nb(Zr–2.5% Nb), ZIRLO$^{TM}$(Zr–1.0%Nb–0.5%Sn–0.1%Fe) [105]. With moderate amount of alloying elements, the corrosion resistance of zirconium alloys can be significantly improved compared to the unalloyed metal [106].

Despite the great engineering success, the mechanisms through which the alloying elements influence the corrosion processes remain elusive. The chemical and microstructural evolution of zirconium passive film is a complicated and convoluted process. To understand the role that the alloying elements potentially play, we first take a look at the overall corrosion reaction. Oxygen gets incorporated into the film through the reduction of water to atomic hydrogen on the oxide surface:

$$H_2O + 2e^- \rightarrow O^{2-} + 2H$$

Oxygen diffuses through the oxide layer through a vacancy migration mechanism and the anodic reaction is the oxidation of zirconium metal at oxide/metal interface:

$$Zr + 2O^{2-} \rightarrow ZrO_2 + 4e^-$$

The hydrogen atoms generated in the reduction reaction could either recombine and form hydrogen gas, or diffuse through the oxide layer into zirconium metal. The latter is a detrimental process called hydrogen pickup.[107] When hydrogen reaches its solubility limit in the metal, zirconium hydrides begin to precipitate, potentially leading to embrittlement [53].

Apart from the chemical reaction, microstructure evolution of the oxide film is also a key factor in determining the corrosion kinetics of zirconium alloy [108]. Zirconium oxide exists in two phases in the passive film, the monoclinic phase (M-$ZrO_2$), which is the thermodynamically stable phase, and the tetragonal phase (T-$ZrO_2$), which is stabilized by the local compressive stress close to the oxide/metal interface [109]. The T-to-M phase transformation is a volume expansion process and can be detrimental to the oxide film integrity, leading to the formation of equiaxed grains or film cracking.

In this paper, we survey the chemo-mechanical effect of each doping element in zirconium oxide based on first-principle calculations and try to link these atomistic insights with experimentally-observed alloy properties. We categorize the effects of the dopants on two aspects. First, alloying elements modulate the transport of oxygen and hydrogen in the passive film by changing the chemical composition of the oxide matrix.

By calculating defect concentration diagrams from first-principles, we show how the alloying elements entering $ZrO_2$ affect the oxygen and hydrogen diffusivities and thus change their incorporation kinetics. Second, we quantify the change in the critical pressure of T-to-M phase transformation with inserted doping elements and discuss the mechanical response of the oxide film including chemical expansion and phase transformation.

We have to note that to fully explain the degradation behavior of different zirconium alloys, various other factors come into play such as crack initialization [110], grain size and orientation [111], secondary phase particle formation [112], and irradiation [113]. The goal of this work is to separate out the effects of point defects, that exist throughout the passive film growth process and influences the sub-processes listed above.

We explore the effects of four common alloying elements in zirconium, Cr, Fe, Sn and Nb starting with developing equilibrium defect concentration diagrams of doped $ZrO_2$. By comparing the concentration change of important electronic, oxygen, and hydrogen defects, we observe that Cr and Fe accelerate oxide growth and suppress hydrogen pickup, while Nb has the opposite effect. Following the chemical effect, we discuss the effect of major point defects on phase stability. We identify four defects that have significant effect on phase stability. $V_O^{\bullet\bullet}$ and $H_i^{\bullet}$ stabilize the tetragonal phase, and $V_{Zr}^{''''}$ and $H_{Zr}'''$ stabilize the monoclinic phase. Fe and Cr promote the concentrations of the former two while decreasing the concentrations of the latter two, leading to an overall stabilization of tetragonal phase $ZrO_2$. Nb doping shows the opposite trend of stabilizing monoclinic phase $ZrO_2$. Last, we discuss the implication of these findings by looking at experimental observations comparing the different types of zirconium alloys in literature.

## 3.2 Methods

We performed DFT calculations for dopants in M-$ZrO_2$ and T-$ZrO_2$ using Vienna Ab initio Simulation Package (VASP) [86-88, 114]. The generalized gradient approximation (GGA) with Perdew-Burke-Ernzerhof (PBE) functional is used [89, 90]. To obtain defect formation energies in both phases, we used a supercell consisting of 2×2×2 conventional unit cells of $ZrO_2$ (32 unit formula). The potentials treat $4s^24p^64d^25s^2$ for zirconium, $2s^22p^4$ for oxygen, $3s^23p^63d^64s^2$ for iron, $3s^23p^63d^54s^1$ for chromium, $5s^25p^2$ for tin, $4p^65s^24d^5$ for niobium as valence electrons. Energy cut-off is set to 700 eV and a 2×2×2

*k*-point grid is used. The convergence criterion for the ionic relaxation is set at 0.01 eV/ Å for force. For calculations containing Fe and Cr, a Hubbard U correction of 5 eV is applied to the transition metal dopants.

With the formation energies of individual intrinsic and extrinsic defects, we can further predict their equilibrium concentrations at different temperatures and oxygen partial pressures by minimizing the total free energy of the system under the global charge neutrality constraint. Details of constructing such defect equilibria diagrams for doped $ZrO_2$ can be found in our previous works [115, 116]. To compare the effects of different dopants on transport properties of the oxide matrix, we fix doping concentrations to 10 ppm, which is a typical concentration of alloying elements in the passive films formed on zirconium alloys. Throughout the paper, the notation [defect] is used to represent the fractional concentration of the defect species and Kröger-Vink notations[117] for defects are used.

To understand the mechanical effect of the metal dopants, we performed DFT calculations on the dominant types of defects species with varying cell volumes, with 8 to 15 volume calculations for each defect. These calculations give energy-volume (*E*-*V*) profiles of the system under hydrostatic pressure. We then fit the obtained relationships to Birch-Murnaghan equation of state [118, 119]:

$$E(V) = E_0 + \frac{9V_0B_0}{16}\{[(\frac{V_0}{V})^{\frac{2}{3}} - 1]^3 B_0^{'} + [(\frac{V_0}{V})^{\frac{2}{3}} - 1]^2[6 - 4(\frac{V_0}{V})^{\frac{2}{3}}]\}. \quad (3.1)$$

The fitting provides the equilibrium volume $V_0$, energy $E_0$, and bulk modulus $B_0$. $B_0^{'}$ is the isothermal derivative of $B_0$ with respect to hydrostatic pressure *P*.

With the fitted parameters, we can further evaluate the formation enthalpy $H(P) = E + PV$ for individual point defect with the stress-volume (*P*-*V*) relationship provided by Birch-Murnaghan equation of state:

$$P(V) = \frac{3B_0}{2}[(\frac{V_0}{V})^{\frac{7}{3}} - (\frac{V_0}{V})^{\frac{5}{3}}]\{1 + \frac{3}{4}(B_0^{'} - 4)[(\frac{V_0}{V})^{\frac{2}{3}} - 1]\}. \quad (3.2)$$

## 3.3 Results and Discussion

In this section, we present the chemo-mechanical effects of extrinsic dopants (Cr, Fe, Sn, and Nb) in zirconium oxide and elucidate their implications on oxidation and hydrogen

pickup kinetics of zirconium oxide passive films. The section is organized as follows. First, we show the detailed profiles of equilibrium defect concentrations in doped $ZrO_2$ and compare them with the undoped case. We quantify the induced change in oxygen self-diffusivity, electronic conductivity, and hydrogen content in the oxide matrix. Second, we compare the volume changes brought about by individual defect species and analyze the net effect of each dopant on the phase stability of $ZrO_2$. Last, we provide a discussion on the overall implication of the presented chemo-mechanical effects on oxide film integrity.

A. Chemical effects of dopant insertion

We first quantify the change in defect chemistry brought about by the four doping elements we examine, with a special focus on electronic, oxygen, and hydrogen defects. *Figure 3-1* shows the equilibrium defect concentrations in intrinsic and doped M-$ZrO_2$ at T = 600 K, $P_{H_2O} = 10^{-5}$ atm. For undoped $ZrO_2$ (Figure 3-1(a)), the dominant defects are holes and $V_{Zr}^{''''}$ at high $P_{O_2}$, transitioning to holes and $O_i''$ at intermediate $P_{O_2}$, and electrons compensated by $H_i^{\bullet}$ at low $P_{O_2}$. The dominant type of oxygen defect is $O_i''$ over the whole $P_{O_2}$ range, with its concentration gradually decreases with lower $P_{O_2}$. The dominant type of hydrogen defect transitions from $H_{Zr}'''$ at high $P_{O_2}$ to $H_i^{\bullet}$ at low $P_{O_2}$, reaching a minimum of total hydrogen content at $P_{O_2} = 10^{-12}$ atm.

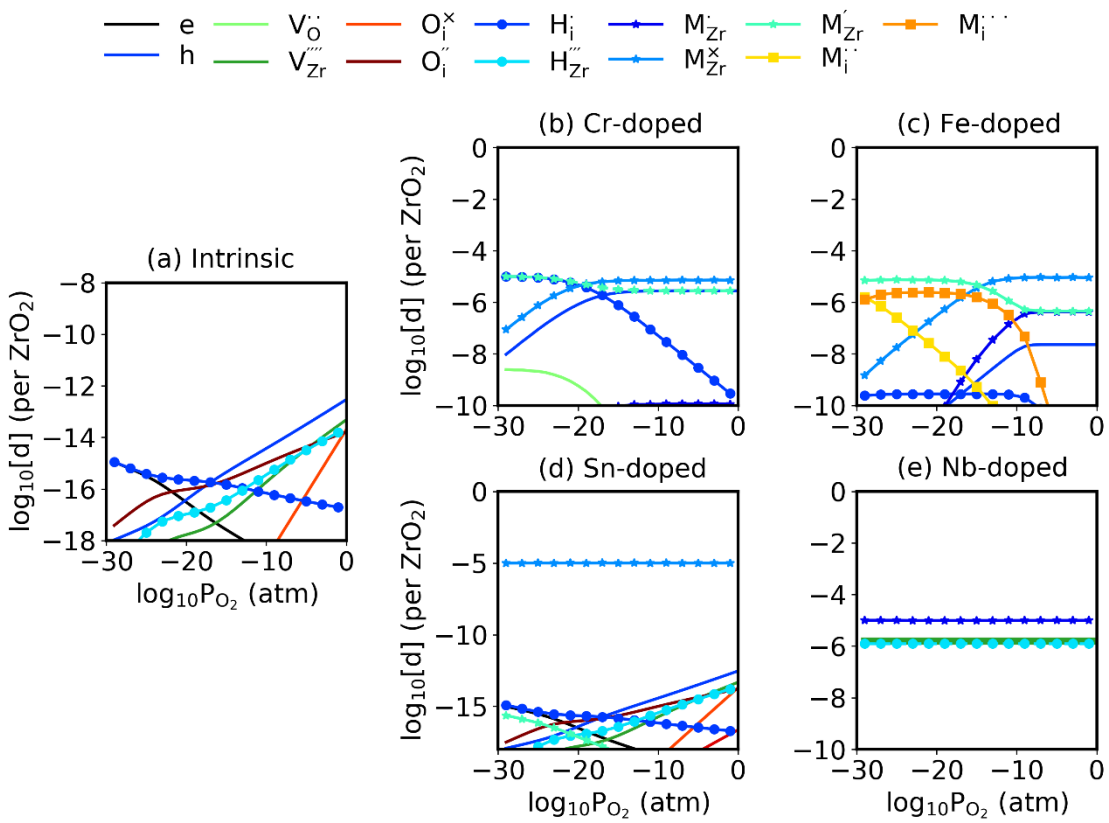


Figure 3-1. Equilibrium defect concentrations in M-$ZrO_2$ predicted at T = 600 K, $P_{H_2O}$ = $10^{-5}$ atm, with varying $P_{O_2}$ for (a) undoped, (b) Cr-doped, (c) Fe-doped, (d) Sn-doped, and (e) Nb-doped. For all doped cases, the dopant concentrations are fixed at 10 ppm.

For Cr-, Fe-, Sn-, and Nb-doped $ZrO_2$, defect profiles are presented in Figure 3-1(b)(c)(d) and (e), we observe a major distinction between isovalent (Sn) and aliovalent (Cr, Fe, and Nb) dopants. Sn exists in $ZrO_2$ lattice predominantly in the 4+ valence state as $Sn_{Zr}^{\times}$. In Figure 3-1(d), the concentration of $Sn_{Zr}^{\times}$ is close to 10 ppm while the concentration of aliovalent $Sn_{Zr}'$ is below $10^{-15}$. As a result, the concentrations of other intrinsic and hydrogen defects almost do not change compared to the intrinsic case.

For aliovalent dopants, the defect profiles are drastically different from undoped $ZrO_2$. Both Cr and Fe can exist in +3, +4, or +5 valence states in substitutional sites, i.e. $M_{Zr}'$, $M_{Zr}^{\times}$, and $M_{Zr}^{\cdot}$. With 10 ppm doping concentration, the dominant compensation mechanism in the high oxygen partial pressure range is $M_{Zr}'$ compensated by $M_{Zr}^{\cdot}$. The

net effect is decreasing in electron chemical potential, raising the concentrations of positively charge defects and reducing the concentrations of negatively charged defects. As a result, in both Figure 3-1 (b) and (c), we observe a significant increase of hole and $H_i^{\bullet}$ concentrations comparing to the undoped case. At low oxygen partial pressures, $Fe_{Zr}'$ is compensated by $Fe_i'''$ while $Cr_{Zr}'$ is compensated by $H_i^{\bullet}$.

Nb exists in the $ZrO_2$ matrix in the form of $Nb_{Zr}^{\bullet}$ over the entire oxygen partial pressure range. It increases the electron chemical potential and thus increases the concentrations of positively charged defects. In Figure 3-1 (e), $Nb_{Zr}^{\bullet}$ is compensated by $V_{Zr}''''$ and $H_{Zr}'''$. The concentrations of the latter two defect species are enhanced by eight orders of magnitude comparing to their concentrations in undoped $ZrO_2$.

With the established understanding of defect equilibrium profiles, we now turn to the effects of these dopant species on oxygen transport, electronic conductivity, and hydrogen content in $ZrO_2$. In Figure 3-2 (a), we show oxygen self-diffusivity $D_{tot}$ profiles of differently-doped $ZrO_2$ at $T$ = 600 K, $P_{H_2O} = 10^{-5}$ atm. For undoped $ZrO_2$, $D_{tot}$ is dominated by oxygen interstitial ($O_i''$) diffusion and thus decreases with lowering oxygen partial pressure, showing a 1/10 slope in the high oxygen partial pressure range. Since Sn does not change the concentrations of intrinsic defects, $D_{tot}$ of Sn-doped $ZrO_2$ almost does not change from undoped $ZrO_2$.

Since Cr and Fe serves as acceptor dopants and decrease $[O_i'']$, in the high $P_{O_2}$ range, oxygen self-diffusivities of Cr- and Fe-doped $ZrO_2$ are lower compared to undoped $ZrO_2$. However, for Cr-doped $ZrO_2$ at highly reducing conditions, the oxide goes into a vacancy-diffusion dominated regime and $D_{tot}$ begins to increase with decreasing $P_{O_2}$. As a result, when $P_{O_2} < 10^{-10}$ atm, Cr has a promotion effect on oxygen diffusion with a -1/2 $\log D_{tot}$-$\log P_{O_2}$ slope. Nb promotes $[O_i'']$ over the whole oxygen pressure range and enhances oxygen transport.

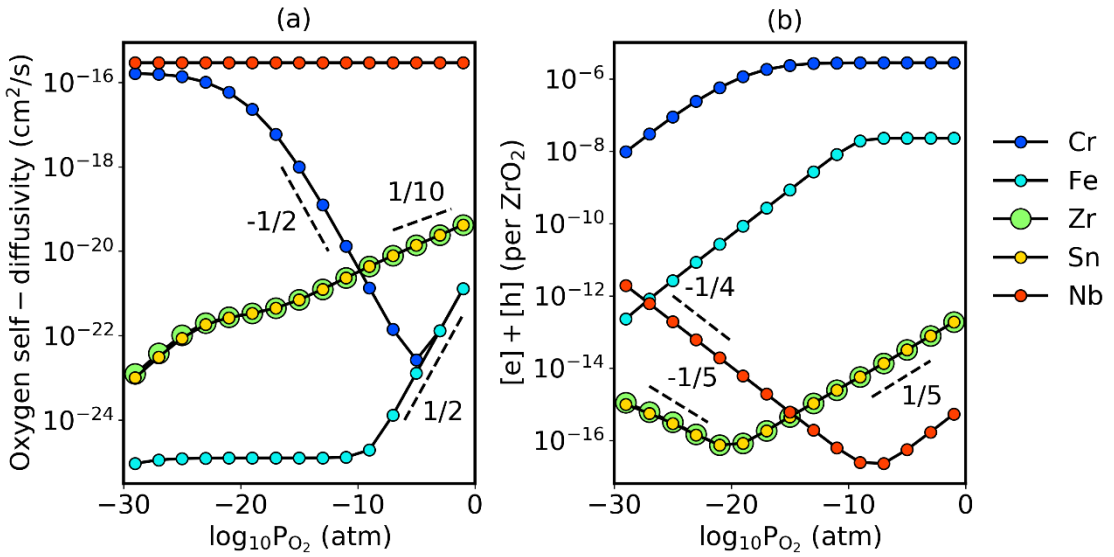


Figure 3-2. (a) Oxygen self-diffusivity and (b) total concentration of electrons and holes at T = 600 K, $P_{H_2O} = 10^{-5}$ atm for intrinsic and doped M-$ZrO_2$. The legends show the corresponding dopant types with Zr being the undoped case. The sum of electron and hole concentrations represents the total electronic conductivity of the oxide matrix.

Figure 3-2 (b) shows the total concentrations of electrons and holes for the five differently doped $ZrO_2$. This quantity serves as an indicator of the total electronic conductivity of the oxide film. In undoped $ZrO_2$, the dominant electronic carrier transitions from electron ($P_{O_2} < 10^{-20}$ atm) to hole ($P_{O_2} > 10^{-20}$ atm), exhibiting a valley shape curve as a function of $P_{O_2}$. Cr and Fe doping enhance p-type conductivity. As a result, hole conduction is dominant, and the total conductivity is enhanced over the whole $P_{O_2}$ range. Meanwhile Nb increases n-type conductivity, increasing electron concentration in the low $P_{O_2}$ range and decreasing hole concentration in the high $P_{O_2}$ range.

In *Figure 3-3* we show the same diagram for total hydrogen solubility [$H_{tot}$ ](Figure 3-3 (a)). A similar valley shape with varying $P_{O_2}$ is observed again in total hydrogen solubility of undoped $ZrO_2$. On the left branch ($P_{O_2} < 10^{-12}$ atm), the dominant contributor to [$H_{tot}$ ] is $H_i^{\bullet}$ and on the right branch $H_{Zr}'''$ . This transition leads to a minimum hydrogen solubility at about $10^{-12}$ atm [116]. Cr and Fe promote $H_i^{\bullet}$ concentration, while Nb

promotes $H_{Zr}'''$ concentration. As a result, total hydrogen solubility increases regardless of the aliovalent dopant type.

In Figure 3-3 (b), we look at the $H_i^{\bullet}$ concentration. Here $[H_i^{\bullet}]$ is an indicator for hydrogen diffusion kinetics, assuming interstitial hydrogen has a lower migration barrier comparing to trapped hydrogen ($H_{Zr}'''$). For Cr and Fe, which enhance $[H_i^{\bullet}]$, we expect higher hydrogen solubility as well as faster hydrogen diffusion kinetics compared to undoped $ZrO_2$. However, Nb decreases the $H_i^{\bullet}$ concentration compared to intrinsic $ZrO_2$ and can slow down hydrogen diffusion kinetics in the oxide matrix.

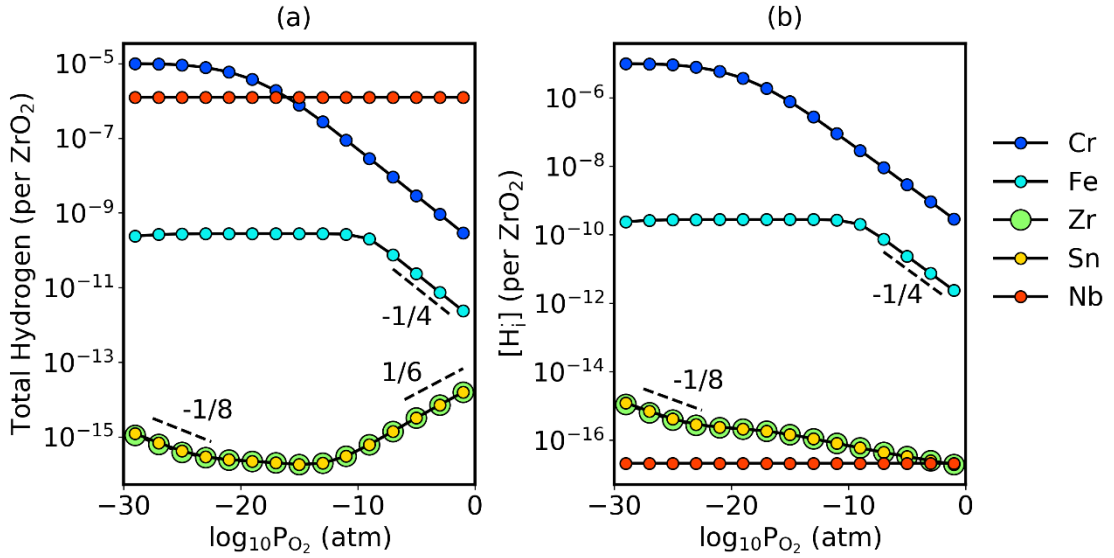


Figure 3-3. (a) Total hydrogen content and (b) concentration of hydrogen interstitial $H_i^{\bullet}$ in M-$ZrO_2$ at T = 600 K, $P_{H_2O} = 10^{-5}$ atm. The former quantifies the total hydrogen solubility in the oxide matrix while the latter links to hydrogen diffusivity in $ZrO_2$.

B. Mechanical effects of dopant insertion

In the previous section, we discussed defect chemical changes associated with the four dopants surveyed. The main conclusion is that Cr and Fe serve as p-type dopants and Nb serves as n-type dopant. The former two promote the concentrations of positively charged species and the latter promotes negatively charged species. In this section, we look at how each defect species changes the cell volume and phase stability of $ZrO_2$ and infer the overall effect of each dopant on the microstructural evolution of the passive film.

Volumetric changes in the material accompanies compositional changes induced by extrinsic atom insertion, which is termed *chemical expansion* [120]. In Table 3-1, we list the volume change effects of important defect species in M-$ZrO_2$ and T-$ZrO_2$ for the compositions that we surveyed in Figure 3-1. We observe that metal substitutional defects ($Cr_{Zr}^{\times}$, $Cr_{Zr}^{\prime}$, $Fe_{Zr}^{\times}$, $Fe_{Zr}^{\prime}$, $Sn_{Zr}^{\times}$, and $Nb_{Zr}^{\bullet}$) generally have small volume change effect on the oxide material. Among these dopant defects, volume changes are associated with the charges of the defect species, with the negative species expanding the cell and positive species contracting the cell. The largest fractional change of the metal dopants is 1.0% volume expansion induced by $Nb_{Zr}^{\bullet}$.

Intrinsic defects and hydrogen defects, on the other hand, appear to have a larger volume change effect. In Table 3-1, the largest volume changes are caused by $V_O^{\bullet\bullet}$ and $H_i^{\bullet}$ (contraction), and $V_{Zr}^{\prime\prime\prime\prime}$ and $H_{Zr}^{\prime\prime\prime}$ (expansion). According to the defect chemistry analysis in Section IIIA, Cr and Fe promote the concentrations of the former two while suppress the concentrations of the latter two. Nb has the reverse effect. This leads to the conclusion that overall, Cr and Fe contracts the oxide cell while Nb expands the oxide cell.

Table 3-1. Equilibrium volumes (in $Å^3$) for the dominant defect species as obtained by fitting E-V data to Birch-Murnaghan equation of states. The absolute volumes are the equilibrium volumes of one defect in 32 $ZrO_2$ divided by 32 (per unit formula). The relaxation volumes are the volumes of the defective cell minus the volume of the perfect cell in the same phase, divided by 32. The fractional volume changes are calculated with respect to perfect T-$ZrO_2$.

| | M-$ZrO_2$ | | T-$ZrO_2$ | |
|---|---|---|---|---|
| | Absolute Volume ($Å^3$) | Relaxation Volume ($Å^3$) | Absolute Volume ($Å^3$) | Relaxation Volume ($Å^3$) |
| Perfect | 36.76 (+4.2%) | / | 35.28 (0) | / |
| $V_{Zr}^{\prime\prime\prime\prime}$ | 36.70 (+4.0%) | -0.06 | 36.71(+4.0%) | +1.42 |
| $h^{\bullet}$ | 36.56(+3.6%) | -0.20 | 35.02(-0.7%) | -0.26 |
| $V_O^{\bullet\bullet}$ | 36.33(+3.0%) | -0.43 | 34.53(-2.1%) | -0.75 |
| $Cr_{Zr}^{\times}$ | 36.63(+3.8%) | -0.13 | 35.19(-0.3%) | -0.09 |

| | | | | |
|---|---|---|---|---|
| $Cr_{Zr}'$ | 36.86(+4.5%) | +0.10 | 35.63(+1.0%) | +0.35 |
| $Fe_{Zr}^{\times}$ | 36.70(+4.0%) | -0.06 | 35.25(-0.1%) | -0.03 |
| $Fe_{Zr}'$ | 36.92(+4.6%) | +0.16 | 35.59(+0.9%) | +0.31 |
| $Sn_{Zr}^{\times}$ | 36.74(+4.1%) | -0.02 | 35.31(+0.1%) | +0.03 |
| $Nb_{Zr}^{\bullet}$ | 36.39(+3.1%) | -0.37 | 34.93(-1.0%) | -0.35 |
| $H_i^{\bullet}$ | 36.17(+2.5%) | -0.59 | 34.68(-1.7%) | -0.60 |
| $H_{Zr}'''$ | 37.11(+5.2%) | +0.35 | 38.25(+8.4%) | +2.97 |

When it comes to phase stability, intrinsic defects and hydrogen defects also have a more significant effect compared to extrinsic defects. In Figure 3-4, we plot the enthalpy difference $\Delta H$ between the tetragonal and monoclinic phase for perfect cells and cells with intrinsic defects as a function of hydrostatic pressure *P*. $\Delta H > 0$ means that the tetragonal phase has a higher enthalpy then the monoclinic phase and therefore shows the pressure range in which M-$ZrO_2$ is stable. Correspondingly, $\Delta H < 0$ represents the pressure range in which T-$ZrO_2$ is stable. By plotting this $\Delta H$ diagram, we have established a phase diagram for $ZrO_2$ with varying pressure.

Figure 3-4 (a) shows the phase diagram predicted for defect-free $ZrO_2$. The T-to-M transition happens at 10.51 GPa, as has been reported in our previous work [121]. This prediction is in reasonable agreement with the experimentally measured critical transition pressure [109, 122]. In Figure 3-4 (b) (c) and (d) we show the change in critical transition pressure with $V_{Zr}''''$, $h^{\bullet}$, and $V_O^{\bullet\bullet}$, respectively. Among the three, $h^{\bullet}$ has the smallest effect on phase stability, increasing the critical pressure slightly to 12.14 GPa. With $V_{Zr}''''$ or $V_O^{\bullet\bullet}$ in the cell, however, the phase energetics are significantly changed. $V_{Zr}''''$ strongly destabilizes the tetragonal phase while $V_O^{\bullet\bullet}$ strongly stabilizes it, both making the DFT-calculated pressure range (5 ~ 20 GPa) a single-phase region.

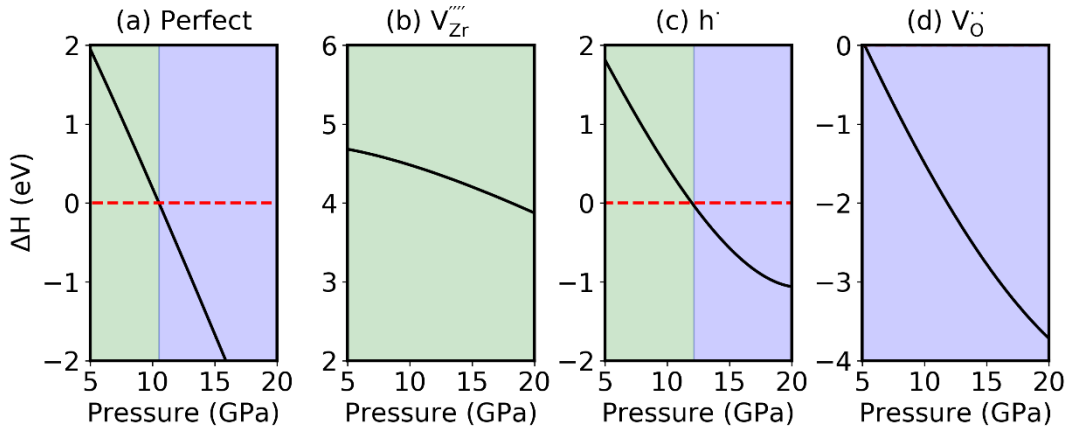


Figure 3-4. Enthalpy difference $\Delta H$ between T-$ZrO_2$ and M-$ZrO_2$ for (a) perfect cell and defective cells with (b) $V_{Zr}^{''''}$, (c) $h^{\bullet}$, and (d) $V_O^{\bullet\bullet}$ in 32 unit formula of $ZrO_2$ with varying hydrostatic pressure. The point where $\Delta H$ reaches zero (intersection with the red dashed line) presents the critical pressure at which T-to-M phase transformation occurs. The green region represents the pressure range in which the monoclinic phase is stable while the blue region represents the pressure range in which the tetragonal phase is stable.

Figure 3-5 shows $\Delta H$ plots for metal dopants and hydrogen defects. We see that the changes in phase stability induced by metal dopants (Figure 3-5 (a-f)) are smaller comparing to $H_i^{\bullet}$ and $H_{Zr}^{'''}$ (Figure 3-5 (g)(h)). The critical transition pressures are 11.46, 18.29, 12.74, 17.90, 13.55, 12.33 GPa for $Cr_{Zr}^{\times}$, $Cr_{Zr}{}'$, $Fe_{Zr}^{\times}$, $Fe_{Zr}{}'$, $Sn_{Zr}^{\times}$, $Nb_{Zr}^{\bullet}$ respectively. $H_i^{\bullet}$ stabilizes the tetragonal phase over a large range of stress and decreases the transition pressure to 5.88 GPa. Contrarily, $H_{Zr}^{'''}$ destabilizes the tetragonal phase, making M-$ZrO_2$ the favorable phase over the entire stress range.

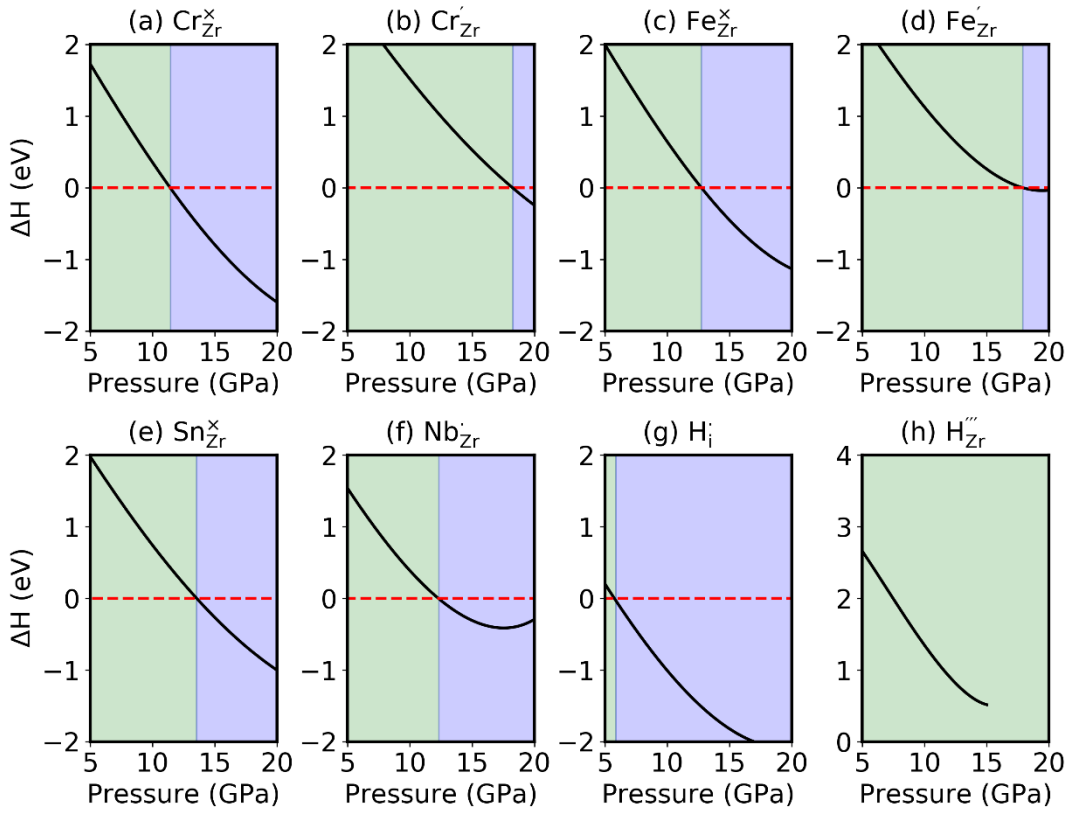


Figure 3-5. Enthalpy difference $\Delta H$ between T-$ZrO_2$ and M-$ZrO_2$ for defective cells with (a) $Cr_{Zr}^{\times}$, (b) $Cr_{Zr}^{\prime}$, (c) $Fe_{Zr}^{\times}$, (d) $Fe_{Zr}^{\prime}$, (e) $Sn_{Zr}^{\times}$, (f) $Nb_{Zr}^{\bullet}$, (g) $H_i^{\bullet}$, and (h) $H_{Zr}^{\prime\prime\prime}$ in 32 unit formula of $ZrO_2$ with varying hydrostatic pressure. The green region represents the pressure range in which the monoclinic phase is stable while the blue region represents the pressure range in which the tetragonal phase is stable.

To summarize, metal dopant defects have limited influence on the enthalpy differences of the two phases. The dopants influence the phase transition mainly through changing the concentrations of intrinsic and hydrogen defects. We have identified four defect species that bring about the most significant changes in phase stability. $V_O^{\bullet\bullet}$ and $H_i^{\bullet}$ strongly stabilize T-$ZrO_2$ while $V_{Zr}^{\prime\prime\prime\prime}$ and $H_{Zr}^{\prime\prime\prime}$ destabilize T-$ZrO_2$. As we have seen in Section IIIA, Cr and Fe increase the concentrations of $V_O^{\bullet\bullet}$ and $H_i^{\bullet}$ while decreasing the concentrations of $V_{Zr}^{\prime\prime\prime\prime}$ and $H_{Zr}^{\prime\prime\prime}$. Nb decreases the concentrations of the former two and increases the concentrations of the latter two. This leads to the conclusion that Fe and Cr stabilizes T-$ZrO_2$ and Nb destabilizes T-$ZrO_2$.

C. Implications for passive film integrity

So far we have presented the chemo-mechanical effects of the four surveyed dopants categorized by their dominant charged states: (1) Cr and Fe exist in $ZrO_2$ as acceptor dopants, increasing the concentrations of $V_O^{\bullet\bullet}$ and $H_i^{\bullet}$, which contract the oxide matrix and stabilize tetragonal phase $ZrO_2$. (2) Nb exists in $ZrO_2$ as donor dopant, increasing the concentrations of $V_{Zr}^{''''}$ and $H_{Zr}^{'''}$, which expand the oxide matrix and destabilizes tetragonal phase $ZrO_2$. (3) Sn exists in $ZrO_2$ dominantly as a neutral defect, which has little effect on the concentrations of intrinsic defects or on phase stability in the bulk. In this section, we investigate related evidence in the literature to further link our results with the overall oxide film integrity of zirconium alloys.

Chemically, the observed change in H and O defects is possibly linked to the inverse relationship between oxidation resistance and hydrogen pickup resistance observed experimentally [123]. While p-type dopants (Fe, Cr) increase $H_i^{\bullet}$ and thus hydrogen diffusivity, they decrease electron and oxygen interstitial concentrations, thus limiting oxidation kinetics. The opposite is true for n-type doping (Nb). This trend is consistent with the observed comparison between Zr-Nb alloy and Zr-Fe-Cr alloy [123]. Zr-Nb alloys have a very low hydrogen pickup fraction but fast oxidation rate while Zr-Fe-Cr alloys have worse hydrogen resistance but slower oxidation kinetics.

Mechanically, the effects of Fe/Cr and Nb on phase fraction are also very consistent with experimental findings. Choudhuri *et al* systematically varied Fe content in Zr-2.5Nb alloy and studied the corresponding corrosion behavior in the autoclave [124]. By Grazing Incidence X-ray Diffraction, they observed a higher fraction of T-$ZrO_2$ in the passive film with higher concentration of Fe. Yilmazbayhan *et al* compared the oxide film structures on Zricaloy-4 (no Nb), ZIRLO$^{TM}$ (9900 ppm Nb), Zr-2.5Nb (25,500 ppm Nb) and Zr-2.5Nb-0.5Cu (24,300 ppm Nb) [125]. They concluded that the fraction of T-$ZrO_2$ of the former two low-Nb-content alloys are observably higher than the latter two. This phase fraction trend is also observed by Maroto *et al* [126].

The effect of Sn is less conclusive from this bulk electro-chemo-mechanical analysis because there is no change in defect concentrations that significantly influences transport properties or phase stability of the oxide matrix. Experimentally, it is inconclusive whether Sn increases or decreases T-phase fraction of the passive film [127, 128]. It is

probable that the dominant influence of Sn doping is not a bulk effect, but through the interplay between $SnO_2$ secondary-phase particles and the $ZrO_2$ matrix.

## 3.4 Conclusion

In this work, we studied the electro-chemo-mechanical effects of Cr, Fe, Sn and Nb in bulk $ZrO_2$. We found that Cr and Fe have similar effects in $ZrO_2$ because they both serve as acceptor dopants and increase the concentration of positively charged intrinsic defects. Sn exists as a neutral substitutional defect and does not significantly change the concentrations of intrinsic defect . Nb exists predominantly in the +5 state and has the opposite effect compared to Cr and Fe. The dopants' influence on phase stability is not a direct effect of cation defects, but through changing the concentrations of intrinsic defects that have a significant impact on phase stability. For all the important dopant species in $ZrO_2$, we identified four species that have the strongest effect on chemical expansion and phase stability. $V_O^{\bullet\bullet}$ and $H_i^{\bullet}$ contract the lattice and stabilize T-$ZrO_2$ while $V_{Zr}^{''''}$ and $H_{Zr}'''$ expand the lattice and destabilize T-$ZrO_2$. Fe and Cr increase the concentrations of the former two and decrease the concentrations of the latter two, leading to an overall stabilization effect for T-$ZrO_2$. The opposite is true for Nb, which destabilizes T-$ZrO_2$. These results, in part, explain the reported inverse relationship between oxidation kinetics and hydrogen pickup of zirconium alloys and are consistent with observed phase fraction trends with varying alloying contents.

# 4 Electro-chemo-mechanical effects of lithium incorporation in zirconium oxide

Understanding the response of functional oxides to extrinsic ion insertion is important for technological applications including electrochemical energy storage and conversion, corrosion, and electronic materials in neuromorphic computing devices. Decoupling the complicated chemical and mechanical effects of ion insertion is difficult experimentally. In this work, we assessed the effect of lithium incorporation in zirconium oxide as a model system, by performing first-principles based calculations. The chemical effect of lithium is to change the equilibria of charged defects. Lithium exists in $ZrO_2$ as positively charged interstitial defect, and raises the concentration of free electrons, negatively charged oxygen interstitials and zirconium vacancies. As a result, oxygen diffusion becomes faster by five orders of magnitude, and the total electronic conduction increases by up to five orders of magnitude in the low oxygen partial pressure regime. In the context of Zr metal oxidation, this effect accelerates oxide growth kinetics. In the context of electronic materials, it has implications for resistance modulations via ion incorporation. The mechanical effect of lithium is in changing the volume and equilibrium phase of the oxide. Lithium interstitials together with zirconium vacancies shrink the volume of the oxide matrix, releases the compressive stress that is needed for stabilizing the tetragonal phase $ZrO_2$ at low temperature and promotes tetragonal-to-monoclinic phase transformation. By identifying these factors, we are able to mechanistically interpret experimental results in the literature for zirconium alloy corrosion in different alkali metal hydroxide solutions. These results provide a mechanistic and quantitative understanding of lithium-accelerated corrosion of zirconium alloys, as well as and more broadly show the importance of considering coupled electro-chemo-mechanical effects related to cation insertion into functional oxides.

## 4.1 Introduction

Ion insertion and extraction is a very common process in a number of technologically important applications, such as batteries [129, 130], solid oxide fuel cells [131-133], ion transport membranes [134], electrochromic devices [135], and neuromorphic computing devices [136]. The response of the host material to extrinsic ions entering into its lattice is a complicated process, involving changes both in the chemical composition and in the

stress state. Chemically, extrinsic doping changes the defect chemistry of the host material and thus influences ionic and electronic conduction. This is coupled to the mechanical response of the host material through chemical expansion/contraction [137]. Furthermore, changes in the defect concentration can alter the atomic structure and phase of the material, resulting in distinct electrical and magnetic properties as well as microstructure evolution [138-140]. Understanding the chemical and mechanical mechanisms in response to ion insertion and extraction is key to the design of better devices and materials. However, the complexity of such coupled processes makes it difficult, if not impossible, to separate contributions of individual factors experimentally and fully identify the underlying mechanisms.

In this work, we assess the coupled chemical and mechanical effects of lithium incorporation in $ZrO_2$ with density functional theory (DFT) calculations. $ZrO_2$ is chosen as the model material. It is the critical passivating layer in the corrosion of zirconium alloys used as fuel cladding in nuclear reactors [48]. It is also widely studied as high-k dielectrics in metal-oxide-semiconductor field-effect transistor (MOSFET) devices [70, 141], as well as resistive switching devices [71, 72]. Electrochemical control of Li content in $CoO_2$ has been shown as utility for resistive processing [136], and it is feasible that Li can similarly tune the electronic conductivity of $ZrO_2$.

In light water reactors, zirconium alloys are used for cladding, enclosing the nuclear fuel. During operation, the tetragonal and monoclinic phases of $ZrO_2$ passive layer grow on the outer layer of the cladding and protect the alloy from corrosion in high temperature coolant water. Lithium accelerated corrosion is a well-known cladding corrosion phenomenon. In nuclear reactors, LiOH is added into the coolant water in contact with the cladding layer in order to balance the pH reduction caused by the boric acid that is added as a neutron absorber [51]. When a zirconium alloy is immersed in aqueous solutions containing high concentration of lithium ion, the oxide growth rate significantly increases [142]. This phenomenon, called lithium-accelerated corrosion, is detrimental because lithium ions tend to concentrate locally at the oxide film surface [143]. The concentrated lithium ions further diffuse through the oxide film and result in localized accelerated corrosion [144]. Here we aim to resolve the mechanisms by which lithium insertion in $ZrO_2$ accelerates corrosion.

Our study revealed two distinct but coupled effects induced by lithium incorporation: (1) Lithium changes the defect chemistry of $ZrO_2$ and increases the concentration of zirconium vacancies, oxygen interstitials and free electrons, and decreases that of free holes. The increase in oxygen interstitials leads to faster oxygen diffusion. The combined effect of increasing electron concentration and decreasing hole concentration leads to an increase in the total electronic conduction by up to five orders of magnitude in the low oxygen partial pressure regime. As a result, a net effect of accelerated oxide growth rate is expected. (2) Incorporation of lithium, together with the accompanying zirconium vacancies, increases the critical compressive stress that is needed for stabilizing tetragonal $ZrO_2$ (T-$ZrO_2$). The T-$ZrO_2$ serves as a coherent protective layer against further oxidation and is only stabilized by the compressive stresses at the metal-oxide interface at the reactor operation temperatures (~300$^o$C) [145]. In the presence of lithium, the critical stress needed for stabilizing the T-$ZrO_2$ is much higher than the stress at the metal-oxide interface and so it transforms into the monoclinic phase (M-$ZrO_2$). This is a volume expansion process and should lead to cracks in the oxide film associated with accelerated corrosion. We validated our results with experimental reports of corrosion in literature and helped explain the differences among corrosion effects of different alkali metal hydroxide solutions.

## 4.2 Methods

DFT calculations were performed with Vienna Ab initio Simulation Package (VASP) [86-88, 114] using the generalized gradient approximation (GGA) with Perdew-Burke-Ernzerhof (PBE) functional [89, 90]. $4s^2 4p^6 4d^2 5s^2$ for zirconium, $2s^2 2p^4$ for oxygen and $1s^2 2s^1$ for lithium are treated as valence electrons. The chemical effect of lithium was assessed by comparing the equilibria of point defects with and without lithium in $ZrO_2$. Calculations related to defect formation energies were done on a supercell consisting of 2×2×2 conventional unit cells of $ZrO_2$ with 700 eV energy cut-off and 2×2×2 *k*-point grid. The perfect cell was pre-relaxed and we keep the volume and cell shape constant when relaxing the defect structures. The calculated defect formation energies were used to simulate the chemical effect of lithium in the dilute limit. Details of calculating the defect formation energies and equilibrium defect concentrations at different temperatures and oxygen partial pressures can be found in [84] for T-$ZrO_2$ and [77] for M-$ZrO_2$. In particular, the latter presents in detail how to model equilibrium defect chemistry with

extrinsic aliovalent doping and we adopt that approach in this work. We consider zirconium oxide equilibrating with the environment of a fixed chemical potential of lithium, $\mu_{Li}$ .

To assess the mechanical effect induced by lithium ionic defects, we perform DFT calculations on several important defect species (1) by varying cell volume hydrostatically and allowing cell shape to change, and (2) by applying planar stress. The defective cell used here are all one defect in 32 unit formula of $ZrO_2$. The resulting energy-volume (*E*-*V*) profile is fitted to the Birch-Murnaghan equation of state [118, 119] to obtain the equilibrium volume $V_0$ and energy $E_0$.

$$E(V) = E_0 + \frac{9V_0B_0}{16}\{[(\frac{V_0}{V})^{\frac{2}{3}} - 1]^3 B_0^{'} + [(\frac{V_0}{V})^{\frac{2}{3}} - 1]^2[6 - 4(\frac{V_0}{V})^{\frac{2}{3}}]\} \qquad (4.1)$$

Here $B_0$ and $B_0$' represent the bulk modulus and its isothermal derivative with respect to pressure respectively. The equilibrium volume acquired from the hydrostatic fixed volume calculations are compared to the volume of perfect cell to obtain defect relaxation volumes.

Further, we evaluate the stress-volume (*P*-*V*) relationship predicted by Birch-Murnaghan equation of state

$$P(V) = \frac{3B_0}{2}[(\frac{V_0}{V})^{\frac{7}{3}} - (\frac{V_0}{V})^{\frac{5}{3}}]\{1 + \frac{3}{4}(B_0^{'} - 4)[(\frac{V_0}{V})^{\frac{2}{3}} - 1]\} \ , \qquad (4.2)$$

which also gives the enthalpy-stress relationship by calculating $H = E + PV$. For biaxial stress, the energy change resulting from stress can be separated into a hydrostatic contribution and a deviatoric contribution. Here we extracted the hydrostatic part by fitting to Birch-Murnaghan equation, which produces consistent pressure compared to the total stress calculated by DFT.

## 4.3 Results and Discussion

In this section, we present the predicted chemical and mechanical effects of lithium incorporation in zirconium oxide of both the monoclinic and the tetragonal phase. We divide this section into three parts. First, we present the defect chemistry of Li-doped

$ZrO_2$ and how the Li doping changes electronic and oxygen transport in M-$ZrO_2$. Second, we look closely at the volume change induced by the dominant defect types in the presence of Li found in the first part, and the implication of those volume changes on the T-to-M phase transformation in $ZrO_2$. Last, we compare lithium with other alkali metal elements to reveal its unique character regarding the coupled chemical and mechanical effect in $ZrO_2$.

A. Chemical effect of lithium insertion into $ZrO_2$

We consider various sites and valence states that lithium could take when incorporated into M-$ZrO_2$. For lithium sitting on a zirconium vacancy site, charge states from -5 to +1 were considered. For interstitial lithium, -1, 0 and +1 charge states are considered. DFT results show that the formation energies of all lithium substitutional defects have too high formation energy to have a significant concentration in the oxide matrix. For interstitial lithium, the dominating valence state is always $Li_i^{\bullet}$.

With the calculated formation energies, we obtained equilibrium concentrations of each defect following the method adopted in [7]. The computational framework captures defect energetics with first-principles calculations and feed them to thermodynamic equilibria and charge neutrality calculations. This model predicts equilibrium defect concentrations as a function of temperature and oxygen partial pressure with no *a priori* assumption of dominant defect species. The defect concentrations in M-$ZrO_2$ as a function of oxygen partial pressure are shown in Figure 4-1 at $T$ = 600 K, which is close to the nuclear reactor operation temperature. The notation [defect] is used to represent concentration of the defect species per unit formula. Figure 4-1(a) shows the equilibria of intrinsic defects in M-$ZrO_2$. Throughout the oxygen partial pressure range, the holes are the dominant type of positively-charged defect. The compensating species changes from being the free electron at low $P_{O_2}$, to $O_i''$ at intermediate $P_{O_2}$, and $V_{Zr}''''$ at high $P_{O_2}$. The situation changes when lithium is incorporated into the oxide matrix, as shown in Figure 4-1(b) with $\mu_{Li}$ = -14.5 eV. The chemical potential for lithium is referenced to that of lithium metal, i.e. for lithium metal $\mu_{Li}$ = 0 eV. This choice of chemical potential corresponds a doping concentration of 10 ppm at intermediate $P_{O_2}$, consistent with experimentally reported Li concentration in the oxide layer on zirconium alloys [146].

We also examined a range of $\mu_{Li}$ which shows that the compensating mechanism does not change within the stability range.

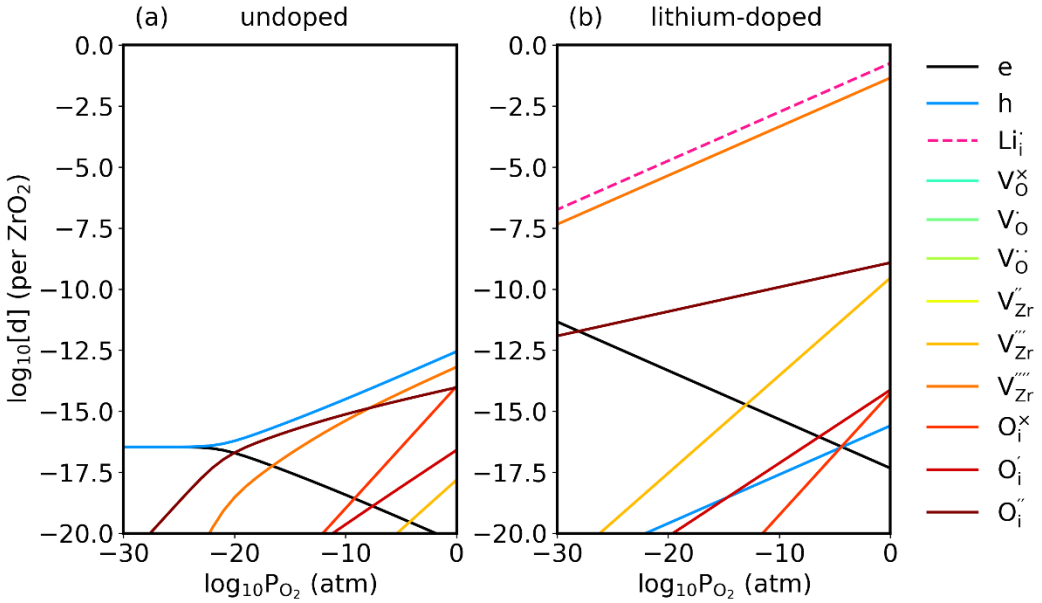


Figure 4-1. Equilibrium defect concentrations predicted at 600 K for (a) undoped m-$ZrO_2$ and (b) Li-doped m-$ZrO_2$. Oxygen vacancies are not visible in the plotted range though they were explicitly calculated. Phonon vibrational free energies are included in calculating defect formation free energies as in Ref. [77].

Knowing that lithium exists in the $ZrO_2$ oxide matrix in the form of $Li_i^{\cdot}$, we can further analyze the change in native defect concentrations. The goal of examining defect chemistry upon lithium insertion is two-fold. First, the oxide growth rate is governed by oxygen diffusion and electronic conduction [51]. By knowing the oxygen-related defects, electrons, holes and cation vacancies, we can understand the net effect of lithium insertion on the corrosion kinetics, here equivalent to the growth rate of the oxide. Second, it is also important to know how the dominant defects in the presence of $Li_i^{\cdot}$ alter the mechanical behavior of the oxide matrix. This is because mechanical stresses can lead to oxide film fracture, exposure of the metal to water and accelerated corrosion. In the following, we present the major changes caused by Li on intrinsic defects related to these two aspects.

First, looking at oxygen-related defects, we find that $O_i''$ is the dominant oxygen defect species both before and after lithium insertion. Comparing Figure 4-1(a) with Figure 4-1(b), $[O_i'']$ is increased by about four orders of magnitude with lithium doping. This directly affects in oxygen diffusivity, shown in Figure 4-2(a). Here the total oxygen self-diffusivity $D_{tot}$ is calculated with random-walk model [115, 147, 148] by

$D_{tot} = \sum_q [V_O^q] D_{V_O}^q + \sum_q [O_i^q] D_{O_i}^q$ , where we use the diffusion coefficient of each defect type $D_{V_O}^q$ and $D_{O_i}^q$ from [149]. Derivations for the self-diffusivity expression in ionic solids can be found in Eq. 3.6 - 3.9 in [147], or Eq. 8. 37 - 8.51 in [148]. At 600 K we see, in both the intrinsic and Li-doped M-$ZrO_2$, a 1/10 log$D_{tot}$-log $P_{O_2}$ slope at the high $P_{O_2}$ regime where $V_{Zr}''''$ is the dominant negatively-charged defect. Because of the increase of oxygen interstitial concentration with lithium doping, $D_{tot}$ rises also by about four orders of magnitude. At the low $P_{O_2}$ regime this enhancement is even more profound. This is because the intrinsic M-$ZrO_2$ enters the hole-, compensation regime with a 1/2 slope in log$D_{tot}$-log $P_{O_2}$ , whereas the Li-doped M-$ZrO_2$ has a 1/10 slope throughout the examined oxygen partial pressure range. At $P_{O_2}$ = $10^{-30}$ atm, we see a ten-order-of-magnitude difference in $D_{tot}$ comparing the two cases.

Next, for implications on electronic conduction, we take a close look at the change in electron and hole concentration. The dominant electronic carrier in the intrinsic M-$ZrO_2$ changes from being hole-dominated at high $P_{O_2}$ to $[e'] \approx [h^\bullet]$ at $P_{O_2}$ = $10^{-23}$ atm. (Figure 4-1(a)). Upon lithium insertion, the hole concentration is greatly suppressed and electron concentration enhanced. The dominant electronic carrier type changes from being hole to electron at $P_{O_2}$ = $10^{-5}$ atm, and we no longer observe a regime where $[e'] \approx [h^\bullet]$. To show the net change in electronic conduction (assuming no change in mobilities), we plot $[e']+[h^\bullet]$ in *Figure 4-2*(b). In hole-dominated region ( $P_{O_2}$ > $10^{-5}$ atm), the total carrier concentration demonstrates a 1/5 slope and decreases by three orders of magnitude upon lithium insertion. In the intermediate $P_{O_2}$ range, intrinsic curve goes from hole-dominated (1/5 slope) to $[e'] \approx [h^\bullet]$ (flat regime). Lithium-doped M-$ZrO_2$ transitions to electron-dominated regime which exhibits a -1/5 slope in most of the $P_{O_2}$ range. The relative

change in electronic conduction changes sign at $10^{-11}$ atm; above this $P_{O_2}$ lithium doping decreases electronic conduction while below it increases electronic conduction. The enhancement in electronic conduction becomes more and more significant with lowering of $P_{O_2}$. We observe a maximum of nearly five orders magnitude increase in the total carrier concentration at $P_{O_2}$ = $10^{-30}$ atm. This $P_{O_2}$ is relevant both at the metal-oxide interface, and in the context of tuning effective $P_{O_2}$ electrochemically, as have been demonstrated for other binary oxides [150-152].

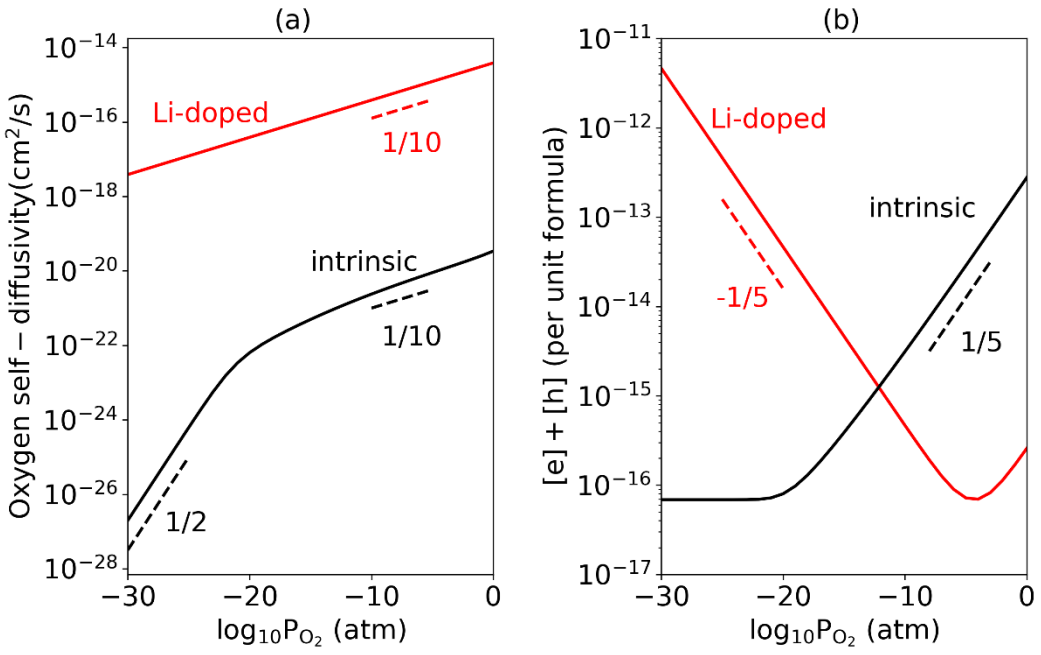


Figure 4-2. (a) Oxygen self-diffusivity and (b) electron and hole concentration at 600 K for undoped M-$ZrO_2$ and Li-doped M-$ZrO_2$.

Considering the above-described effects of Li both on oxygen defects and on electronic defects, a net acceleration of oxide growth is expected with lithium insertion. More specifically, comparing the effect of lithium on oxygen conduction versus electronic conduction, the change in the former (ten orders of magnitude at $P_{O_2}$ = $10^{-30}$ atm) is significantly larger than that in the latter (five orders of magnitude at $P_{O_2}$ = $10^{-30}$ atm). This is consistent with the dominant oxygen defects, $O_i''$, being -2 charged. Upon

lithium insertion, electron chemical potential increases due to the n-type doping effect of lithium, lowering the formation energy of negatively-charged defects. This lowering of formation energy is doubled for -2 charged oxygen interstitials compared to the -1 charged electrons. The effect on electronic conduction is reversed with varying $P_{O_2}$. In the context of zirconium alloy oxidation in water, the $ZrO_2$ layer is exposed to a gradient in oxygen partial pressure. The metal/oxide interface corresponds to the low $P_{O_2}$ regime and the oxide/water interface corresponds to the high $P_{O_2}$ regime. In M-$ZrO_2$ without Li, electronic conduction is more limited in the low $P_{O_2}$ regime where electrons and holes compensate each other and the total conduction has no $P_{O_2}$ dependence. With lithium doping, electron become the dominant electronic carrier at low $P_{O_2}$ and its concentration increases with decreasing $P_{O_2}$.

Besides the above-mentioned defects that are closely related to the oxide growth rate, another important species is $V_{Zr}''''$, and it becomes the dominant charge compensating defect with lithium doping in the entire $P_{O_2}$ range (Figure 4-1(b)). It is noteworthy that the increase in zirconium vacancy concentration must also result in an increase of zirconium diffusion, and thus, also accelerate the rate of oxide growth. However, the migration barrier of zirconium via the vacancy mechanism is much higher (7.18 eV [153]) compared to the migration barrier of oxygen interstitial (0.53 eV [149]). Even in the Li-doped case where $[V_{Zr}'''']$ is several orders of magnitude higher than $[O_i'']$, the contribution of cation diffusion to oxide growth should still be negligible compared to anion diffusion. However, as we shall see in the next section, an increase in $V_{Zr}''''$ contributes greatly to the accelerated corrosion via its mechanical effect.

We performed the same analysis for T-$ZrO_2$. Migration barriers for oxygen defects in T-$ZrO_2$ were used as provided in [115]. We conclude that the major defect chemistry response to lithium insertion is very similar in both phases, with $Li_i^{\cdot}$ and $V_{Zr}''''$ being the dominant compensating species, and all the conclusions made here also hold qualitatively for the tetragonal phase. We observe the suppression of oxygen interstitials and electrons in T-$ZrO_2$ on the same order of magnitude. The only difference is that the transition

between electron versus hole domination as shown in Figure 4-2 comes at a much lower $P_{O_2}$ in T-$ZrO_2$, and therefore only the features at high $P_{O_2}$ are observed.

B. Mechanical effect of lithium insertion into $ZrO_2$

Two types of mechanical response of the oxide to extrinsic doping have been discussed in the literature and considered in this work. First, as we have seen in Section III A, extrinsic doping results in a significant change in defect chemistry. The resulting defect chemistry upon doping causes changes in the lattice parameter. This phenomenon is commonly observed in materials for energy conversion and storage, and often termed as chemical expansion [120]. Second, during the growth of the $ZrO_2$ passive film, T-to-M phase transformation results in volumetric dilation. The corresponding stress buildup cracks the film and leads to a porous microstructure [51]. Experimentally, it has been observed that lithium incorporation could change the relative fractions of T-$ZrO_2$ and M-$ZrO_2$ in the oxide film [144]. It is possible that lithium is behind the detrimental T-to-M phase transformation and the resulting changes in the film microstructure during oxide growth. In this section, we assess both types of mechanical responses.

We have concluded in Section IIIA that the major defect types in Li-doped $ZrO_2$ are $Li_i^{\cdot}$ and $V_{Zr}^{''''}$ in both T-$ZrO_2$ and M-$ZrO_2$. First, we assess the chemical expansion due to these dominant defects. We calculated the volume change introduced by these two types of defects. *Figure 4-3* shows the DFT calculated energy with varying volume (colored dots). By fitting the results to Birch-Murnaghan equation of state (Eq. (4.1), black dashed line), we could arrive at the equilibrium volume (vertical colored dashed line). The corresponding volume change for each defect is calculated by subtracting the volume of perfect cell of the corresponding phase from the defective cell. In ref. [154] it was suggested that this is a viable way to obtain the relaxation volume of charged defects in DFT supercells where the ambiguity of defining pressure in charged cells [155] is removed by fitting to an equation of state. We also note that the fractional volume change does not depend significantly on cell size. The resulting equilibrium volumes are listed in Table 4-1. In both the monoclinic and the tetragonal phase, the incorporation of lithium interstitial leads to volume shrinkage. To understand the contraction effect, in Figure 4-4 we show the atomic structures of perfect M-/T-$ZrO_2$ and defective M-/T-$ZrO_2$ with $Li_i^{\cdot}$. We see that lithium interstitial resides within an oxygen cage and the O-O bonds of this

cage shorten upon the insertion of lithium. This is because the positively charge $Li_i^{\bullet}$ effectively shares the electrons of surrounding oxygens and reduces their ionicity. As a result, the electrostatic repulsion between oxygen ions is suppressed and they are pulled closer towards each other.

On the other hand, the compensating species $V_{Zr}^{''''}$ causes nearly no change of volume in M-$ZrO_2$ and a volume expansion in T-$ZrO_2$ (Figure 4-3). Based on the defect equilibria we obtained in Part IIIA, each $V_{Zr}^{''''}$ should be compensated by four $Li_i^{\bullet}$. In the dilute limit, the net effect of both defects is the sum of their relaxation volumes, which adds up to a 3.2% volume contraction in M-$ZrO_2$ and a 4.8% volume contraction in T-$ZrO_2$. The consequence of this contraction effect will be discussed in detail in Part IIIC.

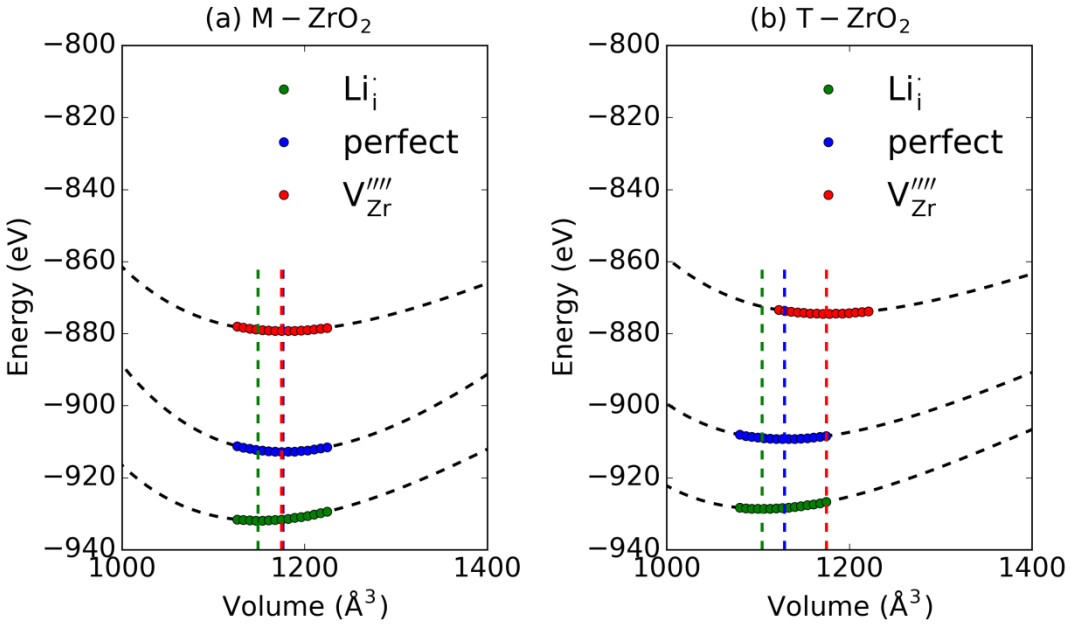


Figure 4-3. Energy variation with volume for (a) M-$ZrO_2$ and (b) T-$ZrO_2$ calculated by DFT (colored dotted lines) and fitted by Birch-Murnaghan equation of state (black dashed line). Equilibrium volume predicted are shown by vertical dashed lines where minimum energy is reached.

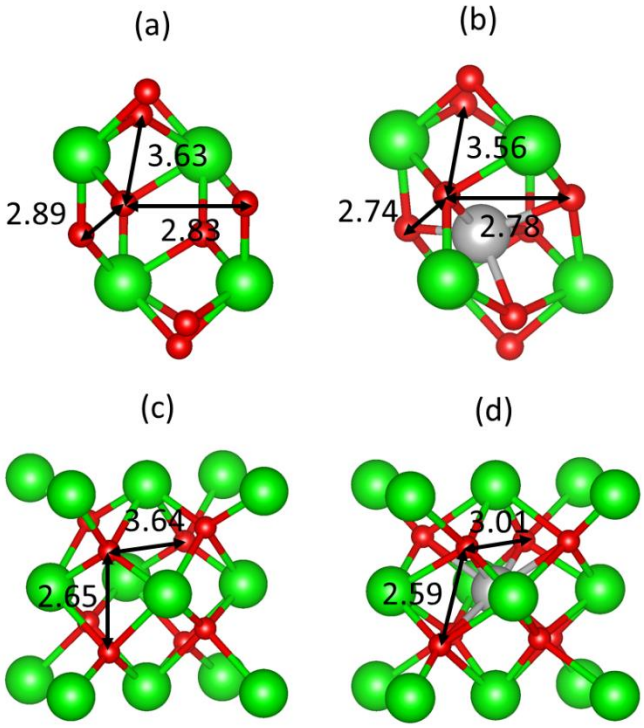


Figure 4-4. Atomic structure of (a) perfect M-$ZrO_2$, (b) $Li_i^{\bullet}$ in M-$ZrO_2$, (c) perfect T-$ZrO_2$ and (d) $Li_i^{\bullet}$ in T-$ZrO_2$. Oxygen-oxygen bond lengths (in Å) within the oxygen cage that surrounds $Li_i^{\bullet}$ are marked on each graph. Green, red, and grey spheres represent zirconium, oxygen and lithium ions respectively.

Table 4-1**.** Equilibrium volume per unit formula (in $Å^3$) for defect-free M-$ZrO_2$ and T-$ZrO_2$, one $Li_i^{\bullet}$ in 32 $ZrO_2$ and one $V_{Zr}^{''''}$ in 32 $ZrO_2$. The fractional volume change is calculated with reference to perfect T-$ZrO_2$. The relaxation volume is defined by subtracting the volume of perfect cell from the defective cell of the same phase divided by 32.

| Perfect | $Li_i^{\bullet}$ | $V_{Zr}^{''''}$ |
|---|---|---|

| M-$ZrO_2$ | Absolute Volume (Å$^3$) | Absolute Volume (Å$^3$) | Relaxation Volume (Å$^3$) | Absolute Volume (Å$^3$) | Relaxation Volume (Å$^3$) |
|---|---|---|---|---|---|
| | 36.76 (+4.2%) | 35.91 (+1.8%) | -0.85 | 36.70 (+4.0%) | -0.06 |
| T-$ZrO_2$ | Absolute Volume (Å$^3$) | Absolute Volume (Å$^3$) | Relaxation Volume (Å$^3$) | Absolute Volume (Å$^3$) | Relaxation Volume (Å$^3$) |
| | 35.28 (0) | 34.52 (-2.2%) | -0.77 | 36.71(+4.0%) | +1.42 |

In order to reveal the effect of lithium on T-to-M phase transformation, we further calculated the hydrostatic stress-enthalpy profile using Birch-Murnaghan equation of state. In Figure 4-5(a) we show the results for perfect T-$ZrO_2$ and M-$ZrO_2$. From the tensile stresses up to a compressive stress of $P$ = 10.51 GPa (shown by vertical line), the enthalpy of M-$ZrO_2$ $H_{\mathrm{M}}^{\mathrm{perfect}}$ is smaller than that of T-$ZrO_2$ $H_{\mathrm{T}}^{\mathrm{perfect}}$. This is consistent with the fact that M-$ZrO_2$ is the stable phase at ambient pressure up to 1205 $^{o}$C [82]. At $P$ = 10.51 GPa, $\Delta H$ crosses zero and we enter the regime where T-$ZrO_2$ is stabilized by compressive stress. Experimentally, critical compressive stress of T-to-M phase transformation was measured to be 6 GPa [109, 122]. Our theoretical prediction is in reasonable agreement with the measured value.

We assessed the effect of defects on the T-to-M phase transformation by calculating how they change this critical compressive stress. In Figure 4-5(b) the *H-P* result for a 2×2×2 $ZrO_2$ cell containing one $Li_i^{\bullet}$ is shown. The transition stress is slightly increased to 11.11 GPa compared to the perfect cell case, which is seemingly a minor effect. Next, we take into consideration the increase of zirconium vacancies, $V_{Zr}^{''''}$, in the presence of lithium insertion (Figure 4-5(c)). The calculated effect of those defects is to substantially increase the critical stress needed to stabilize T-$ZrO_2$. In the stress range examined directly by DFT calculations, -10 GPa ~ 20 GPa, there exists no stress that stabilizes T-$ZrO_2$. When we extrapolate the data range by using the Birch-Murnaghan equation of state, we find

that the T-$ZrO_2$ phase can be stabilized at substantially larger compressive stresses, nearly 60 GPa and above.

The situation remains qualitatively similar when we switch to the planar stress scenario, as shown in Figure 4-5(d)(e)(f). The predicted compressive planar stress to stabilize T-$ZrO_2$ is at or above 12 GPa for the defect free case (Figure 4-5(d)), and almost does not change with the addition of one $Li_i^{\cdot}$ in 32 unit formula of $ZrO_2$ (Figure 4-5(e), 11.79 GPa). The transition stress rises about 20% (from 11.97 GPa to 14.13 GPa) with $V_{Zr}^{''''}$, which is a significant effect in promoting the T-to-M phase transformation in $ZrO_2$.

These results have direct implications for explaining the cyclic kinetics of corrosion on zirconium alloys [48]. During the oxidation process, initially the tetragonal phase $ZrO_2$ is stabilized by interfacial compressive stress. The formed well-textured T-$ZrO_2$ layer slows down oxygen incorporation and the oxide film thickness plateaus. However, the T-to-M phase transformation induced by stress release drives the formation of cracks and pores. Interconnected cracks and pores serve as a fast path for diffusing species and results in acceleration of the corrosion kinetics [111]. Here our results clearly demonstrate that lithium incorporation releases the compressive stress, destabilizes the T-$ZrO_2$ and promotes the volume-expansive T-to-M phase transformation. As a result, lithium incorporation accelerates the transition from passive to the accelerated break-away corrosion process. In the next section we provide a detailed comparison between this prediction and experimental observations.

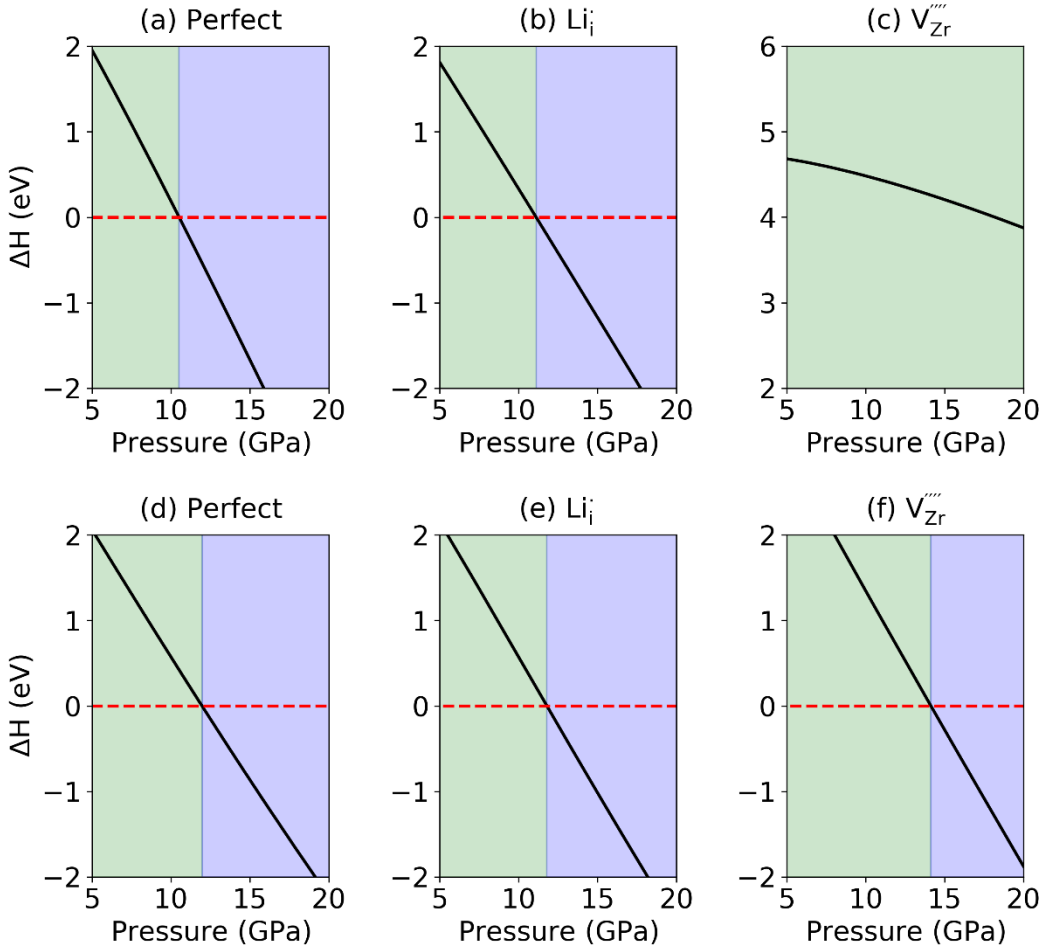


Figure 4-5. Enthalpy difference, $\Delta H$, between the tetragonal and the monoclinic phases of $ZrO_2$, calculated by fixed volume hydrostatic stress in (a), (b) and (c), and planar stress in (d), (e) and (f). Here $\Delta H$ presents the enthalpy of monoclinic phase subtracted from the enthalpy of tetragonal phase. Tetragonal phase is stablized in the pressure range where $\Delta H < 0$ (represented by blue) and monoclinic phase is stabilized where $\Delta H > 0$ (represented by green). The cell configurations are (a)(d) perfect with no defect, (b)(e) with one singly charged lithium interstitial $Li_i^{\cdot}$ and (c)(f) with one quadruply charged zirconium vacancy $V_{Zr}^{''''}$. The boundaries between blue and green regions show the stress at which $\Delta H$ crosses zero, i.e. the critical stress where T-to-M phase transformation happens.

C. Comparing the relative importance of the chemical and mechanical effects of Li insertion in $ZrO_2$.

In the previous two sections, we have concluded that: (1) Chemically, lithium works as a donor dopant in $ZrO_2$. The lithium dopant resides dominantly in the form of $Li_i^{\cdot}$. $O_i''$ concentration is enhanced and leads to faster oxygen diffusion. Electron concentration is increased and hole decreased, leading to a net effect of electronic conduction increase in the low $P_{O_2}$ n-type regime. $V_{Zr}''''$ becomes the dominant negatively-charged defect species compensating the positively-charged lithium interstitial in the entire $P_{O_2}$ range considered. (2) Mechanically, lithium incorporation together with the increased $V_{Zr}''''$ concentration, increases the compressive stress that is needed to stabilize the T-$ZrO_2$ and thus promotes the T-to-M phase transformation in the growing oxide layer. In this part, we resolve the conditions under which the chemical effect or the mechanical effect dominates behind the lithium-accelerated corrosion of zirconium alloys.

In order to do this, we compare the influence of other alkali metal elements with lithium. Chemically, alkali metal elements should behave similarly, but mechanically they can be very different because of the increasing ionic radius going down the column in the periodic table. Jeong et al conducted experiments of zirconium alloy corrosion in aqueous alkali hydroxide solutions (LiOH, NaOH, KOH, RbOH, and CsOH) [156]. They found that with relatively low concentration of the alkali element in solution (4.3 mM), the oxide film growth behaves similarly in all alkali hydroxide solutions with a modest acceleration effect arising from each. The order of the acceleration intensity is strongest for LiOH, and less and less intense as going down the periodic table column. On the other hand, in the high concentration regime (32.5 mM), oxidation film growth kinetics in LiOH solution is very different from all other alkali metal elements, with a significantly higher growth rate compared to the corrosion rate in NaOH, KOH, RbOH, and CsOH. The weight gain in LiOH solution is over 2500 mg/dm$^2$ after 300 days, but lower than 200 mg/dm$^2$ in all other alkali metal solutions.

The observed difference between alkali metal solutions can be well explained by considering both the chemical and mechanical effects. In the low concentration regime, enhancement in oxygen diffusivity and electronic conductivity (chemical effect) with alkali metal element incorporation dominates in the acceleration effect. Since all the alkali metal elements act as interstitial donors and promote the concentration of negatively charged defect species (oxygen interstitial in particular), they all have a

modest and comparable influence on the oxide growth rate. The easiness of alkali metal element entering the $ZrO_2$ film should depend on its ionic radius. The ionic radius of $Zr^{4+}$ is 72 pm, and the ionic radii for $Li^+$, $Na^+$, $K^+$, $Rb^+$ and $Cs^+$ are 76, 102, 151, 161 and 174 pm respectively [157]. From this comparison, being the smallest, it should be easiest for $Li^+$ to get incorporated in the oxide film as an interstitial defect. That is, the doping concentration of lithium as a function of time should be the highest compared to other alkali metals entering the oxide from the hydroxide solutions. As a result, the enhancement of oxygen diffusivity and electronic conductivity is most significant with LiOH, and gradually weakens down the periodic table column.

In the high concentration regime, the sharp increase of corrosion rate in LiOH is most likely related to change in microstructure (mechanical effect) of the oxide film. We have shown in the previous section that lithium incorporation introduces two effects related to phase transformation of $ZrO_2$. First, $Li_i^{\bullet}$ leads to volume shrinkage and releases the compressive stress needed for stabilizing the protective tetragonal phase $ZrO_2$. Second, $Li_i^{\bullet}$ promotes the concentration of $V_{Zr}^{''''}$ which increases the compressive stress needed for stabilizing T-$ZrO_2$. Under expected compressive stresses at the metal-oxide interface, which is reported to be 4~6 GPa with 50 nm thick oxide film [122], the T-$ZrO_2$ should transform to M-$ZrO_2$ when lithium enters the oxide. The induced expansive phase transformation leads to cracks, pores and open grain boundaries in the oxide film and further increases oxidation rate.

Now we ask the question that why this microstructure effect is only seen in LiOH, but not in other alkali hydroxide solution. In Figure 4-6 we show the total relaxation volume of the compensating pair $V_{Zr}^{''''}$ and four $M_i^{\bullet}$, where M stands for the alkali metal element. The volume change of individual defect is calculated using the same approach as described in the previous section, with one defect in 32 unit formula of $ZrO_2$. It is clear that in both T-$ZrO_2$ and M-$ZrO_2$, lithium is the only alkali metal element that leads to a volume shrinkage. All other alkali metal elements lead to volume expansion. In all cases, the effect of $V_{Zr}^{''''}$ increasing the critical pressure for phase transformation exists. However, for Na, K and Rb, chemical expansion increases the compressive stress in the oxide film, and enables the retention of the T phase of $ZrO_2$, that is the more protective phase forming coherently at the metal-oxide interface under compressive stress. As a

result, we do not observe significant microstructure variation in all alkali hydroxide solutions except for LiOH. This provides the ground of explaining the above-mentioned experimental observation.

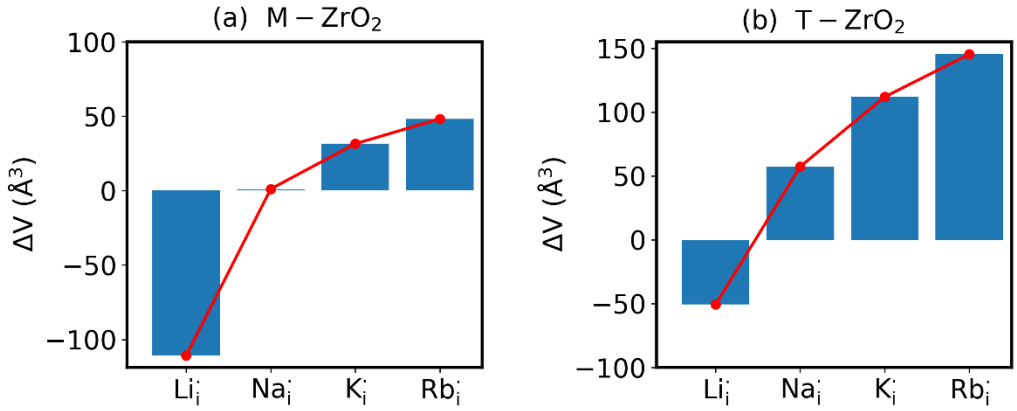


Figure 4-6. Volume change induced by alkali metal element incorporation into (a) monoclinic phase $ZrO_2$ and (b) tetragonal phase $ZrO_2$, considering the four singly charged alkali metal interstitials $M_i^{\cdot}$ compensated by one quadruply charged zirconium vacancy $V_{Zr}^{''''}$.

## 4.4 Conclusion

In this paper we assessed the coupled chemical and mechanical effects of lithium incorporation in $ZrO_2$, and how these effects can contribute to accelerated oxidative corrosion of Zr. We have discovered two major mechanisms: (1) Based on the dilute-limit defect chemistry equilibria, lithium acts as a donor in $ZrO_2$ in the form of $Li_i^{\cdot}$. Upon insertion, $[O_i'']$ is increased by up to ten orders of magnitude, leading to faster oxygen diffusion. Electron concentration is increased by up to five orders of magnitude, and hole concentration decreased by three orders of magnitude. The net electronic conduction is increased in the low $P_{O_2}$ n-type regime. An overall outcome of these two chemical effects should be faster oxide growth rate. At the same time, $V_{Zr}^{''''}$ is greatly enhanced in the entire $P_{O_2}$ range. (2) Based on the mechanical response, lithium incorporation and subsequent increase in $V_{Zr}^{''''}$ increases the compressive stress that is needed to stabilize

T-$ZrO_2$, and this promotes the detrimental T-to-M phase transformation and cracks in the oxide film. By comparing the distinct behavior of LiOH compared to other alkali metal hydroxide solutions, we have identified the first effect being dominant in the low alkali metal concentration regime, and the second effect being dominant in the high concentration regime. We believe that this work shows the importance of examining the response of charged defects to alkali metal ion insertion in the metal oxide, and the coupling of that chemical effect to the mechanical response, for better understanding complex and coupled processes taking place in metal oxidation in alkali hydroxide solutions. The results have implications for understanding the electronic and mechanical properties of $ZrO_2$ in energy conversion, storage and information processing applications as well.

# 5 Predicting point defect equilibria across oxide hetero-interfaces: model system of $ZrO_2/Cr_2O_3$

In this chapter, we present a multi-scale approach to predict equilibrium defect concentrations across oxide/oxide hetero-interfaces. There are three factors that need to be taken into account simultaneously for computing defect redistribution around the hetero-interfaces: the variation of local bonding environment at the interface as epitomized in defect segregation energies, the band off-set at the interface, and the equilibration of the chemical potentials of species and electrons via ionic and electronic drift-diffusion fluxes. Starting from first principles calculation of these three factors, we build a continuum model for defect redistribution by concurrent solution of Poisson's equation for the electrostatic potential and the steady-state equilibrium drift-diffusion equation for each defect. Contrary to prior models where the electric field in the core zone was not numerically handled, our model solves for and preserves the continuity of the electric displacement field throughout the interfacial core zones and the extended space charge zones. We implement this computational framework to a model hetero-interface between monoclinic zirconium oxide, m-$ZrO_2$, and chromium oxide $Cr_2O_3$. This interface forms upon the oxidation of zirconium alloys containing chromium secondary phase particles. The model explains the beneficial effect of the oxidized Cr particles on the corrosion resistance of Zr alloys. Under oxygen rich conditions, the $ZrO_2/Cr_2O_3$ heterojunction depletes oxygen vacancies and the sum of electrons and holes in the extended space charge zone in $ZrO_2$. This reduces the transport of oxygen and electrons thorough $ZrO_2$ and slows down the corrosion rate. Moreover, our analysis provides a clear anatomy of the components of interfacial electrical properties; a zero-Kelvin defect-free contribution and a finite temperature defect contribution. The thorough treatment presented here uncovers a rich coupling between defect chemistry, thermodynamics and electrostatics which can be used to design and control oxide hetero-interfaces.

## 5.1 Introduction

Novel phenomena at oxide hetero-interfaces have been of great interest for both fundamental studies [1] and device applications [2]. In particular, ionic defect redistributions at the interface are known to influence the magnetic, electronic and transport properties of metal oxides [3-5, 158]. Understanding the redistribution of

defects across such interfaces serves as the foundation for studying reaction and diffusion processes in related systems. However, addressing the electronic and ionic structures of the interfacial zone is not a trivial task. The nature of bonds between ions and chemical composition in the oxide crystal could be significantly altered near interfaces [159].

Three aspects, summarized in Figure 5-1 as (a), (b) and (c), need to be addressed comprehensively and at the same level of theory in order to self-consistently describe the redistribution of charged defects at a hetero-interface. These three factors have all been recognized and evaluated in the literature, but were usually treated separately with different modeling methods prior to this work. First (Figure 5-1 (a)), before considering any electronic or ionic defects, the discontinuities of valence band $\Delta E_v$ and conduction band $\Delta E_c$ immediately at the interface need to be calculated. Theoretically, this band discontinuity corresponds to the large electrostatic potential gradient at ideally abrupt defect-free interfaces. This discontinuity is localized in the few atomic layers in the immediate vicinity of the interface and is independent of external perturbations such as dilute doping and applied electric bias. Second (Figure 5-1 (b)), charged species have different electrochemical potentials in equilibrium bulk materials. When two materials are put into contact, electronic and ionic defects start to diffuse, driven by this chemical potential difference. This leads to the build-up of a local electric field, and in turn, drives drift flux in the opposite direction. When the system equilibrates, drift and diffusion fluxes cancel out, leading to a reduced form of the drift-diffusion equation with zero flux [160, 161], which is equivalent to the Poisson-Boltzmann formalism used in the solid state ionics field [43, 162, 163]. Third (Figure 5-1 (c)), atoms near an interface are in a distinct bonding environment compared to atoms in the bulk. Defect formation energies will change due to interfacial lattice relaxation and chemical composition variation. This adds the segregation energy, $E_{D^q}^{seg}$, to the defect formation energy of ions in the vicinity of the interface. This region where the segregation energy is non-negligible is termed as the core zone.

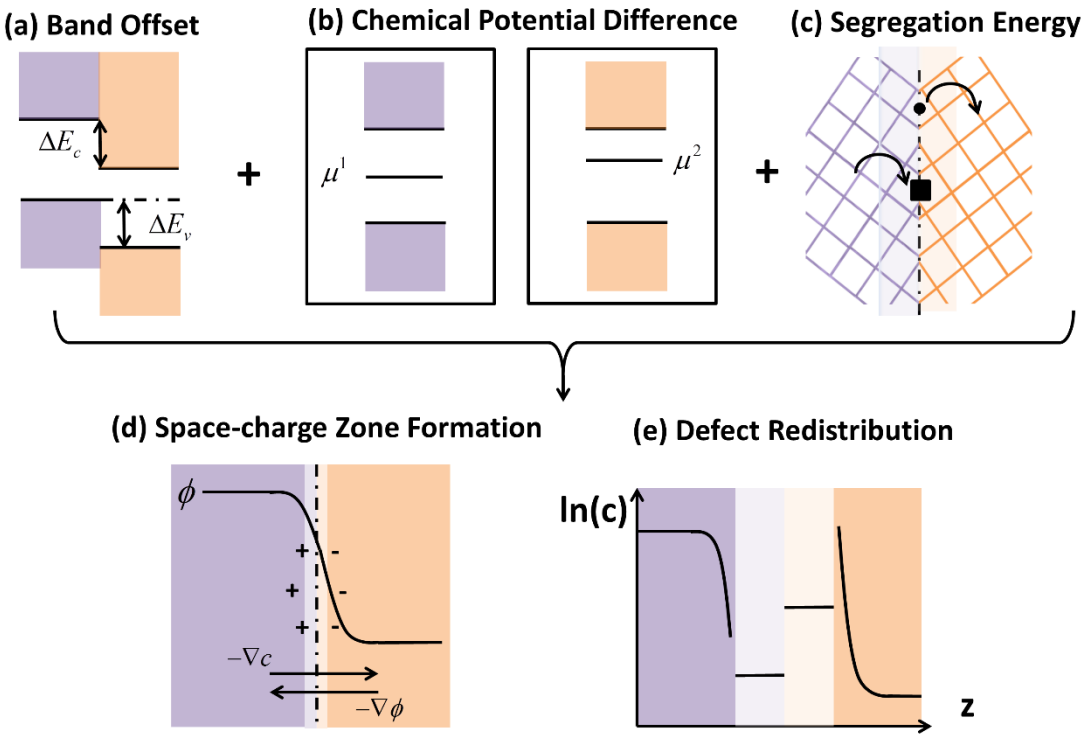


Figure 5-1**.** Schematics for the comprehensive framework for predicting point defect equilibria across hetero-interfaces adopted in this work. Key references and texts, which describe and model various elements of this framework at different levels on a range of problems, are reviewed and cited in the Introduction section. In this work, three important factors are assessed first at the atomistic level: (a) Band offset of the ideal interface. (b) Any species having different chemical potentials, $\mu^1$ and $\mu^2$, when bulk defect equilibria is reached on each side of the interface. This difference drives diffusion flux as the two materials are put into contact and lead to the formation of a space-charge zone. Upon equilibrium, the Fermi level and the chemical potential of each element should be constant throughout the heterojunction, and the electrochemical potential of each type of ionic defect should be constant on the oxide side where it exists. (c) Defect segregation or depletion due to interfacial structural and compositional change. After assessing these three factors at the atomistic level by density functional theory (DFT), these are provided as input into the steady state drift-diffusion model. In this work, the steady state drift diffusion model is solved in a self-consistent way to generate (d) the electrostatic profiles in the space-charge and core zones, and (e) the defect redistribution profiles across the interface with explicit consideration for the interfacial core zone. When equilibrium is reached, the diffusion flux driven by concentration gradient $\nabla c$ and drift flux driven by electrostatic potential gradient $\nabla \phi$ cancel out. Core regions extend for only several

atomic layers in the immediate vicinity of the interface and are drawn with enlarged scale and light colors in (d) and (e).

As already noted above, each of these three factors represented in Figure 5-1 have been recognized and evaluated in literature, but were usually treated separately with different modeling methods. Predicting band offsets (factor (a)) from density functional theory (DFT) calculations has been of interest since decades ago and a number of theories have been developed [18]. One commonly accepted scheme was first proposed by Van de Walle and Martin [19] and applied in a number of studies [20, 21], which aligns the band positions to the electrostatic potential across the heterojunction. These studies consider defect-free interfaces and only evaluate the band off-sets. The electrostatic potential, $\phi$, built by the drift-diffusion mechanism (factor (b)) can extend in space for several hundreds to thousands of nanometers, and is usually studied with finite-element methods in the context of semiconductor engineering. The drift-diffusion model is well-developed for semiconductor heterojunctions [22-24, 160, 161], where only electrons and holes are considered as the mobile species. In that case, there is no need to consider segregation energies since free holes and electrons are assumed to be unaffected by the changes in the bonding at the interface. In such model, only the space-charge potential causes changes in holes and electrons at the interface.

When it comes to ionic or mixed electronic-ionic conductors that are used in electrochemical devices, the ionic defect contribution cannot be neglected any more. Ionic and electronic drift-diffusion models based on the chemical potential difference (factor (b)) have been built for mixed electronic-ionic p-n homojunctions made of p-type and n-type doped $SrTiO_3$ [13]. Similar continuum level studies have also been implemented for metal/oxide interfaces [8] and a gas/oxide interfaces [9] based on first-principle predictions. However, in these two systems the segregation energy term (factor (c)) is still missing from the consideration of the charged point defect redistribution. In fact, in the case of the gas/oxide interface, there is segregation of defects at the interface within the oxide side of the interface, and there is also the adsorption of charged species from the gas side. While Ref. [9] chose to treat the adsorption of charged gas species only, Ref. [162] chose to treat segregation of defects within the oxide only. A complete treatment of segregation/adsorption phenomena at gas/oxide interfaces starting from first-

principles all the way to continuum level treatment is still missing as well, and the recent work on hydrated $BaZrO_3$ surface [164] presents a very encouraging attempt in that direction.

The defect segregation energy $E_{D^q}^{seg}$, which has discrete values in each atomic layer close to the interface, can be evaluated using atomistic simulation methods[25, 164-167] and is explicitly accounted for in this work. In fact, these segregation energies are responsible for the formation of the core zone at the interface which exhibits very different defect concentrations in comparison with the extended space charge zone.

Attempts have been made to establish interfacial defect chemistry theoretically [27-29]. These theories consider equilibrium defect reactions at the interface as boundary conditions. Counting defect reactions corresponds to a canonical formalism in which defects, and in particular electronic defects, are tracked particle by particle. Such a canonical formalism, while tractable if one knows a priori the important defect reactions, is not in the spirit of the predictive power of first-principle modeling [14]. Alternatively, a grand canonical formalism that treats individual point defects and electronic defects such that each of them is in equilibrium with a reservoir is much more compatible with atomistic simulations [14]. So far, first-principles-based models have only been developed for symmetric grain boundaries in the past few years [10-12], in which the segregation energy is included self-consistently in the drift-diffusion model. A symmetric grain boundary is a simplified scenario where there is no band offset on the two sides of the interface and the electrostatic profiles are symmetric across the boundary. Moreover, the electric field in the core zone was not explicitly included into the numerical treatment of grain boundaries.

In this work, we implement a generalized model of hetero-interfaces where no symmetry is assumed and the continuity of the displacement field [168] is adhered to throughout the system by including explicitly the interface core into the solution. To our knowledge this is the first attempt to simultaneously include these three factors listed in Figure 5-1 completely from *ab initio* calculations, without a priori assumption of dominant defect species. On the continuum modeling level, we solve for the first time the Poisson's equation throughout the core zone and the space-charge zone, while preserving the continuity of the electric displacement field throughout the entire space including the core zone. Finally, by using this ability, we deconvolute the contributions to the interfacial

electrostatic profiles arising from the 0K-perfect and the finite temperature defect effects. This model and the explored concepts are applicable to any type of interface system.

Defect equilibria in the bulk provide the boundary conditions needed for the interfacial defect redistribution. In previous work we assessed the defect equilibria in bulk monoclinic $ZrO_2$ [77]. The key idea is to capture the defect structures and formation energies with density functional theory (DFT) calculations and feed it to the thermodynamic model where the total Gibbs free energy of the defective crystal is minimized [14]. However, additional difficulty to tackle is the asymmetry of the hetero-interface. We performed DFT calculations to obtain band alignment and defect formation (segregation) energies at the interface and in the bulk of both sides of the heterojunction (described below). Using these results as input, we are able to solve for the electrostatic potential generated by defect redistribution and defect concentrations across the space-charge region and in the interfacial core layer.

We selected the $ZrO_2/Cr_2O_3$ hetero-interface as our model system which arises in the utilization of zirconium alloys as nuclear cladding material in light water reactors [169]. The oxidation of zirconium alloys by the reactor coolant (light water) could be a severe design-limiting issue under aggressive conditions inside nuclear reactors. Zirconium alloys contain in addition tin, iron, nickel and chromium which tend to precipitate in the form of intermetallics. Upon oxidation, both the host zirconium metal and the intermetallic precipitate to form their respective oxides. The net outcome is multiple interfacial zones at the boundaries between $ZrO_2$ and oxides of the precipitates [54, 55]. Oxygen diffusion kinetics in $ZrO_2$, which is a major consideration in designing oxidation-resistant zirconium alloys, can be significantly altered near the interface between $ZrO_2$ and the precipitate metal oxide. In this work we focus on the interface between monoclinic $ZrO_2$ and hexagonal $Cr_2O_3$. Our results show that throughout all temperatures and oxygen partial pressures $ZrO_2$ exhibits a downward band bending and $Cr_2O_3$ exhibits and upward one. The core and space charge zones of $ZrO_2$ are negatively charged, whereas those of $Cr_2O_3$ are positively charged. However, the predominant defect in each zone varies depending on temperature, oxygen partial pressure and the spatial location with respect to the junction indicating a rich coupling between defect chemistry, thermodynamics and electrostatics. In particular in the core and space charge zones of $ZrO_2$, and under oxygen rich conditions, we observe a depletion of doubly charged oxygen vacancies and a similar depletion in the sum of electron and holes. This depletion

indicates a reduction in electronic and oxygen transport near $Cr_2O_3$ particles dispersed in $ZrO_2$. This, in turn, provides an explanation for the corrosion resistance of Zr alloyed with Cr. Finally we discuss how the potential drop, interface dipole, and interface electric field are made out of two components; a 0 K defect-free contribution and a finite temperature defect contribution.

## 5.2 Methods

In this section we present a comprehensive methodology to model hetero-interfaces. First, we give a brief review of establishing point defect equilibria in the bulk of an oxide. Second, we describe how to construct a stable interface and obtain band offsets by aligning bulk band positions to a reference potential. Third, we introduce our continuum model for the equilibrium space-charge zone. Finally, we demonstrate how we explicitly treat defects in the interfacial, core zone.

All density functional calculations involved in this work were performed with Vienna Ab initio Simulation Package (VASP) [85-88]. We used the generalized gradient approximation (GGA) with Perdew-Burke-Ernzerhof (PBE) functional [89, 90]. We employed pseudopotentials constructed using the projector augmented wave method which treat $4s^2 4p^6 4d^2 5s^2$ electrons for Zirconium, $3s^2 3p^6 3d^5 4s^1$for Chromium and $2s^2 2p^4$ for Oxygen as valence electrons. The plane-wave cutoff energy was set to 450eV. A Hubbard U correction [170] $U_{eff}$ = 5eV was applied to the *d* orbitals of chromium [171].

A. Bulk defect equilibria

We adopt the framework established in our previous work [7] to predict intrinsic point defect equilibria for bulk $ZrO_2$ and $Cr_2O_3$. The results for bulk monoclinic $ZrO_2$ were presented in ref. [77] and the detailed analysis for $Cr_2O_3$ defect chemistry is to be published elsewhere. The formation energy of a defect $D^q$ whose charge is q is computed by:

$$E_{D^q}^{f} = E_{defective}^{DFT} - E_{perfect}^{DFT} - \sum_i \Delta N_i \mu_i + q(\mathrm{E}_{VBM} + \mu_e) + E_{MP} \qquad (5.1)$$

Here $E_{defective}^{DFT}$ is the DFT energy of the defective cell, $E_{perfect}^{DFT}$ is the DFT energy of the perfect cell. $\mu_i$ denotes the chemical potential of each element involved in the cell, and $\Delta N_i$ the relative number of each type of atoms with respect to the perfect cell (e.g.

$\Delta N_{Zr} = -1$ , $\Delta N_O = 0$ for zirconium vacancies). $E_{VBM}$ is the valence band maximum of the perfect cell. $\mu_e$ is the Fermi level of electrons relative to the valence band maximum. $E_{MP}$ is the first-order Makov-Payne correction [15] for the finite-size supercell errors in charged defect calculations.

The chemical potential of oxygen as a function of temperature $T$ and oxygen partial pressure $P_{O_2}$ is calculated by:

$$\mu_{\mathrm{O}}(T, P_{\mathrm{O}_2}) = \frac{1}{2}[E_{\mathrm{DFT}}^{\mathrm{O}_2} + E_{\mathrm{over}} + \mu_{\mathrm{O}_2}^0(T, P^0) + k_B T \ln(\frac{P_{\mathrm{O}_2}}{P^0})] \ , \tag{5.2}$$

where $E_{\mathrm{DFT}}^{\mathrm{O}_2}$ is the DFT-calculated energy of an oxygen molecule. $E_{\mathrm{over}}$ is the correction term for $O_2$ overbinding error created by semilocal functionals [172], which has a value of 1.22 eV for the parameters used in this work [77]. $\mu_{\mathrm{O}_2}^0(T, P^0)$ is the tabulated reference chemical potential for $O_2$ gas at reference pressure $P^0$=0.1 MPa [173]. $k_B$ is the Boltzmann constant. Once $\mu_O$ is known, the chemical potential of cation elements are calculated by

$$\mu_{\mathrm{M}}(\mathrm{T}, \mathrm{P}_{\mathrm{O}_2}) = \frac{y}{x}\left[\frac{1}{y} E_{\mathrm{DFT}}^{\mathrm{M_xO_y}} - \mu_{\mathrm{O}}(T, P_{\mathrm{O}_2})\right] \ , \tag{5.3}$$

where $M_xO_y$ represents monoclinic phase $ZrO_2$ for zirconium and $Cr_2O_3$ for chromium. $E_{\mathrm{DFT}}^{\mathrm{M_xO_y}}$ is the DFT-computed energy of the oxide material.

Fermi level is determined from the charge neutrality condition imposed on point defects $D^q$, electrons $n_c$, and holes $p_v$

$$\sum_{D,q} q[D^q] + p_v - n_c = 0 \, , \tag{5.4}$$

where in this work $[D^q]$ is expressed using the Boltzmann-distribution

$$[D^q] = n_D \exp(-\frac{E_{D^q}^f}{k_B T}) \ . \tag{5.5}$$

Here $n_D$ is the number of possible sites for the defect $D$ per unit formula. Eq. (5.5) is an approximate form of the expression for defect concentration sought by minimizing global Gibbs free energy [8]. They are equivalent when $E_{D,q}^f >> k_B T$ . Similarly, the

concentrations of electrons and holes, $n_c$ and $p_v$ are also functions of Fermi level and are computed by integrating the electronic density of states $g(E)$ as follows:

$$n_c = \int_{E_{\mathrm{CBM}}}^{\infty} g_c(E) \frac{dE}{1+\exp(\frac{E-\mu_e}{k_{\mathrm{B}}T})} \tag{5.6}$$

$$p_v = \int_{-\infty}^{E_{\mathrm{VBM}}} g_v(E) \frac{dE}{1+\exp(\frac{\mu_e-E}{k_{\mathrm{B}}T})} \tag{5.7}$$

Here $E_{CBM}$ is the edge of the conduction band minimum.

B. Interface band alignment

1. Interface construction

We selected oxygen-terminated m-$ZrO_2$(001) surface[76] and $Cr_2O_3$(01-12) surface[174] to construct a coherent interface. Both surfaces are non-polar. This choice was made by surveying all low-energy surface combinations and minimizing the interface misfit. We built a supercell from these two surfaces with 13 atomic layers of $ZrO_2$ and 10 atomic layers of $Cr_2O_3$, as shown in Figure 5-2(c). The as-built slab model was then fully relaxed with a $4\times4\times1$ k-points grid until the forces on ions were less than 0.02eV/Å, allowing cell shape and volume to change. The lattice parameters before and after relaxation are provided in Table 5-1.

Table 5-1. Lattice parameters, a and b, of selected surfaces and relaxed interface. $\varepsilon_a$ and $\varepsilon_b$ define the change in lattice parameter between the unrelaxed and relaxed cells in the respective directions and are calculated by $\varepsilon = (a_{relaxed} - a_{unrelaxed}) / a_{unrelaxed}$ .

| | a(Å) | b(Å) | $\varepsilon_a$ | $\varepsilon_b$ |
|---|---|---|---|---|
| $ZrO_2$(001) | 5.169 | 5.232 | 0.41% | 1.68% |
| $Cr_2O_3$(01-12) | 4.957 | 5.359 | 3.85% | -2.37% |
| After relaxation | 5.148 | 5.320 | | |

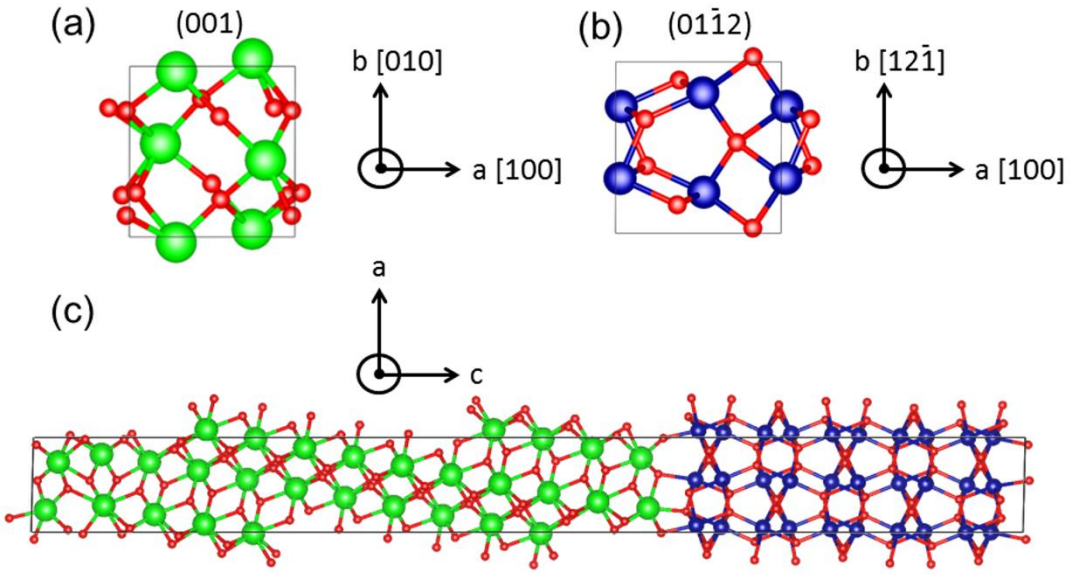


Figure 5-2**.** (a) m-$ZrO_2$(001) and (b) $Cr_2O_3$(01-12) surface cross sections and (c) relaxed interface. Oxygen ions are drawn small and red, Cr ions are medium-sized and blue, Zr ions are largest and green. This figure is generated with visualization software VESTA [97].

We comment on the method of constructing hetero-interfaces with the following: A stable interface should be built from two low-energy surfaces which have matching lattice parameters. It should be noted that the lowest-energy interface doesn't necessarily arise from two lowest-energy surfaces [175]. The most rigorous method is to test all surface combinations and search for the lowest interface energy. Some of these combinations might require an extremely large supercell if the two surfaces have different periodicity. In this work m-$ZrO_2$(001)/$Cr_2O_3$(01-12) is a good combination because both surfaces have rectangular cells and the mismatch is small. Additionally, neither surface is polar, so it avoids electrostatic complications with the infinite slab model [176]. To confirm the stability of the constructed interface, we also performed molecular dynamics simulation on the slab model, which shows that the interface retains its phases and structure.

2. Band position

Much interest has been devoted to predicting band offsets from density functional theory for the last few decades and a number of theories have been developed [18]. The key of

such predictions is to align the band positions of the interface components sought from bulk calculations to a common reference level. Here we adopt the scheme proposed by Van de Walle and Martin [19] and further applied in a number of studies [21, 177], which uses the electrostatic potential across the heterojunction as the reference level.

The electrostatic potential obtained from DFT calculation of the interface under consideration is shown in Figure 5-3(a). To get the macroscopic average, the electrostatic potential is first averaged over the plane parallel to the interface to get $V(z)$, then averaged over one atomic layer along the z direction [178].

$$\bar{V}(z) = \int \omega(z - z')V(z')dz' . \tag{5.8}$$

Here $\omega(z)$ is the filter function which represents the periodicity of the crystalline material. Since the lattice parameters along the z axis for the two materials, $c_1$ and $c_2$, are mismatched, we use the double filtering method [178] where $\omega(z)$ is defined by

$$\omega(z) = \int \omega_1(z - z')\omega_2(z')\mathrm{d}z' . \tag{5.9}$$

$\omega_i(z) = 1/c_i$ when $z \in [-c_i/2, c_i/2]$ and is zero otherwise.

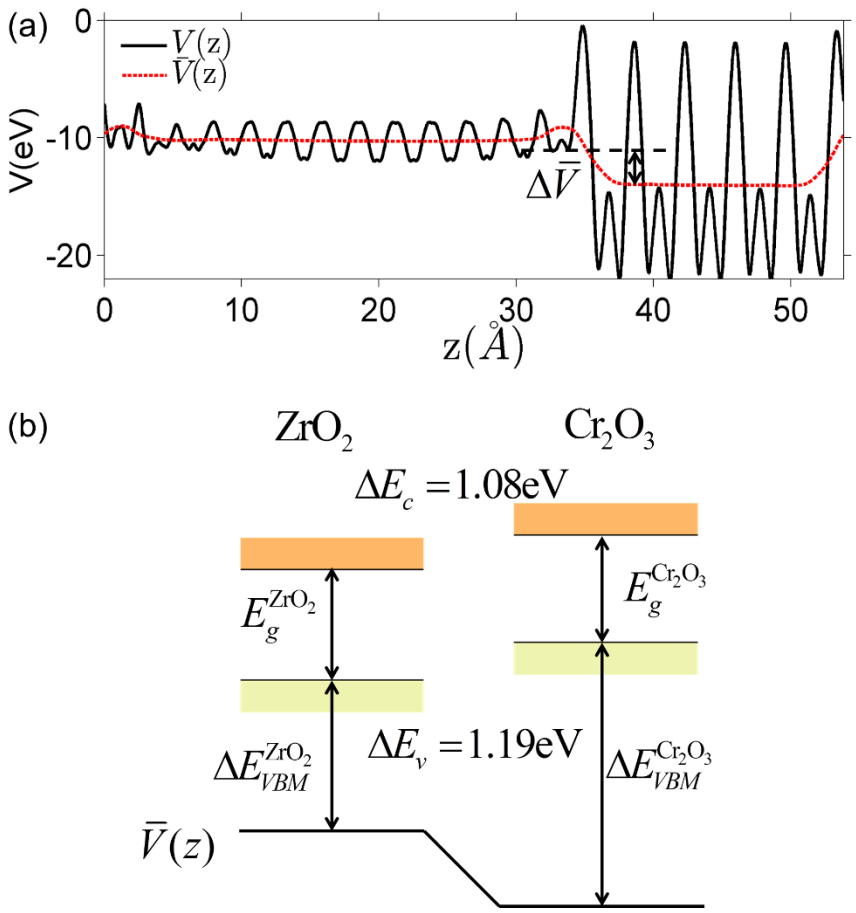


Figure 5-3. (a) Planar (solid black line) and macroscopic average (dashed red line) of electrostatic potential across the $ZrO_2/Cr_2O_3$ interface obtained from DFT calculation. $\Delta\bar{V}^{ZrO_2-Cr_2O_3}$ =3.77 V is the potential difference on both sides of the interface where flat potentials are reached. (b) Aligned band positions. Band gaps of $ZrO_2$ and $Cr_2O_3$ from DFT calculations are 3.49 eV and 3.38 eV, respectively.

The valence-band offset is determined by

$$\Delta E_v^{ZrO_2-Cr_2O_3} = E_v^{ZrO_2} - E_v^{Cr_2O_3} + \Delta\bar{V}^{ZrO_2-Cr_2O_3} \qquad (5.10)$$

$E_v^{ZrO_2}$ and $E_v^{Cr_2O_3}$ are the valence band energies with respect to the local electrostatic potential obtained from two separate bulk calculations. $\Delta\bar{V}^{ZrO_2-Cr_2O_3}$ is the potential difference of the bulk-like regions of the interface, where flat potentials are reached. The aligned band positions are shown in Figure 5-3(b).

We would like to clarify here the concept of band offset. As shown in Figure 5-3(a), the potential in the perfect slab calculation becomes constant within two atomic layers away

from the interface. This potential should not be confused with the space-charge layer potential. The equilibrium space-charge zone forms upon redistribution of various electronic and ionic charge carriers. This redistribution is a finite temperature excitation which cannot be captured directly by a zero-Kelvin DFT calculation. The band offset computed here resulted solely from the localized charge density redistribution due to the abrupt change in bonding environment at the interface. In the next section we will superimpose the defect redistribution on the defect-free heterojunction results and solve for the space-charge zone with a continuum-level model. The band discontinuities will serve as an input. The relationship between defect-free model and defective model will be further discussed at the end of this paper.

C. Equilibrium of space-charge zone

From the above calculation, we obtained the electrostatic profile of the perfect interface. Now we use these results for the perfect interface as the neutral background and superimpose the defect equilibria on it. The redistribution of defects will lead to the formation of an extended space-charge layer around the interface and a localized core layer right at the interface. The core layer is discussed in section D below. In the space-charge layer, defect formation energies are different from bulk by a term of electrostatic potential $\phi_{\text{scl}}$. Adopting a one-dimensional continuum model, $\phi_{\text{scl}}$ is governed by Poisson's equation

$$\frac{d^2\phi_{\text{scl}}(z)}{dz^2} = -\frac{\rho(z)}{\varepsilon\varepsilon_0} \ . \tag{5.11}$$

$\varepsilon_0$ and $\varepsilon_r$ are the permittivity of vacuum and relative permittivity of the host material, respectively. $\rho(z)$ is the total charge concentration including electrons, holes and all other types of charged point defects.

$$\rho(z) = \sum_{D,q} q[D^q](z) + p_v(z) - n_c(z) \ . \tag{5.12}$$

Defect concentrations in equilibrated heterogeneous system change with the electrostatic potential. In the dilute limit where a Boltzmann-like distribution is satisfied, they can be expressed with respect to their bulk value as

$$[D^q]_{\text{scl}}(z) = [D^q]_{\text{bulk}} \exp\left(-\frac{q\Delta\phi_{\text{scl}}(z)}{k_B T}\right), \tag{5.13}$$

where $\Delta\phi_{\mathrm{scl}}(z)$ is the electrostatic potential in the space charge layer referenced to its bulk value.

Eq. (5.11) is solved with the following boundary conditions

$$\frac{d\phi_{\mathrm{scl}}}{dz}|_{z=0}=0 \tag{5.14}$$

$$\frac{d\phi_{\mathrm{scl}}}{dz}|_{z=L}=0 \tag{5.15}$$

z equals 0 and L represent the starting and end points of the modeled heterojunction, respectively. L needs to be large enough to retrieve bulk value far away from the interface. At the interface, the boundary conditions are the continuity of $\phi_{\mathrm{scl}}$ and the continuity of electric displacement field *D*. In this case, the continuity of *D* is equivalent to the global charge neutrality condition

$$\int_0^L \rho(z)dz=0\,. \tag{5.16}$$

The zero point of $\phi_{\mathrm{scl}}$ is arbitrary. Here we take the convention of setting $\phi_{\mathrm{scl}}|_{z=0}$ to zero. The built-in voltage $\phi_{\text{built-in}}=\phi_{\mathrm{scl}}|_{z=L}-\phi_{\mathrm{scl}}|_{z=0}$ will be determined upon completing the solution of Poisson's equation throughout the space charge zones and the core zones.

We point out here that using Eq. (5.13) saves the trouble of solving defect concentrations from drift-diffusion equations coupled with the Poisson equation for the electrostatic potential. The simplified form in Eq. (5.13) is valid when $E_{D,q}^{f}(\mathrm{z})>>k_BT$ for all defects. When the formation energies start to approach $k_BT$, their concentrations need to be described by Fermi-Dirac distribution [8]. In the latter case no analytical solution for the drift-diffusion equation exists and it must be solved numerically coupled with Poisson's equation. It is worth recalling that Poisson's equation in which the charge density stems from defects described by a Boltzmann-like expression under equilibrium [160, 161] as in this work is sometimes also termed as the Poisson-Boltzmann equation [162, 163, 179].

D. Core layer

The method presented above is already sufficient to obtain meaningful information of the space-charge region, such as the built-in potential and space-charge length. However, there still exists an important term we have ignored thus far. Defects close to interface are influenced not only by the electrostatic potential, but also by the varying chemical

bonding environment in the interfacial layer. This effect is rather localized in the first few atomic layers next to the interface, compared to the space-charge zone which could extend to hundreds of nanometers spatially. To evaluate this term, we define the atomic layer in the vicinity of the interface as the core layer and treat defects in the core layer explicitly. This definition is conventional in studies of grain boundaries [10] and dislocations [180]. However, in these existing models the core layer is not solved consistently with the space-charge layer, but treated as a homogeneous zero-electric-field zone. As a consequence of this inconsistency, the electric displacement field is not continuous across the interface although it should be [168]. In this section we discuss how defects in the core layer are simulated and included in the continuum model.

The width of the core layer is taken to be equal to the lattice parameter in the z direction. We assume that outside the core layer, and except for the electrostatic effect, defect formation energies are not altered by the non-uniformities of the interface and remain in their bulk value. Defect formation energies in the core layer are obtained from DFT calculation to accurately evaluate the effect of structural change near interface. The cell used in Sec. B is not sufficient to simulate interfacial defects. A larger cell is required to model isolated, non-interacting point defects. We performed DFT calculations for defects in the core layer with a supercell doubled in the x and y direction and $2\times2\times1$ k-points grid. Expression for defect formation energy is the same as Eq. (5.1) except now all values are obtained from the interface calculations.

Following the arguments in Sec. C, it is straightforward to extend Eq. (5.13) to the core layer and the defect concentration expression in that case reads

$$[D^q]_{\text{core}}(\text{z}) = [D^q]_{\text{bulk}} \exp\left(-\frac{q\Delta\phi_{\text{core}}(z) + E_{D^q}^{seg}}{k_B T}\right). \tag{5.17}$$

$E_{D^q}^{seg} = E_{D^q}^{f,\text{core}} - E_{D^q}^{f,\text{bulk}}$ is the difference in formation energy between defects in bulk and core layer, excluding the contribution of the electrostatic potential. Values of $E_{D_q}^{seg}$ for selected defects are listed in Table 5-2. This value reflects the change of formation energy due to interfacial bonding environment variation and is independent of temperature and oxygen partial pressure.

Table 5-2. Defect formation energy differences (in eV) between bulk and core layer.

| $ZrO_2$ side | $E_{D_q}^{seg}$ | $Cr_2O_3$ side | $E_{D_q}^{seg}$ |
|---|---|---|---|
| $V_O^{\bullet\bullet}$ | 3.61 | $V_O^{\bullet\bullet}$ | -2.84 |
| $O_i''$ | -1.44 | $O_i''$ | -7.75 |
| $V_{Zr}''''$ | -3.00 | $V_{Cr}'''$ | -3.98 |

Poisson's equation is solved explicitly inside the core zone subject to the boundary conditions described in section C and subject to global charge neutrality as described in Eq. (5.16). It is this explicit solution of Poisson's equation inside the core zone that preserves the continuity of the displacement field throughout the heterojunction. Poisson's equation is discretized onto a grid with mesh spacing of 1 Å outside core layer and 0.1 Å inside core layer and numerically solved with Newton's method.

## 5.3 Results

We divide this section into four parts. First, we analyze the electrostatic profiles resulting from the redistribution of charged defects across the interface. In particular we focus on the non-uniformities of the core layer and explicitly inspect the electric field and charge concentrations in this region. In the second part we take a close look at the spatially-resolved concentration profiles of the dominant defects and discuss how the existence of such interfaces influences the corrosion of zirconium alloys. In the third part we elucidate the general implications that this work provides on studying hetero-interface by making a comparison between the contribution of the defect-free interface and defect redistribution. We present all the results obtained at 1200 K for a range of oxygen pressures. Last, we list possible future improvements for the computational method.

A. Electrostatic Profiles

In this section, we represent electrostatic profiles under a selected thermodynamic condition (1200K, $P_{O_2}$ = $10^{-5}$ atm) to demonstrate the features of defect redistribution across the interface. Figure 5-4 shows the electrostatic potential, the band bending diagram, and the formation energy of $V_O^{\bullet\bullet}$ across this hetero-interface.

Under these conditions, the total built-in potential is $\phi_{\text{built-in}}$ = 1.98 V. At the interface, the band discontinuities measured from core/zone boundary in $ZrO_2$ to core/zone boundary in

$Cr_2O_3$ are $\Delta E_v$ = 1.19 eV and $\Delta E_c$ = 1.08 eV, as sought from the method described in Sec. II B. Bands bend down on the $ZrO_2$ side and up on the $Cr_2O_3$ side. As such, the positively charged defect species are depleted and negatively charged defects accumulate in both the space-charge and core zones of $ZrO_2$. The converse occurs on the $Cr_2O_3$ side. The presence of the core layer adds a potential drop of 0.05 V on the $ZrO_2$ side and 0.10 V on $Cr_2O_3$ side. Therefore, right at the interface (core/core) both band discontinuities are increased by 0.05 eV due to defect segregation in the core layer. We plot the formation energy of $V_O^{\bullet\bullet}$ in Figure 5-4 (c) with the circle and square explicitly showing values in the core layer on $ZrO_2$ and $Cr_2O_3$ side, respectively. Outside the core layer (in the space charge zone), $E^f_{V_O^{\bullet\bullet}}$ differs from the bulk value by twice the electrostatic potential change as it is a doubly charge defect. Going from outside the core to its interior, $E^f_{V_O^{\bullet\bullet}}$ raises abruptly by 3.61 eV on the $ZrO_2$ side and drops by 2.84 eV on the $Cr_2O_3$ side. The values here show that formation energy change due to interfacial effects is much more significant than due to the electrostatic potential variations.

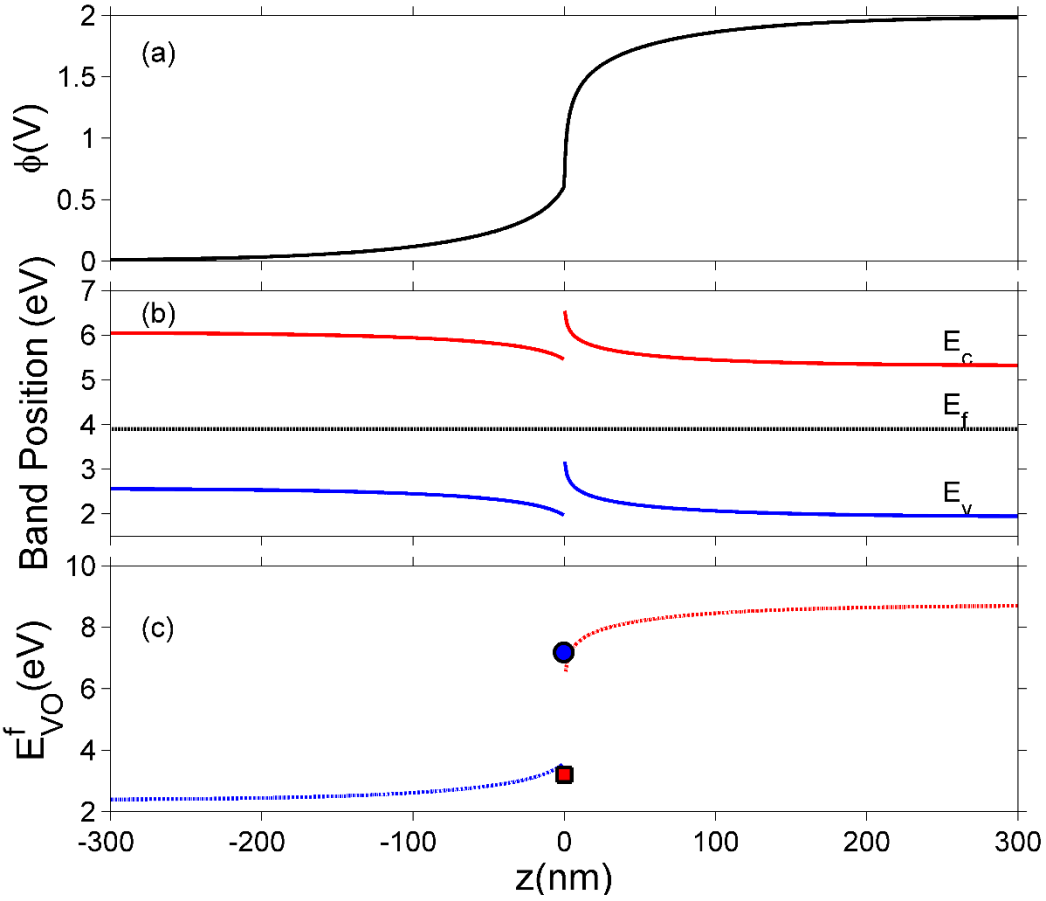


Figure 5-4 (a) Electrostatic potential, (b) band edges positions for valence band $E_v$ and conduction band $E_c$, and the Fermi level $E_f$, (c) formation energy of doubly charged oxygen vacancy calculated at 1200 K and $P_{O_2}$ = $10^{-5}$ atm. The interface is placed at z = 0 with $ZrO_2$ on the left side and $Cr_2O_3$ on the right side. In (c), the blue circle ($ZrO_2$ side) and red square ($Cr_2O_3$ side) show explicitly the formation energy in core layers on each side.

From Figure 5-4 we can see that the electrostatic potential is not smooth at the interface, implying a discontinuity of the electric field. To further examine the interfacial electric field, we zoom on the interfacial zone in Figure 5-5. Several features are captured in this plot. First, the electric displacement field $D = \varepsilon\varepsilon_0 E$ (Figure 5-5(b)) is continuous throughout, as required by Poisson's equation. At $ZrO_2$/$Cr_2O_3$ boundary, there is a discontinuity in both the charge density and the dielectric constant, this results in a discontinuity in the electric field at z = 0. In addition, at the boundaries core/space charge

within each oxide, we assume $\varepsilon$ is constant and not affected by the electric fields. However, because of the abrupt change in charge density (Figure 5-5(c)) at these boundaries, the first derivative of electric field (its divergence) is discontinuous.

Under the above-mentioned thermodynamic conditions and because of the downward band bending of $ZrO_2$ and upward band bending of $Cr_2O_3$, $ZrO_2$ side is negatively charged and $Cr_2O_3$ side positively. The core layer of $ZrO_2$ is more heavily charged in comparison with its space charge layer by several orders of magnitude. This is mainly caused by the segregation of $Cr_{Zr}''$ and $V_{Zr}''''$ to the core layer. On the other hand, the core layer of $Cr_2O_3$ is positively charged due to the abundance of valence band holes and $Zr_{Cr}^{\cdot}$. However, contrary to $ZrO_2$, the charge density in the core layer of $Cr_2O_3$ is less than the charge density in it space charge zone. Details of the defect chemistry will be discussed in the following section.

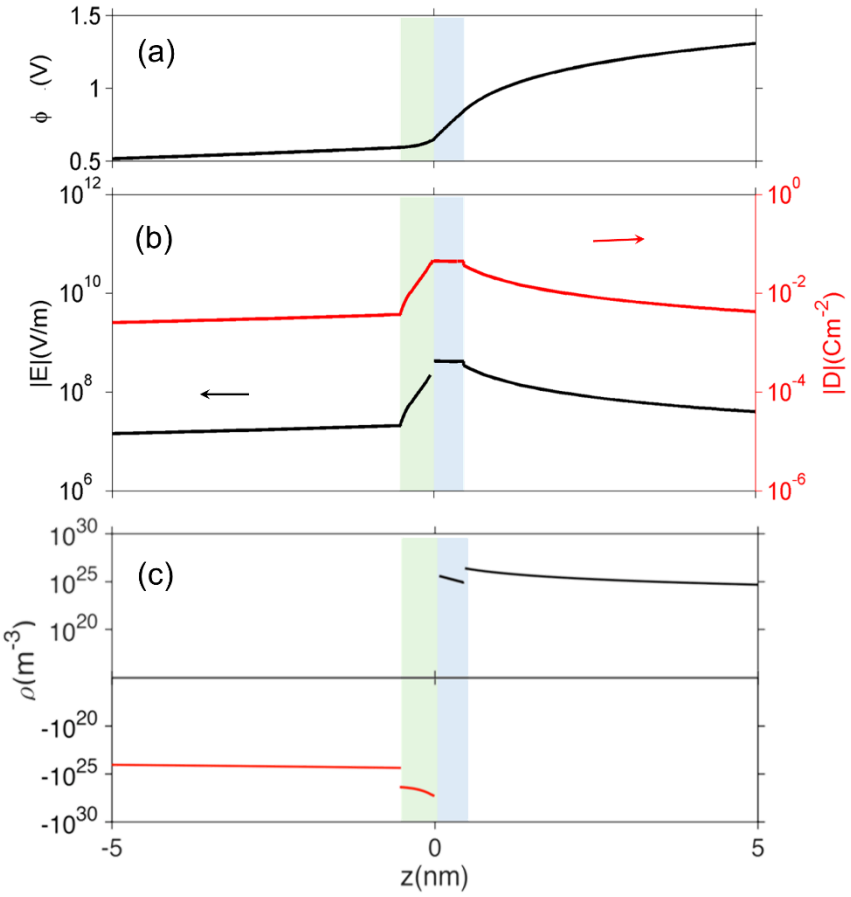


Figure 5-5. (a) Electrostatic potential $\phi$, (b) The magnitude of the electric field E and electric displacement field D and (c) charge concentration $\rho$ close to the interface.

Regions with green and blue background color represent core layer on $ZrO_2$ and $Cr_2O_3$ side, respectively.

It is common in literature to treat the core layer as a homogeneous region where the electrostatic potential is flat and defect concentrations have constant values, excluding it from the continuum solution. This is a reasonable approximation if the core is a single atomic layer. Such approximate models have produced reliable results in reproducing the conductivity of various systems [10, 12, 181-185]. However, this approximation fails to capture the strong electric field localized at an interface. Recent studies have both measured experimentally [186] and predicted theoretically[187, 188] the existence of such large electric fields at a water/oxide interface, an oxide surface, and oxide heterostructures, impacting field-dependent properties such as local bonding interactions, dielectric constants, and 2D electron gas densities.

In this study, we explicitly included the variations of the potential and field inside the core layer into the continuum model. Thus, Poisson's equation is adhered to and the displacement field *D* is continuous throughout the core layer and the space-charge layer. Based in our results, the potential drop in the core layer is on the order of $10^{-3}$ ~ $10^{-1}$ V, as such defect concentrations do not deviate much from the constant-value approximation. The advantage of our method, however, is that we can now quantitatively evaluate the electric field at the interface caused by defect redistribution.

B. Defect Concentrations

In this section we look at the calculated defect concentrations across $ZrO_2/Cr_2O_3$ interfaces and deduce how $Cr_2O_3$ grown on the Cr secondary phase particles may affect the degradation processes in $ZrO_2$ passive films formed on zirconium alloys which are used in nuclear reactors. The alloying of Fe and Cr to the zirconium alloys significantly enhances their corrosion resistance [54]. Zircaloy-4, for example, contains 0.05-0.15% Cr and 0.12-0.18% Fe. These alloying elements have very low solubility in zirconium metal and precipitate as intermetallic secondary phase particles (SPPs) $Zr(Cr,Fe)_2$. These intermetallic precipitates are incorporated in the oxide layer as it starts to grow, and later, these incorporated precipitates get oxidized. It has been observed that $Cr_2O_3$ will grow as an outer shell as $Zr(Cr,Fe)_2$ precipitates are oxidized and thus, form an interface with the $ZrO_2$ host [55]. The existence of these interfaces will impact the transport of oxygen, hydrogen, and electrons inside the $ZrO_2$ layer and thus, affect the corrosion rate of the

underlying zirconium alloy. To quantify this interfacial effect, defect concentrations in the space-charge and core layers are needed.

In Figure 5-6(a) we show the defect concentrations of undoped bulk m-$ZrO_2$ at 1200 K and different oxygen partial pressures. $ZrO_2$ exhibits oxygen deficiency at low $P_{O_2}$ with positively-charged oxygen vacancies compensating electrons. The dominant type of oxygen vacancy is $V_O^{\bullet}$ at $P_{O_2}$ <$10^{-15}$ atm and then switches to $V_O^{\bullet\bullet}$ at higher oxygen partial pressures. $ZrO_2$ becomes an intrinsic semiconductor at $P_{O_2}$ >$10^{-7}$ atm where electronic defect (holes and electrons) predominate. The results here differ from our previously reported result for bulk m-$ZrO_2$ [77] because the vibrational free energy is excluded here in order to be consistent with the results for the interface, where vibrational free energy calculations are prohibitively too expensive.

When $ZrO_2$ is brought into contact with $Cr_2O_3$, chromium ions diffuse into $ZrO_2$ and introduce chromium substitutional defects. We assume the diffusion length $L_D$ of defects are longer than the space-charge zone width $L_{scl}$ , thus complete equilibrium is reached. Far enough from the interface ( $L_{scl} < L < L_D$ ), local charge neutrality is maintained with addition of $Cr_{Zr}$ defects, as shown in Figure 5-6(b). Chromium ions tend to stay in their +3 oxidation state, acting as acceptors in $ZrO_2$. $Cr_{Zr}'$ is compensated by oxygen vacancies at low $P_{O_2}$ (dominant charge states for the vacancy changes from +1 to +2 as $P_{O_2}$ gets higher). At much higher $P_{O_2}$ $Cr_{Zr}'$ is compensated by holes. Dissolution of chromium into $ZrO_2$ extends the regime of $P_{O_2}$ over which the oxygen vacancy predominates. Approaching to the interface in the space-charge layer in Figure 5-6(c), positively-charged defects are depleted and negatively-charged defects are accumulated. $Cr_{Zr}'$ and electrons predominate in this zone, leading to a negatively-charged space-charge layer. In the core zone, $Cr_{Zr}$ defects are enriched significantly, as a sign of intermixing between $ZrO_2$ and $Cr_2O_3$. Multiple oxidation states (0 to -3) of chromium exist in the core zone with concentrations much more appreciable than the rest of $ZrO_2$ thanks to their segregation energy in the core zone. Moreover $V_{Zr}''''$ and $O_i''$ start to populate the core zone of $ZrO_2$ at high $P_{O_2}$ , showing that the segregation energies in the core zone not only affect extrinsic defects, but intrinsic ones, as well. By tracing the

dominant defect in the core zone as a function of $P_{O_2}$ we observe a switch from doubly charged $Cr_{Zr}''$ when $P_{O_2}$ < $10^{-7}$ atm to quadruply charged $V_{Zr}''''$ when $P_{O_2}$ > $10^{-7}$ atm. This shows the strong coupling between thermodynamic conditions, defect chemistry and the electrostatics of oxide heterojunctions with implications for the possibility of experimentally controlling these junctions via controlling growth conditions.

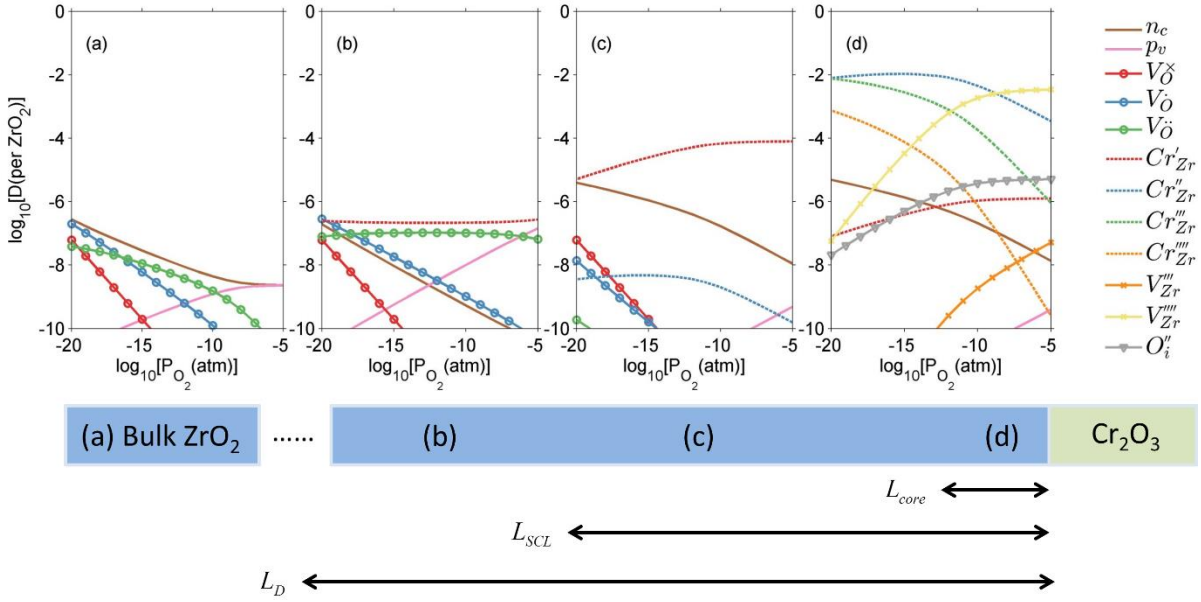


Figure 5-6. Defect concentrations at 1200 K and different oxygen partial pressures in $ZrO_2$ (a) in bulk, (b) far from the space-charge zone but within the reach of Cr defects, (c) outside the core layer within the space-charge zone, and (d) in the core layer.

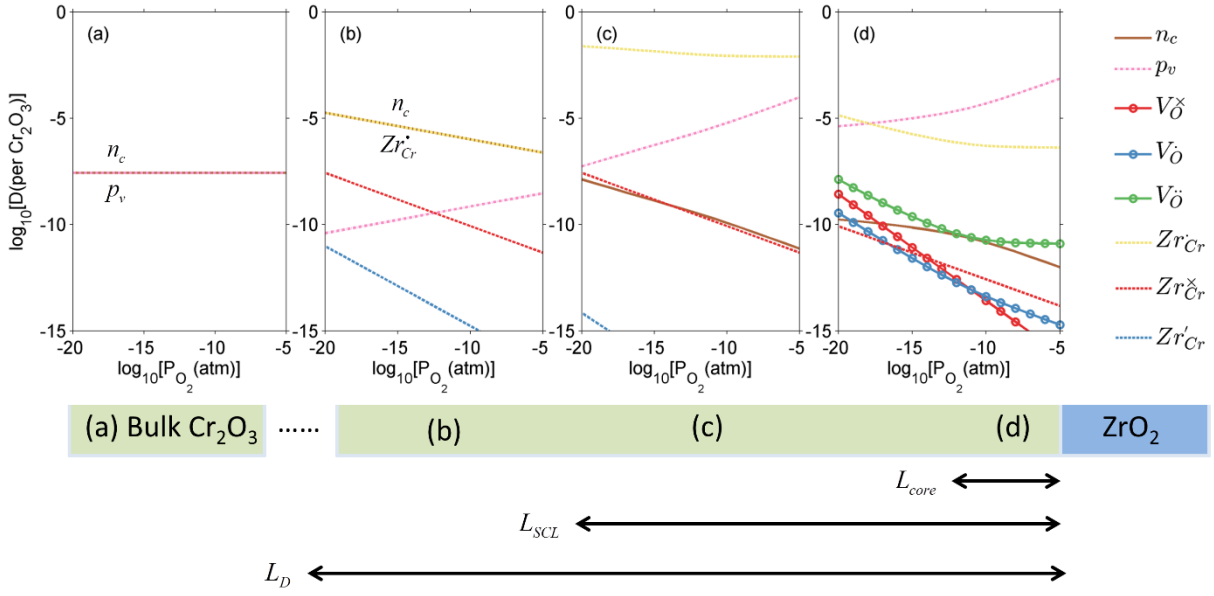


Figure 5-7. Defect concentrations in $Cr_2O_3$ at 1200K and different oxygen partial pressures (a) in bulk, (b) far from the space-charge zone but within the reach of Zr defects, (c) outside the core layer within the space-charge zone, and (d) in the core layer.

Similar analysis can be done on the $Cr_2O_3$ side, as shown in Figure 5-7. In undoped bulk $Cr_2O_3$, there is no significant concentration of ionic defects (Figure 5-7(a)) and only electronic defects predominate. This is consistent with the conclusions of the conductivity experiments conducted on undoped $Cr_2O_3$ [189]. Far away from the interface such that local charge neutrality is maintained but within the diffusion length of Zr defects, $Zr_{Cr}^{\bullet}$ and $Zr_{Cr}^{\times}$ (Zr in +4 and +3 oxidation states, respectively) start to show up with appreciable concentrations. Getting closer to the interface, the bands of $Cr_2O_3$ bend up, and the concentration of the positively-charged $Zr_{Cr}^{\bullet}$ is increased. Inside the core layer, oxygen vacancies tend to segregate but the predomination in this zone remains for $Zr_{Cr}^{\bullet}$ and holes. The core zone of $Cr_2O_3$ maintains the predomination of singly positively charged defect throughout all oxygen partial pressures considered here at 1200 K but with a switching from $Zr_{Cr}^{\bullet}$ to holes at $P_{O_2}=10^{-18}$ atm. This again brings up the rich coupling between thermodynamics, chemistry and electrostatics in oxide hetero-interfaces.

For symmetric grain boundaries in oxides, it is customary to postulate that the core zone has a charge opposing and compensating that of the space charge zone [10, 12]. The symmetry of the grain boundary justifies this postulate. At a hetero-interface, however, the symmetry is broken and in the case of the $ZrO_2/Cr_2O_3$ system studied here we found that the core and the space charge have similar charge (both are negative in the case of $ZrO_2$ and both are positive in the case of $Cr_2O_3$). When the space charge and the core zone possess similar charges, the electric compensation occurs on the other side of the junction (the other oxide). In fact this charge compensation scenario in heterojunctions suggests the possibility of the presence of a thermodynamic point of zero charge in analogue with what happens when an oxide is immersed in an aqueous solution [32]. That is a point in which the two sides of the junction are uncharged. We systematically varied temperature (between 400 K to 1400 K) and oxygen partial pressures (between $10^{-30}$ atm to 1 atm) to search for such a neutral point in the $ZrO_2/Cr_2O_3$ system but did not observe it. Its absence in this system does not preclude its existence in other oxide hetero-interfaces.

We turn now to the implications of this analysis on zirconium alloys in nuclear reactors. The growth rate of zirconium oxide layer is thought to be limited by either electron transport or oxygen diffusion in $ZrO_2$ [51]. Figure 5-8 shows the concentrations of free electrons, holes and $V_O^{\bullet\bullet}$ throughout the heterojunction at various oxygen partial pressures at 1200 K. By looking at the concentration distribution of oxygen-related defects and electronic defects, we can analyze how electron transport and oxygen diffusion are changed in the space-charge layer of $ZrO_2$ compared to its bulk due to the change in the concentration of these defects in the space-charge layer. In Figure 5-8(a), because the bands bend down on the $ZrO_2$ side, the concentration of electrons is space charge layer compared to bulk, and increased in the subsequently holes are decreased as well in this layer. This enhancement of electron concentration has a favorable effect on preventing hydrogen, generated by the corrosion reaction, from getting into $ZrO_2$ [77, 123]. In addition, the sum of electron and hole concentrations is plotted in Figure 5-8 (b). If we assume that the mobilities of electrons and holes are on the same order of magnitude, this quantity should give us an estimation of the change in total electronic conductivity in the space-charge layer. Figure 5-8(b) shows that when $P_{O_2} < 10^{-12}$ atm, the space charge layer of $ZrO_2$ is in its n-type regime. In this case, the total electronic conductivity in the space-

charge zone is increased. On the other hand, when $ZrO_2$ becomes p-type at higher $P_{O_2}$, the total electronic conductivity is decreased in the space-charge layer in comparison to bulk due the downward band bending. If electron transport is the rate limiting step of the corrosion reaction, then the oxidized Cr precipitates lying in the oxygen rich, and hence the p-type part of $ZrO_2$, closer to the interface with water coolant in the nuclear reactor, have a desirable of effect of slowing down the electronic conductivity and consequently reducing the corrosion rate. In fact, the $ZrO_2$ oxide layer grown is exposed to a gradient in oxygen chemical potential between an oxygen poor zone at the interface with the underlying Zr alloy and an oxygen rich zone at the interface with water. As such, even if the electronic conductivity is enhanced around the precipitates in the oxygen-poor part of $ZrO_2$ (n-type), it is inevitable that this conductivity is reduced around the precipitates in the oxygen-rich part (p-type).

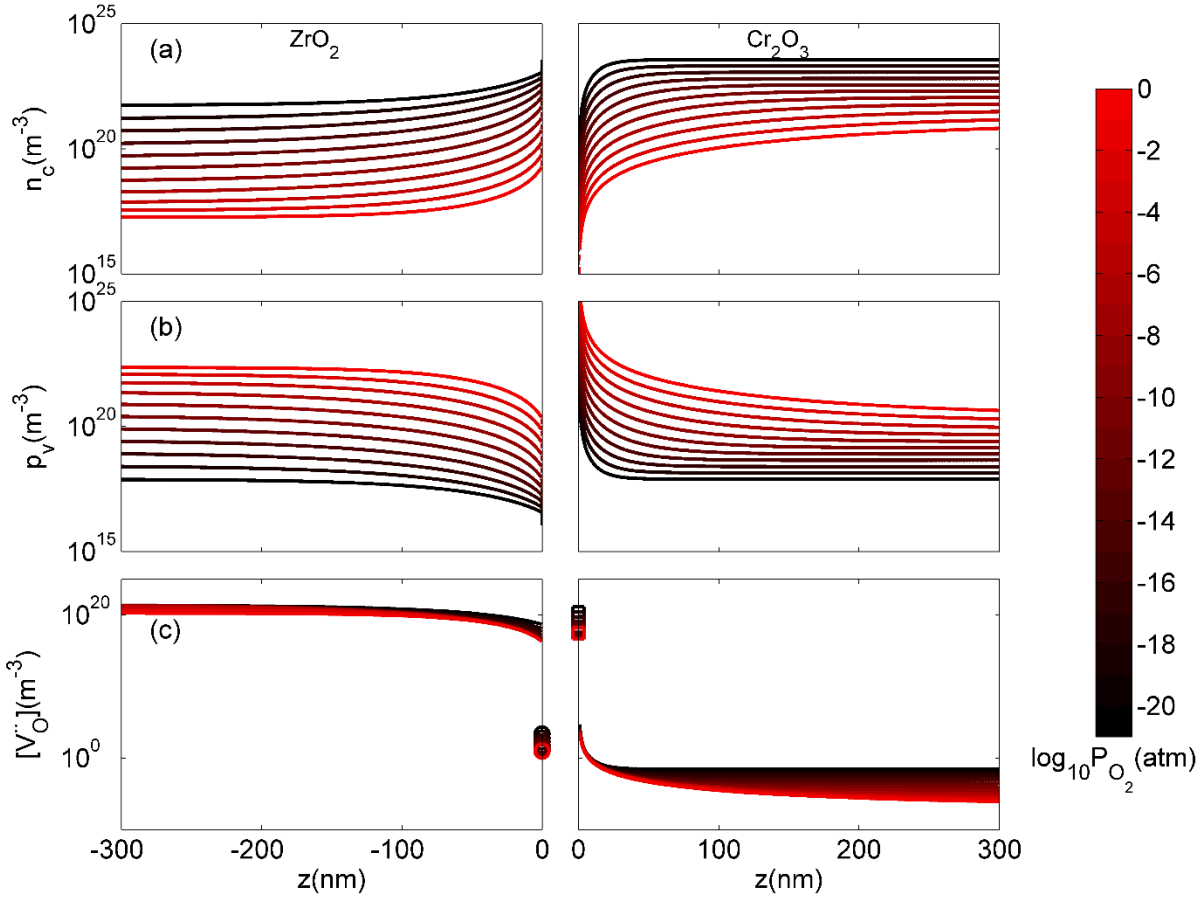


Figure 5-8. Spatially-resolved concentrations of (a) electrons, (b) sum of electrons and holes and (c) $V_O^{\bullet\bullet}$ as a function of oxygen partial pressure at T=1200K. Circles and

squares in panel (c) represent the concentrations in the core layer on the $ZrO_2$ and $Cr_2O_3$ sides, respectively.

$Cr_2O_3$ has low oxygen diffusivity (~ $10^{-16}$ $cm^2/s$ at 1200 K, 0.1 atm [190]) compared to monoclinic $ZrO_2$ (~ $10^{-13}$ $cm^2/s$ at 1200 K, 0.4 atm [101]), which indicate that the in-precipitate oxygen diffusion should be negligible, especially that the concentration of $V_O^{\bullet\bullet}$ in $Cr_2O_3$ is several orders of magnitude lower than in $ZrO_2$ as shown in Figure 5-8(c). Since the precipitates are discrete particles that do not form a continuous path through which oxygen ions can diffuse, we focus here on oxygen diffusion in the matrix, $ZrO_2$.The extended space charge zones around the oxidized Cr precipitates can form a significant fraction of the matrix with possibilities for space charge percolation. Figure 5-8(c) shows that oxygen vacancies are strongly depleted throughout the space-charge layer and in particular in the core zone on $ZrO_2$ side, which indicates that oxygen diffusion in $ZrO_2$ is suppressed around the Cr oxidized precipitates. This observation suggests that if oxygen diffusion is the rate limiting step of the corrosion reaction, then the presence of oxidized Cr precipitates has also a desirable effect of slowing down oxygen diffusion in the extended space charge zones around them. While the conclusions here are based on the defect profiles evaluated at 1200 K, they are still applicable to lower temperatures closer to the actual reactor operation temperature. Modeling the space charge zone at lower temperatures becomes more challenging in the dilute limit because the difference in the spatial extend of the core layer and the pace charge layer becomes increasingly large.

C. Potential drop, electric field and interface dipole: finite temperature vs. 0 K

In this study, we have obtained two sets of solutions of Poisson's equation: (1) from first-principle calculations on the defect-free interface at 0 K, and (2) from continuum level modeling of defect equilibria, where ionic and electronic defects redistribute due to chemical and electrical forces and reach thermal equilibrium at finite-temperature. Therefore, our multi-scale method allows us to separate the contributions of the perfect crystal (0 K) and the defect formation and segregation (finite T) on the potential drop, the electric field, and the interface dipole obtained from solving Poisson's equation. These three quantities are all experimentally measurable [191] and are important for understanding the physical and chemical properties of hetero-structures [192, 193]. In

this section we compare the origins and consequences of these two contributions. The summary of the comparison is shown in Table 5-3.

Table 5-3. Potential drop across the interface, maximum electric field and dipole moment density calculated for the two sets of solution of Poisson's equation: the perfect interface from 0 K DFT calculations, and the defect contribution from the continuum model. The defective interface results are calculated at T=1200K and $P_{O_2}$ = $10^{-5}$ atm. The dipole density p is evaluated using $p = \int z\bar{\rho}(z)dz$ .

| | Potential drop (V) | Maximum electric field (V/m) | Dipole density (e/m) |
|---|---|---|---|
| Perfect interface at 0 K | -3.8 | $4.9\times10^{9}$ | $3.0\times10^{11}$ |
| Defect contribution at finite temperature | 2.0 | $-4.3\times10^{8}$ | $1.2\times10^{9}$ |

Figure 5-9 shows a comparison between the macroscopic averages of the solution of Poisson's equation of the defect-free interface and the solution of Poisson's equation for the charged defects at T=1200K and $P_{O_2}$ = $10^{-5}$ atm. The potential drop across perfect interface $\Delta V$ , as shown in Figure 5-9(a), is -3.8V. This potential drop results from the forming of polar bonds at the interface. Electrons distribute unevenly on the two sides of the interface and a localized interface dipole is built. Notice from Fig. 9 that the electrostatic potential becomes flat, and electric field and charge concentration of the defect-free interface become zero already at one atomic layer away from the interface. Because of the highly localized nature of this potential drop, electric field and charge concentrations have very high values right at the defect-free interface. In the system under consideration, the maximum electric field is $4.9\times10^{9}$ V/m and the interface dipole density $3.0\times10^{11}$ e/m.

In contrast, the effect of the defects is extended in space (hence the denotation space charge). As shown in Figure 5-9, the length of space-charge layer is several hundred nanometers. The potential drop is 2.0 V across the space-charge layer, with only 0.2 V drop in the core zone. The maximum electric field is $-4.3\times10^{8}$ V/m and the dipole density

is $1.2\times10^{9}$ e/m, which are order-of-magnitude lower than the perfect interface contribution. The two contributions are, however, mathematically additive as required by the superposition principle [194].

These two effects coexist in every interface between two semiconductors (or insulators) and can both influence the interface properties. However, because of the difference in spatial scales of these two effects, either could be dominating at different spatial positions around the interface. When electrostatic profiles are discussed in literature, these two effects are seldom distinguished or contrasted. We believe that the highly localized nature of the field and the dipole arising from the defect-free interface gives rise to the catalytic activity of exposed or barely hidden interfaces [195]. It can also influence the transport processes right at the interface (parallel or across). On the other hand, the field and dipole generated by defects at finite temperatures influence the transport processes over an extended region around the interface.

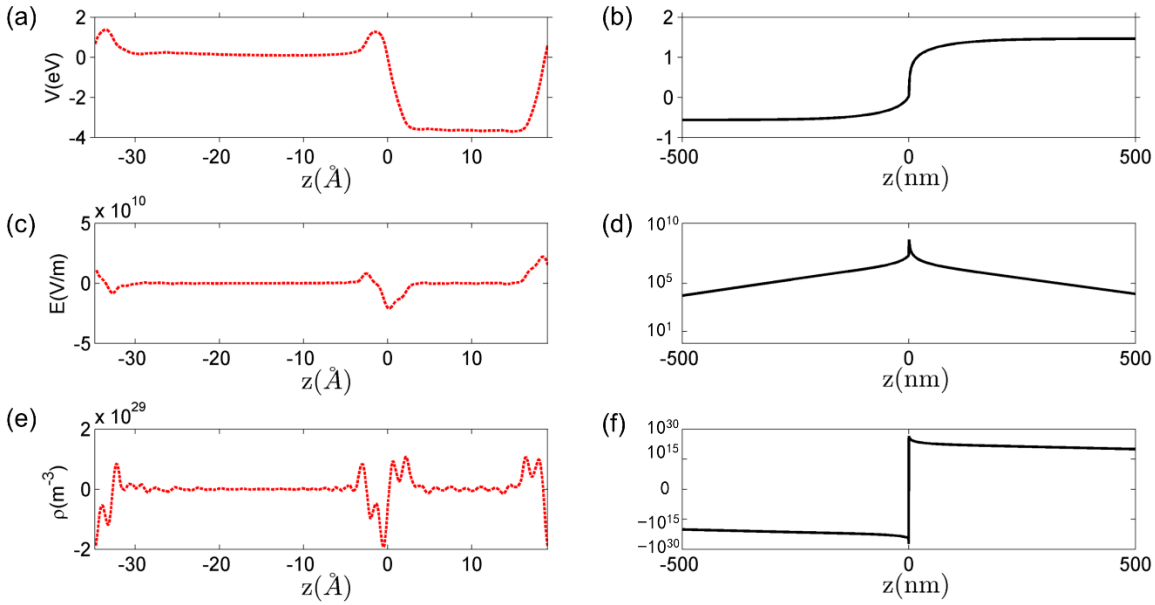


Figure 5-9. Macroscopic average of (a) electrostatic potential V, (c) electric field E and (e) charge density $\rho$ from the perfect interface calculated by DFT at 0 K, compared with the same quantities (b), (d) and (f) contributed by the redistribution of defects.

D. Possible future improvements for the computational method

There are several improvements that could be made to further refine our predictions. First, the Fermi-Dirac distribution could be used instead of the Boltzmann distribution in calculating defect concentrations. This requires including explicit solutions of the drift-

diffusion equations for all defects. This is particularly important when the formation energies start approaching $k_BT$. Second, we did not consider finite temperature effects in this work. To accurately evaluate defect concentrations at various temperatures, formation energy should be replaced by formation free energy, by adding the contribution of phonons and the electronic entropy [7]. Third, it has been reported in the literature that the formation energy of a point defect with respect to its distance to the interface should be an oscillating function, which gradually approaches its bulk value after a few atomic layers [25, 166, 196]. In this work we only treat the first atomic layer as the core layer, which is the computationally affordable approximation for evaluating segregation energies for all types of defects in the system at this time. In principle we could obtain spatially-resolved defect formation energy profiles from first-principles calculations by inserting defects in each atomic layer and add as many core layers as needed into the continuum model. Fourth, we treated electrons and holes as free carriers in the bulk, space-charge layer and the core zone and thus their concentrations were calculated by applying Fermi-Dirac distribution to the electronic density of states. However, it is known that these electronic defects can self-trap in polarizable oxides forming small polarons which is indeed the case for holes in monoclinic $ZrO_2$ [197]. Small polarons should be treated as point defects when calculating their concentrations. The self-trapping energy for holes in monoclinic $ZrO_2$ is only 0.13 eV [197] indicating that the results presented here remain qualitatively correct even if self-trapping is accounted for. However, it is of interest to explore the differences in self-trapping energies between bulk and the core region in future work. Finally, more accurate electronic structure methods, such as hybrid functionals [20] and $G_0W_0$ [198], might be needed to correctly predict band alignment at the interface and electronic structures of the defects. Additional modeling difficulties could arise while going to more complicated oxide systems, but the framework provided here addresses defect chemistry at hetero-interface in a generalized way and could potentially be applied to other oxide interfaces and surfaces.

Lastly, results for temperatures lower than 800 K are not presented because the space charge layer length becomes too large (~100 microns at 600 K), requiring the use of a very coarse mesh to do the calculations, and also because these really large space charge zones are beyond the thickness of the corrosion passive films. In reality, the space charge length could be significantly reduced by other alloying elements that exist in the system, which is not considered in this work.

## 5.4 Conclusion

We present a framework to predict the equilibrium defect concentrations across a hetero-interface starting from first principles-based calculations. Our method takes into account both long-range Coulomb interaction in the space charge layer and the localized effects of band discontinuity and bonding environment variation, allowing for a comprehensive description of defect redistribution across hetero-interfaces.

The addition of core layers explicitly into the solution provides a closer view on the electric field and defect chemistry in the vicinity of the interface. Our model features a consistent treatment of Poisson's equation throughout the core and space charge layers preserving the continuity of the displacement field, whereas existing studies treat the core layer as a field-free homogeneous zone. Our results suggest that the variation in the formation energy of defects can be up to several eVs in the core region, causing a localized change in the electrostatic potential on the order of 0.1 V inside the core zone. Consequently, a giant electric field arises in this zone and hence it deserves explicit modeling when studying oxide interfaces.

Our selected model interface, $ZrO_2/Cr_2O_3$, is of interest to understand and improve the performance of zirconium alloys as nuclear cladding materials. This interface arises from the oxidation of the host Zr and the Cr secondary phase particles embedded inside the host. Here we clarified the beneficial effect of this interface in improving the corrosion and hydrogen resistance of Zr alloys. In particular, in the extended space charge layer around these particles and under oxygen rich conditions, we predict a decrease in the total electronic defect concentrations and in the oxygen vacancy concentration. Both of these results should decrease the oxidation kinetics. In spite of the reduction in the sum of electronic charge carriers under oxygen rich conditions, we observe an increase of electron concentration in the $ZrO_2$ space-charge zone compared to the bulk for all oxygen partial pressures. This has the positive effect of promoting hydrogen evolution and suppressing hydrogen pickup inside the alloy. Both effects are beneficial towards protecting the integrity of zirconium alloy. The model and analyses presented here provide a utility to understand the effect of alloying elements on the corrosion resistance of alloys when these alloying elements tend to precipitate as secondary phase particles and oxidize in the passive layer.

This systematic study also facilitates a comparison of two contributions to the interfacial electrostatic properties; a 0 K contribution originating from the formation of a perfectly abrupt interface, and a finite temperature excitation due to the equilibration of electronic and ionic defects. Finally, we discussed several improvements to enhance the predictive power of the herein presented model. Although here we discussed applying the model to the problem of zirconium alloy corrosion resistance, we believe that it is broadly applicable to oxide interfaces arising in several applications such as lithium batteries, fuel cells, and computer memories.

# 6 Unravelling water structure, kinetics and thermodynamics at water/monoclinic-$ZrO_2$ interface via *ab initio* molecular dynamics

In this work, we present a comprehensive analysis of structural, kinetic and thermodynamical nature of water in contact with $ZrO_2$ $(\bar{1}11)$ surface by *ab initio* molecular dynamics calculations. We observe that water molecules in the immediate first layer has a preferred orientation with one O-H bond lying parallel to the surface and the other hydrogen atom pointing away from the surface, which originates from surface Zr-O and $O_s$-H bonding. This short-range interaction leads to an ordered structure with alternating hydrogen-rich and oxygen-rich layers that persist for more than 5 Å away from the surface. The surface structural perturbation also leads to a shortened hydrogen bond distance and distorted hydronium ion solvation shell, which leads to faster proton hopping dynamics and lowered solvation free energy of hydronium ion. In presenting these properties in a spatially-resolved way, we demonstrate a clear link between interfacial water structure and localized dynamics and thermodynamic effects. This work provides atomistic understanding of proton interacting with $ZrO_2$ surface in water environment and allows for further engineering of oxide surfaces for desired hydrogen activity.

## 6.1 Introduction

Understanding oxide/water interface properties is fundamentally important for a wide range of electrochemical applications such as corrosion [48, 51, 199], photochemical water splitting [200-203] and heterogeneous catalysis [204-206]. Interfacial water structure has been found to be distinct from that of bulk and as such it brings about distinct kinetics and thermodynamics. [207] *Ab initio* molecular dynamics (AIMD) technique has proven to be an effective method for studying water properties both in bulk [208-210] and at oxide/water interface including $CeO_2$ [211], ZnO [212], $TiO_2$ [213], $Fe_2O_3$ [214], MgO [215], and $ZrO_2$ [216]. However, while the immediate first layer of water at the interface is widely studied, there is a general lack of knowledge of the spatially-resolved properties as water transitions from bulk structure far away from the interface to disturbed interfacial structure. This extended interface effect is related to

mesoscale electric double layer forming and further influences the interaction between liquid electrolyte and charged defects in the oxide material [217]. A quantitative evaluation of water structure, kinetics and thermodynamics in the extended interfacial zone is needed for a more accurate description of the electrochemical processes therein.

With this goal in mind, in this paper we present our work of AIMD simulation on monoclinic-$ZrO_2$/water interface. Zirconium oxide is a well-studied oxide material for its application in catalysis, thermal coating, biomaterial and as a component of the nuclear cladding in nuclear reactors [46, 84, 218]. $ZrO_2$/water interface are particular of interest in two scenarios. First, this interface serves as the source of oxidation and hydrogen pickup for zirconium alloys in nuclear water reactors [116]. Zirconium alloy is exposed to high-temperature coolant water (about 500~700 K) in a pressurized water reactor (PWR). As the corrosion process happens, a $ZrO_2$ layer grows on the alloy and protects it from the corrosive environment [145]. At $ZrO_2$ surface, water is reduced to atomic hydrogen through the cathodic reaction $H_2O + 2e^- \rightarrow O^{2-} + 2H$. The hydrogen atoms generated in the reduction reaction could either recombine and form hydrogen gas, or diffuse through the oxide layer into zirconium metal. The latter is a detrimental process called hydrogen pickup. When hydrogen reaches its solubility limit in the metal, zirconium hydrides start to precipitate, which could potentially lead to embrittlement. [53] An atomistic understanding of $ZrO_2$/water interface is required for further quantifying hydrogen pickup rate and potential engineering towards better corrosion resistance for zirconium alloy. Second, biomedical grade zirconia is prone to ageing when attacked by water, which raises questions on whether we should continue to use zirconia in clinical implants. [219] This degradation process, which happens at intermediate temperatures, is referred to as low temperature degradation (LTD). Understanding water structure and dynamics on $ZrO_2$ surface also provides knowledge of LTD kinetics and future engineering of zirconia-based biomaterials.

We organize the analysis of AIMD simulation into three parts. First, we present spatially-resolved structural information for water and hydronium ion solvation shell. By analyzing density profile, bond angle distribution and radial distribution function, we arrive at a full picture of the interfacial water structure with a more close-packed hydrogen bond network and distorted hydronium solvation shell. Second, we quantify the hopping barrier for proton both in the interfacial zone and in the bulk-like region. We observe a

reduction by half at the interface, which corresponds to a ten-time-faster proton hopping rate at room temperature. This accelerated proton dynamics is linked back to the structure of interfacial water with surface bonding and strengthened hydrogen bond. Third, we show the solvation free energy profile of hydronium ion as a function of its distance towards $ZrO_2$ surface. An adsorption free energy of 0.20 eV is found for hydronium ion and 0.15 eV for hydroxide ion at the surface at room temperature. The comprehensive analysis and quantification of structural, kinetic and thermodynamic properties in a spatially-resolved fashion allow us to establish a clear link between them and provide mechanistic understanding of proton interacting with $ZrO_2$ surface.

## 6.2 Methods

AIMD calculations were performed for $ZrO_2$/water system with Vienna Ab initio Simulation Package (VASP) [85-88]. The simulation cell contains 96 unit formula of monoclinic phase $ZrO_2$ with $(\bar{1}11)$ surface orientation and 80 water molecules, as shown in Figure 6-1. $(\bar{1}11)$ surface has been shown to be the surface orientation with the lowest energy.[76] The middle layer of $ZrO_2$ was fixed at the ideal bulk positions to represent bulk material. 40 configurations with $H^+$ and $OH^-$ ions sitting at different distances towards $ZrO_2$ surface are set as initial frames. To overcome the time length limitation of AIMD simulation, each configuration is first equilibrated with simple point charge model for water [220] and an Lennard-Jones potential for $ZrO_2$ [218] using the GULP code [221, 222] for 10 ns. The output structure is further equilibrated in AIMD employing velocity rescaling thermostat for 1 ps, during which the velocities are scaled every 10 steps. 1 ps run in NVT ensemble is performed as the production phase for each of the 40 configurations. A time step of 0.25 fs and a temperature of 330 K are used throughout. The simulation cell size is 13.6 Å × 13.6 Å × 27.2 Å with a water film thickness of 14 Å. AIMD calculations are done by sampling the reciprocal space at the gamma point only using the generalized gradient approximation (GGA) with Perdew-Burke-Ernzerhof (PBE) functional [89, 90]. An energy cut-off of 400 eV is used. Dispersion corrections are applied using the Grimme-D3 method with Becke-Jonson damping [223, 224]. For the purpose of comparison, same simulations are also performed for bulk water of 256 water molecules with no $ZrO_2$ surface with a density of 0.98 g/cm$^3$.

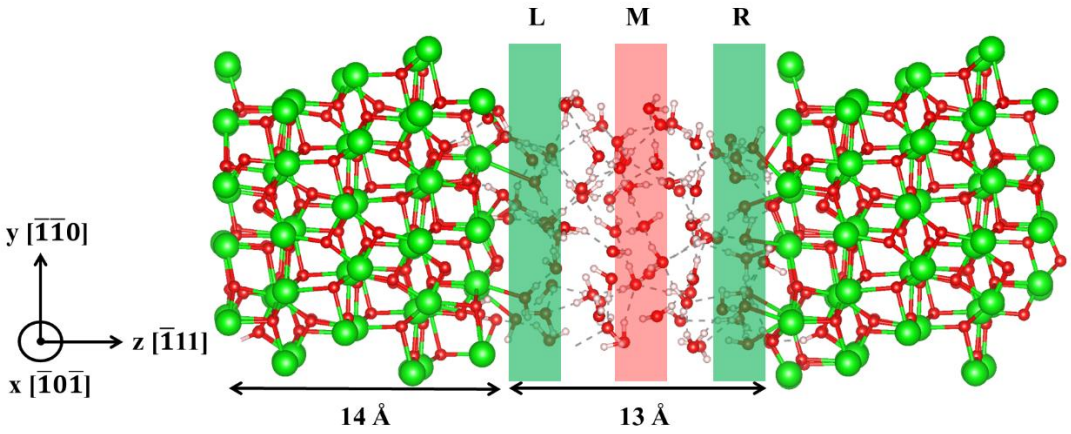


Figure 6-1. m-$ZrO_2$ ($\bar{1}$11)/water interface as modeled in AIMD simulation. A water film of 13 Å thickness is used. Hydrogen ions are drawn small and white, oxygen ions medium-sized and red. Zr ions are largest and green. The three shaded areas left (L), middle (M), and right (R) will be analyzed separately to show the difference between bulk-like water (region M, red shading) and interfacial water (region L and R, green shading). The figure is generated with visualization software VESTA [97].

To demonstrate the interfacial effect on water structure and dynamics, spatially-resolved analysis is performed with gridding in the direction perpendicular to the surface. As schematically shown in Figure 6-1, three regions, left (L), middle (M) and right (R) are selected with left and right regions being close to the surface and middle region away from the surface. In the z direction, the zero position is referenced to the highest oxygen from the $ZrO_2$ surface in the initial frame in the production run. Each region is 2 Å in thickness. For all the structural and dynamical properties studied in this work, we examine the differences between the three regions to demonstrate the effect of $ZrO_2$ surface. It is to be noted that due to the symmetry of the simulation cell, left and right layers are equivalent and representing interfacial region. Middle layer, as we show in the results section, retains the properties of bulk water.

The spatially-resolved radial distribution functions are defined as such: for each pair of atom type A and B, $g_{AB}(r)$ in region G counts the distribution of all type B atoms within a distance of r and $r+dr$ away from atom A, with A limited in region G. When $r$ is small, A and B atoms in the pair are both in region G with a high probability. When $r$ is large, B

atom is most likely outside region G. In these analyses we focus on the radial distribution function variation in the short range in order to see the effect of surface.

## 6.3 Results and Discussion

In this section, we present spatially-resolved structure, kinetic and thermodynamic properties of water at $ZrO_2$ surface. First, we analyze the structural information provided by AIMD simulations by looking at atom density, bond angles, and pair correlation functions. We observe strong dissociative adsorption with hydrogen attached to surface oxygen ($O_s$) and water oxygen attached to surface zirconium, which makes surface hydroxyl hydrogen worse hydrogen bond donor and surface oxygen better hydrogen bond acceptor. This interface effect gives rise to O-H bonds ranging between 1.1 – 1.4 Å, which falls in the gap between intramolecular O-H bond (< 1.0 Å) and intermolecular hydrogen bond (~ 1.8 Å in bulk water). Increased ionicity of water oxygen also leads to a shortening of hydrogen bond and increases the compactness of surface hydrogen bond network. This structural change is also manifested in the solvation shell of surface hydronium ions, where we observe symmetry breaking of the three hydrogen atoms within the hydronium ion due to surface adsorption. Second, we take a close look at the proton exchange reaction dynamics. The results show that proton hopping barrier is reduced by half at the interface, which is clearly linked to the shortened hydrogen bond and formation of surface hydroxyl groups. Finally, we demonstrate the solvation free energy profiles of hydronium ion and hydroxide ion as a function of their distances to the surface and discuss their structural origins based on the electrostatic interaction between the ions and the background charge of interfacial water.

A. Structure of interfacial water

We start with thermally-equilibrated liquid water structure from force field modeling. During the AIMD equilibration, we observe preferred dissociative adsorption ocurring at the interface, which has also been reported previously for water film on $ZrO_2$ surface [78]. In

Figure 6-2 we plot the xy planar-averaged atom density of hydrogen and oxygen on water side. The density profile clearly exhibits heterogeneity in z direction within 3 Å to $ZrO_2$ surface. Within the immediate 1-Å-thick water layer, the densities of oxygen and hydrogen are approximately the same. In the next 2-Å layer, we see alternating oxygen-rich layers and hydrogen-rich layers, where the maxima of oxygen density meets the

minima of hydrogen and vice versa. This alternating feature fully disappears beyond 5 Å away from $ZrO_2$ surface and we see a relatively constant density right in the middle region, with the density of hydrogen being two times that of oxygen.

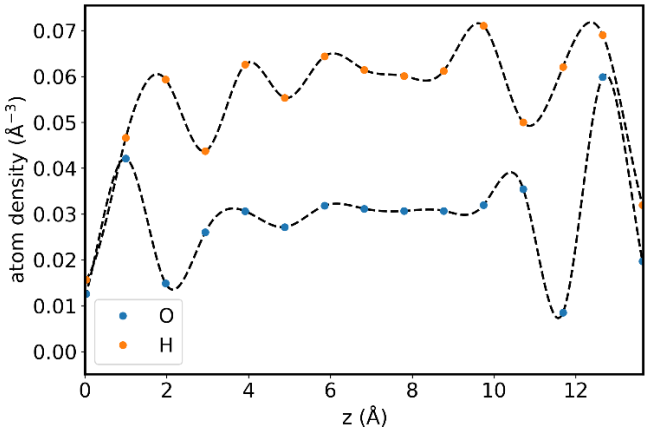


Figure 6-2. Planar-averaged atomic density of oxygen and hydrogen as a function of the distance z from $ZrO_2$/water interface. The origin of z axis is set to the z coordinate corresponds to the top surface oxygen layer.

To further understand the localized structure of adsorbed water molecules, in Figure 6-3 we show the joint probability distribution of the angles between the two O-H bonds in each water molecule and $ZrO_2$ surface normal **n**. The distribution is spatially-resolved in regions L, M, and R defined above. Following the distribution plot, in the middle layer (Figure 6-3(b)), the bond angle distribution tends to be isotropic with respect to the surface normal. However, looking at the left and right regions which are close to the surface, we see a preferred orientation with one O-H bond parallel to the surface ($\cos(\theta) = \pm 1$) and the other perpendicular to the surface ($\cos(\theta) = 0$) with hydrogen pointing away from surface. This preference explains the local density feature shown in

Figure 6-2. In the immediate vicinity of the surface, there exists a layer with O-H pairs lying parallel to the surface, leading to comparable O and H atom densities. The other hydrogen atom, which points away from the surface, contributes to the second layer which is hydrogen-rich.

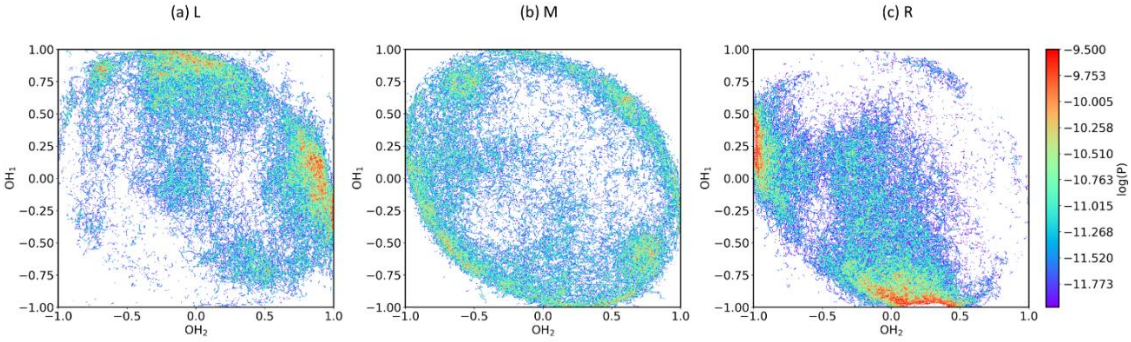


Figure 6-3. Joint probability distribution of O-H bond angle with respect to $ZrO_2$ surface normal **n** plotted in log scale. Here $H_1$ and $H_2$ refers to the two nearest neighbor hydrogen atoms to the oxygen. Suppose vector $\mathbf{r}_{OH_i} = \mathbf{r}_{H_i} - \mathbf{r}_O$, where $\mathbf{r}_{H_i}$ and $\mathbf{r}_O$ represents the coordinates for corresponding hydrogen and oxygen ions. The coordinates ($OH_1$, $OH_2$) of each point in the shown distributions represent $\frac{<\mathbf{r}_{OH_i}, \mathbf{n}>}{|\mathbf{r}_{OH_i}|}$. The case $OH_i = 0$ represents an O-H pair lying parallel to $ZrO_2$ surface and $OH_i = \pm 1$ represents an O-H pair lying perpendicular to $ZrO_2$ surface. L, M, and, R regions notations are used as shown in Figure 6-1.

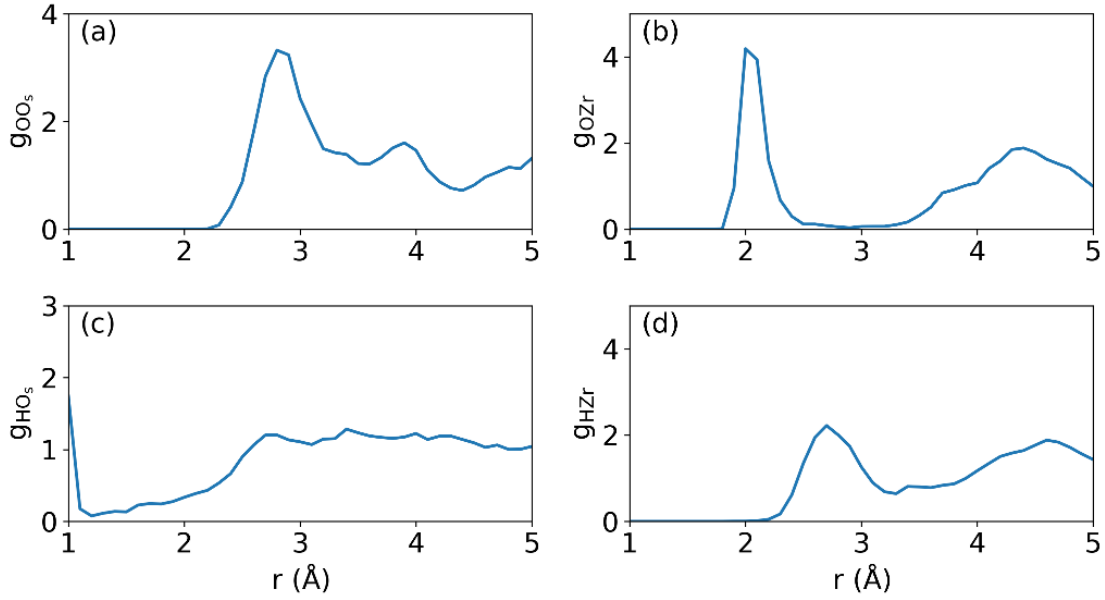


Figure 6-4. Radial distribution functions of interfacial water molecules in region L with surface zirconium atoms and oxygen atoms ($O_s$).

Figure 6-4 shows the radial distribution function of surface atoms of $ZrO_2$ relative to interfacial water in region L. By comparing peak positions of radial distribution functions of oxygen and hydrogen, we can conclude that hydrogen atoms are attached to surface oxygens $O_s$, with a sharp peak at ~ 1 Å (Figure 6-4(c)). This peak represents surface hydroxylation and we observe a 50% dissociative adsorption rate of surface water molecules, hydroxylating 20% of twofold-coordinated surface oxygens. The first-layer hydrogen forms an O-H bond parallel to the surface. The oxygen atom it attaches to sits closer to surface zirconium (2.0 Å) comparing to surface oxygen (2.8 Å). This Zr-O bond length is comparable to surface Zr-$O_s$ bond (1.9 ~ 2.2 Å). Bader charge analysis shows that hydrogen atoms attached to surface oxygens has a lower valence state, or reduced ionicity, comparing to bulk water. Oxygen from water attached to surface zirconium atoms, on the other hand, shows increased ionicity. The net effect is that $ZrO_2$ surface donates electrons to surface water, thus sustaining the first water layer which has similar O and H density and a net negative charge.

The change in surface water ionicity is accompanied by change in water and hydronium ion structures. In Figure 6-5 we take a close look at radial distribution functions of interfacial water comparing the three regions (L, M, R) with bulk results (red dashed line). It is obvious that the middle region retains the structure of bulk water both in the peak positions and peak heights. Interfacial water, as represented by region L and R, exhibits the following features which differ from bulk water: (1) The second $g_{OH}$ peak distance, which represents intermolecular hydrogen bond, is shortened by about 0.2 Å. This indicates a strengthened hydrogen bond of interfacial water. The interfacial water oxygens become better hydrogen bond acceptors due to their bonding with surface zirconium. (2) For bulk water, no O-H pair exists in the range of $r_{OH}$ = 1.1 – 1.4 Å, which is a clear separation between well-defined intramolecular O-H bond and intermolecular hydrogen bond. However, we observe O-H bond length within this range appears in region L and R. This appearance is a result of dissociative water adsorption, describing the interaction between surface hydroxyl group and water oxygen. (3) The first $g_{OO}$ peak and the second $g_{HH}$ peak are also shifted to lower values of $r$ by 0.15 Å and 0.2 Å, respectively. This observation can be seen as a consequence of the shorter hydrogen bond, which draws water molecules in the first solvation shell closer.

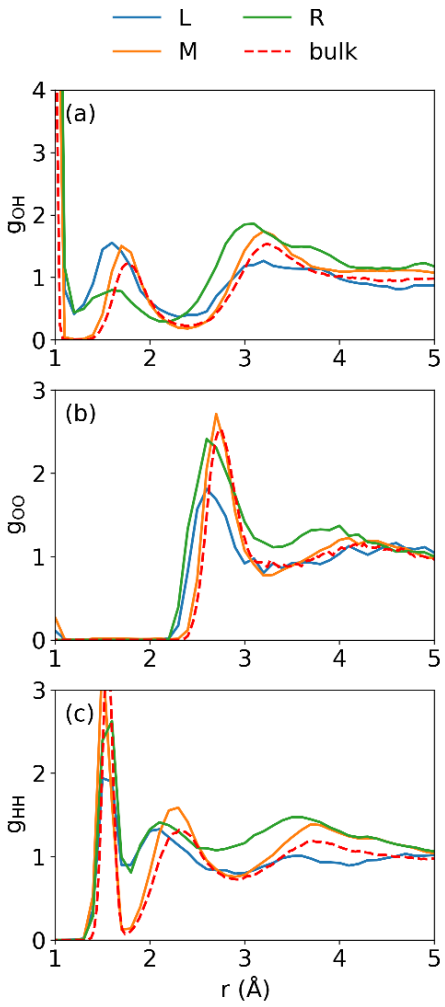


Figure 6-5. Radial distribution functions for bulk water (red dashed line) and water interfacing with $ZrO_2$ (solid lines).

Knowing the interfacial water structure, in Figure 6-6 we further analyze the solvation shell of hydronium ion $H_3O^+$. The oxygen bonded with excess hydrogen is annotated as $O^*$ and the excess hydrogen as $H^*$. For hydronium ion in bulk, the three protons are equivalent to a first approximation and all form hydrogen bonds with $H_2O$ molecule [208]. Due to the ionic nature of $H_3O^+$, the first-peak $O^*O$ distance (2.5 Å) is shorter than OO distance in pure water (2.8 Å). In Figure 6-6(a), we see that this first $O^*O$ peak is suppressed and slightly lengthened by 0.1 Å in L and R region, which reverses the trend in interfacial OO radial distribution (first peak shortened). This phenomenon can be explained by looking at $g_{O^*H}$ and $g_{H^*O}$ in *Figure 6-6* (b) and (c). We observe that for hydronium ion in bulk water, $O^*$ differs from O in that it is not a proton acceptor and

cannot form hydrogen bond with surrounding hydrogen atoms. The second OH peak at $r_{OH}$ = 1.4 – 2.2 Å, which represents hydrogen bond, disappears for $O^*H$. Instead, the three hydrogens in $H_3O^+$ all bond with $O^*$ with bond length 0.9 – 1.5 Å. However, at the interface, as shown in Figure 6-6(b), the peak at 1.5 Å reappears, now representing the bond between $O^*$ and $H^*$. This is also reflected in $g_{H^*O}$ plot (*Figure 6-6*(c)) where we see the first sharp $H^*O$ peak at initiating at 1.3 Å disappears for region L and R. In all, this indicates the broken symmetry of $H^*$ and the two other hydrogen atoms. Because of the bonding between $H^*$ and surface oxygen $O_s$, $O^*H^*$ interaction is significantly weakened. $H^*$ is driven further away from $O^*$ (*Figure 6-6* (b) (c)), and subsequently, driven way from the other hydrogen atoms within the hydronium ion (Figure 6-6 (d)).

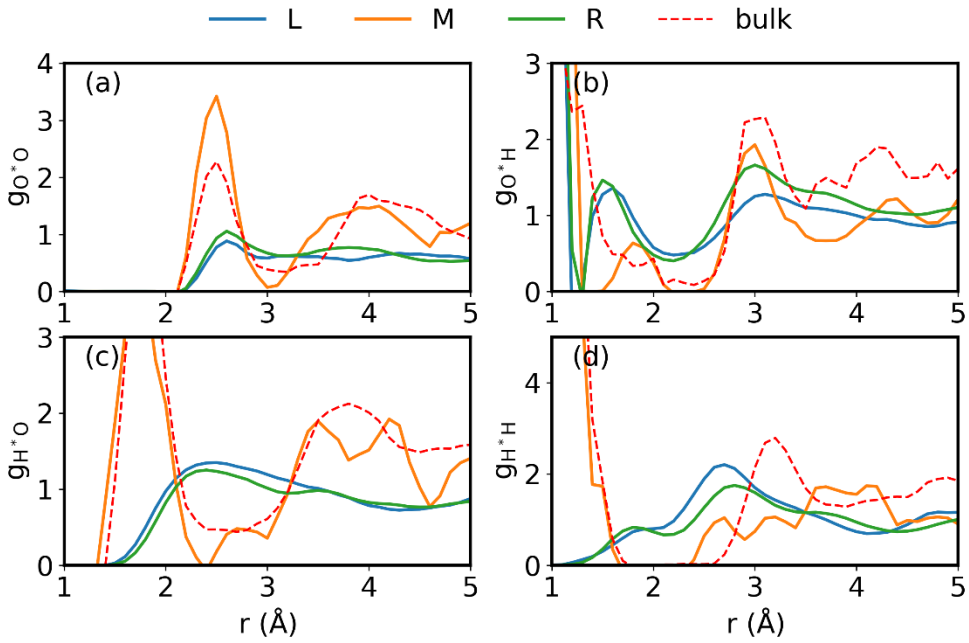


Figure 6-6. Spatially-resolved radial distribution functions of hydronium ion (a) $O^*$-O, (b) $O^*$-H, (c) $H^*$-O and (d) $H^*$-H. $O^*$ represents the oxygen atom that is bonded with the extra proton. $H^*$ represents the hydrogen atom that is furthest to $O^*$ out of the three hydrogen atoms in $H_3O^+$.

As a summary for all structural effect of $ZrO_2$ surface presented in this section, we summarize the atomic structure and bond length information schematically in Figure 6-7. We observe that due to surface Zr-O and $O_s$-H bonding, geometrically, water molecule is

flattened by the surface with one O-H bond lying parallel to the surface. This bonding angle preference at the interface also leads to alternating hydrogen-rich and oxygen-rich layers. Meanwhile, Zr-O bonding increases the ionicity of oxygen, shortening hydrogen bond length between oxygen atom in water molecule and the neighboring hydrogen donor. Surface dissociative adsorption gives rise to O-H bond lengths between 1.1 – 1.4 Å, which belong neither to intramolecular O-H bond nor intermolecular hydrogen bond. In the case of hydronium ion, surface effect breaks the symmetry of the three hydrogen atoms. $H^*$ is strongly bonded to surface oxygen and thus the bond length of $O^*$-$H^*$ is observably longer than the bonds between $O^*$ and the other two hydrogen atoms. However, due to the increased ionicity of $O^*$, the interfacial hydronium ion is in all more closely bonded comparing to bulk hydronium ion. The distinct interfacial water structure changes its dynamics drastically, as will be discussed in Sec IIIB.

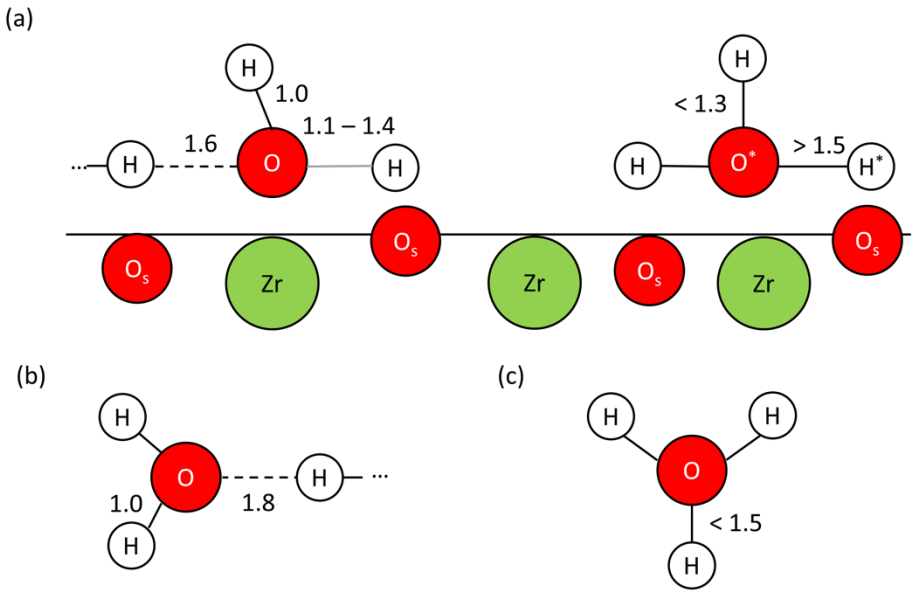


Figure 6-7. Schematic plot for atomic configuration and bond lengths for (a) water molecule and hydronium ion at $ZrO_2$ surface, (b) water molecule in bulk water, (c) hydronium ion in bulk water. Hydrogen bonds are presented by dashed lines. Black solid lines represent intramolecular bonds and black dashed line represent intermolecular hydrogen bonds. In (a) we see O-H bond length between 1.1 – 1.4 Å on the surface which does not belong to either of the two types and represented by a grey solid line.

B. Proton dynamics at $ZrO_2$/water interface

In this section, we quantitatively demonstrate surface effect on proton transfer dynamics by calculating the free energy landscapes of proton hopping between two oxygen atoms at different distances towards $ZrO_2$ surface. By identify the two nearest neighbor oxygen atoms $O_1$ and $O_2$ for one hydrogen atom H, we can define the proton hopping reaction coordinate $\delta = R_{O_1\text{-}H} - R_{O_2\text{-}H}$, where $R_{O_1\text{-}H}$ and $R_{O_2\text{-}H}$ are the distances between $O_1$ and $O_2$ to H. $\delta$ = 0 represents that the hydrogen atom is shared by the two oxygen atoms, i.e. in the middle of the proton exchange process. We construct a two-dimensional free energy landscape of the proton hopping reaction by calculating $\Delta G = -k_B T \log P(R_{O\text{-}O}, \delta)$, where $P$ is the probability distribution of $O_1$-H-$O_2$ complexes with respect to $\delta$ and oxygen-oxygen distance $R_{O\text{-}O}$. The resulted free energy maps can provide both energetics and atomic configurations of the proton hopping process.

Proton hopping free energy landscapes in region L, M and R and in bulk water as comparison are shown in Figure 6-8. We observe that the energy map in the middle region is both qualitatively and quantitatively very similar to that in bulk water. The energy minima locate within $R_{O\text{-}O}$ range of 2.7 - 2.8 Å, which is consistent with the first $g_{OO}$ peak as shown in Figure 6-5 (b). We can also tell that for the proton exchange reaction to happen in bulk water, the distance between $O_1$ and $O_2$ should be below 2.6 Å. The minimum energy path yields a hopping barrier of about 150 meV in bulk as well in region M, which is consistent with previous studies [211, 212].

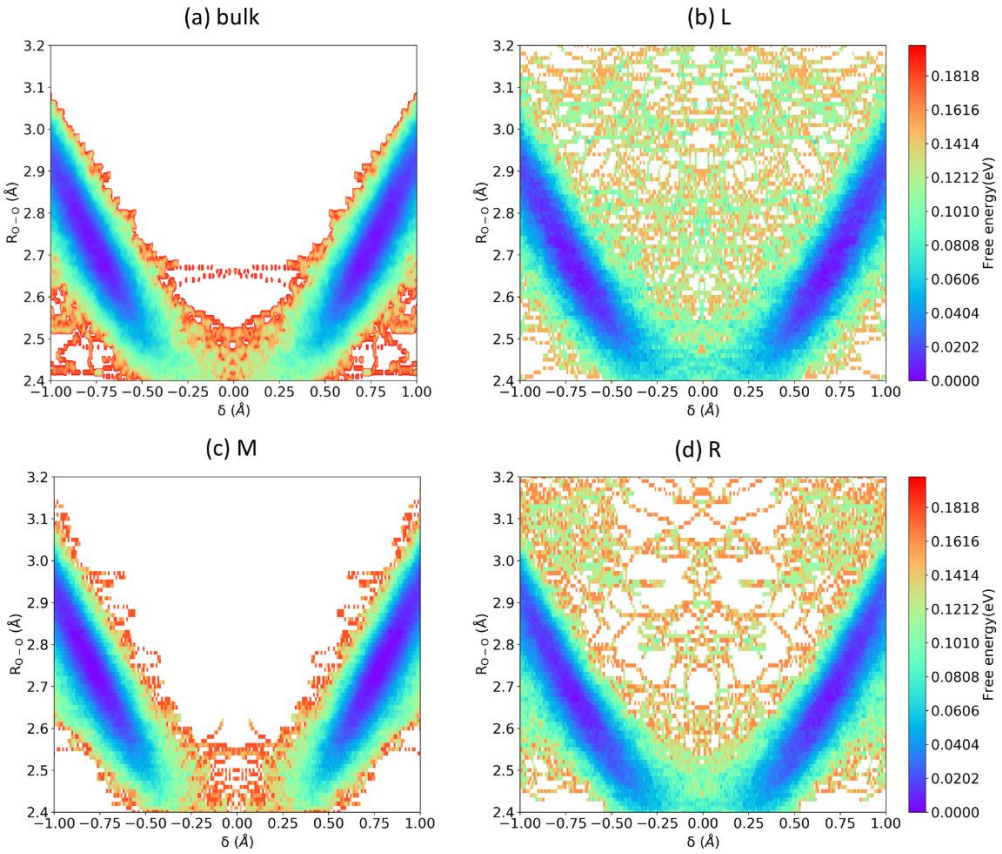


Figure 6-8. Calculated free energy landscapes of proton hopping process (a) in bulk water, (b) (c) (d) in L, M and R regions at $ZrO_2$/water interface respectively. For each region, the zero point of free energy is referenced to the minimum value within the region. White-colored regions represent configurations that have zero probability.

Now we look at region L and R, which are significantly influenced by surface effect. The saddle point free energy ($\delta$ = 0, $R_{O\text{-}O}$ 2.4 – 2.5 Å) is notably lowered at the interface. Hopping barrier is reduced to about 80 meV, which corresponds to a ten-times-faster reaction rate at room temperature. We also observe that are a large area in the middle of the energy map ($\delta$ -0.25 – 0.25 Å, $R_{O\text{-}O}$ > 2.6 Å), which previously has zero probability in bulk, now becomes possible proton hopping route. This observation is a direct result of hydrogen bonding to surface oxygen $O_s$, as confirmed by the results in *Figure 6-9*. We show the same free energy landscape of proton hopping between surface oxygen $O_s$ and oxygen in water. Here the shape of the probability distribution is closer to that in bulk, where O-O distance has to be under 2.6 Å for the exchange reaction to happen. This

surface-oxygen-assisted hopping process allows for more flexible O-O configuration and also shows a low barrier of about 80 meV.

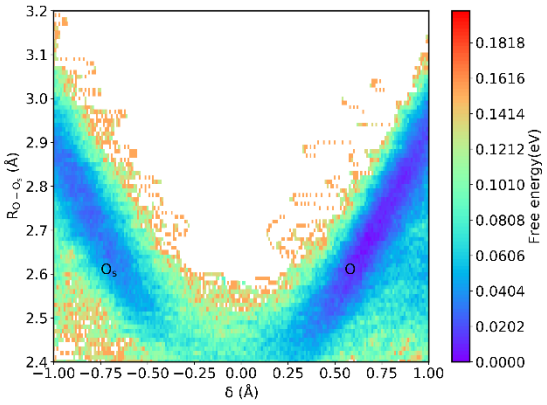


Figure 6-9. Calculated free energy landscape of proton hopping between surface oxygen ($O_s$) and water oxygen (O).

From the above analysis we can conclude that proton hopping happens about ten times faster in the interfacial zone, which can be linked back to the structural effect in Sec IIIA. First, interfacial water structure features a more close-packed hydrogen bond network. The distinction between intramolecular O-H bond and intermolecular hydrogen bond is not as sharp as in bulk water due to the appearance of surface hydroxyl bond (ranging from 1.1 – 1.4 Å). Intermolecular hydrogen bond is also shortened comparing to bulk water. Because of these two factors, hydrogen from the proton donor water molecule is more likely to hop towards the oxygen to which it is hydrogen bonded. This leads to the lowered hopping barrier in region L and R. Second, we have shown that hydrogen in the first layer in the vicinity of $ZrO_2$ surface is strongly bonded with surface oxygen. This allows for the surface assisted hopping mechanism in Figure 6-9 as the dissociatively adsorbed hydrogen hops between surface oxygen and water oxygen.

C. Thermodynamics of hydronium and hydroxyl ions at $ZrO_2$/water interface

In this section, we investigate the thermodynamics of hydronium ions and hydroxide ions at $ZrO_2$/water interface by sampling their probability distribution as a function of *z*.

Following the same free energy formation $\Delta G = -k_B T \log P(z)$, we can obtain the solvation free energy profiles at different positions towards $ZrO_2$ surface for both ions as shown in Figure 6-10. Both curves display symmetric features as required by the equivalence of the two surfaces in the simulation cell, which is an evidence of sufficient sampling. We observe that hydronium ion profile exhibits a minimum followed by a maximum within 3 Å in the vicinity of the surface, followed by another energy minimum at about 5 Å. Similar behavior has been shown previously for metal ion approaching calcite surface [225]. It mainly results from the electrostatic interaction between the positively charged ion and the water structure forming the solvation shell. The first energy minimum originates from the distorted solvation shell of hydronium ion close to the surface. In the interfacial zone where hydrogen network is more compact, the distinction between covalent O-H bond and hydrogen bond is blurred and the barrier for oxygen to obtain an excess proton is lowered. The second energy minimum originates from the electrostatic potential built up by the alternating hydrogen-rich (positively charged) and oxygen-rich (negatively charged) layers. Due to the alternating nature of the density profile close to the surface, $G(H_3O^+)$ profile also displays multiple minima and maxima.

For hydroxide ions, we observe a relatively wide free energy well within 5 Å of the surface. The widening of the energy well indicates that the point charge model for hydronium ion and metal ions does not apply to hydroxide ions. Due to its diatomic structure, its electrostatic interaction with the background water molecule solvent is more complex. By analyzing the bond angle, we observe that O-H bonds are polarized to pointing away from the surface within 5 Å in *z*, which correlates with the width of the energy well.

We observe that there exists a thermodynamic well of 0.2 eV for hydronium ions to be trapped within 1-2 Å from $ZrO_2$ surface, which coincide with the length scale of Stern layer of the electric double layer theory [226]. Combining the thermodynamic profile with the density information, we can conclude that a Stern layer crowded with excess proton is expected at $ZrO_2$/water interface. Such quantification allows for further numerical modeling of hydrogen evolution reaction at the surface and hydrogen entering zirconium oxide.

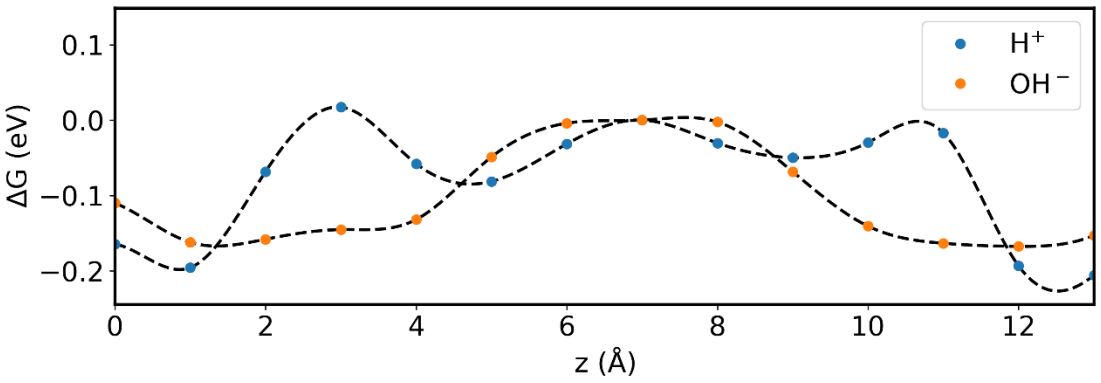


Figure 6-10. Solvation free energy profiles of hydronium ion and hydroxide ion as a function of their positions towards $ZrO_2$ surface.

## 6.4 Conclusion

In this work, we systematically studied the structural, kinetical and thermodynamical effect of $ZrO_2$ surface on water via *ab initio* molecular dynamic calculations. The spatially-resolved analysis clearly reveals links between hydrogen bond network, proton hopping dynamics and solvation thermodynamics. We discover that due to surface $O_s$-H bonding and Zr-O bonding, interfacial water appears to be more close-packed and displays an ordered structure with alternating hydrogen-rich and oxygen-rich layers within 5 Å from the surface. This condensation is accompanied by shortened hydrogen bond and shortened OH covalent bond within hydronium ions. The structural distortion lowers the barrier of proton exchange reaction by half and allows for surface-assisted proton hopping to happen. Solvation free energy profiles of hydronium ions also indicate a connection between structural effect and thermodynamic properties, giving adsorption free energy of 0.20 eV. The results here provide mechanistic and quantitative understanding of proton dynamics and thermodynamics at $ZrO_2$/interface, which could guide further engineering of oxide surface towards desired water-oxide interactions.

# 7 First-principles based quantification of charged species redistribution at electrochemical interfaces: Model system of zirconium oxide

Modeling the local distribution of charged ions and ionic defects at oxide/liquid solution interface is key to understanding related electrochemical processes, such as corrosion, hydrogen evolution, and oxygen reduction or evolution reactions. Based on the grand canonical approach which defines the electrochemical potential of individual charged species, a unified treatment of defects on the solid side and ions on water side can be established. This approach is compatible with first-principles calculations where the formation free energy of individual charged species can be calculated. In this chapter, we apply this framework to the system of $ZrO_2$/water interface, which is important in a wide range of applications including catalysis, biomaterials, and corrosion. Defect formation energy in $ZrO_2$ and the adsorption free energy of $H^+$ and $OH^-$ ions in water at $ZrO_2$ surface calculated by first-principle methods are fed into a continuum model which produces the equilibrated distribution of these charged species. The continuum model considers explicitly the ion adsorption in the vicinity of the interface, and the diffuse layer and space charge layer in the extended area. Such a unified description reveals the influence of solution chemistry on oxide defect chemistry, and vice versa. We benchmarked this model by comparing predicted $ZrO_2$ solubility and point of zero charge with experimentally-measured values, which yielded great consistency. Our results show that $ZrO_2$ surface immersed in water is negatively charged with hydrogen substitutional defects. This framework based on the grand canonical approach allows easy inclusion of additional charged species into the system. The structure, defect chemistry and dynamical behaviors of the electric double layer and space charge layer are carefully analyzed with different pH, water chemistry and doping elements in zirconium oxide, which serves as the basis for modeling reaction and transport kinetics under these effects.

## 7.1 Introduction

Point defect redistribution in space charge layer at oxide surfaces, interfaces, grain boundaries and dislocations has been shown to alter the magnetic, electronic, and transport properties of metal oxides [4, 179, 227-231]. The formation of electric double

layer at an electrode/electrolyte interface has also been demonstrated for influencing electrokinetics of such interfaces, which is important for engineering interfacial capacitance [232-234] and catalytic activity [235-237]. Both factors come into play at an electrochemical interface, which poses significant challenge to the field of first-principles computational electrochemistry in terms of both accurately evaluating the interplay between interfacial charged species atomistically and validating such results with macroscopically-measurable values [238]. In recent studies there has been a great momentum both in applying novel first-principle based methods to solid/liquid interface [239-241], and in establishing thermodynamic framework that links atomistic-level simulations with macroscopic properties [217, 242-244]. So far such first-principles based thermodynamic framework has demonstrated the capability of predicting electrochemical phase diagrams under variable potential and pH [245-247]. However, constructing a spatially-resolved charged species redistribution profile across an electrochemical interface including full description of oxide defect chemistry has not been addressed by first-principle based methods.

In this work, we extend the established first-principle based framework for modeling defect redistribution across oxide hetero-interfaces (Ref. [91] and the refences therein) to oxide/water interface. This extension is made possible by recognizing the similarity between space charge layer structure in oxide materials and electric double layer structure in liquid solution, as shown in

Figure 7-1. At an oxide surface/interface, we consider a core layer, where charged defects have non-zero segregation energies due to structural relaxation, and a space charge layer, where defects redistribute through the mechanism of drift-diffusion (

Figure 7-1(a)). For electric double layer, the Stern-Gouy-Chapman model [248] defines a surface adsorption layer, or Stern layer, where ions adsorb specifically to the solid surface, and a diffuse layer, where ions redistribute under electrostatic forces and chemical gradient (

Figure 7-1(b)). In both cases, the space is separated into an interfacial layer with local segregation/adsorption and an extended redistribution region governed by drift-diffusion model [179]. Combining this insight with the unified grand canonical description of charged defects in solids and ion species in water solution [217], we are able to model an

oxide/water interface in a same way as oxide/oxide interface, as schematically demonstrated in

Figure 7-1(c).

In the following sections, we first give a comprehensive introduction of the first-principle based framework for modeling charged species redistribution across an electrochemical interface. We demonstrate the capability of this model on the monoclinic-$ZrO_2$/water interface system, which is of interest in the context of zirconium alloy corrosion in nuclear water reactors [51] and degradation of bio-compatible $ZrO_2$ [219]. In both cases, the kinetics of oxygen and hydrogen incorporation into $ZrO_2$ matrix is the key property to engineer. We first studied the change in water chemistry and interfacial electrostatic profiles with changing water pH. These results are validated by comparing predicted $ZrO_2$ solubility and point of zero charge (PZC) with experimentally-measured values and great consistency is achieved. We also applied this model to $ZrO_2$ with different dopants aiming at providing doping strategies that minimize oxygen and hydrogen incorporation. The results revealed an intrinsic trade-off between desired bulk defect chemistry and space charge chemistry. While doping with 5+ dopants could decrease the concentration of positively-charged hydrogen interstitials in bulk $ZrO_2$, it also increases the local hydrogen concentration interfacial zone. On the other hand, doping with 3+ dopants depletes hydrogen in the space charge layer, meanwhile increases hydrogen interstitial concentration in bulk. These results demonstrate a complex interplay between bulk defect chemistry and interfacial effect at an electrochemical interface and manifest the value of such unified model which links point defect chemistry with electrochemical properties.

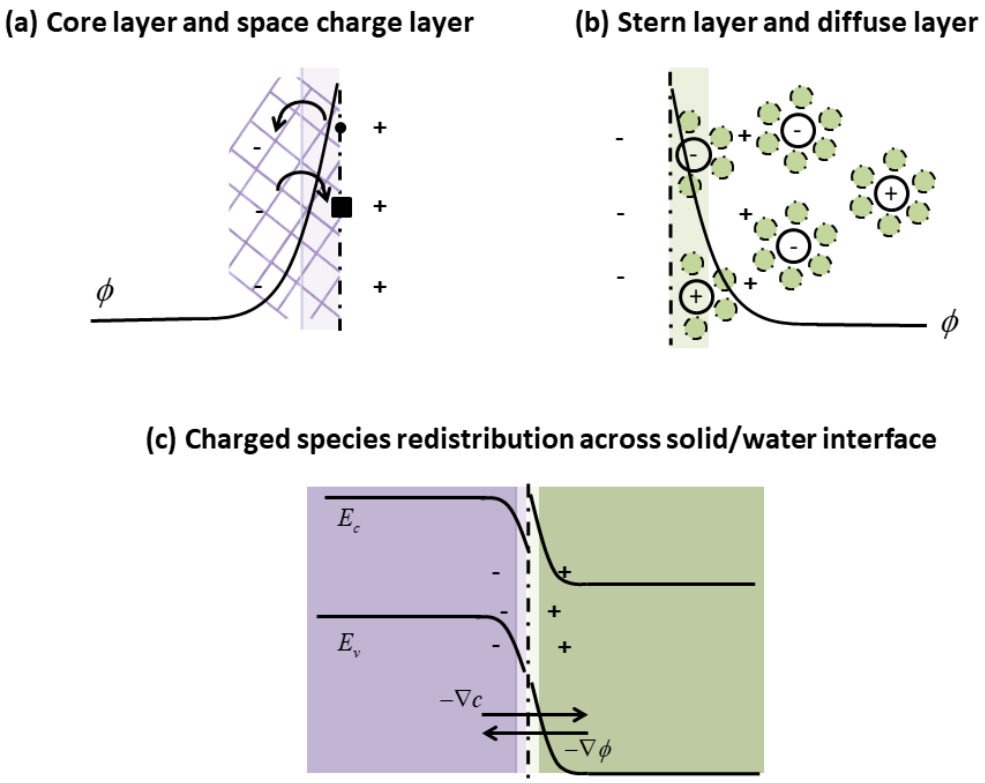


Figure 7-1. Schematics of (a) core and space charge layer at a solid surface/interface, (b) Stern layer and diffuse layer in liquid solution in contact with solid surface, and (c) the unifying picture of charged species redistribution across solid/water interface, where core layer is analogous to Stern layer, and space charge layer to diffuse layer. By incorporating the grand canonical description of ion species in water, the framework for solid/solid interface [91] is extended to solid/water interface.

## 7.2 Methods

In this section we provide a detailed method description for linking water chemistry with point defect chemistry and self-consistently predict the redistribution profiles. First, we briefly review how to predict bulk defect equilibria in bulk oxide material. Second, we discuss how to predict water chemistry in equilibrium with dissolved oxide and validate our prediction by comparing to experimental observations. Last, we present the formulism of continuum level modeling of space charge layer and electric double layer in a self-consistent way.

DFT calculations involved in this work were performed with Vienna Ab initio Simulation Package (VASP). [85-88] Generalized gradient approximation (GGA) with Perdew-Burke-Ernzerhof (PBE) functional is used throughout. [89, 90] We used pseudopotentials constructed using the projector augmented wave method which treat $4s^2 4p^6 4d^2 5s^2$ electrons for zirconium and $2s^2 2p^4$ for oxygen as valence electrons. The plane-wave cutoff energy was set to 450eV. Details of obtaining defect chemistry of m-$ZrO_2$ with metal dopants and hydrogen defects can be found in [116]. Details of establishing continuum-level modeling framework in oxide/oxide interface systems can be found in [91].

A. Predicting Bulk defect chemistry of $ZrO_2$

Predicting bulk defect equilibria of $ZrO_2$ from first-principles has been well-established [84, 116] and validated [115, 249]. Here we briefly describe the grand canonical framework [14] and will draw the analogy between point defects in solid and ions in water [217] in the next section. To predict point defect equilibria from first-principles calculation, we define the formation energy of each charged defect $D^q$ with

$$E_{D^q}^f = E_{defective}^{DFT} - E_{perfect}^{DFT} - \sum_i \Delta N_i \mu_i + q(E_{VBM} + \mu_e) + E_{MP} \tag{7.1}$$

Here $E_{\text{defective}}^{\text{DFT}}$ and $E_{\text{perfect}}^{\text{DFT}}$ represent the DFT-calculated energy for defective cell and perfect cell, respectively. $\mu_i$ is the chemical potential for each chemical species in the system and $\Delta N_i$ is the relative number of atoms for element *i* with respect to the perfect cell. For example, $\Delta N_O = -1$ for oxygen vacancy. $E_{VBM}$ denotes the valence band maximum and $\mu_e$ is the Fermi level referenced to $E_{VBM}$. $E_{MP}$ is the first-order Makov-Payne correction [15] for the finite-size supercell errors in charged defect calculations.

In the context of doped $ZrO_2$ immersed in water solution, we define the chemical potential of each element as follows. The chemical potential of oxygen is determined by oxygen partial pressure $P_{O_2}$ and temperature *T*.

$$\mu_O(T, P_{O_2}) = \frac{1}{2}\left[ E_{DFT}^{O_2} + E_{over} + \mu_{O_2}^0(T, P^0) + k_B T \ln\left(\frac{P_{O_2}}{P^0}\right)\right] \tag{7.2}$$

Here $E_{\text{DFT}}^{O_2}$ is the energy of oxygen molecule calculated by DFT. $E_{over}$ is the correction term for oxygen overbinding created by semilocal functionals [172]. With the parameters

used in this work, $E_{over}$ equals 1.12 eV [77]. $\mu^0_{O_2}(T, P^0)$ represents the tabulated free energy of oxygen gas at reference pressure $P^0 = 0.1$ MPa reference to 0 K. $k_B$ is the Boltzmann constant. With $\mu_O$ defined, $\mu_{Zr}$ and $\mu_H$ can be defined as follows.

$$\mu_{Zr}(T, P_{O_2}) = E_{DFT}^{ZrO_2} - 2\mu_O(T, P_{O_2}) \tag{7.3}$$

$$\mu_H(T, P_{O_2}) = \frac{1}{2}\left[E_{DFT}^{H_2O} + \mu^0_{H_2O}(T, P^0) - \mu_O(T, P_{O_2})\right] \tag{7.4}$$

$E_{DFT}^{ZrO_2}$ and $E_{DFT}^{H_2O}$ represent the DFT calculated energy for one unit formula of $ZrO_2$ and one water molecule respectively. $\mu^0_{H_2O}(T, P^0)$ is the reference free energy of liquid water. Noticing that this term should also be included in the formulism for $\mu_{Zr}$. However, the free energy change of solids with temperature and pressure is negligible comparing to liquid or gas and therefore excluded in this work.

When dealing with doped $ZrO_2$, the dopant element M is included as a fourth element. Here we consider that the dopant could either form interstitial defect $M_i$ or substitutional defect $M_{Zr}$. We use a fixed concentration scheme for treating extrinsic doping, where $\mu_M$ is tuned to satisfy the desired doping level given the chemical potential of all other elements.

Now the only undetermined term in Eq. (7.1) is the electron Fermi level $\mu_e$. This term is solved from the total charge neutrality constraint

$$\sum_{D,q} q[D^q] + [h] - [e] = 0 \tag{7.5}$$

Here we are summing over all charged defects and adding the charge of free electrons $[e]$ and holes $[h]$. In this work, $[D^q]$ is expressed by

$$[D^q] = n_D \frac{\exp\left(-\frac{E^f_{D^q}}{k_B T}\right)}{1 + \sum_{q'} \exp\left(-\frac{E^f_{D^{q'}}}{k_B T}\right)} \tag{7.6}$$

where $n_D$ is the number of possible sites for the defect to reside per unit formula. In the denominator we are summing over all defect species that could take the same site with $D^q$. This expression is derived from minimizing total free energy of the system and the denominator arises because of the form of configurational entropy [8].

$[e]$ and $[h]$ can also be expressed as a function of $\mu_e$ as follows:

$$[e] = \int_{E_{CBM}}^{\infty} g(E) \frac{dE}{1 + \exp\left(\frac{E - \mu_e}{k_B T}\right)} \tag{7.7}$$

$$[h] = \int_{-\infty}^{E_{VBM}} g(E) \frac{dE}{1 + \exp\left(\frac{\mu_e - E}{k_B T}\right)} \tag{7.8}$$

Here $g(E)$ is the electronic density of states (DOS) calculated by DFT. $E_{CBM}$ is the conduction band minimum.

B. Quantifying ion concentration in water

The idea of treating liquid water as large-band-gap amorphous semiconductor dates back to the 1970s and is widely acknowledged [30]. Numerous attempts, both experimental and computational, have been made to measure the absolute energy positions for liquid water [31-33]. One commonly accepted value is from Coe[34] with electron affinity of -0.12 eV and band gap of 7.0 eV. With this description, ions in liquid water could be treated in similar ways as charged point defects in solids, which serves as a bridge between electrochemistry and semiconductor physics [35]. We arrive at an expression for Gibbs free energies of ion which is very similar to Eq. (7.1):

$$\Delta G_{D^q}^{f,bulk} = \Delta G_{D^q}^{f,0}(T) - \sum_i \Delta N_i \mu_i + q\mu_e \tag{7.9}$$

Here $\Delta G_{D^q}^{f,0}$ is the standard Gibbs free energy of formation at temperature $T$, which is well-tabulated for common ion species [250]. We should notice that the numerical values of $\mu_i$ are different in water and in solid. Previously because we are dealing with DFT-calculated values for defect formation energies, $\mu_i$ are referenced to 0 K condition. In Eq. (7.9), $\mu_i$ are referenced to standard condition. A detailed formulism of how $\mu_H$ and $\mu_O$ are calculated with varying potential and pH can be found in Ref. [217]. In this paper, we use the oxygen-rich condition as in [217] where the chemical potential of oxygen atom is calculated from oxygen molecules. In other word, $\mu_O = 0$ ($T°$ = 298.15 K, $p_{O_2}°$ = 1 bar). At this condition, the Fermi level of water lies at -5.5 eV at pH = 7. The corresponding $\mu_H$ is calculated by $\mu_H = [\Delta G°(H_2O) - \mu_O]/2$.

Analogous to extrinsic doping in semiconducting solids, we can also tune water chemistry with intentional additives. In this study we considered water chemistry with

varying pH, which is achieved by adding fictitious $A^+$ or $B^-$ ions into the system. This representation could correspond to any base or acid given that they do not react actively with $ZrO_2$.

With this formulation, the grand canonical approach described previously could also account for equilibrium ion concentration in water solution. We can solve for $\mu_e$ under the constraint of total ion charge neutrality as in Eq. (7.5) (7.6). In the case of water, electron and hole concentrations are set to zero. The advantage of this approach comparing to considering dissociation reaction equilibrium is that it is much easier to include multiple ions into the system, as long as their standard formation energies are known. We will demonstrate the power of this scheme with the case of $ZrO_2$ dissolved in water solution.

In this work all results presented are at room temperature for benchmarking $ZrO_2$ solubility data and point of zero charge. However, this solution scheme is transferrable to elevated temperature case given that ion formation free energy data are available.

C. Continuum level modeling of space charge layer and electric double layer

By making the analogy between ions in water solution and defects in solid, we can now unify the concepts of electrical double layer and space-charge zone. Immediately, previously defined in the vicinity of the interface is equivalent to the adsorption energy of ions attached to solid surface. The core zone at solid-solid interface corresponds to the compact layer (or Stern layer) in electrical double layer. The advantage of this generalization is that the previously established modeling scheme for solid-solid interface [91] can now be easily applied to solid-water interface, and serves as the basis of our universal treatment framework. In this section, we brief review the continuum level modeling process to obtain profiles of space-charge layer and electric double layer.

The formation free energies of charged species in bulk as in Eq. (7.1)(7.9) can to extended to interface by adding the electrostatic potential term and segregation energy (adsorption energy) term.

$$E^f_{D^q}(z) = E^{f,bulk}_{D^q} - q\Delta\phi + E^{seg}_{D^q} \tag{7.10}$$

$$\Delta G^f_{D^q}(z) = \Delta G^{f,bulk}_{D^q} - q\Delta\phi + E^{ads}_{D^q} \tag{7.11}$$

Here $z$ represents the one-dimensional axis perpendicular to the interface. $\Delta\phi = \phi(z) - \phi^{bulk}$ is the electrostatic potential difference between bulk and location $z$. In this work, we considered the adsorption free energy only for $H^+$ and $OH^-$ ions, which are the two dominating ion species in the related chemical environment. The adsorption free energies are 0.20 eV for $H^+$ and 0.15 eV for $OH^-$ as found in our previous work [251]. Defect segregation energy at $ZrO_2$ surface is neglected given that defect concentrations are much lower comparing to ion concentrations. Eq. (7.10)(7.11) can be plugged back into Eq. (7.6) and produces the local charge density ρ

$$\rho(z) = \sum_{D,q} q[D^q](z) + [h](z) - [e](z) \tag{7.12}$$

With these definitions, we can solve Poisson's equation that governs the electrostatic potential distribution.

$$\frac{d^2\phi(z)}{dz^2} = -\frac{\rho(z)}{\varepsilon\varepsilon_0} \tag{7.13}$$

$\varepsilon_0$ and $\varepsilon_r$ are the permittivity of vacuum and relative permittivity of the host material. Eq. (7.13) is solved with boundary condition

$$\left.\frac{d\phi}{dz}\right|_{z=0} = 0 \tag{7.14}$$

$$\left.\frac{d\phi}{dz}\right|_{z=L} = 0 \tag{7.15}$$

Here $z = 0$ and $L$ represents the two ends of the simulation cell, i.e. bulk oxide and bulk water. At the interface, a Dirichlet boundary condition $\phi = \phi_{boundary}$ is used, where $\phi_{boundary}$ is determined by the global charge neutrality constraint

$$\int_0^L \rho(z)dz = 0 \tag{7.16}$$

## 7.3 Results and discussion

In this section, we apply the described framework on the interface between doped-$ZrO_2$ and water. This system is of interest in the context of zirconium alloy corrosion in nuclear water reactors [48]. In particular, we look into oxygen and hydrogen incorporation in $ZrO_2$ passive film with varying pH and doping concentration. We divide this section into four parts. First, we show the predicted water chemistry with dissolved $ZrO_2$ at varying

pH values and benchmark the prediction with experimental measurements at room temperature. A good agreement is reached between the prediction and experimental measured $ZrO_2$ solubility. Second, we examine the electrostatic profiles across $ZrO_2$/water interface with changing pH. We compare the resulted point of zero charge with experimentally-measured values. Third, we discuss the implication of these results in the context of the kinetics of zirconium alloy corrosion by examining the effect of different alloying element on surface space charge. We conclude that by including surface space-charge effect, we can nicely explain the inverse relationship between hydrogen pickup fraction and oxidation kinetics [123] and the effect of different dopant elements. Last, we discuss the possible improvements and extensions of the current model.

A. Water chemistry with dissolved $ZrO_2$

Following the method described in Part IIB, we predict the equilibrium ion concentrations in water with dissolved $ZrO_2$. Here Zr-related species are not predicted by considering any specific dissolution reaction equilibrium, but by including their formation free energies following the grand-canonical representation. In Figure 7-2(a) we list the specific Zr-related species included in this work and plot their equilibrium concentrations with varying pH. Looking closely at water chemistry, the dominant ion species across the pH range are either HB or AOH, with $B^+$ and $A^-$ being the fictitious ion representing controlled additive. With negligible additives ($< 10^{-7}$ mol/L), water remains a pH of 7. The value of this model is the concentration profile of Zr-related ion species as a function of pH. In the intermediate pH range (2 - 13), $ZrO_2$ does not dissolve significantly into water and the dominant dissolution species is $Zr(OH)_4$. In the strong acidic regime, we observe a rise of solubility in the form of $Zr^{4+}$ and in the strong alkali regime a rise of $Zr(OH)_6^{2-}$.

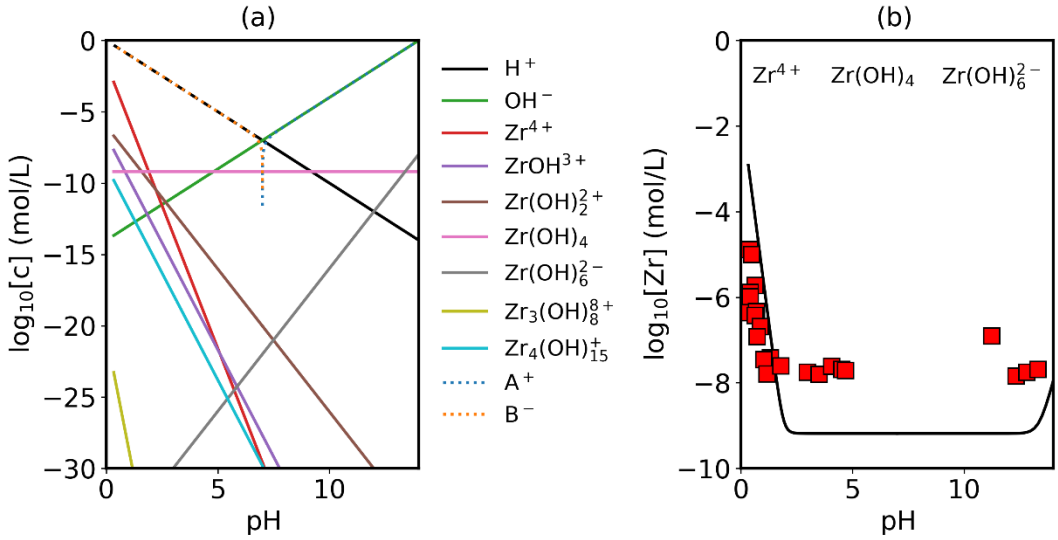


Figure 7-2. (a) Predicted water chemistry in equilibrium with $ZrO_2$ as a function of pH at room temperature. pH controlling is realized by adding fictitious $A^+$ or $B^-$ ions into the system. (b) Calculated zirconium solubility in water as a function of pH (black line) in comparison with experimental measurements (red squares) [252]. Transition in the slope of the curve corresponds to change in dominant Zr-related species in water going from $Zr^{4+}$ (acid condition) to $Zr(OH)_4$ (neutral condition) to $Zr(OH)6^{2-}$ (alkali condition).

Adding up the concentrations of Zr-related species in Figure 7-2(a), we arrive at Figure 7-2(b) which predicts zirconium solubility in water as a function of pH. We compare our prediction with experimentally measured values [252]. It should be noted that the detection limit of experiment cited here is about $10^{-8}$ M and measured points around this value are likely to be over-estimating the solubility. Our key observation is that the predicted transition point in the acidic regime where $ZrO_2$ begins to dissolve significantly matches well with experiment. In this regime our predicted solubility also reaches quantitative agreement comparing to experimentally-measured values. This predictive model is useful for low-solubility material system where it takes months to reach equilibrium state and hard to get accurate measurement experimentally. In addition, it provides insight into the concentration of each dissolution product. With this validation of water chemistry with dissolved $ZrO_2$, we can further combine this information with bulk defect chemistry of $ZrO_2$ (details in [116]) and observe the redistribution of these charged species, which are discussed in remaining of this section.

B. Electrostatic profile across $ZrO_2$/water interface with changing pH

In this section we closely examine the resulted electrostatic profile across $ZrO_2$/water interface and look at how the profiles change with pH. A closely related validation criterion here is the predicted point of zero charge, the pH level at which total charge density on surface reaches zero. In Figure 7-3, we first look at the redistribution profiles in water solution with pH = 7. We observe that there is a potential built-up of 0.7 eV across the interface, accompanied by enrichment of negatively charged defects on $ZrO_2$ side and positively charge ions ($H^+$) on water side. This is also reflected in Figure 7-5 (c), where we observe negative charge built up in $ZrO_2$ and positive charge built up in water. In Stern layer, the built-up effect is more significantly given the higher adsorption energy of $H^+$ comparing to $OH^-$. In this case of pH-neutral water, we observe a 8-order-of-magitude increase in $H^+$ concentration in Stern layer comparing to bulk water, which is consistent with previous ab initio molecular dynamics observation of favored instantaneous dissociative adsorption [251].

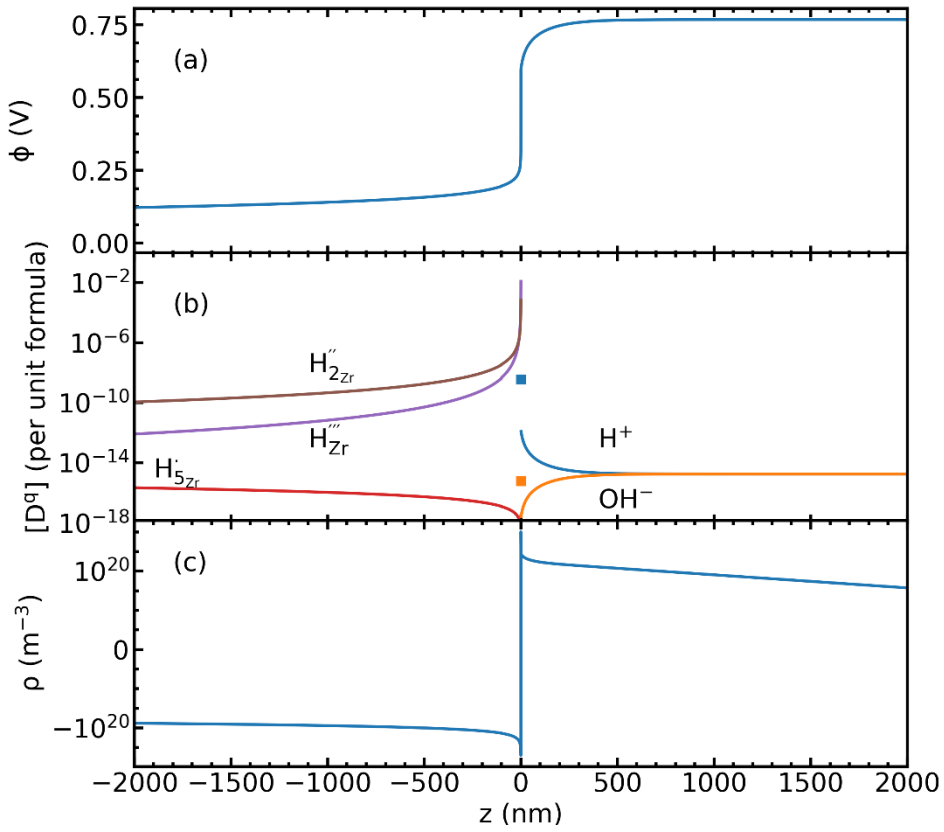


Figure 7-3. (a) Electrostatic potential $\phi$, (b) concentration of charged species, and (c) charge concentration $\rho$ across $ZrO_2$/water interface at pH = 7 oxygen-rich condition. The

interface is placed at z = 0 with the left side being $ZrO_2$ and the right side being water. $H^+$ and $OH^-$ concentrations in Stern layer are explicitly marked with squares.

At point of zero charge, there is no potential built-up in diffuse layer. In other words, segregated defects and specifically-adsorbed ions add up to a charge-neutral $ZrO_2$ surface. In Figure 7-4 (a) we show the electrostatic potential profile with varying pH value of the water solution. Changing pH influences the electrostatic profile in two ways. First, increasing pH corresponds to increasing Fermi level in water, and thus a larger potential difference on the two sides. This change is clearly demonstrated in Figure 7-4(a) if we compare $\phi$ in the bulk region of the two sides. Second and more importantly, varying pH changes the total charge in Stern layer. At lower pH and higher $H^+$ concentration, the magnitude of $H^+$ segregation is much greater comparing to $OH^-$ and therefore Stern layer could effectively screen the negative charge of $ZrO_2$. The combination of both effects leads to a flip of sign in $\Delta\phi_{\text{diffuse}}$ at pH = 4. The potential drop in diffuse layer as a function of water pH is plotted in Figure 7-4(b). At the point where $\Delta\phi_{\text{diffuse}} = 0$, the negative charge on $ZrO_2$ side is completely compensated by the positive charge in Stern layer and the surface is effectively charge neutral. In our model, this predicted PZC is at pH = 4.1.

Experimentally, reported values of PZC of $ZrO_2$ are somewhat scattered, ranging from 3.9 [253], 5.5 [254] , 6.5 [255], to 8.5 [256]. One possible explanation of the scattering is that the measured PZC changes with background electrolyte concentration [253]. It has been observed that when using $NaNO_3$ as background electrolyte, PZC of $ZrO_2$ increases with increasing $NaNO_3$ concentration, from 3.6 with 0.001 M $NaNO_3$ to 4.2 with 0.1 M $NaNO_3$. This indicates a favorable adsorption of $NO_3^-$ comparing to $Na^+$. In the modeling framework of our work, we assume no specific adsorption of the background electrolyte species other than electrostatic interaction, therefore we expect that the predicted value is lower than realistic values. Considering these evidences, we believe it is reasonable that the model predicted value falls in the lower range of the experimentally-measured values.

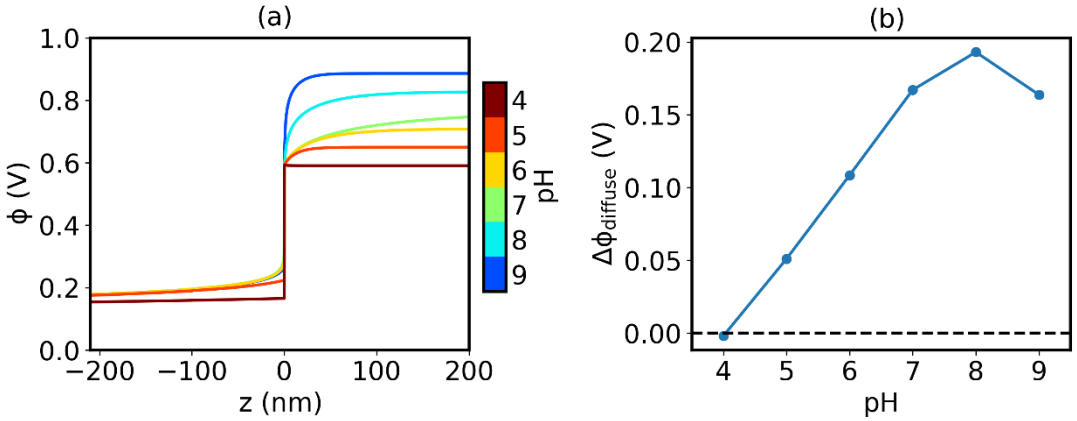


Figure 7-4. (a) Electrostatic potential profile with varying pH of water solution. (b) Potential drop in the diffuse layer $\Delta\phi_{diffuse}$ as a function of pH. The point where the potential drop reaches zero corresponds to PZC.

C. Effect of dopants and implication for zirconium alloy corrosion kinetics

One great strength of using grand canonical description of charged species is that it is very straightforward to add defect species into the model without enumerating all related defect reactions. To demonstrate this capability and to address the oxygen and hydrogen incorporation engineering problem, we applied this model to differently-doped $ZrO_2$ and examined the subsequent change in space charge layer profile. Four types of dopants are studied, Cr and Fe, which exist in a mixture of 3+, 4+ and 5+ valence state, Sn, is dominantly 4+, and Nb, which is dominantly 5+. In all four cases, we fix the bulk doping concentration to be 10 ppm, which is representative of realistic impurity concentration in $ZrO_2$ grown natively on zirconium alloy. [123] The resulted surface defect concentration profiles are shown in Figure 7-5.

In all cases, the surface remains negatively charged at pH = 7, meaning that negatively charged defect species accumulate in the space charge region while positively charged species deplete. In Sn-doped $ZrO_2$, since Sn exists dominantly in the form of $Sn_{Zr}^{\times}$, the dopant has little effect on either the bulk defect chemistry or the charge defect redistribution. The effect of aliovalent dopants is more complicated. In the case of Cr and Fe, we observe a mixture of $M_{Zr}^{\cdot}$ (5+ valence state), $M_{Zr}^{\times}$ (4+ valence state), and $M_{Zr}^{\prime}$ (3+ valence state). Chromium exists in $ZrO_2$ in approximately equal concentration of $Cr_{Zr}^{\times}$

and $Cr_{Zr}^{'}$, with a far lower contribution from $Cr_{Zr}^{\cdot}$. Iron exists dominantly in the form of $Fe_{Zr}^{\times}$, with less contribution from 3+ valence state comparing to chromium. In other words, despite that the dopant concentration is fixed to 10 ppm in bulk, Cr contributes more negatively charged doping species comparing to Fe. This is reflected in both the length and the potential of the space charge layer profile. Because Cr contributes effectively more charged defect concentration, the space charge layer length is significantly shortened. The magnitude of space charge effect follows a monotonically decreasing trend going from Cr to Nb. Cr and Fe decrease the Fermi level of $ZrO_2$ and therefore increases Fermi level difference between $ZrO_2$ and water. Reverse is true for Nb where only about 0.2 eV built-up potential is found on $ZrO_2$ side.

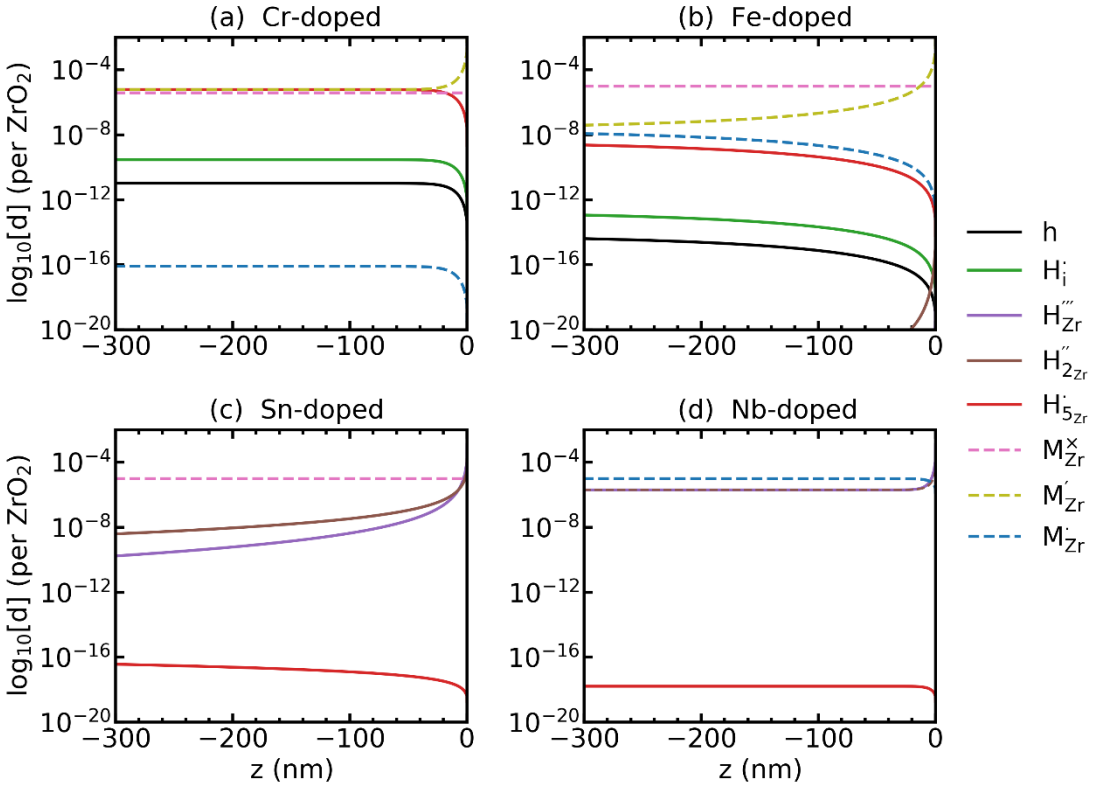


Figure 7-5. Defect redistribution in the space charge layer of doped-$ZrO_2$ in contact with water at standard hydrogen electrode condition. Various dopants are shown for comparison with (a) Cr-doped, (b) Fe-doped, (c) Sn-doped, and (d) Nb-doped. For each dopant, a fixed doping level of 10 ppm in bulk is considered.

To study the effect of these dopants on oxygen and hydrogen incorporation in $ZrO_2$, in Figure 7-6 we compare the concentration of related defect species in bulk (dashed line) and at surface (solid line) for differently-doped $ZrO_2$. In Figure 7-6 (a), we show the concentrations of $H_i^{\bullet}$ and $O_i^{''}$, which are representative of hydrogen and oxygen diffusion kinetics in $ZrO_2$. We observe a monotonic decrease in $H_i^{\bullet}$ and increase in $O_i^{''}$ going from acceptor dopants to donor dopants, which resulted from the corresponding increase in Fermi level. Similar trend is observed for electrons and holes (Figure 7-6(b)). Since the dominating electronic defect under this condition is always holes, 5+ dopants contribute to decreasing electronic conductivity. Figure 7-6 (c) shows the total hydrogen solubility in bulk $ZrO_2$ and local hydrogen solubility at the surface. In bulk we observe a valley shape curve as shown in our previous work. [116] On the left branch of the valley the dominant charge compensation mechanism is $M_{Zr}^{'}$ with positively charged hydrogen defects. On the right branch of the valley the dominant charge compensation mechanism is $M_{Zr}^{\bullet}$ with negatively charged hydrogen defects. Due to the sign change of dominant hydrogen defect species, the effect of surface space charge layer on local hydrogen concentration is reversed. For Cr- and Fe-doped $ZrO_2$, positively charged hydrogen defects are depleted in the space charge layer, leading to reduction in surface hydrogen concentration. For Nb-doped $ZrO_2$ the trend is reversed, and surface hydrogen concentration is increased. $H^+$ adsorption effect also follows a monotonic decreasing trend due to the decreasing magnitude of space charge effect going from Cr to Nb (Figure 7-6(d)). With varying dopant concentration, these conclusions remain qualitatively unchanged.

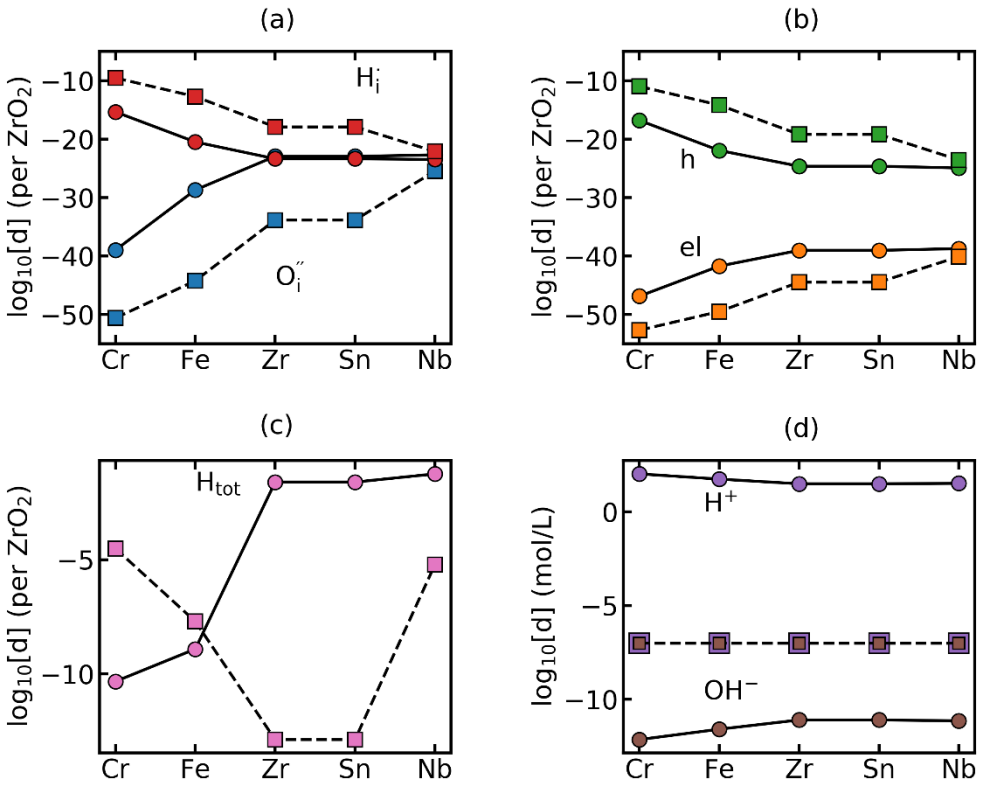


Figure 7-6. Comparison of surface (represented by solid line and circles) and bulk concentration (represented by dashed line and squares) of species related to oxygen and hydrogen incorporation in differently doped $ZrO_2$. (a) $H_i^{\bullet}$ and $O_i''$, (b) free electrons and holes, (c) total concentration of hydrogen, and (d) $H^+$ and $OH^-$ in bulk water and at surface. All calculations are done at pH = 7. Dopant concentrations are fixed to 10 ppm in bulk. Doping label Zr represents undoped $ZrO_2$.

The above analysis links to oxygen and hydrogen incorporation kinetics in $ZrO_2$. We predict that Nb decreases hydrogen diffusivity and increases free electron concentration, which reduces the amount of hydrogen incorporated into $ZrO_2$ matrix. This effect is accompanied by increased oxygen diffusivity. This observation is consistent with corrosion experiment where high oxidation rate and low hydrogen pickup rate is observed in Zr-Nb alloy comparing to pure zirconium and Nb-free zirconium alloy [123]. For zirconium alloys containing Fe, Cr, and Sn, the situation is more complicated because these dopants can exist both in dissolved form and in precipitates. Experimental evidence has shown that these elements influence degradation rate through coupled chemical and

mechanical mechanism [127, 257]. The space-charge profiles presented here contribute toward decoupling of these effect.

## 7.4 Conclusion

In this work we have demonstrated a first-principles based computational framework for modeling charged species redistribution at a solid/liquid electrochemical interface. The method uses a unified grand canonical description for ion species in water solution and charged defects in oxide material, which allows for easy surveying of different water and oxide chemistry. The application of this model on $ZrO_2$/water system has yielded great consistency with experimental measurement in terms of predicting $ZrO_2$ solubility and point of zero charge. We also investigated the interfacial profiles change with various dopants in $ZrO_2$. The effect of dopants is a coupling between Fermi level change in bulk and the magnitude of the space charge layer, resulting in a trade-off between oxidation rate and hydrogen pickup fraction. This framework allows for thermodynamic modeling of oxide/water interface with varying defect chemistry and water chemistry and is useful for discovering engineering strategies of electrochemical interfaces.

# 8 *Ab initio* prediction of defect equilibria at grain boundaries: model system of monoclinic-$ZrO_2$

We predict defect redistribution profiles at $ZrO_2$ Σ3 (100) twin boundary, Σ5 (210) [001] grain boundary, and Σ5 (310) [001] grain boundary based on *ab initio* calculations. The modeling framework combines defect energetics from first-principles calculations and continuum level modeling, and produces spatially-resolved defect concentration at equilibrium both in the space charge layer and in the grain boundary core. Such a framework allows easy survey in the multidimensional thermodynamic space of temperature, oxygen partial pressure, and dopant concentration. Our results show that under most relevant thermodynamic conditions, grain boundaries in $ZrO_2$ induce a positive space charge potential, with a positively-charged core and negatively-charged space charge layer. In the extended space charge layer, oxygen interstitials and electrons accumulate, leading to enhancement in oxygen diffusivity and n-type electronic conductivity. We surveyed Cr-, Fe-, Sn-, and Nb-doped $ZrO_2$ and show that aliovalent dopants strongly change the magnitude of the space charge potential. In Cr- and Fe-doped $ZrO_2$, which exhibit the largest space charge potentials, we observe up to ten orders of magnitude increase in oxygen diffusion coefficient, and five orders of magnitude increase in electronic conductivity. These results show that defect redistribution at grain boundaries is one of the governing factors in determining transport properties in polycrystalline $ZrO_2$, and that by such predictive modeling, a detailed understanding of point defect redistribution at extended defects is achievable.

## 8.1 Introduction

Ionic and electronic conductivities are key parameters in materials engineering of many technologically-important applications, such as solid oxide fuel cells [258], chemical sensors [259], membranes separators and reactors [260], and resistive switching devices [261, 262]. Predicting ionic and electronic conductions of oxide materials in the multidimensional thermodynamic space of temperature, chemical environment, and doping concentration serves as an important step towards their rational design. There have been many successes in *ab initio* prediction of transport properties of bulk oxide materials, for example, ZnO [263], $ZrO_2$ [17, 249], $CeO_2$ [264], MgO [265]. Such density functional theory (DFT) studies provide detailed information of defect concentrations and

mobility, and are proven to agree quantitatively with experimentally-measured values [14, 266].

However, practically-used materials are polycrystalline in many cases, and their transport properties can deviate greatly from the bulk. One important cause of this deviation is defects segregating to the grain boundary cores, leading to the formation of space charge in the vicinity of grain boundaries [267, 268]. Engineering defect redistributions at grain boundaries by intentional doping has been reported to result in orders of magnitude change in ionic and electronic conductivities [269, 270]. While many first-principles studies report defect segregation energies [271-276] and space charge profiles [277-280] at grain boundaries, to date, a full DFT-based study of transport in polycrystalline oxides remains intractable due to the complexities in the interplay between point defects and different types of grain boundaries.

In this work, we provide a detailed *ab initio* prediction for defect redistribution profiles with varying temperatures, oxygen partial pressures, and doping contents in monoclinic-phase $ZrO_2$. Transport properties of $ZrO_2$ have long been studied in the context of corrosion kinetics of zirconium alloys used as cladding of nuclear fuel in light water cooled nuclear reactors [51]. Doped $ZrO_2$ is also used as oxygen-ion conducting electrolyte [281], coating layer [282, 283], active layer of resistive memory [72]. There have been many reports on oxygen and electronic conduction in polycrystalline $ZrO_2$ [284-287]. Its detailed bulk defect chemistry has also been well-established [116], making it a good model system for exploring defect redistribution at grain boundaries.

We aim to address how space charge effects change with thermodynamic conditions and grain boundaries structures. We compare the grain boundary space charge profiles at three types of grain boundaries Σ3 (100) twin boundary, Σ5 (210) [001] grain boundary, and Σ5 (310) [001] grain boundary, for undoped and Cr-, Fe-, Sn-, and Nb-doped $ZrO_2$. We show that while the space charge potentials of $ZrO_2$ remain positive under most of the conditions surveyed, their magnitudes can change significantly with grain boundary type, dopant type, temperatures, and oxygen partial pressures. In Fe- and Cr-doped $ZrO_2$, where the largest space charge potentials are observed, accumulation of electrons and oxygen interstitials in the space charge layer leads to up to ten orders of magnitude increase in oxygen diffusion coefficient, and five orders of magnitude increase in electronic conductivity. These results demonstrate the importance of defect redistribution

in determining transport properties of polycrystalline oxides, and give examples of how such profiles can be predicted based on an *ab initio* computing framework.

## 8.2 Methods

We combine DFT calculations for defect segregation energies with continuum-level modeling to obtain charged defect redistribution profiles at grain boundaries. The framework is similar to what has been established in our previous work on $ZrO_2/Cr_2O_3$ interface [91]. First, we performed DFT calculations on three types of CSL grain boundaries of M-$ZrO_2$, Σ3 (100) twin boundary, Σ5 (210) [001] grain boundary, and Σ5 (310) [001] grain boundary. The atomic structures of these grain boundaries are shown in Figure 8-1. The CSL grain boundary structures are generated using Aimsgb [288]. DFT calculations are done with Vienna Ab initio Simulation Package (VASP) [86-88, 114] using the generalized gradient approximation (GGA) with Perdew-Burke-Ernzerhof (PBE) functional [89, 90]. The bulk defect energetics calculated in our previous work are used here to obtain bulk defect concentrations [116].

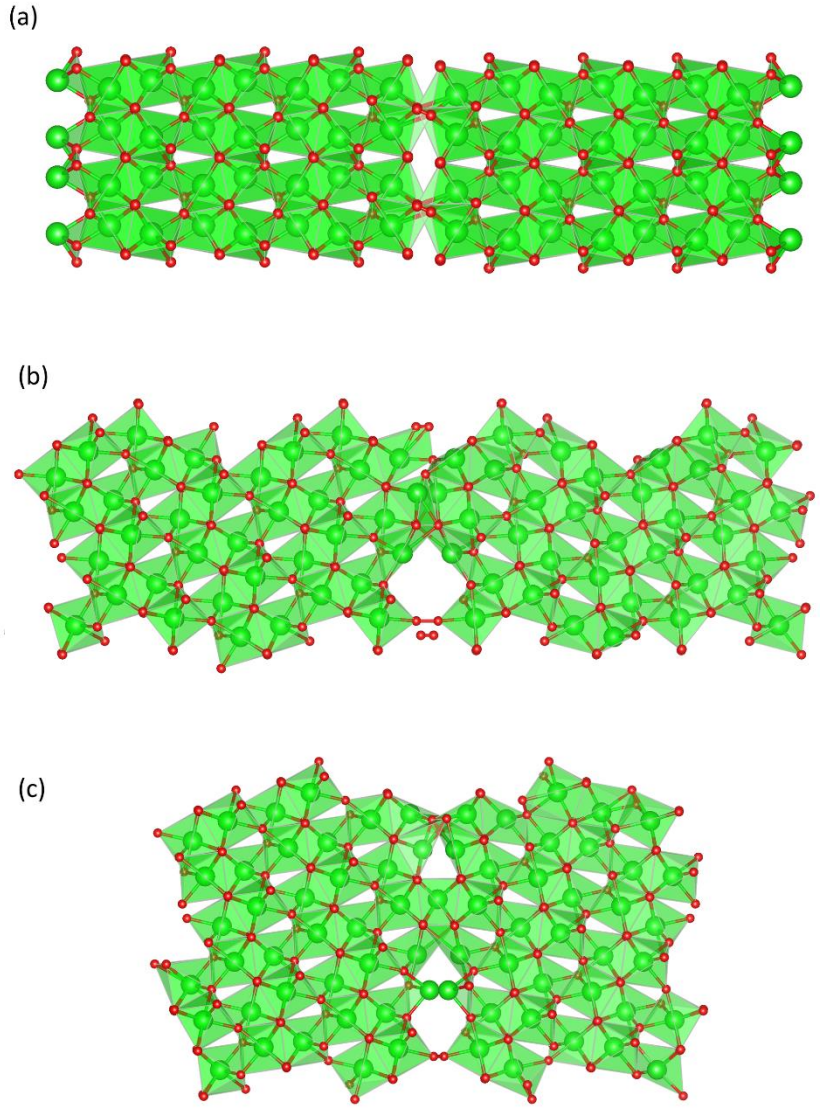


Figure 8-1. Atomic structures of M-$ZrO_2$ grain boundaries. (a) Σ3 (100) twin boundary, (b) Σ5 (210) [001] grain boundary, and (c) Σ5 (310) [001] grain boundary. The large green spheres and small red spheres represent zirconium atoms and oxygen atoms respectively. Visualizations are generated using VESTA [97].

Segregation energies of important defect species are calculated by putting the defects in the immediate layer at the grain boundary. With the obtained segregation energies, we further feed the DFT-calculated values into our self-consistent continuum level model, which generates the space charge layer profiles under the constraint of global charge neutrality by solving one-dimensional Poisson's equation.

$$\frac{d^2\phi(z)}{dz^2} = -\frac{\rho(z)}{\varepsilon\varepsilon_0} \tag{8.1}$$

Here $\phi(z)$ is the electrostatic potential across the grain boundary. $\rho(z)$ is the local charge density. $\varepsilon_0$ and $\varepsilon_r$ are the permittivity of vacuum and relative permittivity of the host material. $\rho(z)$ is calculated by adding up the charges of local defects.

$$\rho(z) = \Sigma_{D,q} q[D^q](z) + [h](z) - [e](z) \tag{8.2}$$

The boundary conditions are set to

$$\frac{d\phi}{dz}|_{z=0} = 0 \tag{8.3}$$

$$\phi|_{z=L} = \phi_0 \tag{8.4}$$

Here $z = 0$ represents the end of the simulation cell away from the grain boundary. $z = L$ represents the location of the grain boundary. Considering the symmetry of the model, the calculation represents a grain of size 2$L$.

$\phi_0$ is determined by the global charge neutrality condition

$$\int_0^L \rho(z)dz = 0 \tag{8.5}$$

We also define the total voltage drop $\Delta\phi$ as $\Delta\phi = \phi|_{z=L} - \phi|_{z=0}$. This notation will be used for further analysis in the result section. Notice that when grain size is small, space charge regions can overlap and $\phi$ does not reach 0 at $z = 0$. As a result, $\Delta\phi$ is not always equal to $\phi_0$.

We calculate the effective oxygen self-diffusion coefficient in polycrystalline $ZrO_2$ by spatially averaging local oxygen self-diffusivities $D_{\mathrm{O}} = \sum_q [\mathrm{V}_O^q] D_{\mathrm{V_O}}^q + \sum_q [\mathrm{O}_i^q] D_{\mathrm{O_i}}^q$. The diffusivities for the specific defect species $V_O^q$ and $\mathrm{O}_i^q$ are reported in our previous work for bulk $ZrO_2$ [249]. In this work, the changes in migration barriers in the vicinity of the grain boundary are not considered. The predicted $D_{\mathrm{O}}$ represents only change in oxygen defect concentrations weighted by their diffusivities in bulk.

## 8.3 Results and discussion

In this section, we present the results on grain boundary space charge layer profile predictions for $ZrO_2$ in three parts. First, we examine the bulk defect concentrations and their redistribution at the grain boundaries for undoped $ZrO_2$. Second, we show the space charge layer profiles for Cr-, Fe-, Sn-, and Nb-doped $ZrO_2$ and discuss how the dopants change space charge effect. Last, we quantify the effective conductivities and oxygen diffusivities with varying grain sizes and discuss the implications on transport properties of polycrystalline $ZrO_2$.

A. Space charge profiles at grain boundaries for undoped zirconium oxide

In this part, we show in detail the space charge effects and their change with temperatures and oxygen partial pressures for undoped $ZrO_2$. In order to understand defect redistribution at grain boundaries, we first look at the bulk defect equilibrium diagram for $ZrO_2$ at 1000 K in Figure 8-2 (a). When $P_{O_2} > 10^{-10}$ atm, the dominant defect species are holes and $O_i''$. Going to more reducing condition, $[O_i'']$ decreases, leading to the regime where the dominant defect pair is electrons and holes. We also observe an increase in $[V_O^{\bullet\bullet}]$ with lowering $P_{O_2}$.

In Figure 8-2 (b), we show the segregation energies of these important ionic defect species, namely $V_O^{\bullet\bullet}$, $V_{Zr}''''$, and $O_i''$ at the three types of grain boundaries investigated here. For the close-packed (001) twin boundary, the segregation energies for all three defect species are positive, meaning that they do not tend to segregate to the grain boundary core. For Σ5 (210) [001] grain boundary and Σ5 (310) [001] grain boundary, which are more open, we start to observe negative segregation energies. Out of the three defect species, $V_O^{\bullet\bullet}$ is one having the strongest tendency to segregate to the core, with a segregation energy of -3.2 eV at Σ5 (210) [001] grain boundary, and -3.8 eV at Σ5 (310) [001] grain boundary.

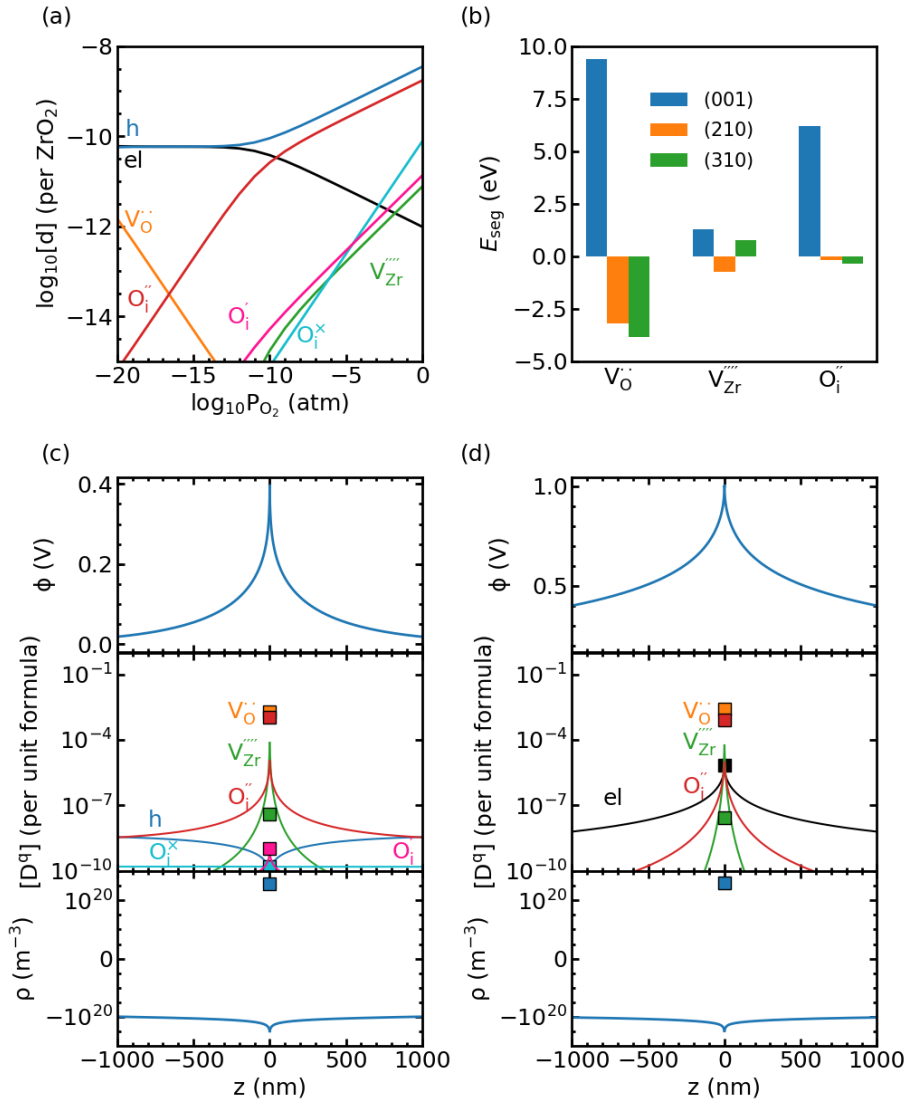


Figure 8-2. (a) Equilibrium defect concentrations as a function of oxygen partial pressure in bulk undoped $ZrO_2$ at T = 1000 K. (b) Segregation energies of intrinsic and hydrogen defects at the three types of grain boundaries studied. (c) Electrostatic profile, defect redistribution profile, and local charge density at a Σ5 (310) [001] grain boundary with L = 5000 nm, T = 1000 K, and $P_{O_2}$ = 1 atm. The squares at z = 0 show the defect concentrations in the core layer. (d) Same profiles as (c) at a lower $P_{O_2}$ of $10^{-20}$ atm.

The concentrations of charged defects and their segregation energies in the core region together determine the sign and magnitude of core charge. To demonstrate this, in Figure 8-2 (c) and (d), we show the space charge layer profiles at Σ5 (310) [001] grain boundary

at $P_{O_2}$ = 1 atm, and $P_{O_2}$ = $10^{-20}$ atm, respectively. In both cases, space charge potentials are positive due to a positive core formed by segregation of $V_O^{\bullet\bullet}$. However, in the former case, $\phi_0$ = 0.4 V while in the latter 1.0 V. This difference results mainly from the increase of $V_O^{\bullet\bullet}$ concentration at low $P_{O_2}$.

The positive core is charge-compensated by negatively-charged space charge region. In the high $P_{O_2}$ case (Figure 8-2 (c)), $V_{Zr}''''$ and $O_i''$ are accumulated in the space charge region and compensate for the core charge. In the low $P_{O_2}$ case (Figure 8-2 (d)), electron and $O_i''$ are the dominant contributors to the negative charge of the space charge zone.

Now we compare the space charge effects of the three types of grain boundaries by comparing $\Delta\phi$ with varying partial pressures and temperatures in Figure 8-3. As we have seen in Figure 8-2, $V_O^{\bullet\bullet}$ segregation controls the magnitude of space charge potential. This understanding provides insight when interpreting trends in $\Delta\phi$ change. First, comparing across grain boundary types (Figure 8-3 (a) (b) and (c)), $\Delta\phi$ increases going from (100), to (210), to (310) grain boundaries. This is largely determined by the trend in segregation energy of $V_O^{\bullet\bullet}$ in Figure 8-2 (b), where the segregation is most significant at the Σ5 (310) [001] grain boundary.

Second, considering the trend in $\Delta\phi$ changing with oxygen partial pressure within each grain boundary type, we observe a monotonic increase in $\Delta\phi$. This goes back to the comparison between Figure 8-2 (c) and (d), where bulk $V_O^{\bullet\bullet}$ concentration is higher at lower $P_{O_2}$, and thus leads to higher space charge potential.

Last, Figure 8-3 also shows that $\Delta\phi$ increases with increasing temperature. Rising temperature leads to an overall increase in the concentrations of intrinsic defects, and among them, the concentration of $V_O^{\bullet\bullet}$. This means at higher temperature, more $V_O^{\bullet\bullet}$ segregate to the core, giving rise to higher $\Delta\phi$.

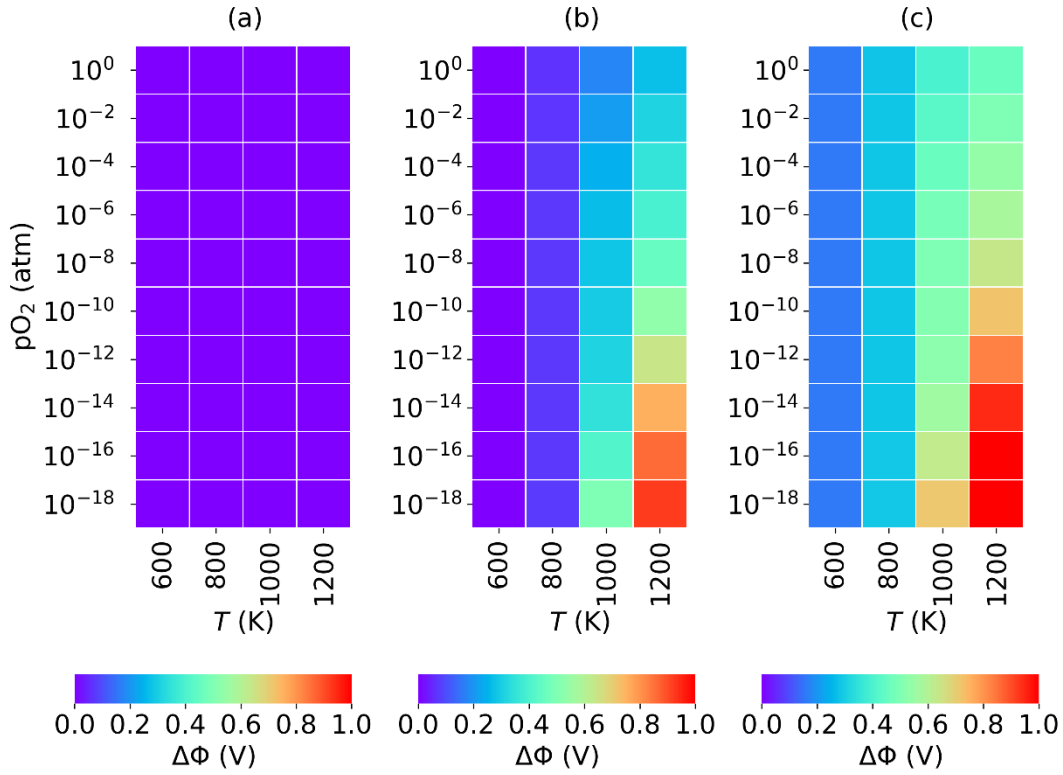


Figure 8-3. Space charge potential drop $\Delta\phi$ across the grain with L = 5000 nm for undoped $ZrO_2$ with varying temperatures and oxygen partial pressures for (a) Σ3 (100) twin boundary, (b) Σ5 (210) [001] grain boundary, and (c) Σ5 (310) [001] grain boundary.

B. Space charge profiles at grain boundaries for doped zirconium oxide

In this section, we examine the space charge profiles of doped $ZrO_2$, which can be very different from the undoped case. The grand-canonical description of point defects allows for easy inclusion of different types of dopants. Here we investigate Cr-, Fe-, Sn-, and Nb-doped $ZrO_2$. For all calculations in this work, dopant concentrations are fixed to 10 ppm.

Figure 8-4 shows the electrostatic potential and defect redistribution profiles for the four doped cases at $T$ = 1000 K, and $P_{O_2}$ = 1 atm. The effects of these defects correlate with their dominant valence state. For Sn, which is dominantly 4+ and exist in $ZrO_2$ as neutral defect $Sn_{Zr}^{\times}$, the change in space charge profiles comparing to the undoped case is almost negligible. Though $Sn_{Zr}^{\times}$ segregates to the core, it does not change the core charge and

therefore the profiles are very similar to the undoped case (Figure 8-4 (c)). However, when Cr, Fe and Nb (Figure 8-4 (a) (b) and (d)), which are aliovalent dopants, segregate to the core, they contribute to the core charge density and thus are important in determining the space charge potential.

Now we examine the defect concentration profiles of Cr, Fe and Nb in detail. For Cr-doped case (Figure 8-4 (a)), the dominant extrinsic defect species in the core is $Cr_{Zr}^{\bullet}$, with a segregation energy of -5.1 eV. With this strong segregation of Cr, $\phi_0$ is increased to 1.3 V. Similarly, for Fe (Figure 8-4 (b)), we observe strong segregations of $Fe_i^{\bullet\bullet\bullet}$, leading to $\phi_0$ = 2.1 V. The large positive space charge potentials are accompanied by accumulation of negatively-charged defects in the space charge layer. In both cases, $M_{Zr}'$, where M represents the metal dopant, is the dominant defect type in the space charge layer.

For Nb-doped $ZrO_2$ (Figure 8-4 (d)), Nb exists in the form of $Nb_{Zr}^{\bullet}$, which is compensated by $V_{Zr}''''$ and $O_i''$. $Nb_{Zr}^{\bullet}$ does not tend to segregate to the core layer. It has a positive segregation energy of 2.3 eV at Σ5 (310) [001] grain boundary. Its compensating species, $V_{Zr}''''$ and $O_i''$, also has relatively small segregation energies (0.8 eV and -0.3 eV at Σ5 (310) [001] grain boundary). As a result, total charge density in the core layer is low and the space charge potential is low. In Figure 8-4 (d), a $\phi_0$ of 0.12 V is observed.

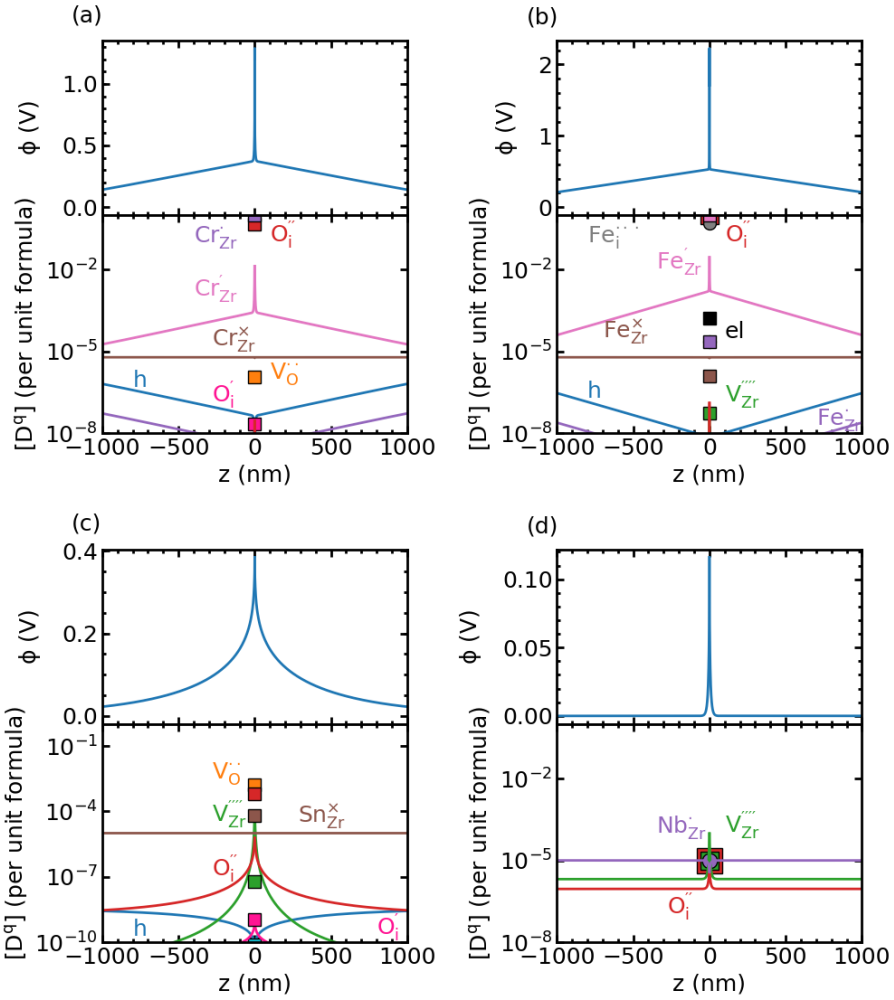


Figure 8-4. Electrostatic potential and defect concentration profiles across the grain with L = 5000 nm for Σ5 (310) [001] grain boundary for (a) Cr-doped, (b) Fe-doped, (c) Sn-doped, and (d) Nb-doped $ZrO_2$ at T = 1000 K, and $P_{O_2}$ = 1 atm. The cation dopant concentrations in the bulk are fixed to 10 ppm.

In Figure 8-5, we can compare the effects of these dopant species across grain boundary types and oxygen partial pressures. Comparing between the three types of grain boundaries, we still see the trend that space charge potentials are generally small at Σ3 (100) twin boundary due to non-favorable defect segregation. For the other two Σ5 boundaries, Cr- and Fe- doped ones have the largest space charge potentials comparing to the other three cases due to large energy gain in $Cr'_{Zr}$ and $Fe'''_{i}$ segregation. Nb-doped ones have the smallest space charge potentials due to depletion of $Nb'_{Zr}$ in the core layer.

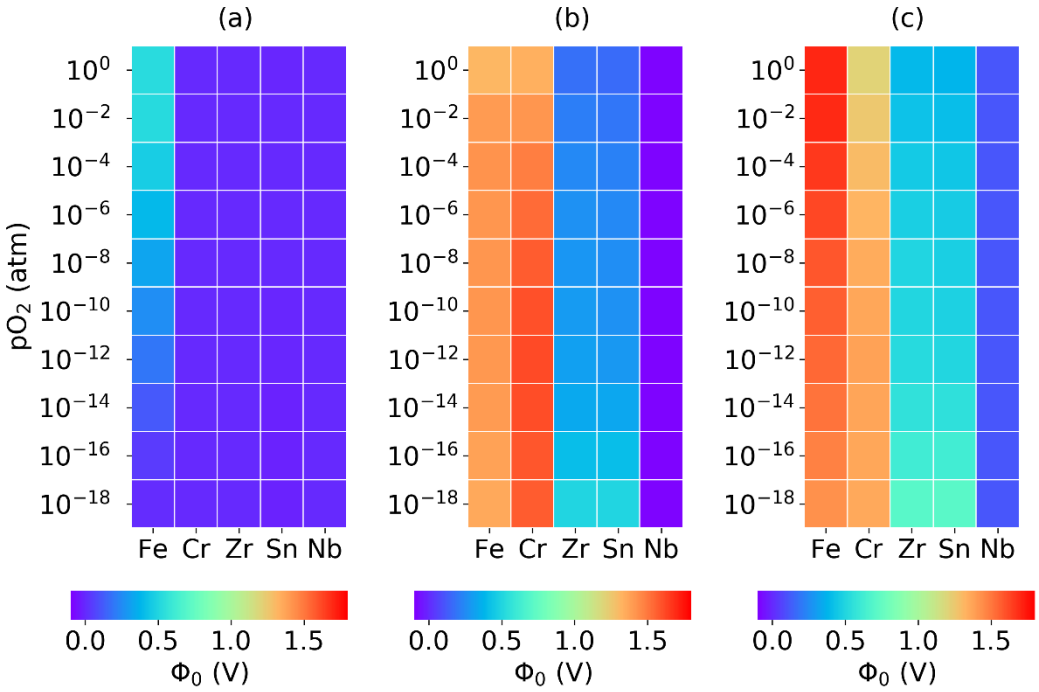


Figure 8-5. Space charge potential drop $\Delta\phi$ across the grain with L = 5000 nm at T = 1000 K for $ZrO_2$ with different dopants and oxygen partial pressures for (a) Σ3 (100) twin boundary, (b) Σ5 (210) [001] grain boundary, and (c) Σ5 (310) [001] grain boundary. The label Zr represents undoped $ZrO_2$.

Last, we comment on the temperature-dependence space charge effect in doped $ZrO_2$. Since the aliovalent dopants, whose concentrations do not depend strongly on temperature, dominantly determine the core charge, $\Delta\phi$ change with temperature is much smaller comparing to the intrinsic case.

C. Implications on oxygen and hydrogen transport in polycrystalline zirconium oxide

With the established knowledge of spatially-resolved defect concentrations profiles at grain boundaries, in this section we discuss how grain boundaries change the oxygen diffusion and electronic conduction in polycrystalline $ZrO_2$. To do this, we investigated

the space charge profiles with varying $L$ of 100 nm, 500 nm, 1000 nm, and 5000 nm. In Figure 8-6 (a) and (b), we show how the electrostatic potentials change for undoped $ZrO_2$ with varying grain sizes at T = 1000 K, $P_{O_2}$ = 1 atm and $10^{-20}$ atm, respectively. The change in grain size hardly affects $\phi_0$, with all $\phi_0$ close to 0.4 V in Figure 8-6 (a) and 1.0 V in Figure 8-6 (b). However, smaller grain size leads to more significant overlapping between grain boundary space charge layers, resulting in higher $\phi$ in the bulk of the grian.

In Figure 8-6 (c) and (d), we compare the averaged oxygen diffusion coefficient $D_O$ and [e]+[h] concentration between bulk and the polycrystalline model with different grain sizes. In Figure 8-6 (c), $D_O$ in bulk increases with increasing $P_{O_2}$, indicating an interstitial-dominated transport mechanism. $\log_{10} D_O$ shows a 1/6 slope with $\log_{10} P_{O_2}$ in the high $P_{O_2}$ range and a ½ slope in the low $P_{O_2}$ range. Because of the accumulation of $O_i''$ in the space charge region, the effective $D_O$ increases with decreasing grain size. Going from $L$ = 5000 nm to $L$ = 100 nm, we see a two-order-of-magnitude increase in $D_O$.

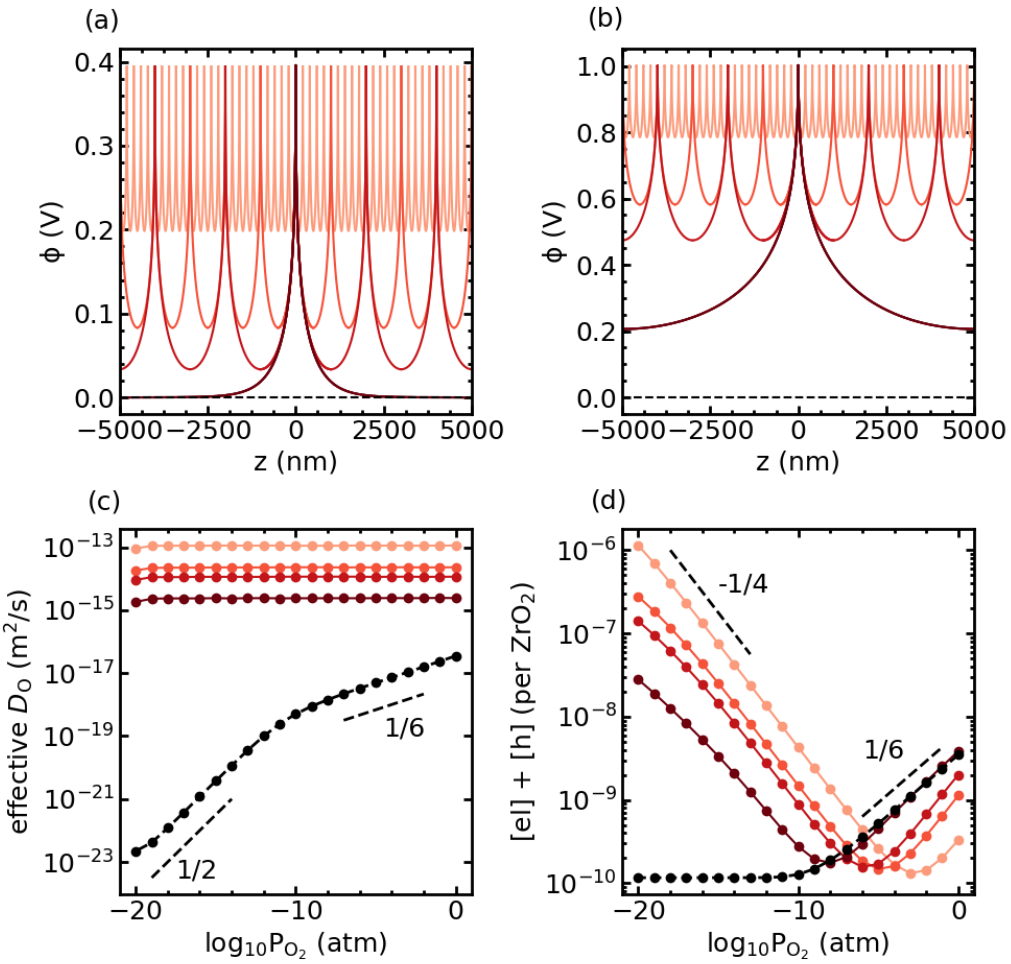


Figure 8-6. (a) Electrostatic profiles at a Σ5 (310) [001] grain boundary with varying grain sizes at T = 1000 K, $P_{O_2}$ = 1 atm for undoped $ZrO_2$. The four colored lines represent grain sizes of 10 μm, 2 μm, 1 μm, and 0.2 μm, respectively. The black dashed line represents bulk $ZrO_2$ in which there is no space charge effect. (b) Same profiles as in (a) at a lower $P_{O_2}$ of $10^{-20}$ atm. (c) Resulted averaged oxygen self-diffusivity at T = 1000 K as a function of $P_{O_2}$. (d) Resulted averaged [e]+[h], which represents the total electronic conductivity at T = 1000 K as a function of $P_{O_2}$.

In Figure 8-6 (d), we look at the averaged [e]+[h] as an indication of how the total electronic condutivity changes with grain size. In bulk $ZrO_2$, we see a constant [e]+[h] in the low $P_{O_2}$ regime, where the dominant compensation mechanism is electron

compensated by holes. In the high $P_{O_2}$ regime, hole concentration starts to dominate, exhibiting a 1/6 slope. In the polycrystalline cases, space charge potential promotes electron concentration, leading to a transition to electron-dominated regime at low $P_{O_2}$. This transition pressure corresponds to the minimum in [e]+[h], and the transition point shifts to higher $P_{O_2}$ with decreasing grain size. The overall effect is a decrease in electronic conductivity in the high $P_{O_2}$ p-type conducting regimes, and increase in electronic conductivity at lower $P_{O_2}$.

In Figure 8-7, we show a similar analysis comparing $D_O$ for doped $ZrO_2$ and how it changes with grain size. Figure 8-7 (a) shows bulk $D_O$ for Cr-, Fe-, Sn-, and Nb-doped $ZrO_2$ as a function of $P_{O_2}$. The Sn-doped one is identical to that of undoped $ZrO_2$, with a dominant interstitial mechanism. Using Sn-doped $ZrO_2$ as a reference, Nb promotes the concentration of $O_i''$, and thus increase $D_O$ overall $P_{O_2}$ range. Fe decreases the concentration of $O_i''$ and leads to an overall decrease in $D_O$. Cr is similar to Fe when $P_{O_2} > 10^{-2}$ atm. With lowering partial pressure, it drives the oxide into a vacancy-dominated regime where $D_O$ starts to increase with $P_{O_2}$.

Figure 8-7 (b) (c) and (d) show the comparison between bulk $D_O$ and averaged $D_O$ with different grain sizes for Cr-, Fe-, and Nb-doped $ZrO_2$. For Sn-doped one, the profiles are very similar to the undoped case (Figure 8-6 (c)) and are not reproduced here. We see that due to the large positive space charge potential promoting $O_i''$ accumulation in the space charge region, Cr- and Fe-doped $ZrO_2$ display two to ten orders of magnitude increase in $D_O$. For Nb-doped $ZrO_2$, the change is much less pronounced. Going from bulk to L = 100 nm, $D_O$ is increased by five times.

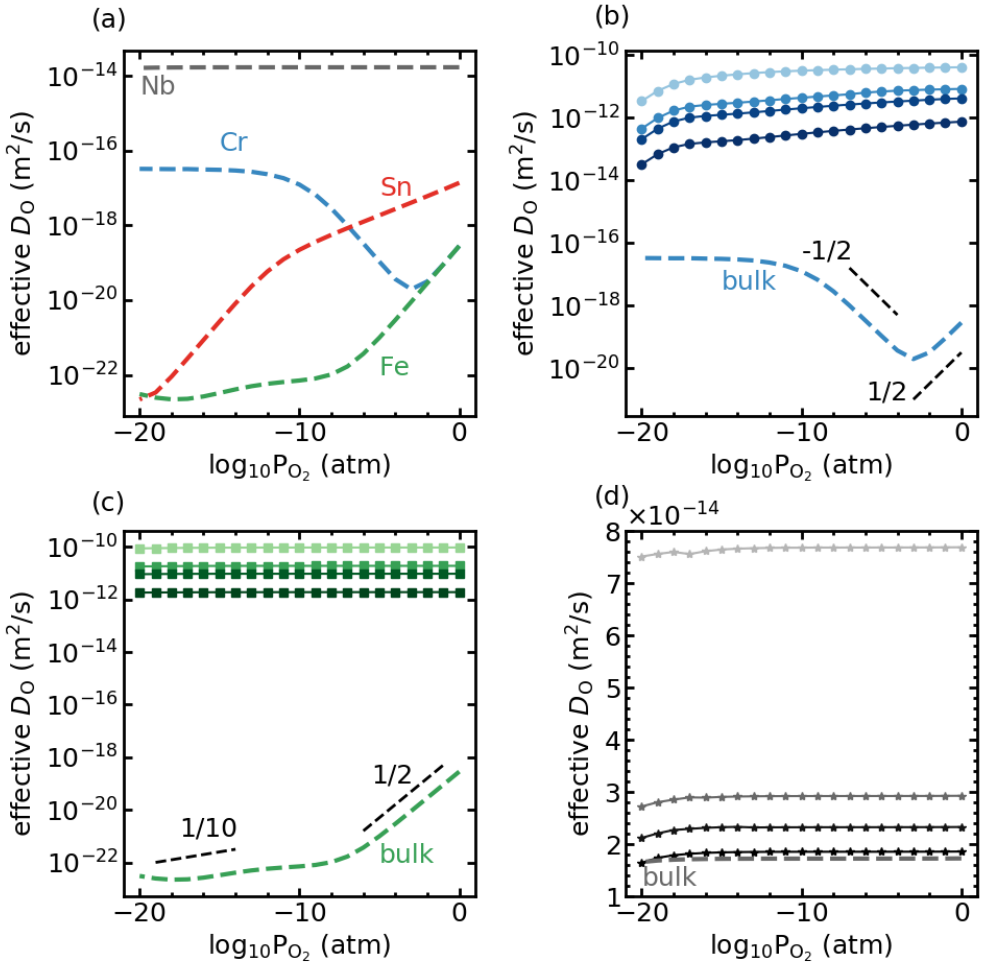


Figure 8-7. (a) Oxygen self-diffusivities as a function of $P_{O_2}$ at T = 1000 K for Cr-doped, Fe-doped, Sn-doped, and Nb-doped bulk $ZrO_2$. The dopant concentrations are fixed to 10 ppm. (b-d) Comparison between averaged oxygen self-diffusivities in polycrystalline $ZrO_2$ with varying grain sizes versus their bulk value for (b) Cr-doped $ZrO_2$, (c) Fe-doped $ZrO_2$, and (d) Nb-doped $ZrO_2$ at T = 1000 K. The colored solid lines represent average grain sizes of 10 μm, 2 μm, 1 μm, and 0.2 μm going from darker color to lighter color. The dashed lines show the bulk values for reference as in (a).

To summarize, we have showed the effect of grain boundaries on oxygen diffusion and electronic conductivity in undoped and doped $ZrO_2$. Under most of the thermodynamic conditions examined, due to the positive space charge potential, electrons and oxygen interstitials are promoted in the space charge region while holes and oxygen vacancies are depleted. For Cr-doped and Fe-doped $ZrO_2$, in which the space charge potentials are

the most significant, we observe enhancement in oxygen diffusivity up to ten orders of magnitude, and in electronic conductivity up to five orders of magnitude. These results strongly suggest that grain boundaries govern the transport properties of polycrystalline $ZrO_2$. Out of them, the grain boundaries with open structures are likely to have a stronger effect comparing to close-packed grain boundaries.

## 8.4 Conclusion

In this work, we have predicted from first-principles calculations the defect redistribution profiles at three types of grain boundaries in $ZrO_2$, Σ3 (100) twin boundary, Σ5 (210) [001] grain boundary, and Σ5 (310) [001] grain boundary. Our results show that, defect segregations are not energetically favorable at the close-packed Σ3 (100) twin boundary, leading to negligible space charge effect. For the latter two Σ5 grain boundaries, positive space charge potentials are observed under most of the temperature, oxygen partial pressure, and doping content conditions considered here. In undoped and Sn-doped $ZrO_2$, the positive charge of the core layer is contributed dominantly by segregation of $V_O^{\bullet\bullet}$, with space charge potentials ranging from 0.5 V ~ 1.0 V. In Fe-doped and Cr-doped cases, the segregation of $Fe_i^{\bullet\bullet\bullet}$ and $Cr_{Zr}^{\bullet}$ leads to larger space charge potential up to 2 V. In Nb-doped $ZrO_2$, the space charge potential is diminished due to depletion of $Nb_{Zr}^{\bullet}$ in the core. The negatively-charged space charge region accumulates electrons and oxygen interstitials, while depleting holes and oxygen vacancies. This leads to enhancement in total oxygen diffusion coefficient and electronic conductivity up to ten and five orders of magnitude, respectively. Our results show that defect redistribution in the vicinity of the grain boundaries is an important factor governing ionic and electronic transport in polycrystalline oxides, and that, by combining first-principles calculations and thermodynamic modeling, *ab initio* predictions of the redistribution profiles are achievable.

# 9 Computational insight for field assisted sintering of $TiO_2$

In this chapter, we decouple Joule heating, bulk diffusion, and grain boundary effects in determining field assisted sintering (FAST) behavior using $TiO_2$ as a model system. In the FAST process, when external bias is applied during sintering, near instant densification can happen at a critical temperature and field strength. This technique could halve the sintering temperature and reduce the sintering time needed. It is a promising technique in shortening consolidation time and lowering sintering temperatures. Mechanistically the interplay between electric field and the polycrystalline material is a complicated process and the governing factor for rapid densification during FAST is still under debate. Here we approach this problem from computational modeling in the model system of rutile $TiO_2$. We separately quantified the effect of Joule heating and ion diffusion by studying defect equilibria in bulk and their redistribution at grain boundaries. In the bulk, we predicted the equilibrium defect concentrations at various pressures and temperatures from first-principles calculations. For grain boundaries, we studied the defect concentration change in space charge layers formed at grain boundaries with external bias. These results indicate that the local atomic structure and space charge layer profile of grain boundaries are important in understanding electric field effects on polycrystalline materials.

## 9.1 Introduction

The idea of using electric fields to assist sintering process has been an old one. A review paper by Grasso *et al* counts 642 related patents published from 1906 to 2008 [289]. The most commonly used method, spark plasma sintering (SPS), in which pulsed DC current is applied to ceramic powders, reduces the time for completing the full densification process to minutes [290]. In 2010, Cologna *et al* demonstrated rapid densification within five seconds on yttria-stabilized zirconia (YSZ) with electric field strength > 75 V/cm [62]. The discovery of this flash sintering (FS) behavior triggered many related studies since then, and similar phenomenon has been observed for many other polycrystalline ceramic materials including $Al_2O_3$ [58], $SnO_2$ [59], ZnO [60] and $TiO_2$ [61].

Despite the successful commercialization of the SPS method and the rapid development of FS technique, mechanistic understanding of how external electric fields change the

sintering process is still limited on the atomistic level due to the complexity of the process. While it has been recognized that the onset of the flash event is mainly controlled by a thermal runaway process [64], there are many studies suggesting other non-thermal effects that electric fields could potentially have [291]. Apart from Joule heating, electric fields can induce defect generation [292-294], defect redistribution [66], changes in grain boundary mobility [295], electro-migration [296], and local dielectric breakdown [297].

In this study, we select $TiO_2$ as a model system, predict its defect equilibria from first-principles, and link the obtained electronic conductivity and ionic diffusivity profiles to its FAST behavior. We investigate undoped, Ta (donor) doped, and Ga (acceptor) doped $TiO_2$ and show that by controlling dopant content and oxygen partial pressure, one can modulate Joule heating and ionic transport of $TiO_2$ and thus the FAST process. In particular, in the donor-controlled regime of Ta-doped $TiO_2$, one can fix the conductivity (and thus Joule heating effect) while promoting Ti diffusivity by lowering oxygen partial pressure. This method allows for the decoupling of thermal effect from ionic dynamics.

Based on the knowledge of bulk defect chemistry, we also modeled the distribution of electric field at Ta/Ga-doped $TiO_2$ grain boundaries on the continuum level. The two differently-doped cases show different signs of grain boundary space charge due to dopant segregation. The model shows a homogeneous distribution of external bias in Ta-doped $TiO_2$, and a heterogenous distribution in Ga-doped $TiO_2$, where the potential is mainly screened at the grain boundary and electrode/electrolyte interface. This result suggests that an inhomogeneous Joule heating effect is expected in acceptor-doped $TiO_2$.

## 9.2 Methods

A. Bulk defect equilibria and cation diffusivity

DFT calculations are performed on rutile $TiO_2$ with Vienna Ab initio Simulation Package (VASP) [86-88, 114]. The generalized gradient approximation (GGA) with Perdew-Burke-Ernzerhof (PBE) functional is used with Hubbard U correction of 4.2 eV applied on the 3d states of Ti. To calculate the formation energies of defects, we used a supercell containing 24 unit formula of $TiO_2$. We used an energy cut-off of 700 eV and a 2×2×2 *k*-point grid. Ionic structures are relaxed until the forces on atoms are less than 0.01 eV/ Å.

Defect formation energies obtained from DFT are further fed into a thermodynamic model to predict equilibrium defect concentrations. We further computed the migration barriers of Ti interstitials and Ti vacancies, and computed the total Ti self-diffusivity following a random-walk diffusion model.

B. Modeling space charge layer profile

We performed continuum-level modeling to obtain the space charge layer profiles across a grain boundary in Ta-doped and Ga-doped $TiO_2$. The model assumes a space charge potential of 0.3 V for the Ta-doped case and -0.3 V for Ga-doped $TiO_2$. Poisson's equation is solved assuming that intrinsic defects can freely redistribute in the space charge layer, while the dopant can only segregate to the grain boundary core. We further modeled the profile change under applied bias assuming only electronic carriers can freely redistribute under applied bias. This model gives a picture of local potential and electric field distributions at grain boundaries in doped $TiO_2$ under an applied external electric field.

## 9.3 Results and discussion

In this section, we summarize the results obtained by computational modeling in two parts. First, we compare bulk defect concentrations, cation diffusivity, and electronic conductivity in undoped, Ta-doped, and Ga-doped $TiO_2$. Second, we show the defect redistribution profiles at grain boundaries for doped $TiO_2$, and explain their implications for the transport properties of polycrystalline titania ceramics.

A. Modeling of $TiO_2$ defects concentrations and diffusivities

We predicted the equilibrium defect concentrations in bulk rutile $TiO_2$ utilizing a first-principles based framework as provided in [8]. The resultant concentrations, as a function of oxygen partial pressure $P_{O_2}$ , are shown in Figure 9-1. For intrinsic $TiO_2$ (Figure 9-1(a)), we observe that at high $P_{O_2}$, the dominant compensating mechanism is hole compensated by $V_{Ti}''''$. And at lower $P_{O_2}$, $Ti_i^{\cdots}$ is compensated by electrons. The transition occurs at higher $P_{O_2}$ as temperature is increased. In other words, the range in which $Ti_i^{\cdots}$ dominates over $V_{Ti}''''$ is extended at higher temperature.

To understand the effect of donor and acceptor dopants in $TiO_2$, in Figure 9-1(b) and (c), we show the equilibrium defect profiles with 1% Ta and Ga doping, respectively. The Ta

donor predominantly substitutes on Ti sites in $TiO_2$ in the form of $Ta_{Ti}^{\cdot}$, which is compensated at these lower temperatures by the formation of $V_{Ti}^{''''}$ rather than electrons. It serves effectively as a donor dopant, promoting the concentration of electron over the whole $P_{O_2}$ range. For the Ga-doped case, the $Ga_{Ti}^{'}$ acceptor is predominantly compensated by $Ti_i^{''''}$ rather than holes, although hole compensation begins to become significant at the highest $pO_2$s.

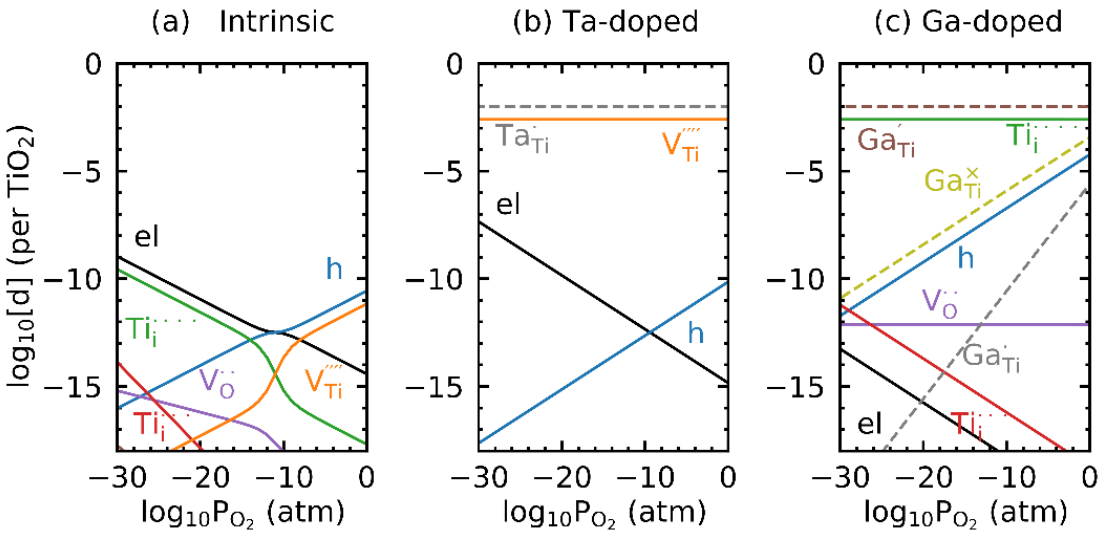


Figure 9-1. Equilibrium defect concentrations at 600 K for (a) undoped $TiO_2$, (b) Ta-doped $TiO_2$, and (c) Ga-doped $TiO_2$ with varying oxygen partial pressure. For the doped cases, dopant concentrations are fixed to 1%.

In Figure 9-2, we examine the defect concentrations in the three cases at 1200 K. At this higher temperature, we observe different defect compensation pairs in the low oxygen partial pressure regime comparing to at 600 K (Figure 9-1). For undoped $TiO_2$, $Ti_i^{''''}$ starts to dominate over $Ti_i^{''''}$ as the main positive defect at $P_{O_2} < 10^{-23}$ atm (Figure 9-2 (a)). Ta-doped $TiO_2$ enters the regime where $Ta_{Ti}^{\cdot}$ is compensated by electrons at low $P_{O_2}$ (Figure 9-2(b)).

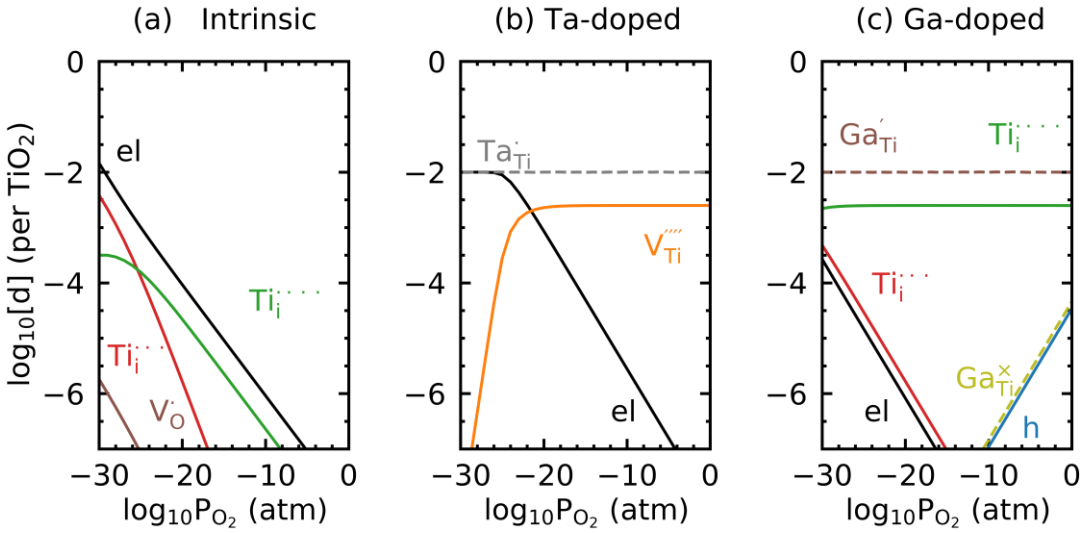


Figure 9-2. Equilibrium defect concentrations at 1200 K for (a) undoped $TiO_2$, (b) Ta-doped $TiO_2$, and (c) Ga-doped $TiO_2$ with varying oxygen partial pressure. For the doped cases, dopant concentrations are fixed to 1%.

With the defect concentration diagrams of the three differently-doped cases, we are in a position to calculate the temperature and $P_{O_2}$ dependence of electronic and ionic conductivities of $TiO_2$. Figure 9-3 shows the Ti self-diffusivity of undoped and Ta-doped $TiO_2$ based on the contributions of both Ti interstitials and vacancies. In Figure 9-3 (a), we compare the predicted $D_{Ti}$ of undoped $TiO_2$ with experimentally measured values from Ref. [298]. Both the prediction and the measured value show a decrease in $D_{Ti}$ with increasing $P_{O_2}$, which proves that $Ti_i^{\cdots\cdot}$ is the faster-diffusing species comparing to $V_{Ti}^{\prime\prime\prime\prime}$ and the dominant contributor to Ti diffusivity. Quantitatively, the predicted values are in reasonable agreement with the measured ones, with underestimation at lower temperatures.

Figure 9-3(b) shows the computed Ti self-diffusivity $D_{Ti}$ of Ta-doped $TiO_2$. Due to the low migration barrier of $Ti_i^{\cdots\cdot}$ relative to $V_{Ti}^{\prime\prime\prime\prime}$, it remains as the dominant contributor to $D_{Ti}$ over most $P_{O_2}$ range. This leads to a constant $D_{Ti}$ in the high $P_{O_2}$ range in which $V_{Ti}^{\prime\prime\prime\prime}$ concentration (thus $Ti_i^{\cdots\cdot}$ concentration) is fixed by $Ta_{Ti}^{\cdot}$. At lower $P_{O_2}$, with decrease in $V_{Ti}^{\prime\prime\prime\prime}$ concentration and increase in $Ti_i^{\cdots\cdot}$ concentration, $D_{Ti}$ increases with decreasing $P_{O_2}$. The transition pressure increases with increasing temperature. This results in a minimum

$D_{Ti}$ at the transition point where $Ti_i^{\cdots\cdot}$ starts to be the dominant contributor at temperatures higher than 1000 K.

It is worth pointing out that due to the low migration barrier of $Ti_i^{\cdots\cdot}$ and considering $Ti_i^{\cdots\cdot}$ concentration is fixed by $Ga'_{Ti}$ in the dopant-dominated regime of Ga-doped $TiO_2$, a very high $D_{Ti}$ (> $10^{-7}$ $cm^2/s$ at 1000 K) and very low migration barrier (0.2 eV) is predicted with 1% Ga concentration. This fast Ti diffusion is not observed in the literature [299]. The difference is possibly due to the formation of defect complexes with high $Ti_i^{\cdots\cdot}$ concentration, impeding its diffusion and increasing its migration barrier.

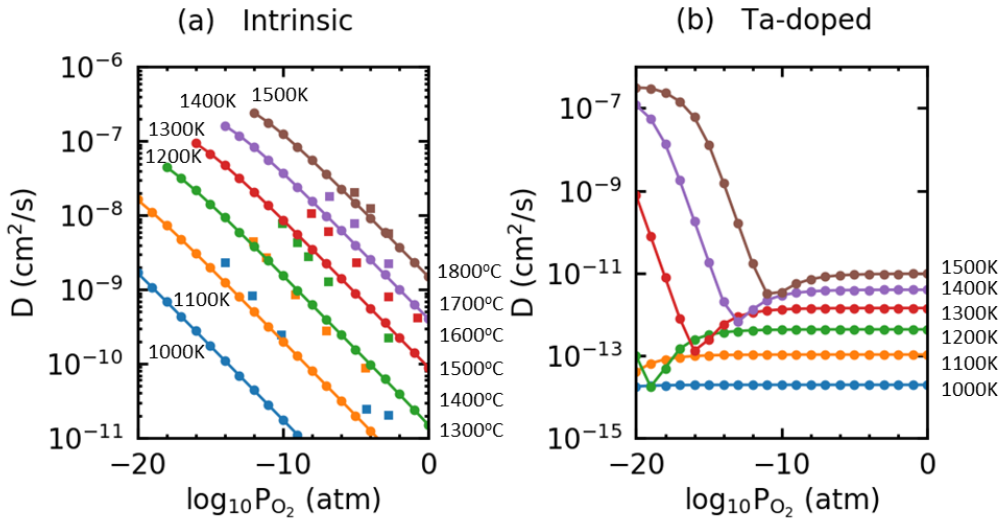


Figure 9-3. (a) Predicted Ti self-diffusion coefficient as a function of at $P_{O_2}$ at various temperatures in undoped $TiO_2$ (circled lines annotated with temperatures in Kelvin). The predicted values are plot against experimentally-measured values (squares annotated with temperature in degree Celsius as reported in [298]). (b) Predicted Ti self-diffusion coefficient as a function of at $P_{O_2}$ at various temperatures in Ta-doped $TiO_2$. Dopant concentration is fixed to 1%.

In Figure 9-4 we show the concentrations of the sum of electron and holes calculated for all three cases, as a reflection of the expected total electronic conductivities. For undoped $TiO_2$, the transition between n-type conductivity and p-type conductivity is predicted to occur at relatively high $P_{O_2}$ (~ 0.05 atm at 1000 K). This transition pressure is pushed to lower $P_{O_2}$ with Ga doping, promoting p-type conductivity. For the Ta-doped case, n-type conductivity dominates over the entire $P_{O_2}$ range. Note that a conductivity plateau is

predicted for $P_{O_2}$s below about $10^{-16}$ atm at 1000 K, reflecting electron charge compensation for the Ta donor rather than Ti vacancies that occurs at higher $P_{O_2}$. The predicted plateau starts at a lower $P_{O_2}$ compared to experimentally reported values, which suggests an overestimation of the reduction enthalpy.

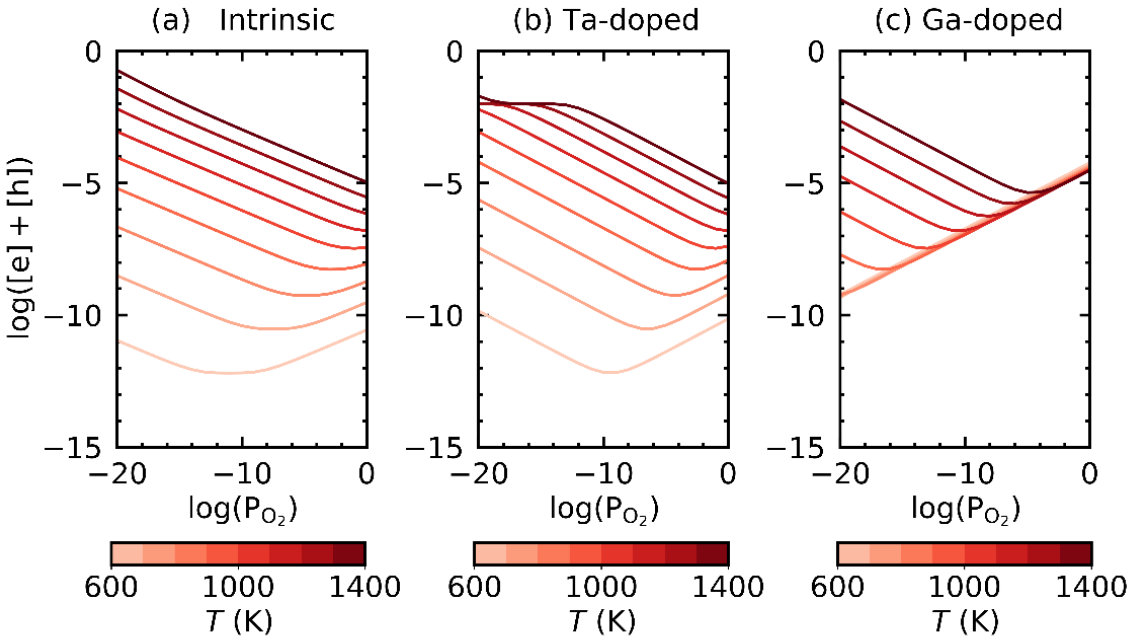


Figure 9-4. Electron plus hole concentrations as a function of $P_{O_2}$ for (a) undoped $TiO_2$, (b) Ta-doped $TiO_2$, and (c) Ga-doped $TiO_2$ at various temperatures. For the doped cases, dopant concentrations are fixed to 1%.

The above analysis of the defect chemistry, Ti diffusion, and electronic conductivity of the three differently-doped $TiO_2$ indicates that we can separately modulate the Joule heating factor and ionic diffusion factor during FAST by controlling doping content and $P_{O_2}$. In particular, the electronic plateau regime of Ta-doped $TiO_2$ (Figure 9-4 (b)) offers a straight forward to fix the Joule heating contribution while tuning $D_{Ti}$ by changing $P_{O_2}$, which we propose as an experimental design.

B. Modeling of mass and charge transport at grain boundaries

Due to the segregation of charged defects to the grain boundary core, defects will redistribute in the vicinity of grain boundaries and form space charge layers. We studied the space charge layer profiles for Ta- and Ga-doped $TiO_2$ from continuum level

modeling in order to understand the different effects that they may have in terms of the transport properties of polycrystalline $TiO_2$.

It has been reported that the dopant type determines the sign of grain boundary space charge in $TiO_2$. Specifically, donor dopant segregation leads to positively charged core and negatively charged space charge layer, with a positive space charge potential. The reverse is true for acceptor dopant. In Figure 9-5 we show the simulated defect redistribution profile for the two doped cases with a space charge potential of 0.3 V for Ta-doped $TiO_2$ and -0.3 V for Ga-doped $TiO_2$ at 600 K, 1 atm. In both cases, the dominant type of Ti defect ($V_{Ti}^{''''}$ for Ta-doped case and $Ti_i^{....}$ for Ga-doped case) accumulates in the space charge layer. The important difference between the two is that, while in both cases, at 600 K, 1 atm, the dominant electronic carrier is the hole, Ta-doped $TiO_2$ has a depletion of holes in the space charge layer while Ga-doped $TiO_2$ has an accumulation of holes. As a result, grain boundaries are electronically blocking in Ta-doped $TiO_2$ and conducting in Ga-doped $TiO_2$.

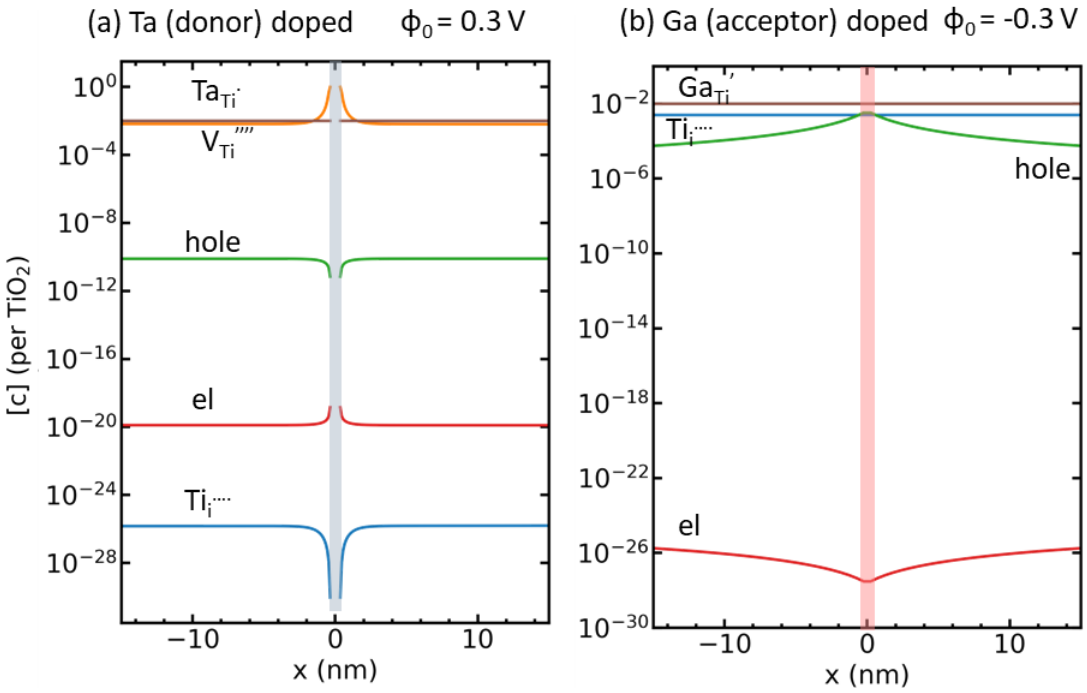


Figure 9-5. Defect concentration profiles in the space charge layer at T = 600 K, $P_{O_2}$ = 1 atm of (a) Ta-doped $TiO_2$ assuming a space charge potential of 0.3 V, and (b) Ga-doped $TiO_2$ assuming a space charge potential of -0.3 V. A grain size of 500 nm is used for the

calculation, with the figure showing a range of 30 nm in the vicinity of the grain boundary. The boundary is placed at x = 0.

Another important difference comes up when an external bias is applied across the grain boundaries. In Figure 9-6 we show the electrostatic potential and electric field profile across grain boundaries with an external bias equivalent to a constant electric field of $E$ = 500 V·cm$^{-1}$ under the same thermodynamic condition as in Figure 9-6, assuming the grain boundary core charge does not change with applied bias. We see that because of the high electronic conductivity under oxidizing conditions in Ga-doped $TiO_2$, the applied bias is mostly screened by the electrode/oxide interface and grain boundaries, leaving a very small electric field in the grain bulk. On the other hand, Ta-doped $TiO_2$ is insulating enough that the screening effect due to defect redistribution is negligible. A uniform electric field of 500 V/cm is maintained throughout the bulk of the grains.

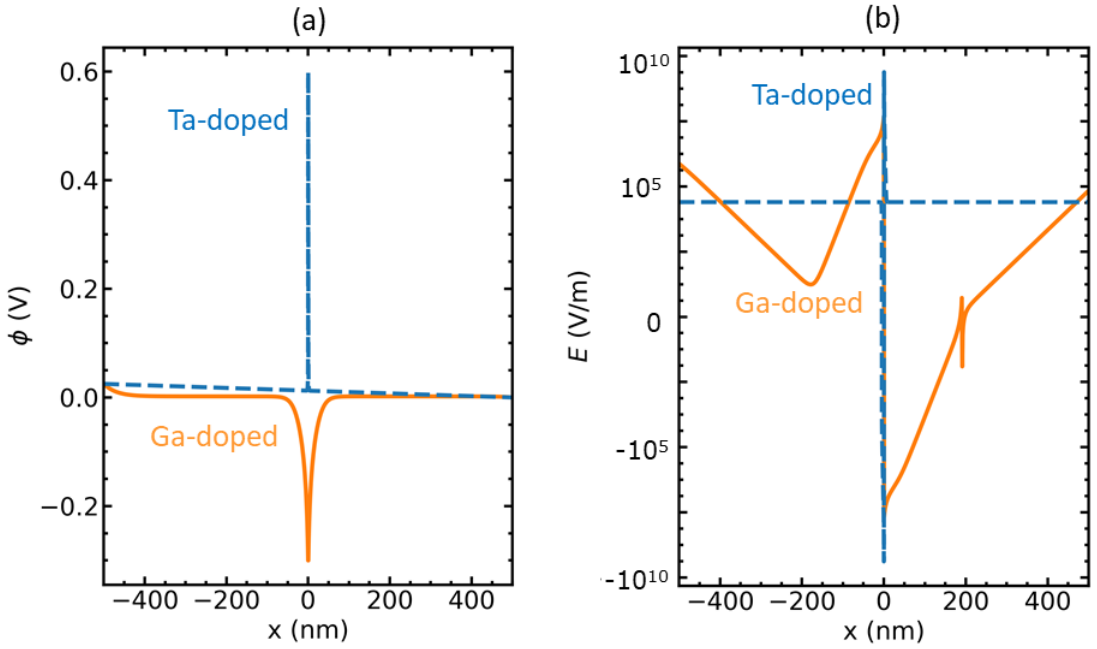


Figure 9-6. (a) Electrostatic profile, and (b) electric field across the Ta/Ga-doped grain boundaries with an external bias equivalent to E = 500 V/cm at T = 600 K, $pO_2$ = 1 atm. A grain size of 500 nm is used for the calculation. The boundary is placed at x = 0.

In summary, we have showed two differences that exist between Ta-doped and Ga-doped $TiO_2$ in terms of space charge effects at grain boundaries. Due to the opposite signs of grain boundary space charge potential, grain boundaries in Ta-doped $TiO_2$ appear to be

electronically blocking while grain boundaries in Ga-doped $TiO_2$ are electronically conducting. Second, because of the difference in total electronic conductivity, external bias is screened by carrier redistribution in Ga-doped $TiO_2$. This leads to inhomogeneous distribution of the electric field in polycrystalline Ga-doped $TiO_2$ and potentially inhomogeneous Joule heating effect.

## 9.4 Conclusion

This project offers insights into the underlying mechanisms active during field assisted sintering experiments. Using $TiO_2$ as a model system allows engineering of the main defect types and concentrations through doping and $pO_2$ management. The modeling of the migration barrier for diffusion of Ti defects shows that interstitials move faster than Ti vacancies. The leading mechanism explaining enhanced sintering under electric field can be largel attributed to Joule heating effects. The effect of the space charge at the grain boundaries was also modeled in the case of donor or acceptor doped $TiO_2$, and shows that grain boundaries are electronically blocking in Ta-doped $TiO_2$ and conducting in Ga-doped $TiO_2$, which can also play an important role on the heat dispersion induced by Joule heating. We also show that an applied electric field will be non-homogeneous in Ga-doped $TiO_2$ because of carrier redistribution.

# 10 Conclusions

## 10.1 Thesis summary

In this thesis, we have systematically studied the modeling of defective oxides based on first-principles calculations. Methodologically, we have contributed on two fronts: First, we add proofs for the predictive power of DFT simulations on defect chemistry and we show that such knowledge can provide mechanistic insights for transport phenomena of these oxides (Chapter 2 - 4). Second, we have built an *ab initio* framework for treating charged species redistribution at various extended defects (oxide/oxide interface in Chapter 5, oxide/water interface in Chapter 6 and 7, grain boundaries in Chapter 8). This line of thought has been proven successful for both $ZrO_2$ (Chapter 2 - 8) and $TiO_2$ (Chapter 9).

On bulk oxide defect chemistry, we have demonstrated various examples of the change in dominant defect species with oxygen partial pressure. In the case of undoped $ZrO_2$, we see change from $V_O^{\bullet\bullet}$ (low $P_{O_2}$) to $O_i''$ (high $P_{O_2}$) as dominant oxygen diffusivity contributor, from electron (low $P_{O_2}$) to hole (high $P_{O_2}$) as dominant electronic carrier, from to $H_i^{\bullet}$ (low $P_{O_2}$) to $H_{Zr}'''$ (high $P_{O_2}$) as the dominant form of hydrogen defect. In the case of undoped $TiO_2$, we see change from $Ti_i^{\bullet\bullet\bullet\bullet}$ (low $P_{O_2}$) to $V_{Ti}''''$ (high $P_{O_2}$) as the dominant contributor to titanium diffusivity. This knowledge allows us to intentionally tune the electron chemical potential by acceptor/donor doping, and thus engineer the transport properties of the oxide material.

On charged species redistribution at extended defects, we have demonstrated that it is possible to model based on first-principles calculations the redistribution profiles in the extended space charge layer/diffusion layer. By adopting a grand canonical description of charged species (point defects in oxide, ions in liquid solution), the framework can be readily applied to different types of interfaces and also allows for easy survey of different chemical environment. We have validated the $ZrO_2$/water interface model by comparing the predicted $ZrO_2$ solubility and point of zero charge with experimentally measure value, which shows great consistency.

On the application level, this thesis contributes towards mechanistic understanding of the degradation process of zirconium alloy as nuclear cladding. We now understand the different roles impurity atoms can play in this process. For lithium-accelerated corrosion, we propose that at relatively low concentration, lithium incorporation accelerates oxygen diffusion in the oxide film by acting as donor dopant. At relatively high concentration, lithium contracts the lattice and destabilizes the protective T-$ZrO_2$. This understanding lays the theoretical foundation of replacing lithium with other alkali metal elements in the coolant water because other metal ions down the periodic table expands the lattice and does not have such a strong destabilizing effect.

For alloying elements entering $ZrO_2$, we can separate them into acceptor (Fe, Cr) and donor (Nb) dopants. The former decreases oxygen diffusivity and stabilizes T-$ZrO_2$, while the latter has the opposite effect. Apart from acting as dopant defects, the impurity cations can also get oxidized and form hetero-interface with $ZrO_2$. Our study on $ZrO_2$/$Cr_2O_3$ shows that the extended space charge region around $Cr_2O_3$ particle exhibits suppressed electronic and ionic conductivity, which serves as an important factor in the correlation between increasing SPP and decreasing corrosion rate.

Chapter 9 of this thesis contributes to understanding and controlling the FAST process. We have shown that in Ta-doped $TiO_2$, by changing the oxygen partial pressure in a $Ti_i^{\bullet\bullet\bullet\bullet}$-controlled regime, one can increase cation diffusivity while maintaining the same Joule heating effect, which leads to greater shrinkage. We have also shown that the different signs of grain boundary space charge potential and bulk conductivities in donor- and acceptor-doped $TiO_2$ leads to difference in local heating. In Ta-doped $TiO_2$, the external bias has a linear drop in the bulk of the grain, indicating a homogeneous heating effect. In Ga-doped $TiO_2$, the bias is screened at the grain boundary and oxide/electrode interface, which lead to inhomogeneous Joule heating effect.

On a broader level, we have shown in this thesis that a fully *ab initio* prediction of chemo-mechanical coupling and extended defect effects is achievable. This allows for direct comparison with experimentally measured properties under varying thermodynamic conditions. In achieving this framework, we are able to validate DFT-based results with real world material properties, and these predictions provide mechanistic insights and designing guidelines for experiments. This framework is broadly applicable to technologically-important problems at electrochemical interfaces.

## 10.2 Perspectives and future work

This thesis has shown many successful examples in using DFT-based methods to study defects in oxide materials, understanding the roles of these defects, and provide rationalized defect engineering strategies. However, this is only one step forward towards full *ab initio* prediction of real-world defective materials. There are many possible directions both in utilizing the framework established in this thesis and in developing new methodologies.

First, due to the limitation of computational cost, DFT studies of extended defects are generally limited to a few well-defined structures and orientations. Though we attempted to address this problem to a certain degree (in Chapter 8 we compared space charge effect at three types of $ZrO_2$ grain boundaries), we cannot establish the full structure-property relationship considering the many possible structures of extended defects. For example, we are still not able to give quantitative prediction of conductivities in polycrystalline oxides. Understanding the effect of individual grain boundary serves as an initial step towards that full prediction. With growing computational power as well as advanced high-throughput methods, a lot more can be achieved on this front for oxide materials.

Second, modeling space charge effect in heavily-doped oxides from first-principles calculation remains an open question. While there are theoretical attempts in literature to include defect-defect interaction in space charge models, it is not clear how to obtain the interaction parameters from DFT calculations. Based on the multi-scale nature of this problem, more efforts are needed in bridging existing empirical models with advanced low-cost high-accuracy *ab initio* methods. These developments will allow further investigations on polycrystals of heavily doped binary oxides and perovskites.

Last, though this thesis has focused mainly on transport properties, the bulk defects and their redistribution also control many other properties of oxide materials, such as light absorption and photoluminescence, photovoltaics, magnetic properties, and thermal transport. The framework provided in this thesis provides the equilibrium concentrations of point defects, which serves as a basis for better understanding of various defect-related properties of defective oxides.

## Bibliography


[1] H. Y. Hwang, Y. Iwasa, M. Kawasaki, B. Keimer, N. Nagaosa, and Y. Tokura, Nature materials **11**, 103 (2012).
[2] J. Mannhart and D. G. Schlom, Science **327**, 1607 (2010).
[3] S. V. Kalinin, A. Borisevich, and D. Fong, ACS Nano **6**, 10423 (2012).
[4] S. V. Kalinin and N. A. Spaldin, Science **341**, 858 (2013).
[5] F. Baiutti, G. Logvenov, G. Gregori, G. Cristiani, Y. Wang, W. Sigle, P. A. van Aken, and J. Maier, Nat Commun **6** (2015).
[6] A. Janotti and C. G. Van de Walle, Physical Review B **76**, 165202 (2007).
[7] M. Youssef and B. Yildiz, Physical Review B **86**, 144109 (2012).
[8] S. Kasamatsu, T. Tada, and S. Watanabe, Solid State Ionics **183**, 20 (2011).
[9] A. R. Hassan, A. El-Azab, C. Yablinsky, and T. Allen, Journal of Solid State Chemistry **204**, 136 (2013).
[10] R. A. De Souza, Physical Chemistry Chemical Physics **11**, 9939 (2009).
[11] J. M. Polfus, K. Toyoura, F. Oba, I. Tanaka, and R. Haugsrud, Physical Chemistry Chemical Physics **14**, 12339 (2012).
[12] M. C. Gobel, G. Gregori, and J. Maier, Physical Chemistry Chemical Physics **16**, 10214 (2014).
[13] S. Saraf, M. Markovich, and A. Rothschild, Physical Review B **82**, 245208 (2010).
[14] C. Freysoldt, B. Grabowski, T. Hickel, J. Neugebauer, G. Kresse, A. Janotti, and C. G. Van de Walle, Reviews of Modern Physics **86**, 253 (2014).
[15] G. Makov and M. C. Payne, Physical Review B **51**, 4014 (1995).
[16] G. Henkelman, B. P. Uberuaga, and H. Jónsson, The Journal of Chemical Physics **113**, 9901 (2000).
[17] M. Youssef and B. Yildiz, Physical Review B **89**, 024105 (2014).
[18] A. Franciosi and C. G. Van de Walle, Surface Science Reports **25**, 1 (1996).
[19] C. G. Van de Walle and R. M. Martin, Physical Review B **35**, 8154 (1987).
[20] A. Alkauskas, P. Broqvist, F. Devynck, and A. Pasquarello, Physical Review Letters **101**, 106802 (2008).
[21] J. C. Conesa, The Journal of Physical Chemistry C **116**, 18884 (2012).
[22] K. Yang, J. R. East, and G. I. Haddad, Solid-State Electronics **36**, 321 (1993).
[23] K. Horio and H. Yanai, Electron Devices, IEEE Transactions on **37**, 1093 (1990).
[24] R. F. Pierret, *Semiconductor device fundamentals* (Addison Wesley, 1996).
[25] S. Kasamatsu, T. Tada, and S. Watanabe, e-Journal of Surface Science and Nanotechnology **8**, 93 (2010).
[26] B. Mario, M. Dario, Y. Bilge, L. T. Harry, T. N. Stefan, H. Stephen, A. M. Paul, and W. W. Graeme, Journal of Physics: Condensed Matter **23**, 255402 (2011).
[27] J. Maier, Solid State Ionics **70–71, Part 1**, 43 (1994).
[28] J. Jamnik, J. Maier, and S. Pejovnik, Solid State Ionics **75**, 51 (1995).
[29] J. Maier, Solid State Ionics **143**, 17 (2001).
[30] F. Williams, S. P. Varma, and S. Hillenius, The Journal of Chemical Physics **64**, 1549 (1976).
[31] A. Bernas, C. Ferradini, and J.-P. Jay-Gerin, Chemical Physics **222**, 151 (1997).
[32] J. Cheng and M. Sprik, Physical Chemistry Chemical Physics **14**, 11245 (2012).
[33] C. G. Van de Walle and J. Neugebauer, Nature **423**, 626 (2003).
[34] J. V. Coe, International Reviews in Physical Chemistry **20**, 33 (2001).

[35] M. Todorova and J. Neugebauer, Physical Review Applied **1**, 014001 (2014).
[36] M. Z. Bazant, K. Thornton, and A. Ajdari, Physical Review E **70**, 021506 (2004).
[37] M. Z. Bazant, K. T. Chu, and B. J. Bayly, SIAM Journal on Applied Mathematics **65**, 1463 (2005).
[38] V. L. Shapovalov, Journal of Colloid and Interface Science **454**, 187 (2015).
[39] D. Boda, W. R. Fawcett, D. Henderson, and S. Sokołowski, The Journal of Chemical Physics **116**, 7170 (2002).
[40] D. M. S. Martins, M. Molinari, M. A. Gonçalves, J. P. Mirão, and S. C. Parker, The Journal of Physical Chemistry C **118**, 27308 (2014).
[41] J. Cheng and M. Sprik, Journal of Physics: Condensed Matter **26**, 244108 (2014).
[42] G. Marie-Pierre, S. Michiel, and S. Marialore, Journal of Physics: Condensed Matter **24**, 124106 (2012).
[43] J. Maier, Nat Mater **4**, 805 (2005).
[44] A. Chroneos, B. Yildiz, A. Tarancon, D. Parfitt, and J. A. Kilner, Energy & Environmental Science **4**, 2774 (2011).
[45] U. Schulz *et al.*, Aerospace Science and Technology **7**, 73 (2003).
[46] J. Chevalier, L. Gremillard, A. V. Virkar, and D. R. Clarke, Journal of the American Ceramic Society **92**, 1901 (2009).
[47] W. Guan, S. Long, R. Jia, and M. Liu, Applied Physics Letters **91**, 062111 (2007).
[48] A. T. Motta, A. Couet, and R. J. Comstock, Annual Review of Materials Research **45**, 311 (2015).
[49] C. Proff, S. Abolhassani, and C. Lemaignan, Journal of Nuclear Materials **432**, 222 (2013).
[50] S. Müller and L. Lanzani, Journal of Nuclear Materials **439**, 251 (2013).
[51] B. Cox, Journal of Nuclear Materials **336**, 331 (2005).
[52] Y. H. Jeong, B. J. Baek, S. Y. Park, and et al., Waterside corrosion of zirconium alloys in nuclear power plants, 1999.
[53] S. Suman, M. K. Khan, M. Pathak, R. N. Singh, and J. K. Chakravartty, International Journal of Hydrogen Energy **40**, 5976 (2015).
[54] D. Pêcheur, F. Lefebvre, A. T. Motta, C. Lemaignan, and J. F. Wadier, Journal of Nuclear Materials **189**, 318 (1992).
[55] Y. Hatano and M. Sugisaki, Journal of Nuclear Science and Technology **34**, 264 (1997).
[56] B. Cheng, P. Gilmore, and H. Klepfer, ASTM SPECIAL TECHNICAL PUBLICATION **1295**, 137 (1996).
[57] P. Rudling and G. Wikmark, Journal of Nuclear Materials **265**, 44 (1999).
[58] M. Cologna, J. S. C. Francis, and R. Raj, Journal of the European Ceramic Society **31**, 2827 (2011).
[59] R. Muccillo and E. N. S. Muccillo, Journal of the European Ceramic Society **34**, 915 (2014).
[60] C. Schmerbauch, J. Gonzalez-Julian, R. Röder, C. Ronning, and O. Guillon, Journal of the American Ceramic Society **97**, 1728 (2014).
[61] S. K. Jha, R. Raj, and I. W. Chen, Journal of the American Ceramic Society **97**, 527 (2014).
[62] M. Cologna, B. Rashkova, and R. Raj, Journal of the American Ceramic Society **93**, 3556 (2010).
[63] J. S. C. Francis, R. Raj, and J. Halloran, Journal of the American Ceramic Society **96**, 2754 (2013).
[64] R. I. Todd, E. Zapata-Solvas, R. S. Bonilla, T. Sneddon, and P. R. Wilshaw, Journal of the European Ceramic Society **35**, 1865 (2015).

[65] H. Majidi and K. van Benthem, Physical Review Letters **114**, 195503 (2015).
[66] W. Rheinheimer, M. Fülling, and M. J. Hoffmann, Journal of the European Ceramic Society **36**, 2773 (2016).
[67] K. T. Wan, C. B. Khouw, and M. E. Davis, Journal of Catalysis **158**, 311 (1996).
[68] F. Audry, P. E. Hoggan, J. Saussey, J. C. Lavalley, H. Lauron-Pernot, and A. M. Le Govic, Journal of Catalysis **168**, 471 (1997).
[69] A. I. Kingon, J.-P. Maria, and S. K. Streiffer, Nature **406**, 1032 (2000).
[70] M. Copel, M. Gribelyuk, and E. Gusev, Applied Physics Letters **76**, 436 (2000).
[71] C. Y. Lin, C. Y. Wu, C. Y. Wu, T. C. Lee, F. L. Yang, C. Hu, and T. Y. Tseng, IEEE Electron Device Letters **28**, 366 (2007).
[72] R. Huang, X. Yan, S. Ye, R. Kashtiban, R. Beanland, K. A. Morgan, M. D. B. Charlton, and C. H. de Groot, Nanoscale Research Letters **12**, 384 (2017).
[73] S. I. Klokishner, O. Reu, C. E. Chan-Thaw, F. C. Jentoft, and R. Schlögl, The Journal of Physical Chemistry A **115**, 8100 (2011).
[74] H. Li, J.-I. J. Choi, W. Mayr-Schmölzer, C. Weilach, C. Rameshan, F. Mittendorfer, J. Redinger, M. Schmid, and G. Rupprechter, The Journal of Physical Chemistry C **119**, 2462 (2015).
[75] G. Bakradze, L. P. H. Jeurgens, and E. J. Mittemeijer, The Journal of Physical Chemistry C **115**, 19841 (2011).
[76] A. Christensen and E. A. Carter, Physical Review B **58**, 8050 (1998).
[77] M. Youssef, M. Yang, and B. Yildiz, Physical Review Applied **5**, 014008 (2016).
[78] S. T. Korhonen, M. Calatayud, and A. O. I. Krause, The Journal of Physical Chemistry C **112**, 6469 (2008).
[79] M.-H. Chen, J. C. Thomas, A. R. Natarajan, and A. Van der Ven, Physical Review B **94**, 054108 (2016).
[80] A. S. Foster, V. B. Sulimov, F. Lopez Gejo, A. L. Shluger, and R. M. Nieminen, Physical Review B **64**, 224108 (2001).
[81] B. Puchala and A. Van der Ven, Physical Review B **88**, 094108 (2013).
[82] J. P. Abriata, J. Garcés, and R. Versaci, Bulletin of Alloy Phase Diagrams **7**, 116 (1986).
[83] A. S. Foster, A. L. Shluger, and R. M. Nieminen, Phys Rev Lett **89**, 225901 (2002).
[84] M. Youssef and B. Yildiz, Physical Review B **86**, 144109 (2012).
[85] G. Kresse and J. Hafner, Physical Review B **47**, 558 (1993).
[86] G. Kresse and J. Hafner, Physical Review B **49**, 14251 (1994).
[87] G. Kresse and J. Furthmüller, Computational Materials Science **6**, 15 (1996).
[88] G. Kresse and J. Furthmüller, Physical Review B **54**, 11169 (1996).
[89] J. P. Perdew, K. Burke, and M. Ernzerhof, Physical Review Letters **77**, 3865 (1996).
[90] J. P. Perdew, K. Burke, and M. Ernzerhof, Physical Review Letters **78**, 1396 (1997).
[91] J. Yang, M. Youssef, and B. Yildiz, Physical Chemistry Chemical Physics **19**, 3869 (2017).
[92] A. R. Allnatt and A. B. Lidiard, *Atomic transport in solids* (Cambridge University Press, 2003).
[93] D. T. Gillespie, Journal of Computational Physics **22**, 403 (1976).
[94] A. Einstein, *Investigations on the Theory of the Brownian Movement* (Courier Corporation, 1956).
[95] See supplemental material for additional details of calculating diffusivity from kMC simulation.

[96] J. Xue, Journal of The Electrochemical Society **138**, 36C (1991).
[97] K. Momma and F. Izumi, Journal of Applied Crystallography **44**, 1272 (2011).
[98] J. Greer, A. Korkin, and J. Labanowski, *Nano and giga challenges in microelectronics* (Elsevier, 2003).
[99] A. S. Foster, A. L. Shluger, and R. M. Nieminen, Physical Review Letters **89**, 225901 (2002).
[100] F. J. Keneshea and D. L. Douglass, Oxidation of Metals **3**, 1 (1971).
[101] A. Madeyski and W. W. Smeltzer, Materials Research Bulletin **3**, 369 (1968).
[102] S. Aronson, J. Electrochem. Soc. **108**, 312 (1961).
[103] V. Inozemtsev, IAEA Nuclear Energy Series No. NF-T **2**, 1 (2010).
[104] H. G. Rickover, L. D. Geiger, and B. Lustman, History of the development of zirconium alloys for use in nuclear reactors, 1975.
[105] G. Sabol, Journal of ASTM International **2**, 1 (2005).
[106] E. Hillner, in *Zirconium in the Nuclear Industry* (ASTM International, 1977).
[107] B. Ensor, A. M. Lucente, M. J. Frederick, J. Sutliff, and A. T. Motta, Journal of Nuclear Materials **496**, 301 (2017).
[108] W. Qin, C. Nam, H. L. Li, and J. A. Szpunar, Acta Materialia **55**, 1695 (2007).
[109] M. Guerain, C. Duriez, J. L. Grosseau-Poussard, and M. Mermoux, Corrosion Science **95**, 11 (2015).
[110] N. Vermaak, G. Parry, R. Estevez, and Y. Bréchet, Acta Materialia **61**, 4374 (2013).
[111] A. Garner, A. Gholinia, P. Frankel, M. Gass, I. MacLaren, and M. Preuss, Acta Materialia **80**, 159 (2014).
[112] K. Annand, M. Nord, I. MacLaren, and M. Gass, Corrosion Science **128**, 213 (2017).
[113] E. M. Francis, A. Harte, P. Frankel, S. J. Haigh, D. Jädernäs, J. Romero, L. Hallstadius, and M. Preuss, Journal of Nuclear Materials **454**, 387 (2014).
[114] G. Kresse and J. Hafner, Physical Review B **47**, 558 (1993).
[115] M. Youssef and B. Yildiz, Physical Review B **89** (2014).
[116] M. Youssef, M. Yang, and B. Yildiz, Physical Review Applied **5** (2016).
[117] F. A. Kröger and H. J. Vink, in *Solid State Physics*, edited by F. Seitz, and D. Turnbull (Academic Press, 1956), pp. 307.
[118] F. D. Murnaghan, Proceedings of the National Academy of Sciences of the United States of America **30**, 244 (1944).
[119] F. Birch, Physical Review **71**, 809 (1947).
[120] S. R. Bishop, D. Marrocchelli, C. Chatzichristodoulou, N. H. Perry, M. B. Mogensen, H. L. Tuller, and E. D. Wachsman, Annual Review of Materials Research **44**, 205 (2014).
[121] J. Yang, M. Youssef, and B. Yildiz, Physical Review Materials **2**, 075405 (2018).
[122] Y.-S. Kim, Y.-H. Jeong, and J.-N. Jang, Journal of Nuclear Materials **412**, 217 (2011).
[123] A. Couet, A. T. Motta, and R. J. Comstock, Journal of Nuclear Materials **451**, 1 (2014).
[124] G. Choudhuri, Jagannath, M. Kiran Kumar, V. Kain, D. Srivastava, S. Basu, B. K. Shah, N. Saibaba, and G. K. Dey, Journal of Nuclear Materials **441**, 178 (2013).
[125] A. Yilmazbayhan, A. T. Motta, R. J. Comstock, G. P. Sabol, B. Lai, and Z. Cai, Journal of Nuclear Materials **324**, 6 (2004).
[126] A. J. G. Maroto, R. Bordoni, M. Villegas, A. M. Olmedo, M. A. Blesa, A. Iglesias, and P. Koenig, Journal of Nuclear Materials **229**, 79 (1996).

[127] K. Takeda and H. Anada, in *Zirconium in the Nuclear Industry: Twelfth International Symposium* (ASTM International, 2000).
[128] A. Garner, J. Hu, A. Harte, P. Frankel, C. Grovenor, S. Lozano-Perez, and M. Preuss, Acta Materialia **99**, 259 (2015).
[129] M. Broussely, P. Biensan, and B. Simon, Electrochimica Acta **45**, 3 (1999).
[130] D. Kundu, E. Talaie, V. Duffort, and L. F. Nazar, Angewandte Chemie International Edition **54**, 3431 (2015).
[131] E. D. Wachsman and K. T. Lee, Science **334**, 935 (2011).
[132] A. Chroneos, B. Yildiz, A. Tarancón, D. Parfitt, and J. A. Kilner, Energy & Environmental Science **4**, 2774 (2011).
[133] E. D. Wachsman, C. A. Marlowe, and K. T. Lee, Energy & Environmental Science **5**, 5498 (2012).
[134] P. N. Dyer, R. E. Richards, S. L. Russek, and D. M. Taylor, Solid State Ionics **134**, 21 (2000).
[135] D. T. Gillaspie, R. C. Tenent, and A. C. Dillon, Journal of Materials Chemistry **20**, 9585 (2010).
[136] E. J. Fuller, F. E. Gabaly, F. Léonard, S. Agarwal, S. J. Plimpton, R. B. Jacobs-Gedrim, C. D. James, M. J. Marinella, and A. A. Talin, Advanced materials **29**, 1604310, 1604310 (2017).
[137] D. Marrocchelli, S. R. Bishop, H. L. Tuller, and B. Yildiz, Advanced Functional Materials **22**, 1958 (2012).
[138] M. V. Patrakeev, J. A. Bahteeva, E. B. Mitberg, I. A. Leonidov, V. L. Kozhevnikov, and K. R. Poeppelmeier, Journal of Solid State Chemistry **172**, 219 (2003).
[139] E. Enriquez, A. Chen, Z. Harrell, P. Dowden, N. Koskelo, J. Roback, M. Janoschek, C. Chen, and Q. Jia, Scientific Reports **7**, 46184 (2017).
[140] Q. Lu and B. Yildiz, Nano letters **16**, 1186 (2016).
[141] A. I. Kingon, J.-P. Maria, and S. K. Streiffer, Nature **406**, 1032 (2000).
[142] S. Müller and L. Lanzani, Journal of Nuclear Materials **439**, 251 (2013).
[143] J. Deshon, D. Hussey, B. Kendrick, J. McGurk, J. Secker, and M. Short, JOM **63**, 64 (2011).
[144] W. Liu, B. Zhou, Q. Li, and M. Yao, Corrosion Science **47**, 1855 (2005).
[145] P. Wang and G. S. Was, Journal of Materials Research **30**, 1335 (2015).
[146] A. Krausová, J. Macák, P. Sajdl, R. Novotný, V. Renčiuková, and V. Vrtílková, Journal of Nuclear Materials **467**, 302 (2015).
[147] Y.-M. Chiang, D. P. Birnie, W. D. Kingery, and S. Newcomb, *Physical ceramics: principles for ceramic science and engineering* (Wiley New York, 1997), Vol. 409.
[148] R. W. Balluffi, S. Allen, and W. C. Carter, *Kinetics of materials* (John Wiley & Sons, 2005).
[149] J. Yang, M. Youssef, and B. Yildiz, Physical Review B **97**, 024114 (2018).
[150] W. C. Chueh *et al.*, Chemistry of Materials **24**, 1876 (2012).
[151] D. Chen, S. R. Bishop, and H. L. Tuller, Chemistry of Materials **26**, 6622 (2014).
[152] M. T. Greiner, L. Chai, M. G. Helander, W.-M. Tang, and Z.-H. Lu, Advanced Functional Materials **23**, 215 (2013).
[153] L. B. Shi, Y. P. Wang, and M. B. Li, Materials Science in Semiconductor Processing **27**, 586 (2014).
[154] M. Youssef, B. Yildiz, and K. J. Van Vliet, Physical Review B **95**, 161110 (2017).
[155] F. Bruneval, C. Varvenne, J.-P. Crocombette, and E. Clouet, Physical Review B **91**, 024107 (2015).
[156] Y. H. Jeong, J. H. Baek, S. J. Kim, H. G. Kim, and H. Ruhmann, Journal of Nuclear Materials **270**, 322 (1999).

[157] R. t. Shannon, Acta crystallographica section A: crystal physics, diffraction, theoretical and general crystallography **32**, 751 (1976).
[158] Q. Cao, Y.-F. Cheng, H. Bi, X. Zhao, K. Yuan, Q. Liu, Q. Li, M. Wang, and R. Che, Journal of Materials Chemistry A **3**, 20051 (2015).
[159] D. Colleoni, G. Miceli, and A. Pasquarello, Physical Review B **92**, 125304 (2015).
[160] P. A. Markowich, C. A. C. A. Ringhofer, and C. C. Schmeiser, *Semiconductor equations* (Springer-Verlag, 1990).
[161] B. Van Zeghbroeck, Colarado University (2004).
[162] R. A. De Souza, V. Metlenko, D. Park, and T. E. Weirich, Physical Review B **85**, 174109 (2012).
[163] S. Kim, J. Fleig, and J. Maier, Physical Chemistry Chemical Physics **5**, 2268 (2003).
[164] J. M. Polfus, T. S. Bjorheim, T. Norby, and R. Bredesen, Journal of Materials Chemistry A **4**, 7437 (2016).
[165] D. M. Duffy, J. H. Harding, and A. M. Stoneham, Journal of Applied Physics **76**, 2791 (1994).
[166] Y. Kuru, D. Marrocchelli, S. R. Bishop, D. Chen, B. Yildiz, and H. L. Tuller, J. Electrochem. Soc. **159**, F799 (2012).
[167] T. Tauer, R. O'Hayre, and J. W. Medlin, Journal of Materials Chemistry A **1**, 2840 (2013).
[168] M. Stengel and D. Vanderbilt, Physical Review B **80**, 241103 (2009).
[169] A. Yilmazbayhan, E. Breval, A. T. Motta, and R. J. Comstock, Journal of Nuclear Materials **349**, 265 (2006).
[170] S. L. Dudarev, G. A. Botton, S. Y. Savrasov, C. J. Humphreys, and A. P. Sutton, Physical Review B **57**, 1505 (1998).
[171] F. Lebreau, M. M. Islam, B. Diawara, and P. Marcus, The Journal of Physical Chemistry C **118**, 18133 (2014).
[172] L. Wang, T. Maxisch, and G. Ceder, Physical Review B **73**, 195107 (2006).
[173] M. W. Chase, S. National Institute of, and Technology, *NIST-JANAF thermochemical tables* (American Chemical Society ; American Institute of Physics for the National Institute of Standards and Technology, [Washington, D.C.]; Woodbury, N.Y., 1998).
[174] N. J. Mosey and E. A. Carter, Journal of the Mechanics and Physics of Solids **57**, 287 (2009).
[175] C. A. J. Fisher * and H. Matsubara, Philosophical Magazine **85**, 1067 (2005).
[176] B. E. Gaddy, E. A. Paisley, J.-P. Maria, and D. L. Irving, Physical Review B **90**, 125403 (2014).
[177] K. Steiner, W. Chen, and A. Pasquarello, Physical Review B **89**, 205309 (2014).
[178] S. Baroni, R. Resta, A. Baldereschi, and M. Peressi, in *Spectroscopy of Semiconductor Microstructures*, edited by G. Fasol, A. Fasolino, and P. Lugli (Springer US, 1989), pp. 251.
[179] J. Maier, *Physical chemistry of ionic materials: ions and electrons in solids* (John Wiley & Sons, 2004).
[180] S. P. Waldow and R. A. De Souza, ACS Applied Materials & Interfaces **8**, 12246 (2016).
[181] S. Kim and J. Maier, J. Electrochem. Soc. **149**, J73 (2002).
[182] R. A. De Souza, F. Gunkel, S. Hoffmann-Eifert, and R. Dittmann, Physical Review B **89**, 241401 (2014).
[183] E. E. Helgee, A. Lindman, and G. Wahnström, Fuel Cells **13**, 19 (2013).

[184] B. Joakim Nyman, E. E. Helgee, and G. Wahnström, Applied Physics Letters **100**, 061903 (2012).
[185] X. Guo and J. Maier, Advanced Functional Materials **19**, 96 (2009).
[186] T. Siebert, B. Guchhait, Y. Liu, B. P. Fingerhut, and T. Elsaesser, The Journal of Physical Chemistry Letters, 3131 (2016).
[187] K. Krishnaswamy, C. E. Dreyer, A. Janotti, and C. G. Van de Walle, Physical Review B **92**, 085420 (2015).
[188] H. Peelaers, K. Krishnaswamy, L. Gordon, D. Steiauf, A. Sarwe, A. Janotti, and C. G. Van de Walle, Applied Physics Letters **107**, 183505 (2015).
[189] A. Holt and P. Kofstad, Solid State Ionics **69**, 127 (1994).
[190] S. C. Tsai, A. M. Huntz, and C. Dolin, Materials Science and Engineering: A **212**, 6 (1996).
[191] S. Balaz, Z. Zeng, and L. J. Brillson, Journal of Applied Physics **114**, 183701 (2013).
[192] X. Li, J. Yu, J. Low, Y. Fang, J. Xiao, and X. Chen, Journal of Materials Chemistry A **3**, 2485 (2015).
[193] Y. Hikita, K. Nishio, L. C. Seitz, P. Chakthranont, T. Tachikawa, T. F. Jaramillo, and H. Y. Hwang, Advanced Energy Materials, n/a, 1502154 (2016).
[194] D. J. Griffiths, *Introduction to electrodynamics* (prentice Hall Upper Saddle River, NJ, 1999), Vol. 3.
[195] J. H. Lee and A. Selloni, Physical Review Letters **112**, 196102 (2014).
[196] A. Lindman, E. E. Helgee, and G. Wahnström, Solid State Ionics **252**, 121 (2013).
[197] K. P. McKenna, M. J. Wolf, A. L. Shluger, S. Lany, and A. Zunger, Physical Review Letters **108**, 116403 (2012).
[198] R. Shaltaf, G. M. Rignanese, X. Gonze, F. Giustino, and A. Pasquarello, Physical Review Letters **100**, 186401 (2008).
[199] A. Aryanfar, J. Thomas, A. Van der Ven, D. Xu, M. Youssef, J. Yang, B. Yildiz, and J. Marian, JOM **68**, 2900 (2016).
[200] A. G. Scheuermann, J. P. Lawrence, K. W. Kemp, T. Ito, A. Walsh, C. E. D. Chidsey, P. K. Hurley, and P. C. McIntyre, Nature materials **15**, 99 (2015).
[201] T. A. Pham, Y. Ping, and G. Galli, Nature materials **16**, 401 (2017).
[202] O. Zandi and T. W. Hamann, The journal of physical chemistry letters **5**, 1522 (2014).
[203] H. Hussain *et al.*, Nature materials **16**, 461 (2016).
[204] A. Indra, P. W. Menezes, and M. Driess, ChemSusChem **8**, 776 (2015).
[205] S. Aranifard, S. C. Ammal, and A. Heyden, Journal of Catalysis **309**, 314 (2014).
[206] M. M. Najafpour *et al.*, Chemical reviews **116**, 2886 (2016).
[207] R. Mu, Z.-j. Zhao, Z. Dohnalek, and J. Gong, Chemical Society Reviews **46**, 1785 (2017).
[208] M. Tuckerman, K. Laasonen, M. Sprik, and M. Parrinello, The Journal of Chemical Physics **103**, 150 (1995).
[209] D. Marx, M. E. Tuckerman, J. Hutter, and M. Parrinello, Nature **397**, 601 (1999).
[210] M. E. Tuckerman, D. Marx, and M. Parrinello, Nature **417**, 925 (2002).
[211] M. Farnesi Camellone, F. Negreiros Ribeiro, L. Szabová, Y. Tateyama, and S. Fabris, Journal of the American Chemical Society **138**, 11560 (2016).
[212] G. Tocci and A. Michaelides, The journal of physical chemistry letters **5**, 474 (2014).
[213] Z.-T. Wang *et al.*, Proceedings of the National Academy of Sciences (2017).
[214] M. E. McBriarty, G. F. von Rudorff, J. E. Stubbs, P. J. Eng, J. Blumberger, and K. M. Rosso, Journal of the American Chemical Society **139**, 2581 (2017).

[215] S. Laporte, F. Finocchi, L. Paulatto, M. Blanchard, E. Balan, F. Guyot, and A. M. Saitta, Physical chemistry chemical physics : PCCP **17**, 20382 (2015).
[216] R. Sato, S. Ohkuma, Y. Shibuta, F. Shimojo, and S. Yamaguchi, The Journal of Physical Chemistry C **119**, 28925 (2015).
[217] M. Todorova and J. Neugebauer, Physical Review Applied **1** (2014).
[218] L. R. Martins, M. S. Skaf, and B. M. Ladanyi, The Journal of Physical Chemistry B **108**, 19687 (2004).
[219] J. Chevalier, Biomaterials **27**, 535 (2006).
[220] O. Teleman, B. Jönsson, and S. Engström, Molecular Physics **60**, 193 (1987).
[221] J. D. Gale, Journal of the Chemical Society, Faraday Transactions **93**, 629 (1997).
[222] J. D. Gale and A. L. Rohl, Molecular Simulation **29**, 291 (2003).
[223] S. Grimme, J. Antony, S. Ehrlich, and H. Krieg, The Journal of Chemical Physics **132**, 154104 (2010).
[224] S. Grimme, S. Ehrlich, and L. Goerigk, Journal of Computational Chemistry **32**, 1456 (2011).
[225] S. Kerisit and S. C. Parker, Journal of the American Chemical Society **126**, 10152 (2004).
[226] R. Burt, G. Birkett, and X. S. Zhao, Physical chemistry chemical physics : PCCP **16**, 6519 (2014).
[227] S. Kim, J. Fleig, and J. Maier, Phys. Chem. Chem. Phys. **5**, 2268 (2003).
[228] F. Baiutti, G. Logvenov, G. Gregori, G. Cristiani, Y. Wang, W. Sigle, P. A. van Aken, and J. Maier, Nature communications **6**, 8586 (2015).
[229] K. K. Adepalli, J. Yang, J. Maier, H. L. Tuller, and B. Yildiz, Advanced Functional Materials **27**, 1700243, 1700243 (2017).
[230] C.-C. Chen and J. Maier, Nature Energy **3**, 102 (2018).
[231] A. Y. Borisevich *et al.*, Physical Review B **86** (2012).
[232] J. Huang, B. G. Sumpter, and V. Meunier, Chemistry **14**, 6614 (2008).
[233] H. Wang and L. Pilon, The Journal of Physical Chemistry C **115**, 16711 (2011).
[234] L. Xing, J. Vatamanu, G. D. Smith, and D. Bedrov, The journal of physical chemistry letters **3**, 1124 (2012).
[235] G. S. Karlberg, J. Rossmeisl, and J. K. Norskov, Physical Chemistry Chemical Physics **9**, 5158 (2007).
[236] E. M. Stuve, Chemical Physics Letters **519-520**, 1 (2012).
[237] Y. Kuan‐Yu and J. M. J., Journal of Computational Chemistry **32**, 3399 (2011).
[238] F. Calle-Vallejo and M. T. M. Koper, Electrochimica Acta **84**, 3 (2012).
[239] F. Ambrosio, G. Miceli, and A. Pasquarello, The Journal of Physical Chemistry B **120**, 7456 (2016).
[240] T. S. Hofer and P. H. Hünenberger, The Journal of Chemical Physics **148**, 222814 (2018).
[241] J. Cheng and M. Sprik, Physical chemistry chemical physics : PCCP **14**, 11245 (2012).
[242] J. Rossmeisl, K. Chan, R. Ahmed, V. Tripkovic, and M. E. Bjorketun, Physical chemistry chemical physics : PCCP **15**, 10321 (2013).
[243] M. H. Hansen and J. Rossmeisl, The Journal of Physical Chemistry C **120**, 29135 (2016).
[244] X. Rong and A. M. Kolpak, The journal of physical chemistry letters **6**, 1785 (2015).
[245] H. Liang-Feng and M. R. James, Journal of Physics: Condensed Matter **29**, 475501 (2017).

[246] L. F. Huang, M. J. Hutchison, R. J. Santucci, J. R. Scully, and J. M. Rondinelli, The Journal of Physical Chemistry C **121**, 9782 (2017).
[247] F. Ambrosio, J. Wiktor, and A. Pasquarello, ACS applied materials & interfaces **10**, 10011 (2018).
[248] J. St»hlberg, Journal of Chromatography A **356**, 231 (1986).
[249] J. Yang, M. Youssef, and B. Yildiz, Physical Review B **97**, 024114 (2018).
[250] W. M. Haynes, *CRC handbook of chemistry and physics* (CRC press, 2014).
[251] J. Yang, M. Youssef, and B. Yildiz, In preparation (2018).
[252] T. Kobayashi, T. Sasaki, I. Takagi, and H. Moriyama, Journal of Nuclear Science and Technology **44**, 90 (2007).
[253] S. Muhammad, S. Hussain, M. Waseem, A. Naeem, J. Hussain, and M. T. Jan, Iranian Journal of Science and Technology **36**, 481 (2012).
[254] Y.-P. Zeng, A. Zimmermann, F. Aldinger, and D. Jiang, Journal of the European Ceramic Society **28**, 2597 (2008).
[255] R. G. de Kretser and P. J. Scales, Journal of colloid and interface science **328**, 187 (2008).
[256] S. Ardizzone and C. L. Bianchi, Journal of Electroanalytical Chemistry **465**, 136 (1999).
[257] Y. Broy, F. Garzarolli, A. Seibold, and L. Van Swam, in *Zirconium in the Nuclear Industry: Twelfth International Symposium* (ASTM International, 2000).
[258] A. Chroneos, B. Yildiz, A. Tarancón, D. Parfitt, and J. A. Kilner, Energy & Environmental Science **4**, 2774 (2011).
[259] A. Dey, Materials Science and Engineering: B **229**, 206 (2018).
[260] Y. S. Lin, Industrial & Engineering Chemistry Research **58**, 5787 (2019).
[261] T. Wan, L. Zhang, H. Du, X. Lin, B. Qu, H. Xu, S. Li, and D. Chu, Critical Reviews in Solid State and Materials Sciences **43**, 47 (2018).
[262] Y. Aoki, C. Wiemann, V. Feyer, H.-S. Kim, C. M. Schneider, H. Ill-Yoo, and M. Martin, Nature communications **5**, 3473 (2014).
[263] P. Erhart and K. Albe, Physical Review B **73**, 115207 (2006).
[264] A. R. Genreith-Schriever, P. Hebbeker, J. Hinterberg, T. Zacherle, and R. A. De Souza, The Journal of Physical Chemistry C **119**, 28269 (2015).
[265] J. Mulroue and D. M. Duffy, Proceedings of the Royal Society A: Mathematical, Physical and Engineering Sciences **467**, 2054 (2011).
[266] A. Goyal, P. Gorai, H. Peng, S. Lany, and V. Stevanović, Computational Materials Science **130**, 1 (2017).
[267] G. Gregori, R. Merkle, and J. Maier, Progress in Materials Science **89**, 252 (2017).
[268] R. A. De Souza and E. C. Dickey, Philosophical Transactions of the Royal Society A: Mathematical, Physical and Engineering Sciences **377**, 20180430 (2019).
[269] Y. Lin, S. Fang, D. Su, K. S. Brinkman, and F. Chen, Nature communications **6**, 6824 (2015).
[270] D. S. Aidhy and W. J. Weber, Journal of Materials Research **31**, 2 (2015).
[271] W. Körner and C. Elsässer, Physical Review B **81**, 085324 (2010).
[272] W. Körner and C. Elsässer, Physical Review B **83**, 205315 (2011).
[273] F. Yuan, B. Liu, Y. Zhang, and W. J. Weber, The Journal of Physical Chemistry C **120**, 6625 (2016).
[274] Z. Mao, S. B. Sinnott, and E. C. Dickey, Journal of the American Ceramic Society **85**, 1594 (2002).
[275] J. A. Dawson and I. Tanaka, Journal of Materials Chemistry A **2**, 1400 (2014).
[276] M. Behtash, J. Wong, S. Jiang, J. Luo, and K. Yang, Journal of the European Ceramic Society **39**, 3812 (2019).

[277] J. M. Polfus, K. Toyoura, F. Oba, I. Tanaka, and R. Haugsrud, Physical chemistry chemical physics : PCCP **14**, 12339 (2012).
[278] J.-S. Kim, J.-H. Yang, B.-K. Kim, and Y.-C. Kim, Journal of the Ceramic Society of Japan **123**, 245 (2015).
[279] D. S. Mebane and R. A. De Souza, Energy Environ. Sci. **8**, 2935 (2015).
[280] X. Tong, D. S. Mebane, and R. A. De Souza, Journal of the American Ceramic Society **103**, 5 (2020).
[281] S. Hong, D. Lee, Y. Lim, J. Bae, and Y.-B. Kim, Ceramics International **42**, 16703 (2016).
[282] J.-Z. Kong, S.-S. Wang, G.-A. Tai, L. Zhu, L.-G. Wang, H.-F. Zhai, D. Wu, A.-D. Li, and H. Li, Journal of Alloys and Compounds **657**, 593 (2016).
[283] K. W. Schlichting, N. P. Padture, and P. G. Klemens, Journal of Materials Science **36**, 3003 (2001).
[284] X. Guo and R. Waser, Progress in Materials Science **51**, 151 (2006).
[285] R. A. De Souza, M. J. Pietrowski, U. Anselmi-Tamburini, S. Kim, Z. A. Munir, and M. Martin, Physical Chemistry Chemical Physics **10**, 2067 (2008).
[286] X. Guo and Z. Zhang, Acta Materialia **51**, 2539 (2003).
[287] U. Brossmann, R. Würschum, U. Södervall, and H.-E. Schaefer, Journal of Applied Physics **85**, 7646 (1999).
[288] J. Cheng, J. Luo, and K. Yang, Computational Materials Science **155**, 92 (2018).
[289] S. Grasso, Y. Sakka, and G. Maizza, Sci Technol Adv Mater **10**, 053001 (2009).
[290] K. A. Khor, L. G. Yu, S. H. Chan, and X. J. Chen, Journal of the European Ceramic Society **23**, 1855 (2003).
[291] S. K. Jha, X. L. Phuah, J. Luo, C. P. Grigoropoulos, H. Wang, E. García, and B. Reeja-Jayan, Journal of the American Ceramic Society **102**, 5 (2019).
[292] C. S. Bonifacio, T. B. Holland, and K. van Benthem, Scripta Materialia **69**, 769 (2013).
[293] J. Narayan, Scripta Materialia **176**, 117 (2020).
[294] H. Majidi and K. van Benthem, Phys Rev Lett **114**, 195503 (2015).
[295] W. Rheinheimer, J. P. Parras, J.-H. Preusker, R. A. De Souza, and M. J. Hoffmann, Journal of the American Ceramic Society **102**, 3779 (2019).
[296] S.-W. Kim, S.-J. L. Kang, and I. W. Chen, Journal of the American Ceramic Society **96**, 1398 (2013).
[297] T. B. Holland, U. Anselmi-Tamburini, D. V. Quach, T. B. Tran, and A. K. Mukherjee, Journal of the European Ceramic Society **32**, 3659 (2012).
[298] K. Hoshino, N. L. Peterson, and C. L. Wiley, Journal of Physics and Chemistry of Solids **46**, 1397 (1985).
[299] D.-K. Lee and H.-I. Yoo, Physical Chemistry Chemical Physics **10**, 6890 (2008).